Title

Ultrafast Carrier-Lattice Dynamics in Nanoparticles and Films using Extreme Ultraviolet Transient Absorption

Author

Porter, Ilana Jessica

Publication Date

2022

Ultrafast Carrier-Lattice Dynamics in Nanoparticles and Films using Extreme Ultraviolet Transient Absorption

by

Ilana Jessica Porter

A dissertation submitted in partial satisfaction of the

requirements for the degree of

Doctor of Philosophy

in

Chemistry

in the

Graduate Division

of the

University of California, Berkeley

Committee in charge:

Professor Stephen R. Leone, Chair
Professor David Attwood
Professor Richard Saykally

Spring 2022

Ultrafast Carrier-Lattice Dynamics in Nanoparticles and Films using Extreme Ultraviolet Transient Absorption

Abstract

Ultrafast Carrier-Lattice Dynamics in Nanoparticles and Films using Extreme Ultraviolet Transient Absorption

by

Ilana Jessica Porter

Doctor of Philosophy in Chemistry

University of California, Berkeley

Professor Stephen R. Leone, Chair

The motion of electrons and nuclei, or of charge carriers and lattice, respectively, in a solid system, are the most fundamental dynamics in nature. Understanding the ultrafast behavior of electrons, holes and phonons is critical to understanding and controlling the light-induced response of materials, most crucially for photovoltaic and photoelectrochemical application. In these materials, it is not understood why nanoparticles and other nanoscale systems exhibit such different macroscopic responses to solar irradiation, such as increased photocurrent or improved charge transfer efficiency. Unfortunately, few techniques exist with which to measure photoexcited phenomena on the femtosecond and picosecond timescales that electronic and nuclear motion occurs, and even fewer are sensitive to both charge carriers and lattice changes. Here, the technique of extreme ultraviolet (XUV) transient absorption spectroscopy is applied to a variety of nanoparticle and nanoscale solar energy relevant material systems to uncover the coupled carrier-lattice relaxation processes following absorption of a solar photon. XUV light initiates a core-to-valence transition, so it is uniquely able to simultaneously measure electrons, holes, and lattice dynamics with few-femtosecond time resolution. XUV is also sensitive to oxidation state and spin state and is element specific, making it ideal for answering the lingering questions in the solar energy field.

In this dissertation, we begin in Chapter 1 with a description of semiconductors and nanoparticles, focusing on the ultrafast dynamics of charge carriers and the lattice. Then, core-level spectroscopy is introduced, and the process of high-order harmonic generation to create the XUV core level spectrum is explored. In Chapter 2, the ultrafast laser and high vacuum setup is presented, followed by an analysis of nanoparticle thin film sample preparation. Chapter 3 delves into the first nanoparticle transient XUV absorption experiment, which utilizes iron oxide nanoparticles (goethite α-FeO(OH)) and bulk iron oxide films (hematite α-Fe_2O_3) to demonstrate a link between morphology, crystal structure and photoexcited

small polaron formation. A nanoscale metal-oxide-semiconductor junction of Ni-TiO_2-Si is explored in Chapter 4, and the ultrafast hole dynamics across all three layers of the junction are revealed. In Chapter 5, a hot phonon bottleneck is demonstrated to slow hot carrier cooling in silicon nanoparticles following above-gap photoexcitation when compared to a single-crystal silicon bulk. Finally, Chapter 6 outlines the current progress studying hot hole and lattice relaxation in the ferroelectric semiconducting halide perovskite $CsGeI_3$ and proposes future directions in nanoparticles and thin films with extreme ultraviolet transient absorption spectroscopy.

To my family

Both smooth and wrinkly brained

Contents

List of Figures

List of Tables

Acknowledgments

There is no way I could have done this without the support of my incredible parents, my amazing brothers, sisters-in-law, niece and nephews, and my most wonderful partner and rat co-parent. Mom, you are my best friend and my rock. I can always call you when I need to be talked off a ledge. Dad, you always put a smile on my face and remind me how nerdy this whole spectroscopy thing is. Zach, you're my sounding board and the other half of my brain. Todd and Chris, your support means so much to me. Emilie, I love you to your asteroid and back. Lenny and Tony, I can't understate how incredibly sweet and loving you have been to me for your entire lives. And Brian, the laser man himself. You are the love of my life, my partner and friend, and my most trusted advisor. I could not have kept my lasers and myself running without you.

I was so lucky to have a superb group of mentors and colleagues throughout the past six years of graduate school. Thank you Scott Cushing for teaching me how to set up a study and take care of a lab. Thanks Lucas Carneiro, Peter Kraus, and Michael Zuerch for teaching me how XUV works. I am grateful to Brett Marsh, Natalie Gibson, Chang-Ming Jiang, Andrew Attar, Ashley Fidler, Marina Yang, Alex Guggenmos, Briana Clarke, Lou Barreau, Romain Geneaux, Juwon Oh, and Chris Kaplan for the support and friendship. Andrew Ross, you're a great help in the lab and on the softball team. Thanks Yuki Kobayashi for being my desk-bud for most of my time in D44. Thank you to my cohort labmates Bethany de Roulet, Kristina Chang, and Chris Tian Xue – we've almost done it! Thanks to my group members Eric Haugen, Yen-Cheng Lin, Nicki Puskar, Xiangyu Xing, Michael Epshtein, Jen-Hao Ou, Kuntal Chatterjee, James Gaynor, Ruoyi Yin, and my collaborators Zhenni Lin, Jakob Dahl, and Ye Zhang. I really appreciate the support and perspective, in the lab and at the lunch table, of Val Scutelnic, Lorenz Drescher, Tymur Parpiiev, John Beetar, Enrico Ridente, and Rafa Quintero-Bermudez. Much appreciation goes to Dante Valdez, Kathleen Buckley, and Kaydren Orcutt, as well as Carl, Roy, Doug, Jody and Ryan. Man-Nung Su, you are a great friend and incredible spectroscopist. I owe a lot to Hung-Tzu Chang, whose help and advice in lab and in teaching was invaluable. I couldn't have done this without Angela Lee - you always make me laugh, even when we are laughing at me. Jonah Adelman, you have helped me so much in lab and have become an amazing experimentalist - I can't wait to see what you discover. I hope to collaborate with you all again!

The biggest thanks must go toward Steve for his guidance and mentorship. I couldn't have asked for a better PI because one doesn't exist. You always challenged me to be better in the lab and supported me through the years of teaching, manuscript writing, and fixing lasers. When things got really difficult, I knew I could count on you to back me up, and your confidence in me was an immense help. Your ability to be at once a scientific genius and a compassionate advisor to your students inspires me for my future career. I can't thank you enough for this opportunity.

Chapter 1

Introduction

From the first discovery of the 'Egyptian blue' synthetic pigment over 4,000 years ago, humans have utilized the unique light absorption properties of nanoparticles.[1] The quantum size effect of nanoparticles versus their bulk counterparts was first described by Michael Faraday in 1857 for colloidal Au.[2] With the discovery of the photovoltaic effect by Becquerel in 1839,[3] and more recently the realization of photoelectrochemical water splitting by Fujishima and Honda in 1972,[4] researchers have investigated nanoparticles for photovoltaic and photoelectrochemical application.[5, 6] While nano-scale materials have been shown to greatly enhance the light absorption, charge transport, and catalytic activity of solar energy materials, an understanding of the photoexcited dynamics that occur on an ultrafast (sub-picosecond or sub-10^{-12} s) timescale has been more elusive. Modern ultrafast spectroscopic techniques, such as optical or IR pump-probe spectroscopy, fail to capture the element-specificity and sensitivity to both charge carrier and lattice required to analyze, control and improve solar devices. In this dissertation, we utilize the technique of ultrafast time-resolved extreme ultraviolet (XUV) absorption spectroscopy, which is sensitive to these properties, to answer some of the lingering questions in the solar energy nanomaterials field.

This chapter will first introduce the light-induced dynamics that occur on an ultrafast timescale in semiconductor materials and the additional considerations for nanoparticles and other nano-scale materials. Next, an overview of core level spectroscopy with ultrafast time resolution will be presented. Finally, the process of producing the extreme ultraviolet light needed to perform core level spectroscopy is discussed.

1.1 Photoexcited Processes in Semiconductors

Semiconductors are a class of solid materials that possess intermediate conductivity between a metal and an insulator. This property is a consequence of the density of electronic states in a semiconductor, which have a range of energies over which no electronic states are possible. This gap of states occurs between a mostly filled continuum of states, or the valence band, and a mostly empty continuum of states, or the conduction band, named because electrons in this band are highly mobile (see Figure 1.1). When this so-called 'band gap' is less than about 2—4 eV, a material is considered to be a semiconductor.[7] Since visible light has the same energy as a semiconductor's band gap, semiconductors can absorb a photon of light by exciting an electron from the valence band to the conduction band, leaving a positively charged 'hole' in its place. It has been of great research and commercial

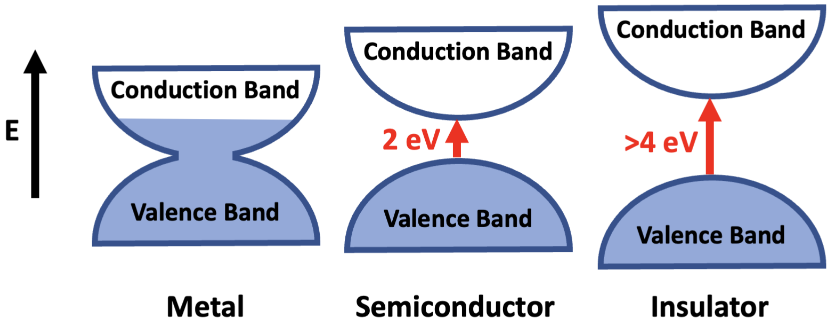

Figure 1.1: **A diagram of the difference between metals, insulators and semiconductors.** The filled states are shown in light blue and the empty states are shown in white. A metal has no gap between filled and unfilled states. A semiconductor has a gap below 2—4 eV, and an insulator has a gap above 4 eV.

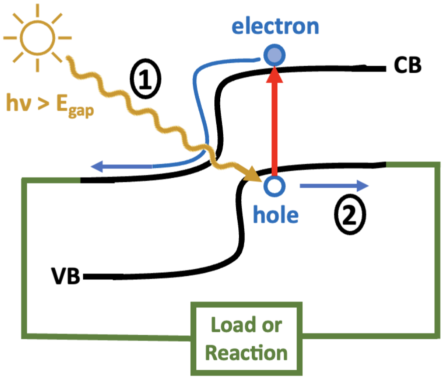

Figure 1.2: **Schematic of light absorption by a photovoltaic or photoelectrode.** In step 1, a photon of solar light with energy above the band gap excites an electron into the conduction band (CB), leaving behind a hole in the valence band (VB). In step 2, the photoexcited carriers migrate into the circuit (load) or to the surface to catalyze a chemical reaction (reaction).

interest to utilize these photogenerated electrons and holes to produce solar energy and to perform catalysis.[8]

The primary property of importance for a material to be a photovoltaic (used in solar-to-energy conversion) or a photoelectrode (used for photoelectrochemistry) is how well it absorbs solar light (step 1 in Figure 1.2). Shockley and Queisser derived an expression for the maximum efficiency limit of a solar cell based on the band gap, with the maximum occurring around 1.1 eV.[9] However, there are additional properties beyond absorption that a photovoltaic or photoelectrode material must possess to be efficient at harvesting solar light. The material must be able to transport charges well in order to generate current in a power line or for the charges to migrate to the catalytic interface (step 2 in Figure

1.2).[10, 11] For efficient transport, the photoexcited charges must have a high mobility, often influenced by doping, and have a long lifetime, aided by minimizing the number of trapping and recombination centers. Both the absorption of light and the thermalization and decay of photoexcited carriers occurs on an ultrafast timescale. Therefore, an understanding of the ultrafast dynamics that underlie solar light absorption in nanomaterials is critical.

In this section, the properties of semiconducting materials in equilibrium will be reviewed, as well as the ultrafast processes that occur following light absorption. Then, the unique properties of semiconducting nanomaterials is discussed.

1.1.1 Properties of Semiconductors

All of the properties of semiconductors are derived from the atoms that comprise the semiconductor and their bonding arrangement.[7] Due to the nearly infinite number of atoms present in a semiconductor crystal, there is a continuous density of electronic states. This density of states (DOS) can be approximated using a variety of methods, including the tight-binding model, which assumes the crystal is composed of molecular bonds, and the free-electron model, which assumes free electrons exist in a periodic potential. While the former model treats electronic motion as migration from one atomic center to the next and the latter model treats it as free conduction, both models result in energy bands with a periodic structure in momentum space, k, that are parabolic in nature. Thus, we can define the effective mass of an electron in the conduction band or of a hole in the valence band as

$$\frac{\hbar^2}{m^*(k)} = \frac{\partial^2 E}{\partial k^2} \tag{1.1}$$

where m^* is the effective mass and E is the energy.

For low densities of electrons and holes, one can apply the Drude transport equation to determine the motion of charge carriers.[12] The equations are as follows

$$m_e^* d\mathbf{v}/dt = -e(\mathbf{E} + \mathbf{v} \times \mathbf{B}) - m_e^* \mathbf{v}/\tau \tag{1.2}$$

$$m_h^* d\mathbf{v}/dt = e(\mathbf{E} + \mathbf{v} \times \mathbf{B}) - m_h^* \mathbf{v}/\tau \tag{1.3}$$

where $\mathbf{v}$ is velocity, $\mathbf{E}$ and $\mathbf{B}$ are the electric and magnetic fields, e is the charge of an electron, and τ is the scattering time. The first term on the right is the Lorentz force on the electron or hole, and the second term is the drag force.[7] This allows us to define the mobility, μ_e, of the charge carrier as

$$\mu_e = |\mathbf{v}|/|\mathbf{E}| = |e\tau/m^*| \tag{1.4}$$

In other words, charge carriers will migrate through the potential field they experience until slowed by scattering. Unfortunately, the Drude model does not clearly define what the scattering time is. A brief description of the types of carrier scattering is given in section 1.1.2.

Another method for describing the motion of charge carriers in a semiconductor is the Hubbard model.[13, 14] This model extends upon the tight-binding model by adding the electron-electron interaction. The Hubbard Hamiltonian can be written in second quantization notation as

$$H_H = t \sum_{i,j,\sigma} c^\dagger_{i\sigma} c_{j\sigma} + U \sum_i n_{i\uparrow} n_{i\downarrow} \tag{1.5}$$

where i and j are the electron sites and σ is the spin, which can be up ($\uparrow$) or down ($\downarrow$), t is the hopping matrix element and the sum for this term is performed over nearest-neighbors only, and U is the on-site interaction matrix element. $c^\dagger_{i\sigma}$ is the creation operator for an electron at site i with spin σ, $c_{j\sigma}$ is the annihilation operator at site j with spin σ, and $n_{i\sigma} = c^\dagger_{i\sigma} c_{j\sigma}$. For a material where the hopping parameter t is much larger than the on-site repulsion term U, the material will be metallic as hopping from site to site is favorable. In the opposite case, where $t \ll U$, the material will be insulating as repulsion will be too strong for electrons to hop. These additional interactions allow the Hubbard model to describe many insulating materials, such as transition metal oxides and Mott insulators, quite well.[15]

Charge Carrier States

In both of these models, the number of conduction band electrons (or valence band holes) greatly affects their mobility, formalized via scattering or via electron-electron repulsion. Here we derive expressions to describe the charge carrier filling in the bands. The occupancy of the conduction band at a given temperature, $n(T)$, can be described with Fermi-Dirac statistics as follows

$$n(T) = \int_{\epsilon_c}^{\infty} d\epsilon g_c(\epsilon) n_F(\beta(\epsilon - \mu)) = \int_{\epsilon_c}^{\infty} d\epsilon \frac{g_c(\epsilon)}{e^{\beta(\epsilon-\mu)} + 1} \tag{1.6}$$

where ϵ is the energy variable, ϵ_c is the conduction band minimum energy, n_F is the Fermi occupation factor, $\beta^{-1} = k_B T$, μ is the chemical potential (also referred to as the Fermi level), and g_c is the conduction band density of states. Assuming parabolic bands of nearly free electrons with mass m_e^*, the DOS very close to the conduction band minimum is approximately

$$g_c(\epsilon \geq \epsilon_c) \approx \frac{(2m_e^*)^{3/2}}{2\pi^2\hbar^3} \sqrt{\epsilon - \epsilon_c} \tag{1.7}$$

for $\hbar$ Planck's constant.

Moreover, when the chemical potential is well below the conduction band minimum, or $\beta(\epsilon - \mu) \gg 1$, the Fermi occupation can be approximated as $e^{-\beta(\epsilon-\mu)}$. Plugging these values in and utilizing integration rules, we arrive at the following expression for the density of electrons in the conduction band

$$n(T) = \frac{1}{4} \left(\frac{2m_e^* k_b T}{\pi\hbar^2} \right)^{3/2} e^{-\beta(\epsilon_c - \mu)} \tag{1.8}$$

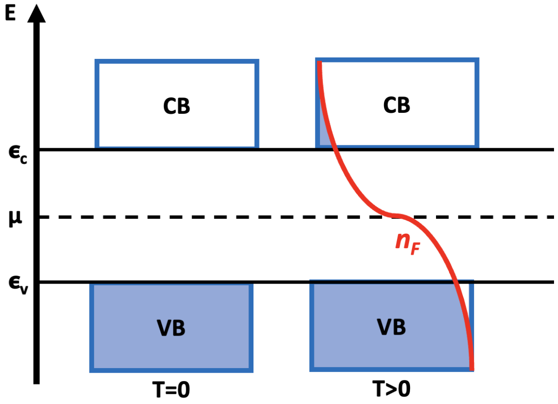

Figure 1.3: **The occupation of electrons and holes at zero and finite temperature.** Filled states are shown in blue and unfilled states are white. At zero temperature, the valence band is completely filled and the conduction band is completely empty. At temperature T>0, there exists a Fermi-Dirac distribution (red line) of electrons (holes) in the conduction (valence) band described by the Fermi occupation factor n_F.

and similarly for the holes with density $p(T)$, mass m_h^* and valence band maximum energy ϵ_v we obtain

$$p(T) = \frac{1}{4}\left(\frac{2m_h^* k_b T}{\pi\hbar^2}\right)^{3/2} e^{-\beta(\mu-\epsilon_v)} \tag{1.9}$$

For an intrinsic (undoped) semiconductor, the number of electrons and holes must be equal. Setting eq 1.8 and eq 1.9 equal and taking the log of both sides, we obtain the following expression for the chemical potential, μ:

$$\mu = \frac{1}{2}(\epsilon_c + \epsilon_v) + \frac{3}{4}(k_b T) log(m_h^*/m_e^*) \tag{1.10}$$

Thus, at zero temperature, the chemical potential will be directly in the middle of the gap.[7] A schematic of the carrier distribution at zero temperature and nonzero temperature is shown in Figure 1.3.

Of course, doped (extrinsic) semiconductors are very often used in photovoltaic and photoelectrochemical applications. A dopant is defined as an impurity state and may either be an electron donor (n-dopant) or an electron acceptor (p-dopant, also called a hole donor). For example, in Si, which has 4 valence electrons, an n-dopant could be P with 5 electrons, and a p-dopant could be B with 3 electrons. Dopants effectively add states within the band gap, with n-dopants adding states near the conduction band and p-dopants adding states near the valence band. Additionally, dopants may be ‘deep’ or ‘shallow’, i.e. close to the midgap or close to the band edge. Deep donors act as recombination centers and are generally unfavorable. Shallow donor states are more likely to be thermally excited into the conduction or valence band, creating an equilibrium population of electrons or holes.

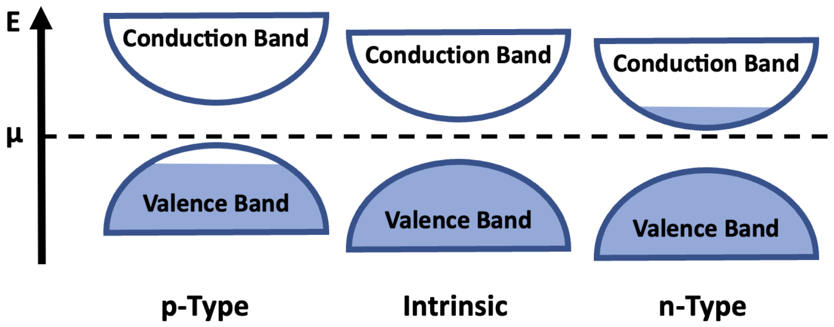

Figure 1.4: **The band alignment of intrinsic vs extrinsic (doped) semiconductors.** The n-type dopants add states within the gap near the conduction band, which thermally excite electrons into the conduction band and raise the chemical potential μ. The p-type dopants add states closer to the valence band, which thermally add holes to the valence band and lower the chemical potential.

Hence, the n-type electron (p-type hole) donor states shift the chemical potential closer to the conduction band (valence band), as shown in Figure 1.4. Detailed engineering of the density of donor and defect states is critical for solar energy devices.[16]

Lattice Vibration States

Aside from the mobile charge carriers, semiconductors and all other solids are composed of a periodic lattice of atoms connected by bonds, which behave akin to springs. Lattice vibrations may be longitudinal, in which the atoms oscillate along the direction of propagation, or transverse, in which the atoms oscillate orthogonal to the propagation. For a monoatomic crystal, there will be two transverse and one longitudinal vibration along each wavevector. For a chain of atoms of length L with interatomic spacing d, the maximum wavelength will be $2L$, and the minimum wavelength will be $2d$.

Expanding upon this 1D treatment of the lattice oscillation, we can derive an expression for the displacement of a single atom from equilibrium, $u_n = r_n(t) - r_n$, where r_n is the equilibrium position of atom n and $r_n(t)$ is the position at time t. Applying Newton's equation of motion for a spring, we obtain

$$u_n = Ae^{-i\Omega t - iknd} \tag{1.11}$$

where A is the amplitude factor, k is the wavevector in the crystallographic basis and Ω is the frequency. To this general expression, boundary conditions describing the particular system of interest can be applied to solve for the relationship between k and Ω, called the 'dispersion relation'. For example, if we apply the boundary condition that the chain of atoms is periodic with distance d, or in other words that $k = k + 2\pi/d$, we obtain the

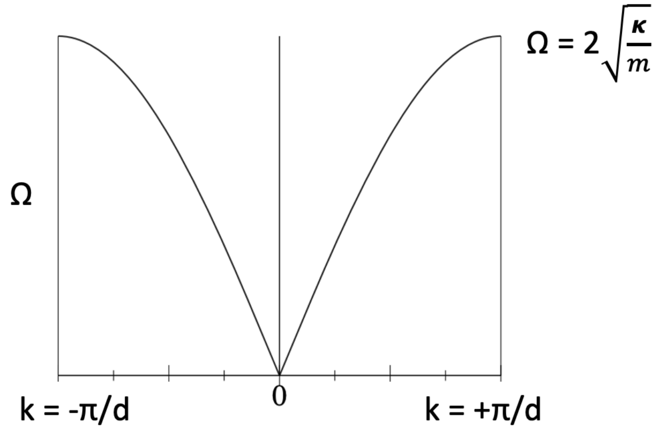

Figure 1.5: **The dispersion relation for a 1D atomic chain.** The relationship between the wavevector k and the frequency Ω is shown for a 1D chain of atoms of mass m, interatomic distance d and spring constant κ. Adapted from reference [7].

dispersion relation

$$\Omega = 2\sqrt{\frac{\kappa}{m}}\left|\sin\left(\frac{kd}{2}\right)\right| \tag{1.12}$$

where m is the mass of the atoms and κ is the spring constant. A graph of this dispersion relation is shown in Figure 1.5.

We define a 'normal mode' to be an oscillation with a fixed sinusoidal frequency Ω. The value of Ω will depend heavily on the mass and electrostatic properties of the constituent atoms. Just like the quantum harmonic oscillator, each normal mode will exhibit vibrations with discrete energies $E_n = \hbar\Omega(n+\frac{1}{2})$. It is useful to define a unit or a quantum of vibrational energy $\hbar\Omega$, which we call a phonon. A phonon is defined by the quantum number n and wavevector k, and has wavelength $\lambda_n \propto 2/n$.[7] Phonons are bosonic in nature, and their occupation is described by the Bose occupation factor $n_B = \frac{1}{e^{\beta\hbar\Omega}-1}$.

Now, let's consider a 1D diatomic chain of atoms with masses m_1 and m_2, spring constants κ_1 and κ_2, and with the same periodic condition of length d. Applying the same laws of motion as previously and solving for the dispersion relation, we obtain two solutions for each wavevector k.[7] These two normal modes at each k are referred to as branches, and the lower energy/frequency branch is called the 'acoustic' phonon branch, as acoustic phonon wavelengths are on the order of sound waves, while the higher energy/frequency branch is called the 'optical' phonon branch, as these are responsible for scattering light in the case of Raman transitions.

Figure 1.6a shows the dispersion relations for both branches. The acoustic phonon branch has nearly linear dispersion near $k = 0$ and approaches zero energy/frequency. These phonons correspond to both masses moving together in the unit cell (Figure 1.6b). The

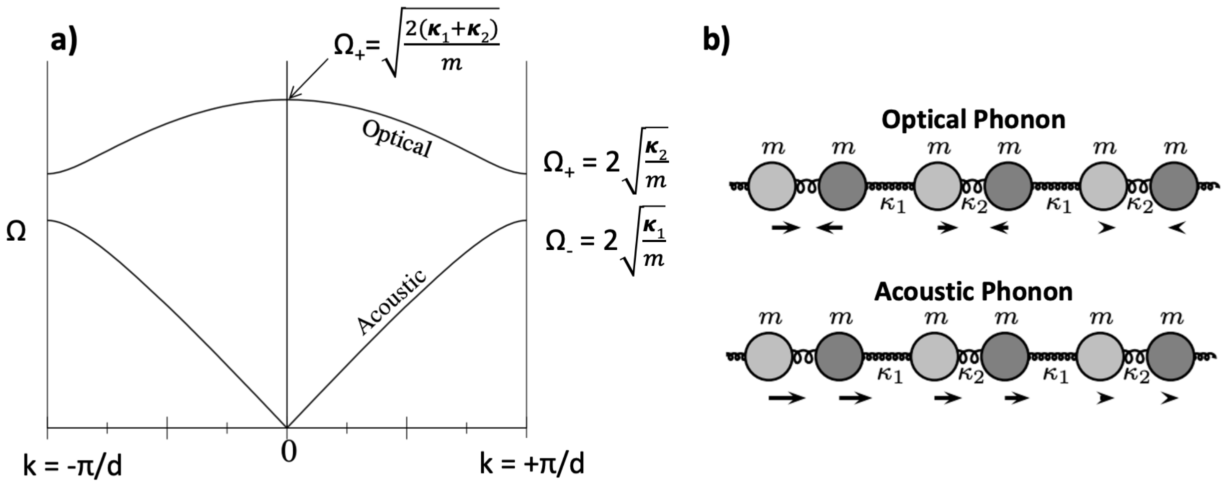

Figure 1.6: a) The dispersion relation for a 1D diatomic chain. There are two solutions for a diatomic chain. The high frequency solution is called the optical phonon branch, and the low frequency solution is the acoustic phonon branch. b) For acoustic phonons, the atoms move together in the unit cell, whereas for the optical phonons, the atoms move against each other. Adapted from reference [7]

optical phonon branch corresponds to the two masses moving against each other in the unit call. The optical phonon frequency approaches a maximum of $\sqrt{2(\kappa_1 + \kappa_2)/m}$ at $k = 0$.

A solid crystal is inherently different from a 1D chain of atoms, but many of the concepts derived above still apply. Just like there will be two phonon modes at each k for the 1D diatomic chain, a 3D crystal with two atoms in each unit cell will exhibit 6 phonon modes at each k, two for each direction of motion. Three of these modes will be acoustic and the other three will be optical, with one longitudinal mode and two transverse modes per branch. Expanding further, a crystal with N atoms per unit cell will exhibit 3 acoustic modes and $3N - 3$ optical modes at each k, although due to crystalline symmetry many of these may be degenerate in energy. In most crystals, the optical phonon frequency is on the order of terahertz (THz) or few-hundred wavenumber (cm^{-1}). An example of the phonon dispersion of the transition metal oxide semiconductor hematite (α-Fe$_2$O$_3$) is shown in Figure 1.7 on the right.

Now that a foundation has been introduced of the charge carrier states and lattice vibrations present in a semiconducting crystal, a review of the ultrafast dynamics that occur following photoexcitation is presented.

1.1.2 Ultrafast Carrier and Lattice Relaxation

The simplified model of parabolic bands presented previously applies quite well to charge carriers near the conduction band minimum (valence band maximum), but is not the reality

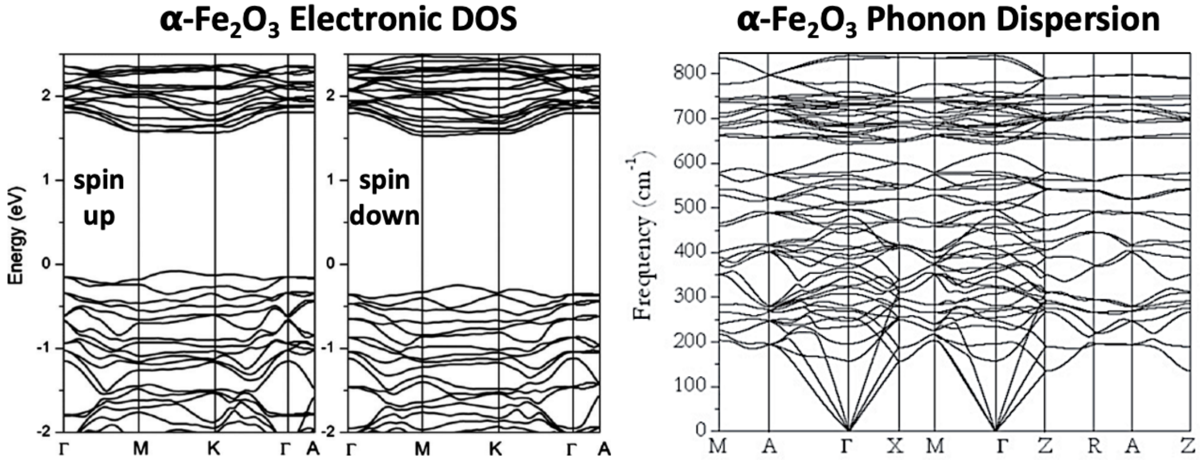

Figure 1.7: On the left is the electronic density of states of hematite, α-Fe_2O_3, versus crystalline momentum k. Adapted from reference [17]. The left panel is for spin up electrons and the right panel is for spin down electrons. On the right is the phonon density of states of hematite in units of wavenumber. Adapted from reference [18].

for most semiconductor materials. Semiconductors will have a distribution of bands of varying energies across crystal momentum space (k-space), as shown in Figure 1.7 on the left for hematite. An electronic transition involving no change in crystal momentum is called a direct transition because only a single photon is needed to initiate this transition (Figure 1.8). An indirect transition occurs when the electron must change momentum, usually assisted by a phonon with wavevector equal in magnitude and direction to the momentum change in order to conserve momentum.[19] Since the indirect transition involves three entities interacting instead of two, it is much less efficient than the direct transition. Many semiconductors, including crystalline Si and Ge, have an indirect transition as their lowest energy transition and are therefore referred to as having an 'indirect band gap'. Hematite's band gap is direct.

Following either a direct or an indirect transition, the photoexcited carriers will have instantaneously gained energy equal to that of the photon absorbed in the transition. Since the ultrafast pump laser has a finite bandwidth, and electrons may be excited from various energies in the valence band, the excited electron and hole populations will have a nonequilibrium energy distribution, i.e. they do not obey Fermi-Dirac statistics. In order to relax back to an equilibrium, a variety of processes occur in the semiconductor on vastly different timescales. A figure of the semiconductor relaxation processes following photoexcitation and their timescales is shown in Figure 1.9. First, the photoexcited carriers thermalize into a hot Fermi-Dirac distribution via carrier-carrier scattering within 100s of as up to $\sim$10 fs. Then, photoexcited carriers cool via carrier-optical phonon scattering on a 100s of fs timescale. Cooled carriers may be trapped by states such as defects, grain boundaries, and polarons

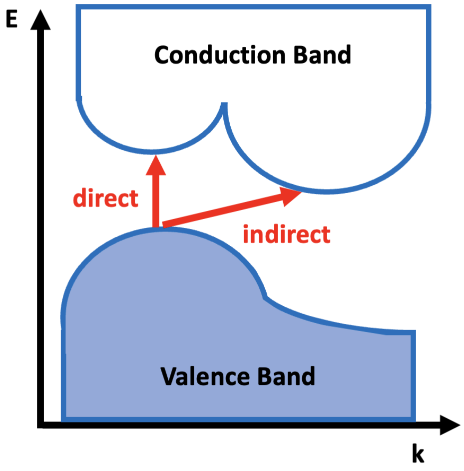

Figure 1.8: **A graphic representation of direct and indirect transitions.** The direct transition occurs from one valence band maximum to one conduction band minimum vertically on the graph, indicating no change in momentum. The indirect transition occurs diagonally with a change in momentum, usually mediated by a phonon.

within ∼1 ps. Next, hot optical phonons decay into acoustic phonons on a 10s—100s of ps timescale. Finally, carriers that have been cooled to the band edge may recombine on a ns to μs timescale. In this section, we will present details on all of these relaxation mechanisms.

Hot Carrier Relaxation

As shown in Figure 1.9, the fastest dynamics that occur in a semiconductor material, and in fact in all types of matter, are those involving electrons. Thermalization of the hot electron and hot hole distribution occurs via scattering, and the thermalization rate will be faster for a higher carrier concentration. Carrier-carrier scattering is an elastic process, meaning the total energy of the hot carrier population is unchanged as the population evolves into a hot Fermi-Dirac distribution with a defined temperature. Free electrons in the conduction band and free holes in the valence band interact via a screened Coulomb potential, and due to differences in effective mass their scattering lifetimes may be very different.[20–22] While electron-electron and hole-hole scattering are predominant in most semiconductor materials and will be the mechanisms discussed here, electron-hole scattering plays a large role in reducing the carrier mobilities of bipolar devices such as transistors and p-n junctions.[23, 24]

Assuming a semiconductor with parabolic bands and that the nonequilibrium hot electrons mainly scatter with colder electrons that obey a Fermi-Dirac distribution, the scattering

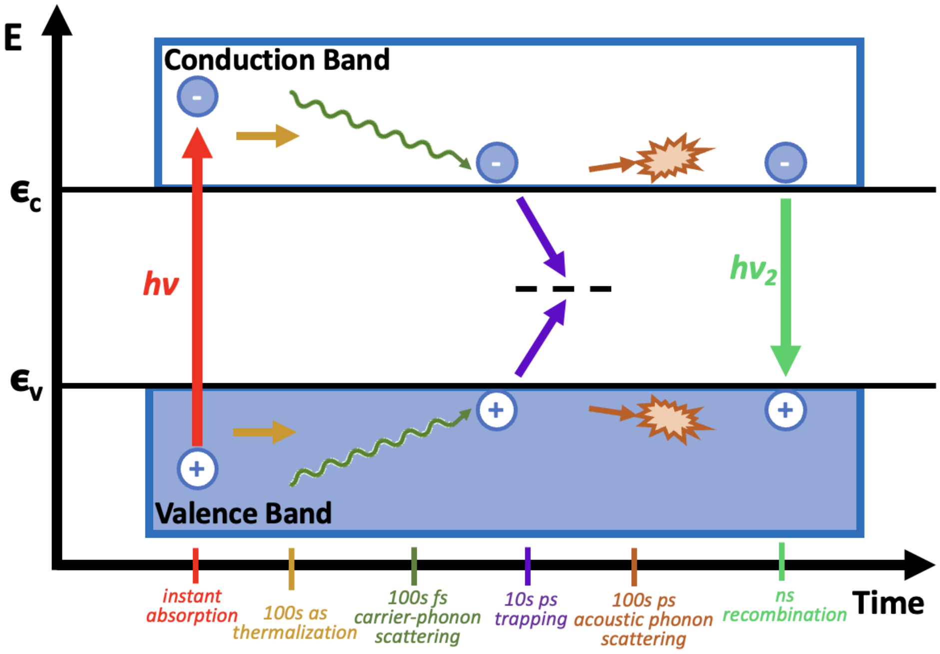

Figure 1.9: **Photoexcited decay dynamics and their timescales in a semiconductor.** From left to right, the initial hot electron and hole population is generated instantaneously via absorption of a photon. Carrier-carrier scattering occurs on the order of 100s of as up to ∼10 fs, depending on the material and carrier. Next, carriers scatter optical phonons on the 10s to 100s of fs timescale. Carriers may be trapped on a ∼0.5 ps up to 10 ps timescale, depending on the trapping mechanism. On the 10s to 100s of ps timescale, acoustic phonons are scattered by optical phonons. Finally, carriers recombine via radiative emission on the ns to ms timescale.

rate depends on the effective mass, temperature and electron energy as

$$\Gamma_{e-e} \propto \frac{\sqrt{mk_bT}}{\epsilon} \tag{1.13}$$

for mass m, temperature T and electron energy ϵ.[25] It is clear from this expression that the lifetime of hot carriers is inversely proportional to their energy, meaning the hottest carriers cool first. The effect of carrier-carrier scattering on the hot carrier lifetime is evident when comparing the metals Cu, which has a filled d band, and Ni, which has a half-filled d band. Scattering within the Ni d band leads to a significantly shorter photoexcited electron lifetime than in Cu due to a reduction in the inelastic mean free path.[26]

Aside from scattering with other carriers, hot carriers may scatter with phonons, ionized impurities (dopants), and grain boundaries. Carrier-phonon and phonon-phonon scattering is presented in the next section. The scattering rate of carriers by ionized impurities goes as

$$\Gamma_{e-i} \propto \frac{N_i m}{\epsilon_s^2} \tag{1.14}$$

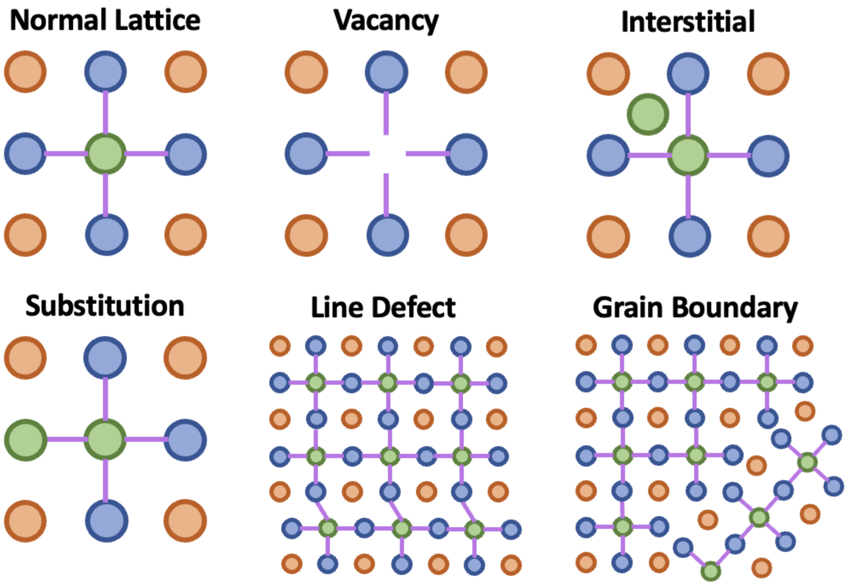

Figure 1.10: **Various crystal defects that may act as charge carrier traps.** In the top left is the normal lattice, which here is a perovskite. A vacancy is a missing atom, a substitution is the wrong atom in a position in the lattice, and an interstitial is an extra atom in between lattice positions. Both line defects and grain boundaries involve incorrect bond lengths and geometries. Surface states, polarons and point defects are not shown.

where N_i is the dopant concentration, m is the carrier effective mass, and ϵ_s is the dielectric constant of the material. At low electron temperatures, scattering by these impurities becomes significant.[22]

Once thermalized and cooled, carriers may be trapped by a variety of localized states, including point and line defects, atomic vacancies, surface and grain boundary states, substitutions, and interstitial atoms; some are shown in Figure 1.10. Polarons will be treated with more detail in the next section. The effect of these traps on the photoexcited dynamics of the semiconductor is to speed up the rate of recombination. Recombination follows three possible mechanisms: a first-order rate law for trapped carriers, which is dependent only on the concentration of free (untrapped) carriers; a second-order rate law from radiative band-to-band recombination of two free carriers; and a third-order rate law from Auger recombination.[27] Which mechanism dominates depends both on the concentration of traps and the hot carrier concentration. In general, Auger recombination and trap-mediated recombination occur much faster than radiative recombination, and the trap-mediated recombination rate is dependent on the depth of the trap state.[28, 29]

Phonon and Lattice Relaxation

Next we consider the role of phonons in the photoexcited decay of semiconductors. A small number of phonons may be directly emitted via an indirect optical transition, but the majority of phonons will be emitted via carrier scattering. Thus, we can derive a Hamiltonian to describe their interaction, H_{e-ph}, which will add perturbatively to the total Hamiltonian of the crystal system.[30] The electron-phonon interaction, first proposed by Fröhlich in 1937,[31] is described by

$$H_{e-ph} = \sum_{k',k,q} g(\mathbf{k}, \mathbf{k}', \mathbf{q}) c^{\dagger}_{k'} c_k (a_q + a^{\dagger}_{-q}) \tag{1.15}$$

where g is the electron-phonon coupling matrix element, $\mathbf{k}$ is the electron's initial momentum, $\mathbf{k}'$ is the electron's final momentum following the scattering event, and $\mathbf{q}$ is the phonon's momentum. $c^{\dagger}_k$ is the creation operator for an electron with momentum k, c_k is the annihilation operator for an electron with momentum k, and $a^{\dagger}_q$ and a_q are the creation and annihilation operators for a phonon with momentum q, respectively.[15] A phonon may either be created or destroyed, but must obey the conservation of momentum $\mathbf{q} = |\mathbf{k} - \mathbf{k}'|$.[31]

Since the energy of optical phonons is closer to that of typical hot carrier energies, they are predominantly scattered over acoustic phonons. Although both carrier-optical phonon and carrier-acoustic phonon scattering occurs, the timescale of acoustic phonon scattering is generally much longer, on the order of 10s of ps.[32] In a polar semiconductor, the longitudinal optical (LO) phonons are largely involved in charge carrier interactions because they induce a transient polarization that may interact via a Coulomb potential with the charge carriers.[33] With large excess electronic energy, in other words $E \gg \hbar\omega_{LO}$ for E the electron energy and ω_{LO} the LO phonon frequency, the scattering rate of electrons with LO phonons can be approximated as $\Gamma_{e-LO} \approx 2\alpha\omega_{LO}$. Here α is the Frölich coupling coefficient

$$\alpha = \frac{e^2}{\hbar}\sqrt{\frac{m_e}{2\hbar\omega_{LO}}}\left(\frac{1}{\epsilon_\infty} - \frac{1}{\epsilon_0}\right) \tag{1.16}$$

for e the charge of an electron, m_e the electronic mass, and ϵ_∞ and ϵ_0 the optical and static dielectric permittivities.[34]

The formalism introduced above assumes the carriers and phonons interact elastically, but this is not always the case, especially for polar semiconductors. When the coupling between charge carriers and the lattice is strong, they may combine to form a quasiparticle state called a polaron, introduced by Landau in 1933.[35] A polaron is a localized charge carrier-lattice state in which the Coulomb potential of the charge carrier distorts the surrounding structure to create a small potential well (Figure 1.11 left panel). The polaron can be defined by a self-energy E_{pol} and an effective mass m^* as follows

$$E_{pol} \approx \hbar\omega_{LO}(-\alpha - 0.0123\alpha^2) \tag{1.17}$$

$$m^* \approx m_e \left(1 + \frac{\alpha}{6} + 0.025\alpha^2\right) \tag{1.18}$$

In effect, the polaron acts to significantly lower the charge carrier mobility as it must deform the lattice to travel. If the coupling between the charge carriers and phonons is just large enough to be inelastic, the polaron behaves as a heavier electron moving in the continuum. This type of polaron is termed 'large' as it spans many unit cells.

In contrast, for larger coupling the polaron is called a 'small' or 'lattice' polaron and only spans a single unit cell. These polarons must 'hop' between discrete lattice sites.[36] Polaronic hopping is a thermally activated process and therefore is extremely slow and may be described with Marcus theory via the following rate law

$$k_{pol} = Ae^{-E_{bar}/k_BT} \tag{1.19}$$

where k_{pol} is the polaron hopping rate constant and E_{bar} is the polaron formation barrier height, given by Marcus theory as $E_{bar} = (E_{pol} + E_{rel})^2/4E_{rel}$ for E_{rel} the lattice relaxation energy of the deformation. Figure 1.11 shows a simplified energy diagram of polaron hopping in the right panel. Small polaron hopping is the cause of the very low charge carrier mobilities observed in transition metal oxides.[37]

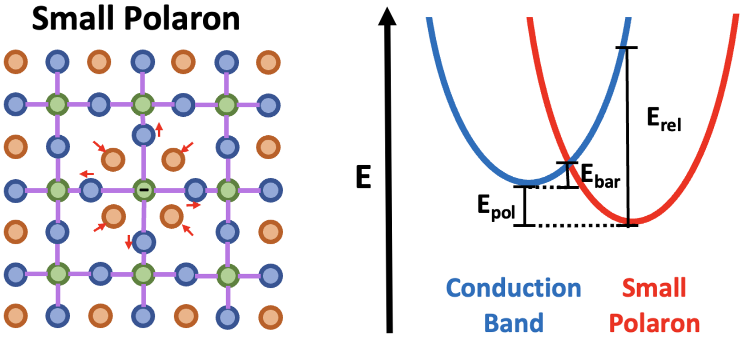

Figure 1.11: On the left is a schematic of the small polaron lattice distortion. On the right is a simplified energy diagram for small polaron hopping. E_{pol} is the polaron self localization energy, E_{bar} is the activation barrier height and E_{rel} is the Marcus theory lattice relaxation energy for the localized polaron distortion.

Aside from carrier-phonon interactions, the optical phonons emitted during carrier relaxation may in turn relax by emitting acoustic phonons. This process must conserve both energy and momentum, so generally one optical phonon (labeled 1) will scatter two acoustic phonons (2 and 3) with the following constraints

$$\mathbf{k}_1 = \mathbf{k}_2 + \mathbf{k}_3 \tag{1.20}$$

$$E_1 = E_2 + E_3 \tag{1.21}$$

At extremely high phonon populations, anharmonicities in the lattice allow scattering of phonons into the next Brillouin zone, altering the condition in eq. 1.20 to be $\mathbf{k}_1 = \mathbf{k}_2 + \mathbf{k}_3 + \mathbf{G}$ where $\mathbf{G}$ is the reciprocal lattice vector. In this process, which is called Umklapp scattering, total momentum is still conserved but crystal momentum is not.[34]

Practically, it is useful to treat the energy transfer from the hot charge carrier population into the optical and acoustic phonon populations in terms of the temperatures of the populations. So called two- and three- temperature models relate the rate of energy transfer to the difference in temperature of the populations and the population specific heat.[38] These models have been successful in fitting thermalized decay processes, but are less applicable to nonthermalized populations.[39]

1.1.3 Processes in Nanoparticles and Films

The description of charge carriers and phonons in semiconductors presented above assumed a nearly infinite lattice, which is a reasonable approximation for bulk materials with Avogadro's numbers of atoms. Once the dimensions of the material shrink below where the infinite lattice assumption is reasonable, the charge carrier and phonon properties are changed.

Charge Carriers in Nanoparticles

For extremely small particles of usually less than 10 nm, the continuous electron density of states approximation breaks down. The electron energy levels become discrete like those of a molecule. This is called the 'quantum confinement' regime and occurs when the electronic wavefunction is smaller than the dimensions of the particle, as defined by the exciton Bohr radius

$$r_{ex} = \frac{\epsilon h^2}{\pi m^* e^2} \tag{1.22}$$

when ϵ is the material's dielectric constant and m^* is the exciton effective mass.[40] Confinement may occur in 1, 2, or all 3 dimensions.

Aside from discretizing the charge carrier states, quantum size confinement increases the band gap of the material by the following factor

$$\Delta E \approx \frac{\hbar^2 \pi^2}{2m^* R^2} \tag{1.23}$$

for a particle of radius R. Both of these effects limit the total number of photoexcited carrier states in a particle, which alters the scattering rate and therefore thermalization. Carrier-carrier scattering has been shown to follow an $n^{-1/D}$ dependence on the carrier density n and the dimensionality D.[41] Decreasing the size of the particle below 10 nm causes up to an order of magnitude longer thermalization time in metal nanoparticles.[42]

Additionally, smaller particles have a higher surface-to-volume ratio than their bulk counterparts, which means an increase in the number of surface states. As described previously, surface and grain boundary states act as charge carrier traps and allow for faster electron-hole recombination. A ten-fold decrease in photoexcited carrier lifetimes has been demonstrated in few-layer thin films when compared to bulk.[43]

Phonon Confinement

Just as charge carriers in a nanoparticle experience confinement effects when the particle dimensions are smaller than their wavelength, phonon states are also altered in small particles. The total phonon density of states and the vibration frequencies are modified, leading to poor thermal conductivity and decreased phonon-phonon and carrier-phonon coupling. The effect of phonon confinement on the hot carrier and phonon decay rates in silicon nanoparticles is addressed in detail in Chapter 5. If we consider a phonon with wavevector k_0, it can be represented by a plane wave of the form

$$\phi(k_0, r) = u(k_0, r)e^{-ik_0 \cdot r} \tag{1.24}$$

where ϕ is the phonon wavefunction, r is position in the crystal lattice, and the function $u(k_0, r)$ is the periodicity of the lattice.[44] This plane wave cannot exist outside of the dimensions of the nanoparticle. Therefore, we can impose a localization function with the form of a sphere with diameter L such as

$$\psi(k_0, r) = Ae^{-\frac{r^2}{2}/\left(\frac{L}{2}\right)^2}\phi(k_0, r) \tag{1.25}$$

where ψ is the confined phonon wavefunction.[45] The additional terms in ψ cause the function to approach zero outside of L, reducing the total number of normal modes. The waves ψ are, by definition, not eigenfunctions of the phonon wavevector k_0, but instead are a superposition of eigenfunctions of wavevectors k with $|k - k_0| \leq 1/2L$. This imparts an uncertainty $\Delta k = \pi/L$ on the vibration frequency and results in asymmetric broadening of the Raman spectrum of nanoparticles.[46, 47]

Phonon confinement of the optical phonons, which have a shorter wavelength than the acoustic phonons, has been observed in semiconductor films of less than 20 nm,[48] and nanoparticles with diameter less than 25 nm.[49] The acoustic phonon states are altered, leading to reduced thermal conductivity, for particles of less than 100 nm.[50] Now that the photoexcited dynamics in semiconductor nanoparticles have been presented, we discuss the spectroscopic tool utilized to observe both the charge carriers and lattice in these materials.

1.2 Core Level Spectroscopy

In order to uncover the light-induced dynamics in semiconductors and other materials relevant for solar energy, a specialized technique is required to first initiate the photoexcited dynamics and then observe the resulting states. Such a technique would need ultrafast time resolution on the order of tens of femtoseconds and be able to resolve element-specific charge carrier and lattice dynamics. The only technique capable of measuring ultrafast processes is pump-probe spectroscopy, in which two pulses of light (an intense pump and a weaker broadband probe) take snapshots at various time delays.[51]

With transient visible/near-IR pump-XUV probe spectroscopy, both carrier and lattice decay processes can be observed in solids. Photoinitiated processes in solar energy relevant materials begin with a near-IR (NIR) or visible photon. A core level spectroscopy is required to obtain element specificity due to the large differences in ionization potentials across elements.[52] The approximately 25—125 eV XUV spectrum produced by high-order harmonic generation (see section 1.3) overlaps with the core transition of most transition metals and other elements commonly used in solar energy materials, such as silicon. Furthermore, the electrons and holes may be measured separately with this technique for certain materials, providing carrier specificity.[20, 21] The specific phonon modes involved in carrier relaxation may be elucidated.[53] In the following sections, an empirical model for the shapes of core level absorption spectra is introduced and then a description of visible/near-IR pump transient core level absorption is provided.

1.2.1 Core Transitions in Solids and Transition Metals

On the most fundamental level, photon-induced core level electronic transitions can be described using the 'Fermi's Golden Rule' formalism.[54] In this formalism, the transition probability $\Gamma_{i\to f}$ from the initial state ϕ_i to the final state ϕ_f is dependent on their relative energies, E_i and E_f, and the photon energy $\hbar\omega$ as follows

$$\Gamma_{i\to f} = \frac{2\pi}{\hbar} |\langle \phi_f | \hat{e} \cdot r | \phi_i \rangle|^2 \delta(E_f - E_i - \hbar\omega) \tag{1.26}$$

where $\hat{e}$ is the photon polarization and $\hat{e}\cdot r$ is the electric dipole moment. It is this dependence on the initial state energy, which for core levels is different across the periodic table, that provides core level spectroscopies with elemental specificity.

For a core level transition in a ground state atom in a solid system, the initial state is composed of a filled core shell and some empty valence or conduction band density of states, ρ. Due to their highly localized nature, the core states are described as discrete states while the valence states are described as continuous state densities, as illustrated in Figure 1.12. Thus, the core level absorption I_{XAS} can be further expanded as

$$I_{XAS} \propto |\langle \phi_f | \hat{e} \cdot r | \phi_i \rangle|^2 \rho \tag{1.27}$$

While the initial state is complicated for many-electron atoms due to many body interactions between the electrons, the final state becomes even more challenging. This is because following the promotion of an electron from the core shell to the empty valence or conduction band states, a positively charged hole is left behind. This so-called core hole imposes a

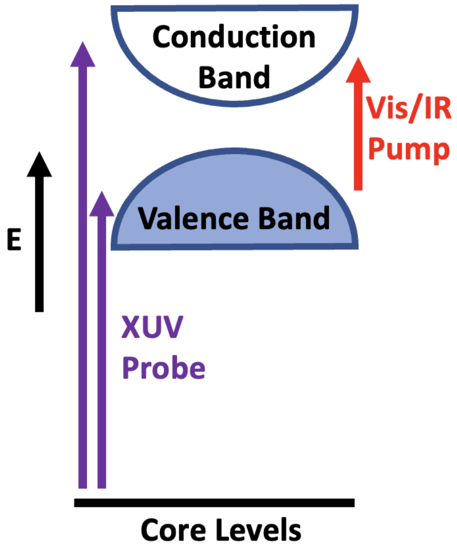

Figure 1.12: **A cartoon of the core and valence levels involved in the XUV transition.** The core levels are treated as discrete localized atomic states. The valence band and conduction band states are treated as continuous.

Coulomb interaction on all the electrons in the system, called the multiplet coupling, which alters their energies to produce the final XUV absorption spectrum.[55] An additional layer of complexity in solids is the distribution of charges on other atoms and hybridization between the central atomic orbitals and the ligand's orbitals, which cause states to branch into multiple states and alter the selection rules for transitions. Furthermore, the core hole is a highly unstable state, and decay channels such as Auger or radiative transitions lead to sub-fs core hole lifetimes and huge intrinsic broadening on the order of tenths of an eV,[56] adding to the confusion of peak assignment. Thus, XUV absorption spectroscopy (XAS) is an inherently many-body process, and simplifications and assumptions are needed to understand core level spectra. Here we present the charge transfer multiplet (CTM) theory of de Groot and Kohtani for predicting core level spectra.

Three effects are considered for the charge-transfer multiplet model of core level transitions. The first is intra-atomic effects, H_{atom}, which include the on-site electron-electron repulsion and spin-orbit coupling. The second contribution is ligand field effects from the crystal symmetry, H_{LF}. The third is charge transfer effects between the atomic orbitals and ligand orbitals, $\underline{L}$. While an atomic multiplet model is effective for describing the core level spectra of rare earth metals, the CTM model is required to fully capture the features of transition metals.[57] This theory is particularly useful for transition metal complexes and polar and ionic solids, but may not accurately describe more correlated systems. First, we discuss the intra-atomic effects.

Atomic Effects on the Core Level Spectrum

An electron's energy can be described using the Schrödinger equation, $H\Psi = E\Psi$. Expanding the Hamiltonian for a single-electron system, we include the kinetic energy K and the Coulomb potential from the nucleus V

$$H^1_{atom} = K + V = \frac{p^2}{2m} + \frac{-Ze^2}{r} \tag{1.28}$$

where p is the momentum, m is the electronic mass, Z is the effective nuclear charge, e is the charge of an electron, and r is distance to the nucleus.

When more than one electron are present in the atom, the electron-electron interaction term and spin orbit coupling terms must be added

$$H_{atom} = \sum_N \frac{p_i^2}{2m} + \sum_N \frac{-Ze^2}{r_i} + \sum_{pairs} \frac{e^2}{r_{ij}} + \sum_N \zeta(r_i) l_i \cdot s_i \tag{1.29}$$

where l and s are the orbital and spin angular momentum, respectively. The electron-electron interaction term, which we will abbreviate as H_{ee}, includes the effects of electron-electron repulsion and exchange. The spin-orbit coupling term, abbreviated H_{ls}, depends on the coupling scheme used in the calculation. For light elements and most valence electrons, an LS-coupling scheme is appropriate. For heavier atoms and the core hole, a jj-coupling scheme is applicable. Thus, core level spectra are usually modeled using an intermediate coupling regime.[55]

For any given electronic configuration, there are a number of possible states composed of electrons with different values of l, s, and j, which can be described using the values for the total spin angular momentum S, the total orbital angular momentum L, and the total angular momentum J. These configurations are normally denoted with term symbols, and each term may have multiple degeneracies or may be forbidden by the dipole transition selection rules.[58] For most of the spectra described in this thesis, the core level spectra are that of transition metal $M_{2,3}$ edges with 2p → 3d transitions. The degeneracy of a $3d^n$ (initial state) configuration is

$$3d^n : \binom{10}{n} = \frac{10!}{(10-n)!n!} \tag{1.30}$$

The degeneracy of a $2p^5 3d^{n+1}$ (final state) configuration is

$$2p^5 3d^{n+1} : 6 \times \binom{10}{n+1} \tag{1.31}$$

For an atom with 5 3d electrons in the ground state, this yields 252 configurations for the initial state and 1260 for the final state. Including the dipole selection rules, we obtain 37 possible initial state configurations and 180 possible configurations for the final state. Since the number and degeneracy of transitions is highly dependent on the number of valence electrons, core level spectroscopies are sensitive to oxidation state.

Once the dipole-allowed states are known, the values of the matrix elements for H_{ee} can be calculated for two-electron terms using tabulated values for the Slater-Condon coefficients. Three-electron and higher terms become increasingly complicated to calculate.[55] The spin-orbit interactions included in the H_{ls} terms act by mixing states such that they become mixtures of the pure atomic states. In general, the core level spin-orbit coupling is much greater than that of the valence, but a partially filled valence d level will have significant S-O coupling and cannot be ignored. We arrive at a Hamiltonian for the final state as follows

$$H_f \approx H_{2e} + H_{ls-2p} + H_{ls-3d} \tag{1.32}$$

where H_{2e} are the 2-electron Slater-Condon terms and H_{ls-2p} and H_{ls-3d} are the spin-orbit coupling terms for the core hole and valence electron configurations, respectively.

Ligand Field Effects on the Core Level Spectrum

For an atom in a solid surrounded by bonds to other atoms, the crystal field-induced effects are included in the CTM theory as an additional term H_{LF} added to the Hamiltonian, $H = H_{atom} + H_{LF}$. H_{LF} can be written

$$H_{LF} = -e\phi(r) \tag{1.33}$$

where ϕ is the potential that describes the crystal surroundings and can be further expanded as the sum of spherical harmonics. In this way, the core level spectrum is treated as though an isolated single atom was placed in a static charge distribution. This simple model captures many features of the core level spectra, such as splitting of states and altered state energies, even though the ligand field effects are treated as a perturbation.

The ligand field will have a symmetry, such as octahedral (O_h) for an atom with 6 identical bonds arranged like the faces of a cube. This octahedral field is a subgroup of the atomic SO_3 symmetry group, so each atomic state branches to one or more states of the ligand field symmetry. For example, the P state in SO_3 will branch to the T_1 state in O_h, and the D state will branch to the $E + T_2$ states. Tanabe and Sugano have described the relationship between the ligand field parameters (Dq, Ds, and Dt) and the Slater-Condon parameters.[61] The effects on the Ti^{4+} core level spectrum of altering the parameter $10Dq$ are shown in Figure 1.13a, and a comparison of the experimentally obtained spectrum to the ligand field theory-predicted spectrum is shown in Figure 1.13b. Consequently, XUV core level spectroscopy is sensitive to differences in the lattice geometry and ligands.

Charge Transfer Effects on the Core Level Spectrum

For many elements, including both the atomic multiplet two electron integrals and the ligand field effects can accurately model core level spectra, but this is not sufficient to

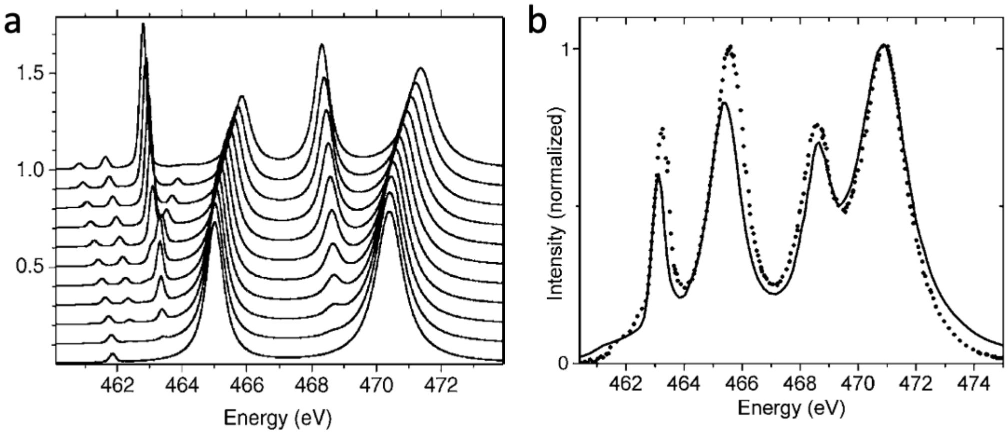

Figure 1.13: a) The effect of increasing ligand field on the core level spectrum of Ti^{4+} for the $3d^0 \rightarrow 2p^5 3d^1$ transition. The bottom spectrum is the atomic multiplet spectrum with no ligand field effects ($10Dq = 0$), and the value of $10Dq$ is increased by 0.3 eV for each additional spectrum. Adapted from reference [59]. b) Comparison of the Ti^{4+} 2p X-ray absorption spectrum of $FeTiO_3$ (dots) and the ligand field theory predicted spectrum (line) using a $10Dq$ value of 1.8 eV. Adapted from reference [60].

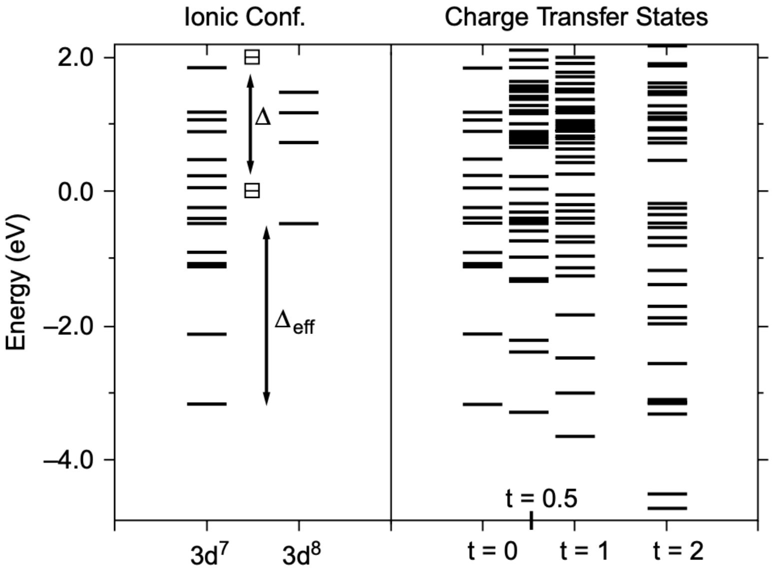

Figure 1.14: The $3d^7$ and $3d^8$ configurations calculated using the atomic and ligand field multiplet model with a crystal field splitting Δ of 2.0 eV are shown on the left. On the right are the possible configurations when including both the $3d^7$ and $3d^8\underline{L}$ states, given for values of the hybridization strength of 0.0 eV, 0.5 eV, 1.0 eV and 2.0 eV. States are only shown with energies below +2.0eV. Adapted from reference [59].

describe transition metal (TM) complexes. To account for all spectral satellites and some contraction of the multiplet peaks, the effect of charge fluctuations to low-energy ligand states $\underline{L}$, must be included.[55] Then, the ground state configuration can either be 3d^n or 3d$^{n+1}\underline{L}$, or even higher-energy configurations. The final state would be either 2p^{5}3d^{n+1} or 2p^{5}3d$^{n+2}\underline{L}$. Altogether, the inclusion of ligand charge transfer opens up new possible transitions in the core level spectrum. The number of configurations for the 3d^7 ground state and 3d^8 final state without including the charge transfer fluctuations is shown in the left panel of Figure 1.14. When possible fluctuations to the ligand orbitals are added, the number of configurations is greatly increased, as shown on the right panel of Figure 1.14 for increasing hybridization strength from 0 to 2 eV.

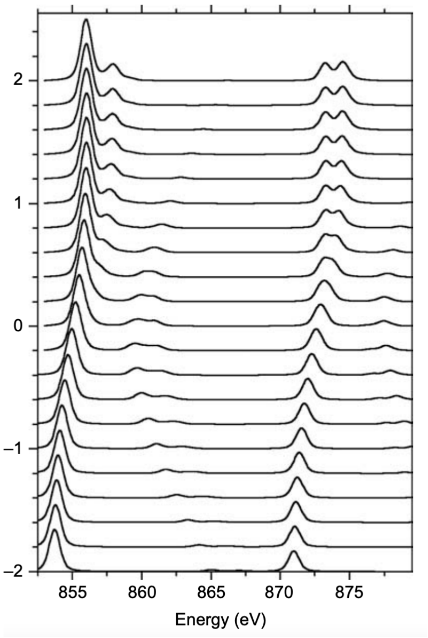

Figure 1.15: The effect of including charge transfer fluctuations to the ligand states on the Ni^{2+} ground state spectrum, which have configurations 3d^8 + 3d$^9\underline{L}$. The top spectrum has a charge transfer energy Δ of +10 eV, and the bottom spectrum has a Δ of -10 eV, with intermediate charge transfer energies for the other spectra. The -10 eV Δ value relates to an almost entirely 3d^9 ground state. Adapted from reference [59].

The magnitude of the charge transfer effects depend on four parameters: the charge transfer energy, or the energy difference between the two configurations, Δ; the on-site Coulomb repulsion, U_{dd}; the core hole potential, $-U_{dc}$; and the ligand p-TM d hybridization, $V(\Gamma)$. The hybridization may be different for the initial and final state configurations, but is usually assumed to be equal. In general, the core hole potential is approximately 1—2 eV greater than the d-d repulsion. Thus, we can write a value for the charge-transfer energy of the final state configuration Δ_f as follows

$$\Delta_f = \Delta + U_{dd} - U_{dc} \approx \Delta - 1,2\text{eV} \tag{1.34}$$

Figure 1.15 shows the effect of including the fluctuations to the ligand states for the Ni^{2+} ground state spectrum, $3d^8 + 3d^9\underline{L}$, for varying values of Δ. Taking these effects into account, the ground state core level spectra of all elements, including transition metals, can readily be explained with the charge transfer multiplet model. Since many assumptions and values are required to apply this model, a program called CTM4XAS has been made available to tabulate the term symbols and calculate the transition probabilities.[57] This theory has been extended by Vura-Weis to more accurately model the increased broadening of the $M_{2,3}$ edges as well as the excited state $L_{2,3}$ and $M_{2,3}$ edges of the first-row transition metals.[62] Other software, such as the Bethe-Salpeter equation applied to Density Functional Theory, can also accurately predict the XAS spectrum of many compounds, especially systems with correlated electrons.[63, 64] While these models can be used to empirically explain ground state core level spectra, the next section will explain the additional components needed to describe the spectra of excited state atoms.

1.2.2 Transient XUV Absorption Spectroscopy

In order to understand and control the sub-picosecond processes that occur in semiconductor nanomaterials, an ultrafast laser pump-probe technique is required. This technique, which has been applied optically to semiconductor materials for over 50 years,[65, 66] utilizes two temporally separated laser beams, the pump and the probe, to first excite a system and then to probe the resulting state. Pump-probe measurements are performed repeatedly on a sample with varying delays between the two pulses, resulting in a time-resolved molecular ‘movie’ of how the states evolve over time.

Normally, the two pulses are produced by splitting the beam from a single ultrafast pulsed laser, commonly by a beam splitter or a polarization-dependent optic.[67] In this way, the pulses are time-synchronized. The temporal relationship between the pump and the probe pulse can be controlled via the path length, as both beams travel at approximately the speed of light. A simplified diagram showing the beam splitter, delay line, sample and detector is shown in Figure 1.16.

If we return to the quantum mechanical description of the electronic configurations discussed above, the pump-probe technique involves two separate transitions. In the first transition, the NIR or visible pump photon excites the photoinitiated process. In the case of semiconductors and metals, this process will be an electronic transition from a valence band state to a conduction band state and may involve a charge transfer from one element to another. The probability of this first transition occurring can readily be calculated from tabulated absorbances and Beer’s Law.[68] In order to create a large enough density of excited states to achieve a good signal to noise ratio in an ultrafast spectroscopy experiment,

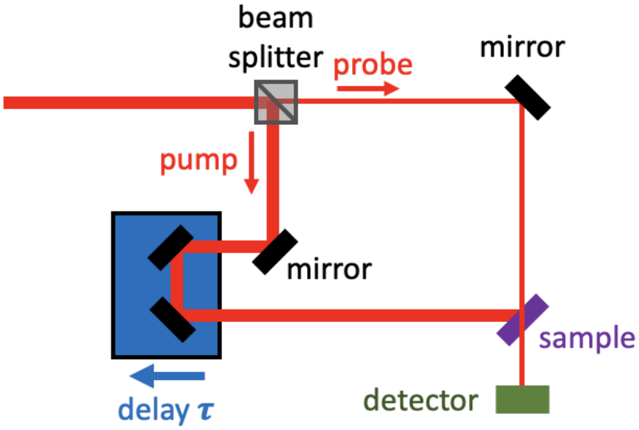

Figure 1.16: **Diagram of a pump-probe spectroscopy setup.** The ultrafast laser pulses enter from the top left and are split in two by a beam splitter (gray box). The weaker probe arm is focused onto the sample (purple) by mirrors (black) and into a detector (green). The more intense pump arm is delayed by a delay stage (blue) by some time τ and is then focused onto the sample. By measuring the probe at varying delays τ, the dynamics of the sample are measured over time.

densities of 10^{19}—10^{21} cm^{-3} are needed.[69] Unfocused solar light (AM1.5 solar irradiance spectrum) will produce an excited carrier density of 10^{14}—10^{16} cm^{-3} in silicon.[70] This implies that the ultrafast dynamics measured in an experiment may proceed at different timescales than those initiated by the sun due to the increased carrier density.[71]

Once excited, the material system will be probed by the weaker XUV beam. For the population of atoms that have not been excited by the pump, their spectra will be the ground state core level transition discussed above in section 1.2.1. For the fraction of excited atoms, both their initial and final states of the XUV transition will be different. For example, in the Fe $M_{2,3}$ edge of α-Fe$_2$O$_3$, the ground state is 3d^5, which has term symbol $^6A_1$ Fe^{3+}.[72] The visible-pumped excited state, which is also the XUV transition initial state, is composed of a localized (intra-atomic) electronic transition and a charge transfer (inter-atomic) transition. For the localized transition, which is an Fe d-d transition, the lowest energy excited state will have term symbol $^4T_1$. Alternatively, the charge transfer transition from oxygen to iron will form a 3d^6 state with term symbol $^5T_2$ Fe^{2+}. These different initial states of the XUV transition will necessarily lead to different final states, and the new state symmetries and degeneracies will further be altered via interaction with the core hole.[57] The spectra calculated using the charge transfer multiplet model for the different excited state term symbols of Fe is shown in Figure 1.17.

In this example, the charge transfer state has a decreased oxidation state from the ground state, and the core level spectrum is red-shifted. On the other hand, increasing the oxidation state of an atom generally relates to a blue-shifting of the spectrum.[73] Accordingly, the

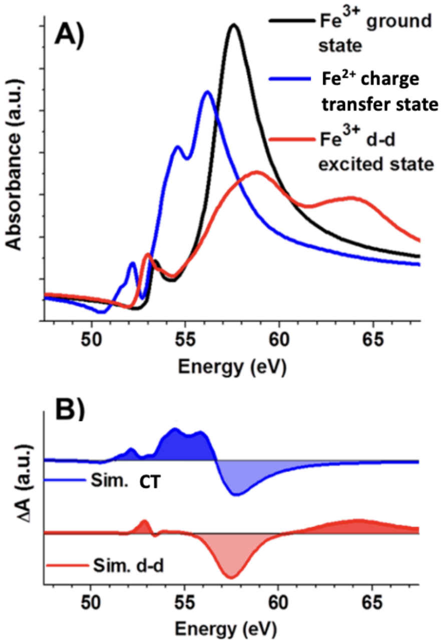

Figure 1.17: **Simulated core level excited states of the Fe $M_{2,3}$ edge of α-Fe_2O_3.** a) The simulated Fe^{3+} ground state of $^6A_1$ symmetry is shown in black. The simulated d-d Fe^{3+} excited state with $^4T_1$ symmetry is shown in red. The simulated oxygen-to-iron Fe^{2+} excited state with symmetry $^5T_2$ is shown in blue. b) The differential XUV absorption (excited state minus ground state) for the d-d transition and the charge transfer transition. Adapted from reference [72].

XUV spectrum is sensitive to oxidation state changes, can separately measure electrons and holes,[56] and can determine the spin state (high spin or low spin) of transition metal compounds.[74]

Recent Solid-State Discoveries with Transient XUV Spectroscopy

Here we will summarize some of the most exciting recent discoveries in solid state materials obtained with XUV time-resolved spectroscopy. Firstly, XUV light can be generated as bursts of a few-hundred attoseconds (see section 1.3.3), which is on the order of electron motion and thermalization. With attosecond pulses, researchers have uncovered ultrafast carrier thermalization in nickel metal[39] and in semiconductors such as Ge and Si/Ge alloys,[75, 76] and the intra-pulse strong field effects on the band structures of a variety of materials.[73] On even shorter timescales, core hole excitons have been observed in wide band gap semiconductors like MgO[77] and have been observed to interact with photoexcited valence electrons in WS_2.[78] Using a four-wave-mixing technique, core excitons and their couplings can be further revealed, and has been accomplished in NaCl.[79]

On a hundred-femtosecond to picosecond timescale, XUV has been applied to study the decay of photoexcited carriers. Carrier-specific (electron and hole) relaxation has been observed in PbI_2[20] and in the hybrid perovskite $CH_3NH_3PbI_3$ (MAPI).[21] Carrier trapping in semiconductors such as NiO and Fe_2O_3 by defects[80] or coupled electron-phonon quasiparticle states like small polarons[81, 82] has been measured, as has small polaron trapping at surfaces and interfaces via XUV transient reflectivity measurements.[83, 84] XUV transient absorption is also uniquely applicable to study interactions between photoexcited carriers and phonons. The two separate carriers and the individual phonons involved in carrier relaxation can be extracted in silicon[53, 56] and in the 2D material 2H-$MoTe_2$,[85] in which coherent phonons are also visible. Coherent phonon vibrations may be observed following optical excitation in $LiBH_4$[86] or by using below-gap pumping in Bi.[87, 88]

Extreme ultraviolet transient absorption has also been applied to the Mott insulating material VO_2 to observe that the photoinitiated insulator-to-metal phase transition is mediated by both electronic and phonon effects.[89] Even the spin crossover event in ferrimagnetic transition metal ferrite materials has been reported with XUV.[90, 91] In this thesis, we will present research that utilizes the powerful technique of XUV transient absorption spectroscopy to study semiconductor nanoparticles and semiconductor and metal containing nm-scale junctions to observe photoexcited charge carrier and lattice dynamics. Next, the procedure for producing ultrashort XUV pulses is described.

1.3 High-Order Harmonic Generation

The generation of sub-100 femtosecond coherent pulses of soft X-ray or extreme ultraviolet light needed to perform transient core level spectroscopy requires specialized equipment. One method to produce such pulses is the free electron laser (FEL), in which microbunches of electrons are laterally accelerated by periodic series of magnets called undulators.[92] The lateral acceleration causes the electrons to emit radiation in a narrow forward cone. The spacing and magnetic field properties of the undulators can be tuned such that these pulses constructively interfere to produce coherent light.[93] Modern FELs can generate coherent, sub-100 fs EUV, soft and hard X-rays, depending on the beam energy, with milliJoule energies per pulse.[94] But these facilities cost billions of dollars to build and require hundreds of staff and scientists to maintain.

A much less costly method to produce short XUV pulses is via generation of high-order harmonics of an ultrashort laser driving field. This method utilizes the 800 nm-centered pulses from a commercial Ti:sapphire laser, which are focused into a noble gaseous medium to create bursts of XUV light (Figure 1.18), albeit with many orders of magnitude less peak power than an FEL.[92] The noble gaseous targets discussed in this dissertation are contained in a semi-infinite gas cell, discussed in more depth in section 2.1.3, but they may be contained in waveguides,[95] or may even be solid-state targets.[96] High-order harmonic generation (HHG) can be performed on a laser tabletop with equipment costs of less than

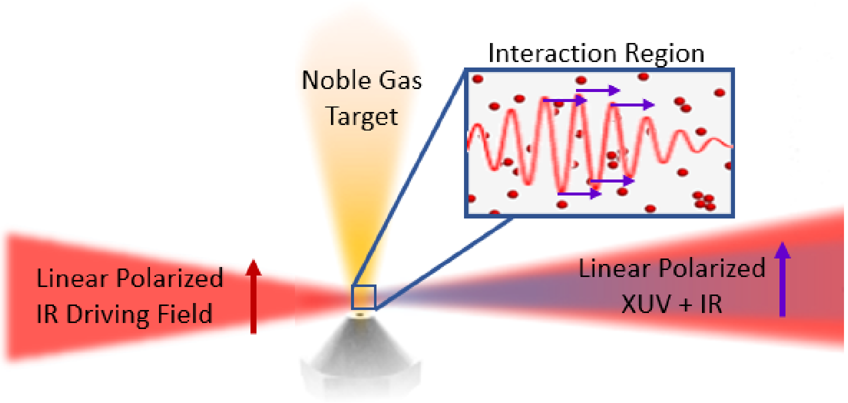

Figure 1.18: A schematic of the high-order harmonic generation noble gas target, shown here as a jet, for a tabletop HHG setup. A linearly polarized IR driving field is focused into the gas, and if the interaction region experiences the correct intensity, gas pressure, and other variables discussed in the text, generates high-order harmonic light in the XUV/soft X-ray region of the spectrum.

1 million dollars, and produces pulses of typically <1 nJ, but may be up to 1 μJ, of energy spanning the 10-1000 eV range.[97] Furthermore, HHG allows for the generation of isolated sub-100 attosecond pulses. In this section, we present the theory behind high-order harmonic generation and the requirements to generate sufficient XUV spectra for application in spectroscopy.

1.3.1 Three-Step Model

In the high-order harmonic generation process, ultrashort pulses of visible/near-IR coherent laser light, called the driving field, are tightly focused into a target medium to achieve extremely high peak electric field strengths of 10 V/Å, achievable with focused laser intensities of 10^{14}—10^{15} W/cm^2. At these field strengths, nonlinear interactions with the medium allow for the emission of coherent bursts of light with energies that are many multiples, or harmonics, of the driving field. The inherently complex interactions can be described via a semi-classical three-step model, shown in Figure 1.19.[92, 98–101] In step one (ionization), electrons in the target medium are tunnel ionized from the parent ion. These electrons are accelerated by the linearly polarized electric field in step two (propagation). Then in step three (recombination), electrons collide with the parent ion and emit XUV radiation.

Ionization

In a typical HHG apparatus, an 800 nm near-IR driving field is focused into a target medium of noble gas with ionization potential I_p. Thus, we start with a linearly polarized electric field, $E(t) = E_0 cos(\omega_0 t + \phi)$ with photon energy $\hbar\omega_0$ much less than the ionization

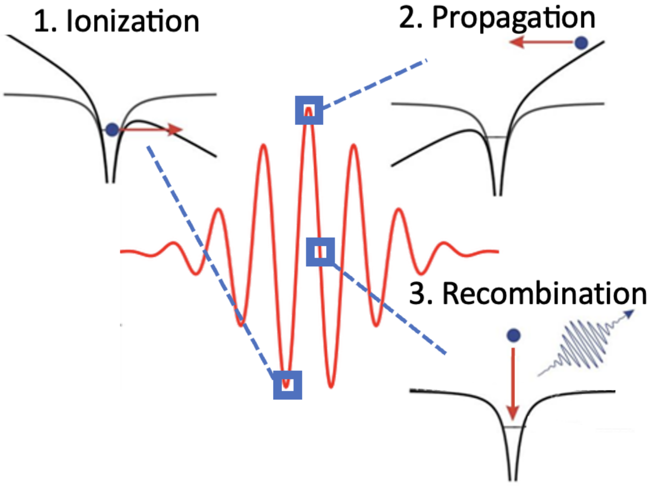

Figure 1.19: **A schematic of the three-step model for high harmonic generation.** In step 1, ionization, the electron is tunnel ionized out of the noble gas atom at a peak of the electric field. In step 2, propagation, the electron is accelerated in the driving field. In step 3, recombination, the electron collides with the parent ion, producing an XUV photon.

potential, $\hbar\omega_0 \ll I_p$.[102] In this regime, direct ionization with a single photon is not possible and instead tunnel ionization by the strong electric field occurs and has been described by Keldysh[103]:

$$\gamma = \frac{\omega_0\sqrt{2m_e I_p}}{eE_0} \tag{1.35}$$

Where γ is the Keldysh parameter, e is the charge and m_e is the mass of an electron. When γ is much greater than 1, or E_0 is small, multiphoton ionization occurs. When γ is less than 1, the atom's potential is distorted by the field, lowering the barrier for ionization and increasing the probability of ionization occurring. For a slowly varying electric field, i.e. a small ω_0 as is the case here, the tunnel ionization is described by a 'quasi-static' field approximation. Ammosov, Delone and Kraĭnov have shown that the probability of tunnel ionization in this regime scales exponentially with laser field intensity.[104] HHG is possible when $\gamma \approx 1$ due to phase matching considerations with the free electron plasma, as will be described in the next section. Moreover, since the field strength E_0 is kept near the threshold, tunnel ionization only occurs near the peaks of the oscillating field (Figure 1.19).

Propagation

After ionization, the free electrons are able to propagate in the laser driving field and gain kinetic energy W_k. The linear field accelerates the electrons away from the parent ion before it switches sign and propels them back toward the parent ion to recombine with some probability and emit radiation with energy $\hbar\omega_{HHG} = I_p + W_k$. Assuming the electron has zero kinetic energy upon ionization and is no longer affected by the field of the parent ion, the electron kinetic energy depends only on the laser field and is described classically with Newtonian mechanics. Thus, W_k is wholly dependent on when the electron was ejected relative to the phase of the field, ϕ_0, and the kinetic energies of the different electron trajectories $W_k(\phi_0)$ can be solved numerically.

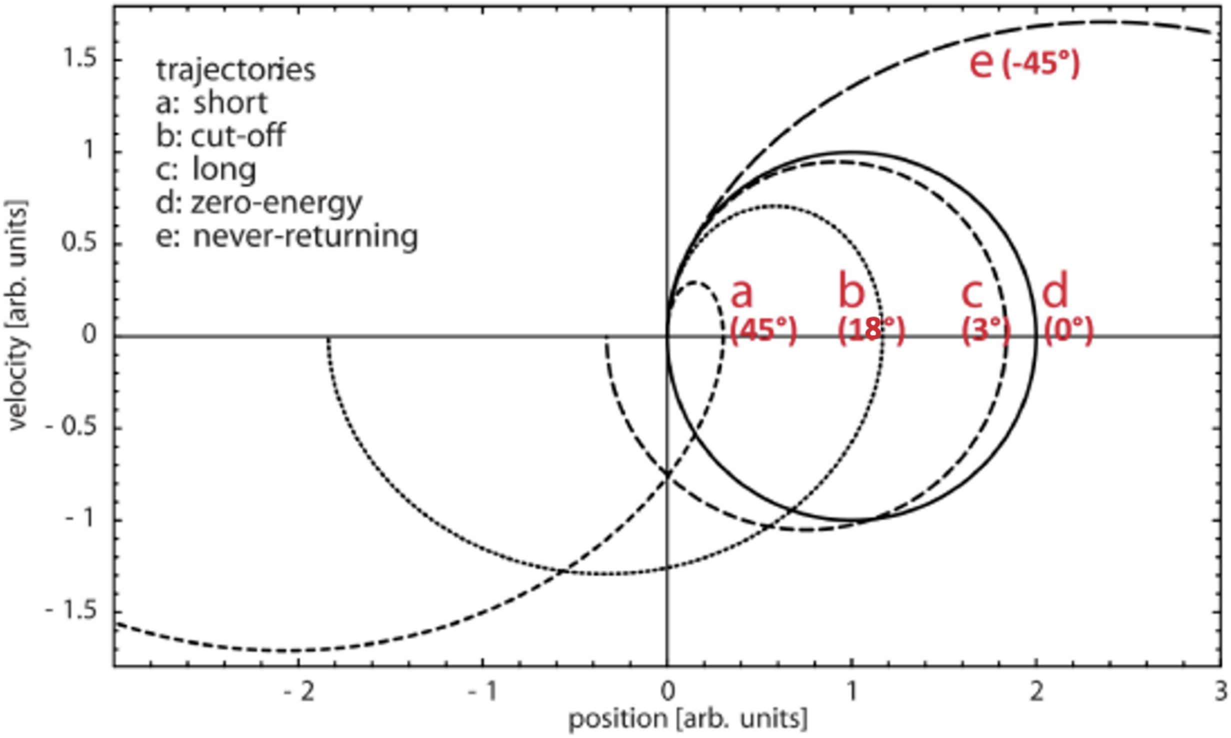

Figure 1.20: **Electron trajectories following ionization at different times relative to the electric field phase.** Trajectories are plotted on a velocity vs. position graph to highlight the kinetic energy gained. Electrons with trajectories a and c are emitted at different times after the peak of the driving field, but recollide with their parent ions with the same kinetic energy. Electrons with trajectory b, which are emitted at approximately 18°, gain the maximum amount of kinetic energy before recollision. Electrons with trajectory d are emitted at the peak of the electric field and gain no kinetic energy. Electrons with trajectory e, emitted before the peak of the field, do not recombine. Adapted from reference [105].

As shown in Figure 1.20 (trajectory e), for electron ejection times of $\pi/2 \leq \phi_0 \leq \pi$ (and $3\pi/2 \leq \phi_0 \leq 2\pi$), no real solutions exist and the electrons are accelerated away from the parent ion without recollision.[97, 105] Directly at the peak field, when $\phi_0 = 0$ (or π), the electron is accelerated away from and back toward the parent ion without gaining any kinetic energy (Figure 1.20 trajectory d), leading to no radiation emission. Nonzero solutions for the kinetic energy exist for ejection after the peak field, when $0 \leq \phi_0 \leq \pi/2$ (and $\pi \leq \phi_0 \leq 3\pi/2$).

Maximum kinetic energy occurs for electrons ejected at approximately 18° (or 198°, which is about $\pi/10$), and is referred to as the cutoff energy, E_{cutoff} (Figure 1.20 trajectory b). The cutoff energy is related to the driving field properties via:

$$E_{cutoff} = I_p + 3.17U_p = I_p + 3.17\overline{W_k} = I_p + 3.17\frac{e^2E_0^2}{4m_e\omega_0^2} \tag{1.36}$$

Where U_p is the ponderomotive energy, or the cycle-averaged 'quiver' energy of an electron in the field. For recolliding electrons ejected at times other than the cutoff, there will be two ejection times and trajectories that correspond to the same kinetic energy. For the 'short' trajectory (a in Figure 1.20), the electron is emitted after the cutoff and spends less time propagating in the field. Likewise, the 'long' trajectory (c in Figure 1.20), is ejected before the cutoff and spends more time propagating in the field. An intuitive picture of the trajectories at different electronic ejection times are shown in Figure 1.21, with color indicating relative kinetic energy gained.

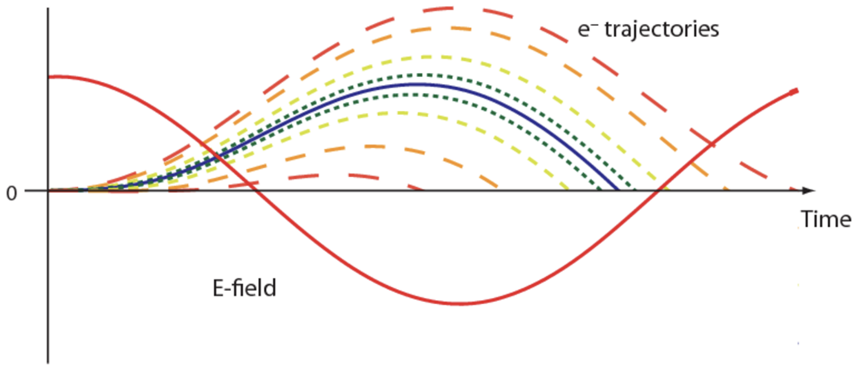

Figure 1.21: **An intuitive picture of the electron trajectories following ionization in the driving field.** Trajectories are plotted on a time vs. position graph, with color indicating relative kinetic energy (red to violet for increasing KE). Adapted from reference [106].

It is clear from eq 1.36 that the maximum energy of the emitted XUV light can be tuned via the target gas ionization potential, the driving field strength, and the driving field wavelength. Practically, the noble gas I_p are not very different in energy (spanning only ∼12 eV) and increasing field strength lowers HHG yield for phase matching conditions discussed below. Increasing the driving field wavelength has been shown to increase HHG cutoff energy up to 1.6 keV,[107] although the longer trajectories and increased wavepacket diffusion decreases the efficiency significantly. The probability of radiative recombination goes as $1/\lambda^4$ or $1/\lambda^6$.[92] Nonetheless, HHG with driving wavelengths longer than 800 nm is commonly used to probe dynamics in the soft X-ray region.[108]

Recombination

Finally, the accelerated electrons may recombine with their parent ions to emit XUV radiation. The probability of recombination is low due to divergence and dephasing of the electronic wavepacket and the quantum mechanical nature of the recollision process.[102, 109, 110] Considering this, along with the low probability of tunnel ionization and omitting the electron trajectories for which recombination is not possible, leads to a high-order harmonic generation efficiency on the order of 10^{-8}.[92] This efficiency may be improved with elliptical driving fields[111] or with a two-color gating technique, discussed in section 1.3.3.

1.3.2 Coherence and Phase Matching

Following the three steps outlined above, each atom in the target gas that falls within the 'interaction region', the volume of the focused laser beam with sufficient intensity, has a probability of emitting XUV radiation in all directions. Due to the coherent driving field, these bursts are coherent and will only constructively interfere in the forward direction.[92, 102] At each half-cycle of the driving field another set of XUV bursts are created at a fixed phase relative to the IR driving field and propagate along with the previous bursts. In order for efficient XUV radiation to be produced, the already-generated high harmonics must match the phase of the newly generated harmonics, i.e. the driving field.[112] This puts a requirement that the phase velocity of the XUV light matches that of the driving IR field, $\nu_p^{XUV} = \nu_p^{IR}$.

The phase velocity is related to the refractive index n of the medium by $\nu_p = c/n$, with c the vacuum speed of light. The medium is not only the target noble gas, but also a free electron plasma generated by the driving field because of the low likelihood of electron recombination following tunnel ionization. Both the free electron plasma (denoted with subscript e) and the atomic gas (subscript g) will interact with both the IR driving field and the XUV emission. Thus, the refractive index that the IR field experiences is

$$n^{IR} = 1 + n_g^{IR} - n_e^{IR} \tag{1.37}$$

where the atomic gas term is positive because it slows the IR field, and the plasma term is negative because it speeds up the field.[97] Likewise, the refractive index that the XUV field experiences is

$$n^{XUV} = 1 - n_g^{XUV} - n_e^{XUV} \tag{1.38}$$

where the atomic gas term is negative in this case because the XUV field is above the gas resonance. In other words, the target gas will slow the IR driving field relative to the the XUV, while the plasma will speed up both fields.

To gain a more physical understanding of the refractive indices, we can substitute parameters of the target gas medium and free electron plasma into n_g and n_e. For a gas, the refractive index is given by $n_g = N_g \cdot n_{atm}$, where N is the number density and n_{atm} is the refractive index at atmospheric conditions. Substituting in $N_g = PN_{atm}$, where P is the pressure and N_{atm} is the number density at atmospheric conditions, we obtain the following expression for refractive index,

$$n_g = PN_{atm} \cdot n_{atm} \tag{1.39}$$

The free electron plasma contribution to the refractive index is given by $n_e = -(\eta_e/2\eta_{cr})$, where η_e is the number density of the plasma.[113] η_{cr} is the critical plasma density $\eta_{cr} = \frac{\pi}{r_e\lambda^2}$, where r_e is the classical electron radius. Rearranged, this gives

$$n_e = -\frac{\eta_e r_e \lambda^2}{2\pi} \tag{1.40}$$

For harmonic order q, $\lambda(q) = \frac{\lambda^{IR}}{q}$. Thus, the plasma refractive index scales with the harmonic order as $1/q^2$, so the plasma's effect on the XUV refractive index will be negligible. Since the plasma will mainly act to speed up the IR field, the plasma pressure can be balanced relative to the pressure of the neutral gas, which slows the field, to produce nearly zero phase mismatch.

A useful measure of phase matching is the coherence length, also called the dephasing length L_π, which is the distance traveled before the two fields are π out of phase. The coherence length needs to be longer than the length of the interaction region, L_{int}, in order to produce high XUV flux. Attwood[92] shows that the simplified expression for L_π is given by

$$L_\pi = \frac{\lambda^{IR}/2qn^q}{\left[\frac{1}{n^{IR}} - \frac{1}{n^q}\right]} \tag{1.41}$$

where n^q is the refractive index of the q^{th} harmonic. We can rearrange the expression to $L_\pi = \frac{\pi}{\Delta k_q}$ by defining Δk_q as the phase mismatch factor for harmonic order q given by [114]

$$\Delta k_q = k_q^{XUV} - qk^{IR} = \Delta k_g + \Delta k_e + \Delta k_{other} \tag{1.42}$$

An example of an additional term in the phase mismatch factor is the effect of the Gouy phase of the focused driving field. This can be overcome by either loosely focusing the beam,[115] or placing the focus before the target gas interaction region,[116] so this and other effects are ignored for the rest of this section.

We can expand eq. 1.42 further by substituting n_g and n_e from equations 1.39 and 1.40. Considering the ionized fraction η, we obtain the following expression for the phase mismatch caused by the neutral gas,

$$\Delta k_g = \frac{2\pi q}{\lambda^{IR}}(1-\eta)PN_{atm} \cdot \Delta n \tag{1.43}$$

for Δn the difference in refractive index between the two fields at atmospheric conditions. The expression for the phase mismatch caused by the free electron plasma is given by

$$\Delta k_e = r_e \lambda^{IR} \eta P N_{atm} \left(q - \frac{1}{q}\right) \tag{1.44}$$

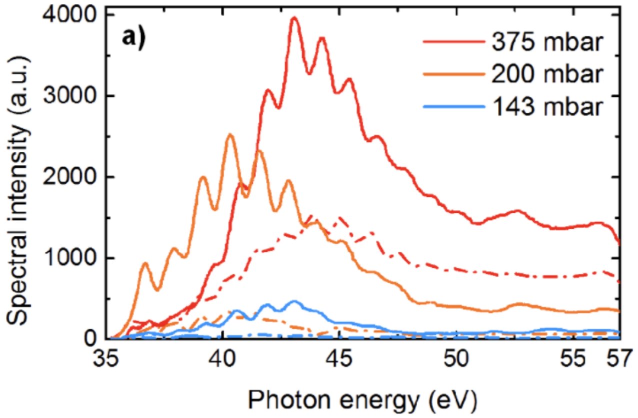

Figure 1.22: The effect of gas pressure on the photon energies of the HHG spectrum. The spectrum blue-shifts and increases in overall intensity as the pressure is increased. Adapted from reference [117].

Altogether, these expressions show that the phase mismatch is particularly sensitive to the target gas pressure and ion fraction, and the phase mismatch will be different for each harmonic order. This provides another method of controlling the energy of the XUV radiation (besides changing the driving field wavelength as mentioned in the above section).

The intensity of a single harmonic order, I_q, can then be estimated using the phase mismatch factor. Assuming a low enough gas pressure that absorption of the XUV light is negligible, or $L_{abs} < L_{int}$, and that the interaction region is shorter than the coherence length, $L_{int} < L_{\pi}$, we obtain the following expression

$$I_q \propto (PN_{atm})^2 \, \frac{\sin^2(L_{int}\Delta k_q/2)}{\Delta k_q^2} \tag{1.45}$$

From this expression it is clear that at a small phase mismatch factor the intensity will scale quadratically with gas pressure and length of the interaction region. But, reabsorption by the gas medium will scale exponentially. Since the absorption cross sections of the noble gases are larger for the lower-order harmonics,[118] increasing the pressure or L_{int} will disproportionately increase the intensities of the higher-order harmonics, blue-shifting the XUV spectrum. An example of the effect of increasing pressure on the photon energies of the HHG spectrum is shown in Figure 1.22. By carefully tuning the target gas pressure, interaction region length, and driving field intensity, and therefore the plasma density, the relative intensities of the harmonics are altered, modulating the XUV spectrum while generating sufficient XUV flux for absorption experiments.[112]

Additionally, the energy of the individual harmonics can undergo a pressure-dependent blue-shift.[119] This is caused by the free electron plasma, which blue-shifts the driving laser field according to the following equation

$$\delta E_f = \frac{h^2(PN_{atm})}{2\pi m_e c}\,\frac{1}{E_f}\,\frac{d\eta}{dt}\,L_{int} \tag{1.46}$$

Where E_f is the energy of the driving laser photons, (PN_{atm}) is the gas density, m_e is the electron mass, c is the speed of light, L_{int} is the length of the interaction medium, and $d\eta/dt$ is the rate of increase of the ionized fraction. Furthermore, optimizing the waveform of the driving field by altering the instantaneous frequency, also referred to as chirp, can improve the phase matching of selected harmonic orders.[120] Chirping the driving field alters the ratio of long trajectories to short trajectories, which can broaden the spectral width of the individual harmonic orders as well.[112]

1.3.3 Generating Even-Order Harmonics

A requirement for the application of high-order harmonic generated XUV light to absorption spectroscopy is a fairly continuous and broad spectrum to resolve chemical features. Alas, a consequence of the three step model is that XUV bursts are produced every half cycle of the driving field, π/ω_0, which interfere with the other bursts to produce a modulated spectrum with harmonics spaced $2\hbar\omega_0$ apart. Since the generating medium is a noble gas, which has inversion symmetry, only odd harmonics of the fundamental field will be produced at energies of $(2n+1)\hbar\omega_0$,[123] creating a highly discontinuous spectrum as shown on the

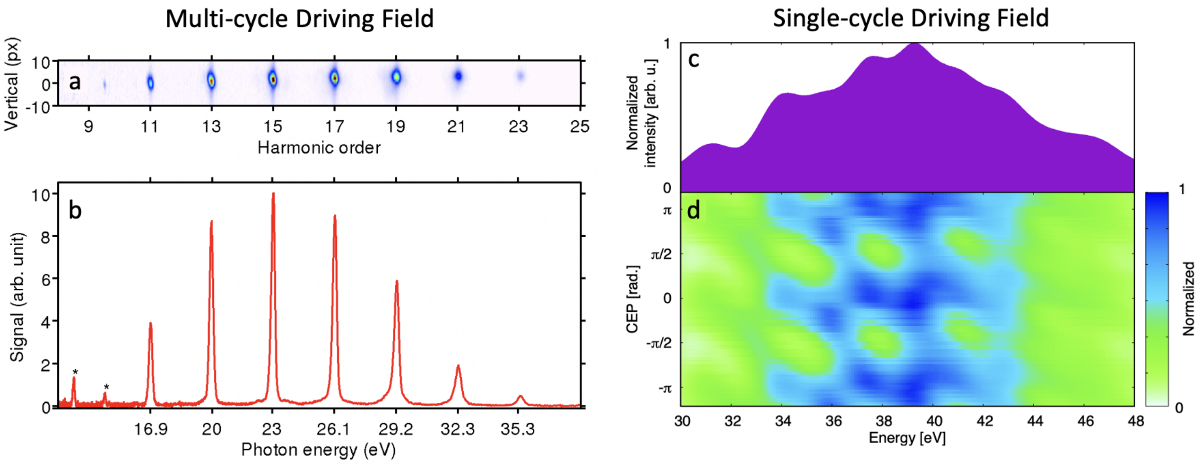

Figure 1.23: a) The spectrometer camera image and b) the integrated spectrum produced by HHG of a laser driving field with multiple cycles. Adapted from reference [121]. c) The integrated spectrum and d) the spectrum for various carrier envelope phases (CEP) produced by HHG of a single-cycle laser driving field. Adapted from reference [122].

left (panels a and b) of Figure 1.23.

It is possible to use a single-cycle driving field, or a few-cycle driving field with amplitude gating,[124] to generate a single XUV burst of a few-hundred attoseconds and thus a continuous spectrum as shown on the right (panels c and d) of Figure 1.23. These methods require an ultra-broadband driving field, which greatly increases the cost and complexity of the experiment, as well as precludes the band-selective or state-selective excitations possible with a narrow-band field.[125] For the experiments presented in this dissertation, with the exception of those in the conclusion, a two-color multi-cycle driving field of approximately 35 fs (>13 cycles) is used to achieve both even and odd harmonics that are broad enough to measure good spectra.

In the two-color gating technique, the 800 nm driving field is combined with a weaker intensity 400 nm driving field produced by second harmonic generation (SHG) in a nonlinear crystal such as β-barium borate (BBO). When the relative intensity, polarization, and time delay between these two fields is optimized, intense even and odd harmonics are produced and they spectrally overlap to generate an XUV continuum.[126, 127] The two color gating field generates even harmonics via a four-wave frequency mixing process between the XUV field, the NIR driving field and the second harmonic field.[126] For example, to generate the 38^{th} harmonic, ω_{38}, an NIR photon (ω_1) and a second harmonic photon (ω_2) can combine with a 35^{th} harmonic photon, $\omega_{38} = \omega_{35} + \omega_1 + \omega_2$. Other possibilities, such as the process $\omega_{38} = \omega_{39} + \omega_1 - \omega_2$, are also possible. The four-waving mixing process is highly sensitive to the phase matching of the three fields.

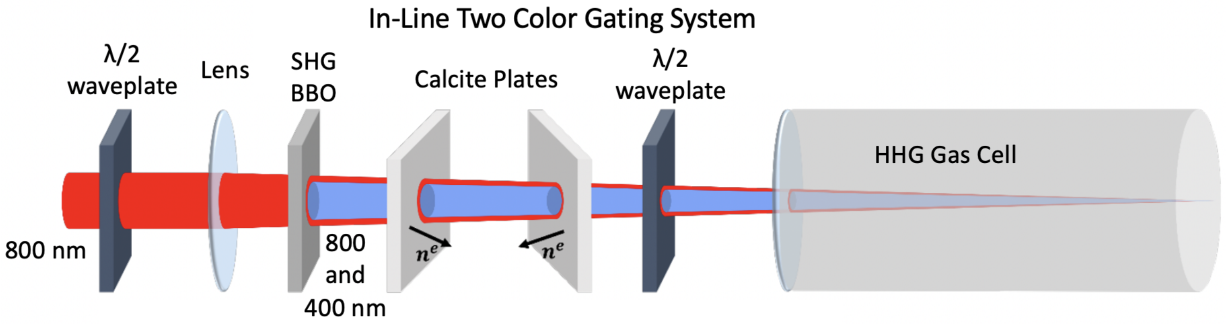

Figure 1.24: **The modified in-line two color gating system.** The 800 nm driving field, moving from left to right, is polarized by a half waveplate and focused into a BBO crystal for second harmonic generation. Both the 800 nm and 400 nm fields are delayed relative to each other by the calcite pair and their polarizations are aligned by another half waveplate before traveling into the gas cell for HHG. Adapted from reference [15]

In previous iterations of the experimental setup used for this dissertation, the two driving field colors were produced separately and recombined with a beam splitter, essentially forming a Mach-Zehnder interferometer.[15, 112] This type of setup is extremely sensitive to fluctuations in beam pointing, and therefore spatial and temporal walk-off between the

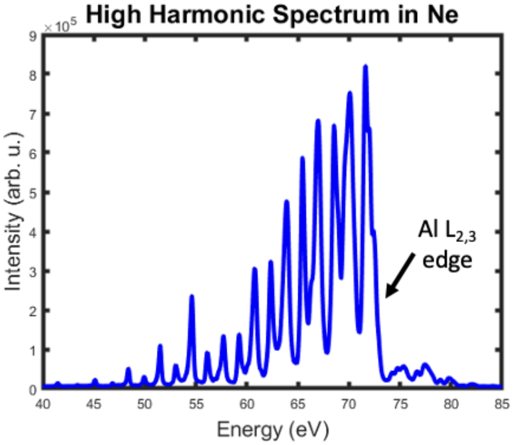

Figure 1.25: **An example of an XUV spectrum produced with the in-line two color gating system.** Both even and odd harmonics are visible, and each individual harmonic is spectrally broad. This produces an XUV continuum under the modulated peak structure. The sharp drop in intensity at approximately 72 eV is caused by absorption by an Al filter.

two colors led to quickly deteriorating XUV spectra and prevented measurements that lasted more than a few hours. To overcome this issue, the Mach-Zehnder style two color gating system was replaced with an in-line second harmonic generation system. This system is a modified version of the MAZEL-TOV apparatus (MAch-ZEhnder-Less for Threefold Optical Virginia spiderwort) designed to produce circularly polarized XUV.[128] As shown in Figure 1.24, this apparatus consists of a waveplate to polarize the 800 nm driving field, followed by the focusing lens for the HHG cell. Next, a BBO crystal converts part of the 800 nm field to its second harmonic. Two matched calcite plates compensate for the time delay between the two colors introduced by the BBO crystal and the other transmissive optics. Finally, a half waveplate aligns the polarization of the two fields and they enter the HHG gas cell. (The half waveplate is replaced with a quarter waveplate in the unmodified MAZEL-TOV system to produce circularly polarized harmonics). Since in this system the 400 and 800 nm beams are co-linear, no spatial or temporal walkoff occurs and measurements can be run for over 8 hours. An example of an XUV spectrum obtained with the in-line two color gating system is shown in Figure 1.25.

The remainder of this dissertation contains five additional chapters. Chapter 2 provides an overview of the experimental apparatus used to obtain the transient XUV spectra, with extra attention spent discussing recent upgrades to the system. Chapter 3 explores photoexcited small polaron formation in goethite (α-FeOOH) nanoparticles and how the timescales differ from that of thin film hematite (α-Fe$_2$O$_3$). In Chapter 4, hot hole migration through all three layers of a Ni-TiO$_2$-Si thin film junction is characterized following Si photoexcitation to determine the role of each layer. Chapter 5 describes photoexcited hot carrier and phonon decay in silicon nanoparticles and provides evidence of a hot phonon bottleneck when compared to silicon thin films. Finally, Chapter 6 will explore the hot hole and lattice response and a possible coherent phonon observed following photoexcitation of the ferroelectric halide perovskite $CsGeI_3$, as well as provide future outlooks on the research.

Chapter 2

The Experiment

The experimental laser apparatus and sample preparation involved in an extreme ultraviolet transient absorption spectroscopy measurement each require specific considerations for a successful experiment. In this chapter, we delve into each of these aspects of the experiment and give extra attention to details not described in previous dissertations.[15, 112] We begin with the laser system and XUV spectrometer in section 2.1, followed by the nanoparticle sample preparation in section 2.2.

2.1 The XUV Spectroscopy System

The complex extreme ultraviolet spectroscopy apparatus, shown in Figure 2.1, involves many optics, vacuum chambers and electronics and takes up two full laser tables. The setup can be divided into two main portions: the ultrafast laser system and the high vacuum system. The laser is a commercially available chirped pulse regenerative amplifier (Spitfire Pro XP, Spectra Physics) pumped by a Q-switched Nd:YLF diode pumped solid state laser (Empower 30, Spectra Physics). The amplifier is seeded by a Ti:sapphire oscillator (Tsunami, Spectra Physics), which is pumped by a 532 nm continuous wave diode laser (Millennia, Spectra Physics). The laser produces near-IR pulses at a repetition rate of 1 kHz and approximately 3 mJ power and 40 fs duration centered at 800 nm. More details of the laser system are provided in section 2.1.1.

The laser pulses are split into a pump arm and a probe arm. The probe arm is sent through the modified MAZEL-TOV apparatus described in Chapter 1 and into the semi-

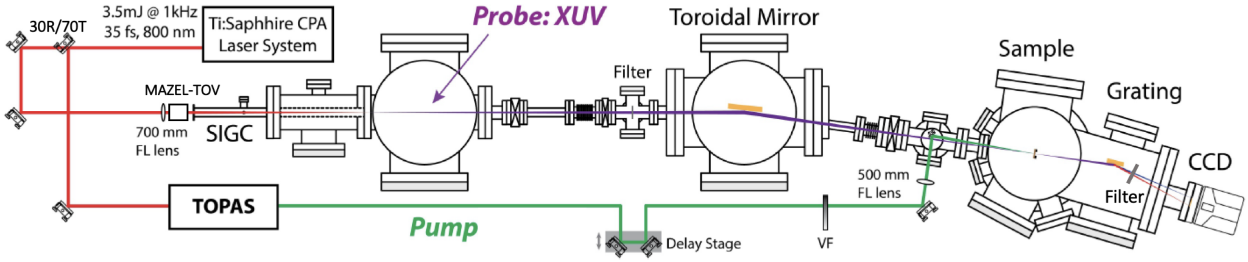

Figure 2.1: **Overview of the extreme ultraviolet transient absorption spectroscopy setup** Major components are labeled and described in the text. The fundamental 800 nm laser beam is shown in red, the XUV beam is shown in purple, and the visible pump light is green. Adapted from reference [15].

infinite gas cell (SIGC) to generate high harmonics (see section 2.1.3). Once generated, the harmonics are directed through the high vacuum chambers (section 2.1.2) and focused onto the sample by a toroidal mirror (section 2.1.4), where they interact with the sample following the NIR or optical pump. Transmitted XUV light is then measured with the CCD camera spectrometer (section 2.1.5).

2.1.1 The Ultrafast Laser System

The laser pulse wavelength, temporal duration and intensity have strict requirements in order to be used for high harmonic generation of XUV light. Primarily, the focused laser intensities of the driving laser must fall in the range of 10^{14}—10^{15} W/cm^2 to balance between tunnel ionization and free plasma generation. The driving field must have a short temporal duration in order to achieve these high peak powers and also to ensure that the generated XUV field is reasonably phase matched with the entire driving field. Also, the driving field wavelength must be in the near-IR or mid-IR range to allow for adequate propagation of the tunnel ionized electrons so that they may gain kinetic energy in the 10s to 100s of eV range. Luckily, Ti:sapphire chirped pulse laser amplifiers possess all of these qualities. A Ti:sapphire laser amplifier can produce 800 nm near-IR pulses that are tens of fs long and with milliJoule pulse power. When focused to approximately hundred micron diameters, this yields the requisite peak power of 10^{14}—10^{15} W/cm^2.

As mentioned above, the $\sim$40 fs laser pulses utilized in this experiment are produced by a commercial Ti:sapphire laser system consisting of 4 units: the 532 nm continuous wave pump laser (Millennia, Spectra Physics), the Ti:sapphire oscillator (Tsunami, Spectra Physics), the Q-switched Nd:YLF amplifier pump (Empower 30, Spectra Physics), and the chirped pulse regenerative amplifier (Spitfire Pro XP, Spectra Physics). A TOPAS-Prime optical parametric amplifier (Light Conversion) is also used in the pump arm to generate narrow-band visible pulses. Details of these lasers are described in the dissertations of former graduate students.[15, 112] Here, we discuss the major modifications that have been applied to the system in the intervening years, aside from the normal cleaning and replacement of damaged optics and electronics that is expected.

The pumping scheme of the Ti:sapphire crystal in the Spitfire Pro has been reconfigured to improve the quality and consistency of the transverse beam mode. Previously, the $\sim$20 Watt average power 532 nm laser pulses from the Empower 30 pump laser entered the Spitfire Pro amplifier, were enlarged by a telescope, and split into two equal portions by a 50/50 beam splitter (Figure 2.2a). These two pump pulses and the seed pulse from the Tsunami oscillator were overlapped in the Ti:sapphire crystal to generate amplified pulses. This setup was sensitive to walkoff between the two pump pulses, creating inhomogeneities in the transverse mode of the output pulses. To upgrade the system, the 50/50 beam splitter was removed, and one of the 45° pump mirrors was replaced with a 0° mirror (Figure 2.2b). In this configuration, the backwards traveling pump pulse is easily overlapped with the forwards travelling pulse by adjusting that one mirror. This improved setup affords a uniform nearly-

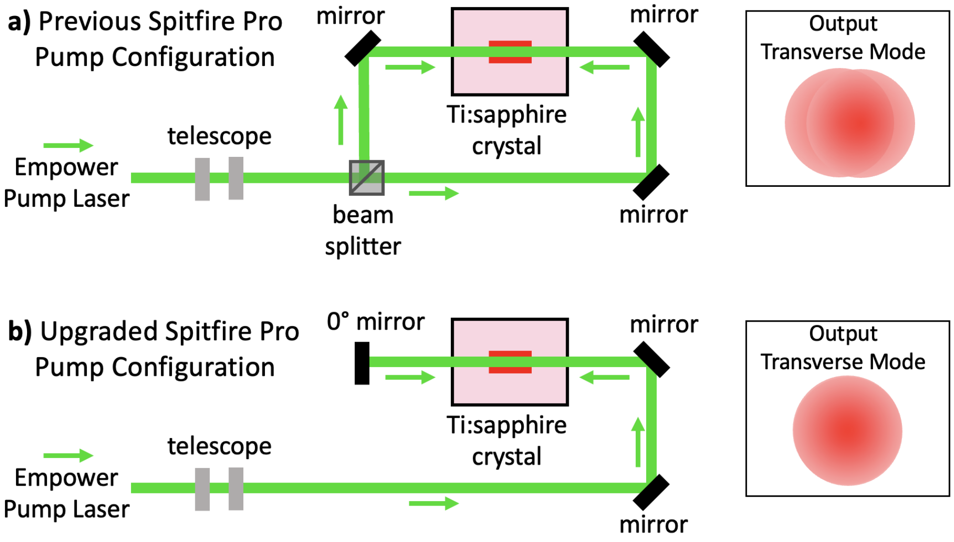

Figure 2.2: **The upgraded Spitfire Pro XP pump configuration** a) The former configuration of the amplifier pump path. The pulses from the Empower 30 laser are enlarged in a telescope and split into two halves with a beam splitter. Each half of the beam is focused into the Ti:sapphire crystal, leading to walkoff and an irregular mode shape. b) The upgraded configuration has no beam splitter, and the Empower pump beam is sent back on itself after passing through the Ti:sapphire crystal, generating a highly uniform output mode.

TEM_{00} transverse mode that is less sensitive to temperature and humidity changes in the room. In fact, since the more uniform mode has a greater focusability, the same intensity of high harmonics can be produced with approximately 80% of the previous driving field intensity.

Once the pulsed laser beam exits the Spitfire Pro XP amplifier, it is guided by a series of dielectric mirrors toward a 30R/70T beam splitter. The less intense portion ($\sim$1 mJ) is the pump, and may be used at the fundamental 800 nm frequency, may be doubled to 400 nm or tripled to 267 nm by nonlinear BBO crystals, or it may be sent into the TOPAS-Prime (Light Conversion) optical parametric amplifier. Following these nonlinear processes to produce visible or UV wavelengths, the pump is then delayed by a 30 cm linear stage (M-531, Physik Instrumente). Its intensity is modulated with a variable filter wheel, and it is focused into the high vacuum system and then onto the sample with a spot size larger than the XUV spot size (Figure 2.1). The more intense portion ($\sim$2 mJ) is used as the driving field for high harmonic generation of the XUV probe. The beam is focused into the modified MAZEL-TOV two color gating assembly (section 1.3.3) and then into the semi-infinite gas cell in the high vacuum system. In the next section, we discuss why high vacuum is needed to perform XUV spectroscopy and how it is achieved.

2.1.2 High Vacuum Safety

A major advantage and also drawback of using XUV light for spectroscopy is that nearly all materials — metals, insulators semiconductors, gases — have a resonance in the XUV region. While this means that a great variety of materials may be studied with this technique, it has ramifications for the thickness of samples. Depending on the sample's XUV cross section, samples studied in absorption mode must be on the 10s to 100s of nm thickness scale in order to allow any XUV light to pass through to the detector. Similarly, the XUV attenuation length in ambient dry air is on the order of 10s of microns.[129] At pressures of 10^{-3} mbar, the attenuation length increases to 10s of meters, and up to kilometers at 10^{-5} mbar. Therefore, XUV spectroscopies require a high vacuum environment, defined as 10^{-3} to 10^{-7} mbar.[130]

Achieving these low pressures is possible with a two-step pumping technique utilizing a 'fore' or 'backing' pump and a 'main' pump, usually a turbomolecular pump (TMP).[131] The backing pumps used in this setup are all Varian scroll pumps that use a spiral shaped compressor to force out gas molecules. Roots pumps and screw pumps can also be used, although they are more costly, and the cheaper rotary vane pumps (Welch) may produce more contamination. The backing pump lowers the chamber pressure to $\sim 10^{-3}$ mbar, low enough that the TMP can safely operate. The Shimadzu TMPs used in this setup were chosen for their low cost and maintenance and their simple operation, but they suffer from high vibration and electrical noise.[130]

Aside from the choice of pumps, the vacuum chambers must be carefully designed to minimize the gas load on the pumps to reach high vacuum pressures. The main contributions to the gas load that the pumps must process are the initial gas inside the chamber, back-streaming and other effects from the pumps, entrapped gases, outgassing and leaks. Leaks and back-streaming are fixable, and the initial gas load and entrapped gases can be mitigated by using small chambers and precise design. A major source of entrapped gases in high vacuum systems are blind-tapped screw holes, which can be overcome with through-tapped holes or vented screws.[132] Outgassing from molecules adsorbed to the chamber's surface is more difficult to solve, and the outgassing rate goes as

$$\frac{dN}{dt} = -kNe^{(-E/k_B T)} \tag{2.1}$$

for surface molecule coverage N, binding energy E, temperature T and rate constant k. Therefore, the outgassing rate can be lowered by reducing the surface binding energy by choosing an appropriate chamber material such as stainless steel. Excess adsorbed molecules can be removed by thorough cleaning with solvent, pre-treatment with heat ('baking'), and by using gloves to avoid fingerprints.

Working with high vacuum equipment and with pressurized bottles of noble HHG gases presents safety hazards in the form of shrapnel released during implosion or explosion. To prevent serious injury, both engineering and administrative safety controls are applied. On

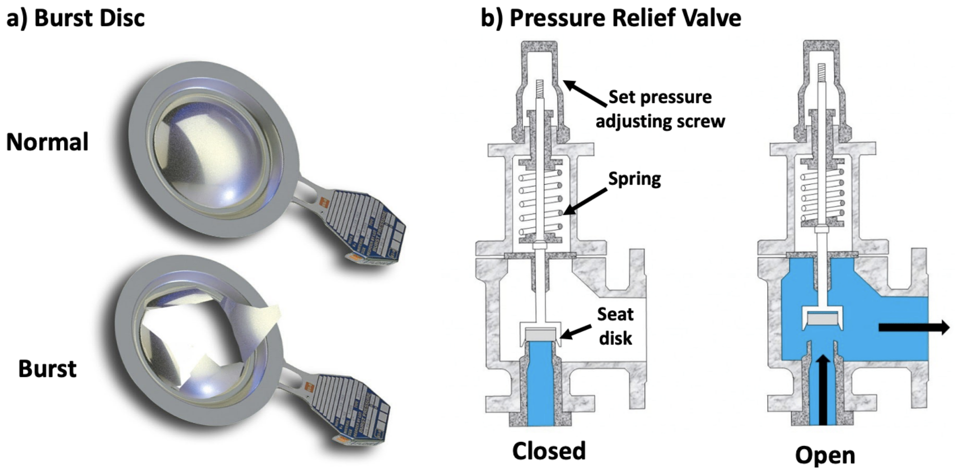

Figure 2.3: **Engineered safety controls for vacuum chamber over-pressurization.** a) A burst disc, also called a rupture disc, shatters when the internal pressure is above a set point. The material breaks open as one piece and does not spew dangerous projectiles in the lab. The top disc is new and the bottom disc is burst. b) A pressure relief valve in which a set screw, which may be adjusted to a range of pressure values, and a spring hold the 'seat disc' in place (left). When the pressure increases beyond the set point, the seat disc is lifted and pressure can escape from the side port (right). Adapted from reference [133].

the engineering side, the number of glass view ports may be reduced or covered by blast shields, and pressure relief valves and burst discs (rupture discs) may be added to the setup (Figure 2.3). For these engineered controls to work well, an understanding of the maximum and minimum allowed pressure of all parts in the system must be known.[134] On the administrative side, thoughtful procedures for filling and purging the vacuum chambers must be devised and posted in the laboratory space, and all laboratory workers should attend the relevant safety training(s) offered by the university.

2.1.3 Semi-Infinite Gas Cell

After the probe arm pulses are focused by a 70 cm focal length lens into the two color gating assembly, they enter the semi-infinite gas cell inside the first high vacuum chamber. The cell is 'semi-infinite' because it is tens of cm long instead of the typical several mm of a finite cell or a jet, like the one shown in Figure 1.18. The SIGC behaves like a waveguide because it can achieve phase matching of the NIR driving field and XUV generated field over a long distance, yielding approximately an order of magnitude greater conversion efficiency than a finite cell.[95, 135] By loosely focusing the driving field, a balance is achieved between the Kerr lensing effect that causes self-focusing and the defocusing by the ionized plasma to produce dispersion-free filamentation. Due to its geometry, the SIGC is much simpler to align into than the few-mm aperture of a waveguide or finite cell and has the benefit of an adjustable interaction length. The SIGC used here is capped on the beam inlet side by a

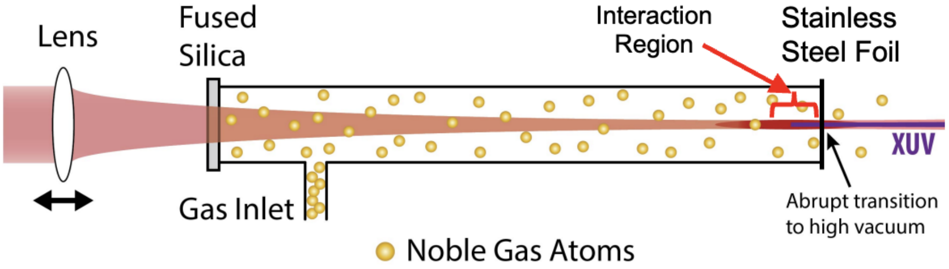

Figure 2.4: **A diagram of the semi-infinite gas cell used to generate high harmonics.** The driving field is focused into the inlet window, which is an anti-reflection coated glass. The gas cell is ∼30 cm long and filled with noble gas. The driving field beam exits the cell by ablating a hole in a 2 mm thick stainless steel foil, allowing for differential pumping. Adapted from reference [112].

piece of anti-reflection coated glass and capped on the outlet side by a 2 mm thick stainless steel foil, with noble gas atoms filling the entire 30 cm length inside. The driving field focus is placed very close to the outlet and ablates a hole in the steel foil, which allows the XUV and NIR light to pass through. This tiny hole separating the inside of the cell from the rest of the vacuum chamber system allows for differential pumping. Although the SIGC used here is pumped with a multi-cycle driving field, single-cycle pulses have been applied to generate continuous harmonics with a SIGC in the XUV and soft X-ray regimes.[136, 137]

As discussed in detail in section 1.3.2, the total intensity and spectrum produced by the high harmonic generation process is mainly dependent on the phase matching between the driving NIR field and the generated XUV field. The phase matching can be tweaked by adjusting the gas pressure, driving field intensity and chirp, and interaction region length. Here we explain how these modifications are achieved in the laboratory and demonstrate their effect on the generated harmonics. Practically, changing the noble gas pressure is accomplished by turning the gas inlet needle valve while monitoring the pressure inside the SIGC with a pressure gauge. A factor that cannot be ignored is the purity of the HHG target gas. Mixtures of two noble gases or of a noble gas and air produce drastically lower XUV flux due to destructive interference,[138, 139] so low-purity noble gases (below 99.999% pure) cannot be used and the gas delivery system must be completely free of leaks.

Changing the driving field chirp is also a simple process, and this involves changing the distance between the gratings in the compressor of the Spitfire Pro. The gratings are on a motorized stage and can be adjusted through the computer software that controls the laser. The purpose of the compressor is to spectrally disperse the laser pulses, allow the different wavelengths to propagate in free space for varying distances, and recombine them, effectively adjusting the relative timing between colors. Therefore, the compressor can add both positive (red first) and negative (blue first) chirp. Negative or anomalous chirped driving pulses have been shown to improve the generated XUV intensity and energy cutoff as well as increase the continuum beneath the peaks.[112, 140] Negative chirp can increase the ratio of long to

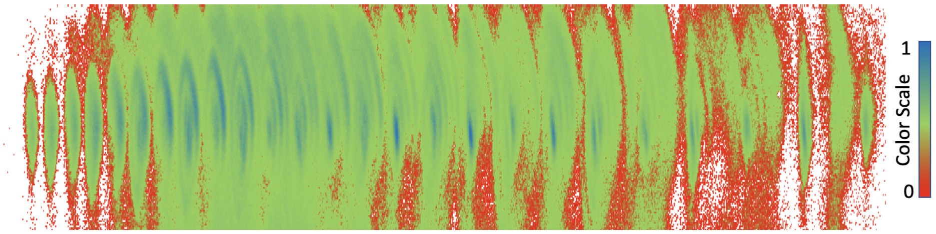

Figure 2.5: **Camera image of the XUV spectrum with long and short trajectories.** The color scale is indicated on the right with red color indicating no XUV counts, blue color for maximum counts, and green color for intermediate counts. The horizontal pixels relate to energy, with higher energies on the left and lower energies on the right. Vertical pixels show the XUV beam divergence. The XUV spectrum is modulated by peaks, corresponding to the even and odd harmonics of the 800 nm fundamental. The wispy parenthesis-like features surrounding the peaks are a consequence of interference between the long and short trajectories.

short trajectories, which appear in the XUV camera image as additional peaks shaped like parentheses surrounding the main peaks that occur at multiples of the driving field energy (see Figure 2.5). These long trajectory features aid in the generation of an XUV continuum by broadening and improve the overall signal-to-noise ratio of the experiment.[141, 142]

The most challenging factors to adjust for optimal phase matching are the interaction region length and driving field intensity, as these factors are intimately coupled. Normally, the interaction length and peak field intensity are both changed simultaneously by adjusting the focusing lens position to move the driving field focus spot, which occurs very close to the end of the SIGC. The lens is placed on a linear stage for repeatabilty, and a comparison of

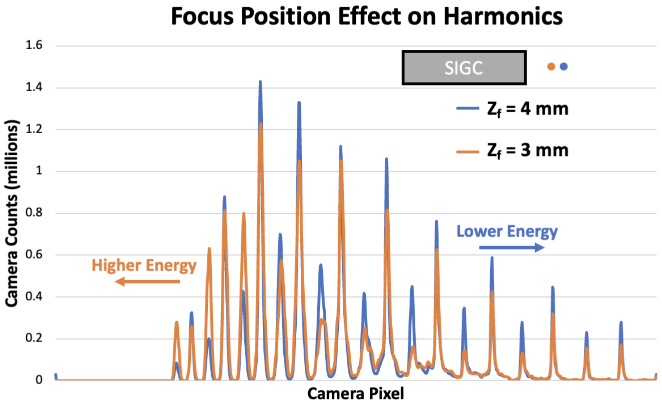

Figure 2.6: **The effect of changing the driving field focus spot on the generated XUV spectrum.** The blue spectrum corresponds to a focal plane approximately 4 mm after the SIGC foil, and the orange spectrum corresponds to a focal plane 3 mm after the foil. Moving the focal plane closer to the end of the gas cell increases the higher energy harmonics, but at the expense of the total harmonic flux. The inset shows the focal plane positions relative to the end of the cell.

two different focal plane positions after the SIGC foil are shown in Figure 2.6. Driving the focal plane into the gas cell causes an increase in the higher-energy harmonics, but a decrease in total XUV intensity. An excellent description of the impact of lens position on the generated harmonics can be found in the dissertation of Chang-Ming Jiang.[112] An additional method to change the focusability and total intensity of the driving field is by closing an upstream aperture, which can increase harmonic flux by an order of magnitude.[143] The total driving field intensity can be altered by swapping out the 30R/70T beam splitter for a different splitting ratio, but this affects downstream alignment and is not done on a daily basis. Adjusting the settings for pump power or number of round trips in the regenerative amplifier of the Spitfire Pro can change the total field intensity. A mismatched field intensity experienced by the Ti:sapphire crystal can lead to pre- and post-pulses and even optics damage, so it is recommended that these adjustments are small and that other laser parameters, such as pulse duration, transverse mode and spectrum, are carefully monitored.

Additionally, the beam pointing and power fluctuations that occur on a daily basis will affect the output of the modified MAZEL-TOV two color gating apparatus, and it can lower even harmonic flux, total XUV flux, or decrease the XUV continuum under the peaks. To redress these effects, daily adjustment of the ϕ (phase-matching) and θ (incidence) angles of the BBO crystal and the calcite crystal pair are needed. Adjustment of the half waveplate angle may also be required.

2.1.4 Focusing and Filtering

Once the harmonics are generated near the NIR focus, both fields diverge into the vacuum chambers. A few steps must be taken to filter out the driving field and refocus the XUV field onto the sample. Since the NIR driving field is much more intense than the generated XUV field by about 8 orders of magnitude, blocking it from heating the sample is of the utmost importance because heating will alter the observed dynamics or even damage the sample. Traditionally, thin metal foils of ∼200 nm or less thickness have been used to filter out the NIR driving field while allowing a majority of the XUV light to pass (Figure 2.7). For example, a 200 nm thick Al film allows 70% of the light between 20 and 70 eV through while blocking all of the 800 nm light (calculated out to 8 decimal places), and a 200 nm thick Zr foil will allow >40% of the light between 80 and 170 eV to pass.[129] Due to the metal resonances in the XUV range, the foils must be swapped out to measure spectra in the range below 70 eV and above ∼75 eV, and samples with edges in the 65-80 eV range are difficult to measure due to low XUV flux. Moreover, these foils are extremely difficult to handle due to their low thickness, and break or oxidize readily in air. Therefore, a different type of NIR filter based off a microchannel plate (MCP) has been proposed and was attempted here.[144]

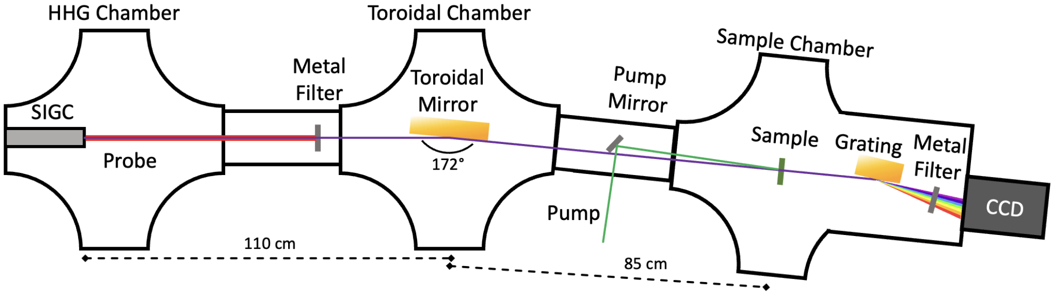

Figure 2.7: **Details of the optics inside the high vacuum system.** From the left, the XUV probe arm (purple) exits the semi-infinite gas cell and co-propagates inside the HHG chamber with the NIR driving field (red). A metal filter between the HHG and toroidal chambers blocks all of the NIR light while allowing the majority of the XUV light to pass. In the toroidal chamber, the gold coated toroidal mirror focuses the XUV light onto the sample with an angle of incidence of 86%. The visible pump (green) enters the high vacuum system and is directed to the sample, after which it is blocked with a physical barrier (not shown) and then a second metal filter. The transmitted XUV probe is dispersed by the grating, passes through the metal filter, and is recorded with the CCD camera.

Microchannel Plate

Microchannel plates are few-mm thick glass pieces with millions of tiny holes cut slightly off-axis from normal incidence. The holes, or channels, are only a few microns in diameter and spaced periodically. MCPs were invented as photon and particle detectors because they act as a series of tiny electron multipliers when a voltage is applied to the plate, although no voltage is applied when they are used for XUV filtering. The holes are on the order of

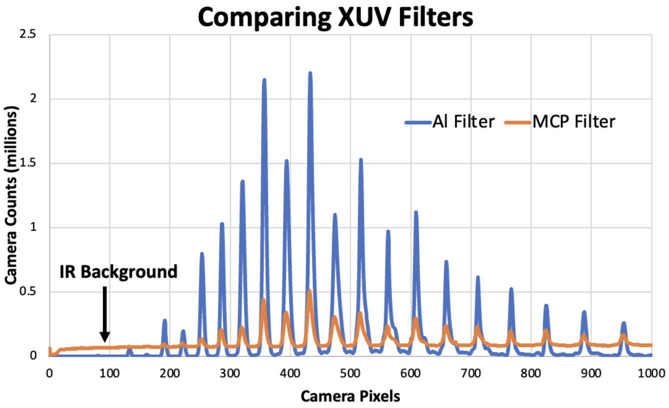

Figure 2.8: **The XUV spectrum transmitted by different NIR filters.** In orange is the spectrum transmitted by the microchannel plate, which has low flux and a clear background signal caused by diffracted NIR light. In blue is the spectrum transmitted by the 200 nm Al filter, which has a much higher XUV flux and no scattered NIR background.

visible and NIR wavelengths, so the driving field will be strongly diffracted by the MCP while the much shorter XUV wavelengths should pass through.[144] Since the plates operate by diffracting light instead of absorbing, there are no XUV resonances and the MCP can theoretically transmit across the entire XUV range.

Practically, the MCPs are not effective as XUV filters. Firstly, the plates must be oriented perfectly to allow the XUV to pass, as any slight deviation will angle the channels and diffract the XUV. To overcome this issue, the plates were installed in the vacuum chamber after the gas cell on a motorized mirror mount with 2 piezo-driven axes. Figure 2.8 shows the resulting harmonic spectrum in orange compared to the spectrum transmitted by a 200 nm Al foil in blue. It is clear from this image that the total XUV flux transmitted is almost five times less intense, even when the incidence angle was optimized. The second issue with using an MCP filter is that the NIR light is diffracted instead of reflected or absorbed. The NIR beam bounces around the stainless steel walls of the vacuum chambers, with a significant portion traveling all the way to the spectrometer to be measured as a constant background, as can be seen in Figure 2.8. The diffracted NIR light can be observed by eye, and was responsible for destroying several samples. Therefore, a metal filter is strongly recommended over an MCP. A new filter design that allows spectrally dispersed light to be transmitted in the full 45—90 eV range is presented later in this section.

Toroidal Mirror

After the filter, the XUV beam enters the toroidal mirror vacuum chamber shown in Figures 2.1 and 2.7, which houses the toroidal mirror. A toroidal mirror is used to focus the XUV beam instead of a standard spherical focusing mirror because of the extremely efficient absorbance of XUV light by metals and films. In order to reflect any appreciable amount of XUV, the reflecting surface must be close to grazing incidence. Spherical mirrors only produce small circular focal spots near normal incidence, but toroidal mirrors can be used near grazing incidence.[145]

A toroidal mirror is shaped like an arc cut from a torus, which is a donut-shaped geometric construct (Figure 2.9). The torus is defined by two radii: the tangential radius, R_t, which defines the distance from the center of the donut hole to the middle of the ring, and the sagittal radius, R_s, which is the radius of the ring. Since there are two radii of curvature on two perpendicular planes, there are two focal distances, s_s and s_t. For an object at distance s from the center of the mirror and angle ϕ from the toroidal mirror normal, we can solve for a single point $s_1 = s_s = s_t$ where the tangential and sagittal focal spots are identical.[146] This occurs when

$$\frac{R_s}{R_t} = cos^2(\phi) \tag{2.2}$$

$$\frac{2cos(\phi)}{R_s} = \frac{1}{s} + \frac{1}{s_1} \tag{2.3}$$

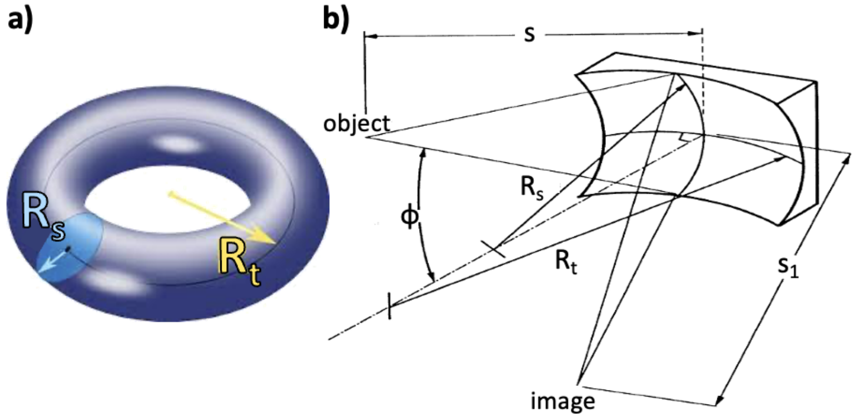

Figure 2.9: **A diagram of the toroidal mirror focal spots.** a) A figure of a torus, with the tangential (R_t) and sagittal (R_s) radii labeled. b) The focal spots for a toroidal mirror of radii R_s and R_t for an object at distance s from the center of the toroidal mirror and angle ϕ from the normal to the mirror. The tangential and sagittal focal spots are identical at s_1. Adapted from reference [145].

In other words, we can design a toroidal mirror for a given angle of incidence and a given distance from the object (XUV source) and image (sample) so that the vertical and horizontal focal spots align, producing a circular astigmatism-free spot. The toroidal mirror used in this setup is designed for an incoming angle of 86° from normal incidence, an object distance of 110 cm, an image distance of 85 cm, and produces a focused XUV spot size of ~200 μm. The mirror is gold coated, so approximately 85% of the XUV light is reflected. XUV setups have been designed with longer focal lengths or two toroidal mirrors to obtain even smaller spot sizes on the order of 10 μm.[147, 148]

Dual-Metal Filter Design

Once the NIR, visible or UV pump excites the sample and the XUV beam probes it, a second filter is needed to remove the pump light and allow the transmitted XUV beam into the spectrometer. In this setup, the pump and probe have a small crossing angle of ~1° and a physical barrier blocks the majority of the pump light from entering the spectrometer chamber. Nonetheless, the pump is so much more intense than the probe that even a small amount of scattered pump light can have an effect on the measurement. Typically, a second metal filter is placed after the sample and grating in the spectrally dispersed first order diffraction beam, as shown in Figure 2.7.

This second post-sample metal filter suffers the same downsides as the filter after the SIGC. They break easily during handling or vacuum chamber pump up/down, and can only measure in specific spectral ranges below 72 eV (Al) or above ~75 eV (Zr). Here we present a new filter design that is Al on one side and Zr on the other side (Figure 2.10a),

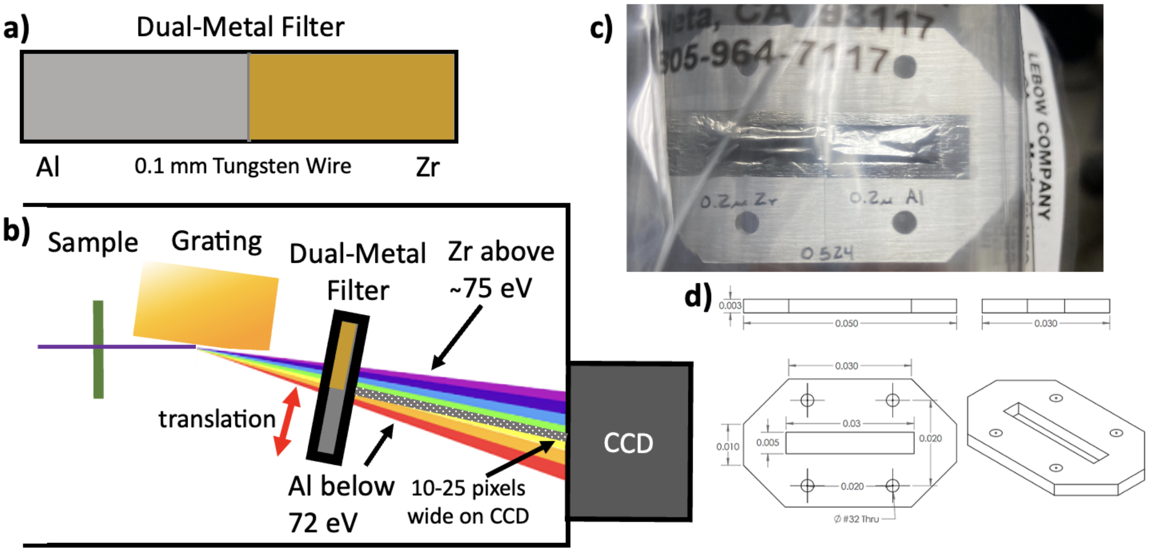

Figure 2.10: **Design of the dual-metal (Al and Zr) XUV filter.** a) A diagram of the filter, which will have a 0.2 μm thick 5 x 15 mm Al foil on one side, a 0.2 μm thick 5 x 15 mm Zr foil on the other side, and a 0.1 mm tungsten (W) wire between them. b) The layout of the spectrometer chamber with the dual-metal filter installed. The filter will be aligned so that the Al side is on the low-energy side of the first order diffraction and the Zr side is on the high-energy side. The filter will be on a translation mount to perfectly align the W foil in the beam, which is expected to block XUV light from reaching 10—25 pixels (0.4—1.0 eV). c) A picture of the completed dual-metal foil, still in the air sealed wrapper. d) Drafts of the filter mount, which will attach to the motorized translation stage mount.

to be placed after the diffraction grating to allow an XUV measurement over the full range of energies produced by the SIGC with no need to ever remove the foil from the vacuum chamber. This foil, which is 200 nm thick 5 x 15 mm Al on one side, 200 nm thick 5 x 15 mm Zr on the other side, and a 0.1 mm tungsten (W) wire in between, is mounted on an electronic translation stage so it can be inserted into the diffracted beam by a varying amount (Figure 2.10b). A picture of the foils that were produced and a technical drawing of the mount used to attach the filter to the translation stage are shown in Figure 2.10c and 2.10d, respectively. The tungsten wire is estimated to block 10—25 pixels worth of light from reaching the CCD camera, which roughly translates to 0.4—1.0 eV, and the blocked pixels can be carefully chosen to not overlap with XUV resonances using the translation stage. When the W is centered, the dual-metal filter can simultaneously measure an XUV spectrum spanning 45—90 eV. The purely Al side and purely Zr side of the foil are each large enough to allow the full first order diffraction beam to pass through, so this filter design supports measurement anywhere in the full 25—110 eV range produced by the SIGC.

A major limitation to this dual-metal filter design is that the beam is not spectrally dispersed between the SIGC and toroidal mirror, so the upstream filter that blocks the

NIR driving field cannot be designed the same way. If the upstream filter is a pure metal filter, it will block the light in this 70—75 eV region, defeating the purpose of the dual-metal design. A possible work-around is the use of a pair of silicon plates angled at the driving field Brewster angle, which has been demonstrated to attenuate the driving field by approximately 10^{-5} while still allowing 0.5 of the XUV flux to reach the camera.[149, 150] This filter blocks the driving field by exploiting the difference in Brewster angles between the NIR and XUV wavelength and not by absorption. The XUV resonance of silicon is near 105 eV, so this type of filter would be ideal for use in combination with the dual-metal filter to observe dynamics in the 65—80 eV range. Unfortunately, the vacuum chamber design may need to be altered to accommodate the different beam path geometry with the silicon plates.

2.1.5 The Spectrometer

As mentioned above, the XUV probe interacts with the sample and is dispersed by a grating. The grating is a variable line-spacing grating (Hitachi), which delivers an approximately flat-field focus across the entire spectrum. Details of this grating can be found in the theses of Chang-Ming Jiang and Lucas M. Carneiro.[15, 112] Here, we discuss the operating principles of the charge coupled device (CCD) camera (PIXIS-XO 400B, Princeton Instruments) used in this experiment.

Invented in 1969 and earning the Nobel Prize for its inventors Willard S. Boyle and George E. Smith in 2009, the CCD is ubiquitous in modern technology such as photocopiers and security cameras.[151] CCD cameras are digital cameras consisting of a grid of tiny CMOS devices, called ‘pixels’, which are each a small p-n junction. When photons strike the pixels, they generate current via the photoelectric effect. This current is collected and read out to a computer pixel-by-pixel in series across each row of the grid where the current is collected in a serial array bucket pixel on the end of the row. The serial array bucket then shifts the charge down one row, called a ‘register shift’, and the image is read out and stored in computer memory (Figure 2.11a).[152] CCD cameras can be small enough to be used for endoscopy, and are sensitive to low-light environments and to light with infrared, visible, UV and X-Ray wavelengths.[153] The low noise, linear behavior, low operating voltages of 5—15 V and rapid acquisition times of 10s of ms make CCD cameras ideal for pump-probe spectroscopy. CCD cameras have a quantum efficiency of approximately 80% and a dynamic range of 10^4, which are useful properties for measuring the low flux and peaked structure of an XUV spectrum.

The noise in the image measured by the CCD comes from four main sources: the dark current, nonuniform pixels, shot noise and read noise. Dark current, D, is the result of thermally-excited charge carriers in the semiconductor material of the CMOS pixels.[154] The CCD camera used in this experiment can be cooled down to -60 °C to reduce the effect of dark current on the measurements, which tends to be on the order of 10^{-3} photoelectrons per pixel per second.[155] Non-uniformity in the pixel gain and dark current can be

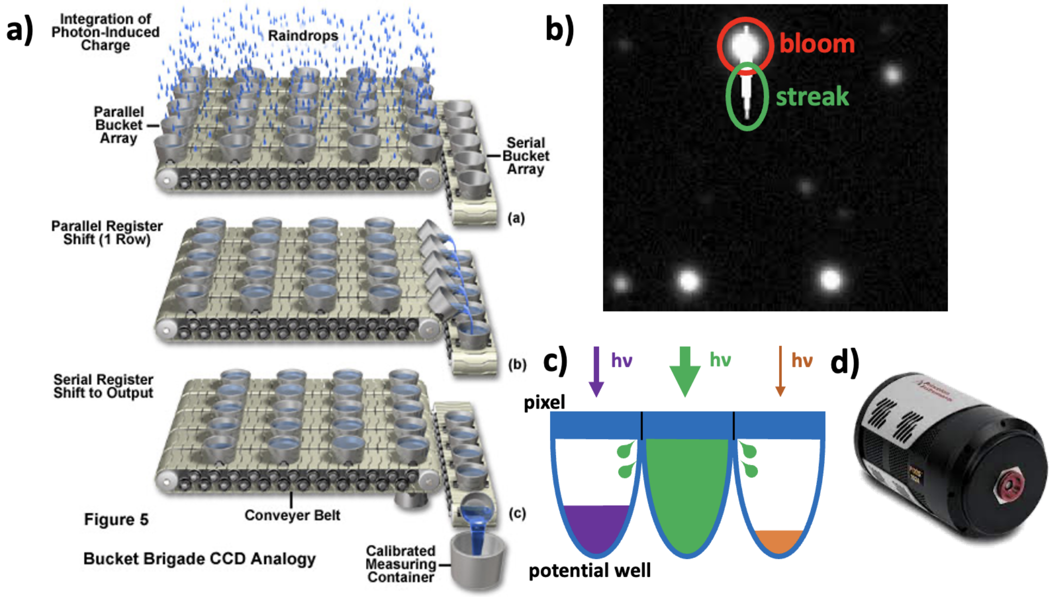

Figure 2.11: **The design and working principle of charge coupled devices (CCDs).** a) A schematic of how a CCD reads out the pixels. Pixels can be thought of as buckets collecting photons, which are raindrops. The buckets along a row transfer their raindrops along the row and are collected at the end of the row in a special bucket called the serial array bucket. Then, the serial array shifts down one row at a time to be collected and measured by the computer. Adapted from reference [154]. b) Common artifacts that occur when operating a CCD camera near saturation. Blooming, circled in red, happens when too many photons in one pixel overflow into the neighboring pixels. Streaking, shown in green, occurs when an overfilled pixel leaks into the other pixels in the row during readout. c) A cartoon of a saturated pixel, in green, overflowing into the neighboring (orange and purple) pixels. d) A picture of the CCD used here, the PIXIS-XO 400B.

corrected with a flat-field correction (FFC), and the CCDs used here automatically perform the correction.[156] Shot noise is an inescapable consequence of the discrete quantum nature of photons and electrons, but its effect on the noise can be mitigated with higher photon counts. Read noise, N_r, is also unavoidable and depends on the specifics of the camera used, which here is approximately 16 electrons RMS.[155] We have found that the read noise of the CCD used in this experiment is affected by the temperature the camera is cooled to and increases below about -20 °C, likely due to increased noise from the thermoelectric cooler. The CCD is generally kept at -20 to -15 °C to minimize total noise. An expression for the signal-to-noise ratio (SNR) of a camera with quantum efficiency Q_e for a photon flux of P is

$$SNR = \frac{PQ_e t}{\sqrt{PQ_e t + Dt + N_r^2}} \tag{2.4}$$

CCD cameras have a nearly linear behavior, meaning that the current generated at a given wavelength is linear with respect to photon flux for the majority of the dynamic range.

Once the pixels reach $\sim 10^5$ electrons each, or their ‘full well capacity’, the semiconductor portion of the CMOS device cannot accommodate any more photoelectrons. The pixel’s charge per photon becomes nonlinear near this saturation fluence, which may cause overflow into neighboring pixels called ‘blooming’. The overflow electrons can further effect the pixels along the same row as the saturated pixel during readout in an effect called ‘streaking’. An image of blooming and streaking is included in Figure 2.11b. When operating the CCD for an XUV transient absorption experiment, the measured XUV intensity is kept well below the saturation threshold. In the following subsection, we discuss all the details of how an XUV transient absorption measurement is obtained.

Data Acquisition and Noise Reduction

At each time step, the transient signal is calculated as the difference between the absorbance of the probe spectrum measured with the pump on and with the pump off, called a differential absorption. The goal of a transient absorption measurement is to observe the ultrafast pump-induced changes to the sample. Thus, all other sources of changes to the sample or to the probe spectrum must be controlled. One source of signal inhomogeneities is sample ‘rastering’ or moving the sample around between measurements to avoid laser-induced damage. The thin film and nanoparticle samples studied here tend to be very delicate and the signal-to-noise ratio of the experiment requires multiple hours of averaging, so rastering is essential. To overcome the artifacts in the transient spectrum caused by inhomogeneities in the sample, care must be taken to produce perfect even films, as will be discussed in section 2.2, and longer scans or more averaging will reduce the impact on the spectrum.

Another source of unwanted artifacts is that the samples may become heated and add signals from heat-induced lattice expansion to the spectrum. Since the XUV flux produced in the SIGC is fairly low on the order of nJ, multiple XUV bursts are recorded for each pump-on or pump-off camera image. Typically an integration time of 0.5—1.0 second is used, corresponding to 500—1000 laser pulses each image. Therefore, the sample may still hold residual heat from the previous pump pulse in the train that arrived 1 ms earlier, and this heating causes a spectral background across the entire transient measurement (Figure 2.12). Steady-state changes to the sample temperature over hours will be subtracted out in the pump-on minus pump-off calculation. It is the few-ms transient heating by the pump during the pump-on measurement which can cause signals to appear in the transient spectrum. While this constant background can be subtracted post-measurement, it is less clear what the affect the excited/expanded lattice has on the other dynamics observed, so it is preferred to reduce the background heat as much as possible.

A method to limit the heat background is by ‘chopping’ the pulse train to a lower repetition rate. A chopper is a well calibrated fan blade that alternately blocks or allows pulses to pass. In the measurements described in Chapter 6, a chopper reduces the repetition rate of both the pump and probe by 10, down to a rate of 100 Hz or a pulse every 10 ms. This drastic reduction in laser pulses delivered per second requires an increase in CCD integration

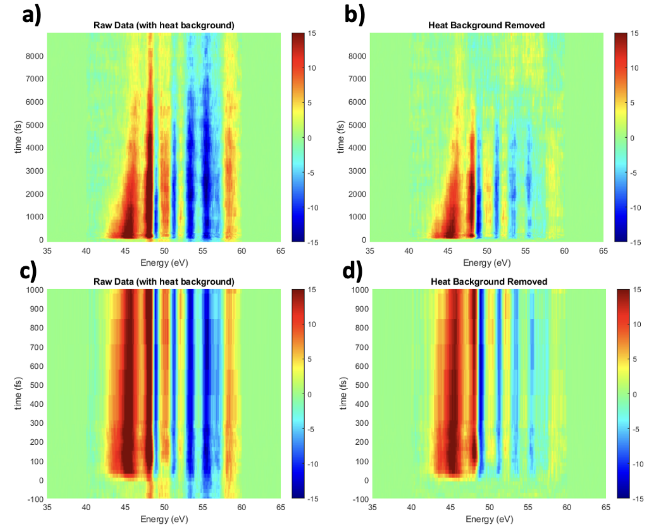

Figure 2.12: **An example of a heat background in an XUV transient absorption measurement.** a) The raw differential transient absorption of $CsGeI_3$ at the I $N_{4,5}$ edge following photoexcitation for the first 8.5 ps. The color scale indicates differential absorbance in units of milli-optical density (mOD). b) The same measurement of $CsGeI_3$, but with the constant background spectrum caused by heating of the lattice removed. c) The raw data and d) the heat background-subtracted data shown between 100 fs before and 1 ps after time zero.

time and in total measurement time, but also allows the sample to cool between pump shots and lowers the heat background significantly. Thus, the decision to chop the pulse train must be made carefully based on the signal-to-noise ratio of the measurement.

The changes to the measured signal described above are both caused by the sample. There are two additional sources of noise that have a major effect: electrical noise and laser shot noise. Sources of electrical noise are the CCD camera, which can add noise from dark current, readout, and other sources described by eq. 2.4, interference from coiled wires, RF noise from the turbo pump controllers or chillers, and elsewhere. These sources are insignificant compared to the noise caused by fluctuations in the laser intensity. Pulse-to-pulse fluctuations from a Ti:sapphire amplifier are on the order of <0.5% RMS, but these fluctuations are amplified significantly during the high-order harmonic generation process. If the intensity noise of the fundamental driving field is δ_1, then the noise of the n^{th} harmonic goes as $\delta_n = \delta_1\sqrt{n}$. Add in the effects on the harmonic intensity caused by fluctuations in air humidity, dispersion, dust, pointing drift, HHG gas pressure and more, and the measured RMS stability of the HHG intensity is on the order of 8.5%.[157] Stable optics mounts, clean optics, precise gas inlet valves, and vibration damping of the entire system can reduce the noise enough that an XUV transient absorption measurement is possible over multiple hours. In order to reduce the averaging time further, higher repetition rate sources and greater XUV flux are needed.

2.2 XUV Nanoparticle Samples

As described above, the samples measured in an XUV transient absorption experiment must be both thin enough so that they don't completely absorb the XUV probe spectrum and uniform enough to be raster scanned. The optimal thickness of the sample depends on the XUV cross section of the constituent elements. The sample should be close to the penetration depth to maximize the transient changes while still allowing enough XUV light to pass through to the detector to overcome Poisson noise. Transition metal elements like nickel or iron have penetration depths on the order of 10s of nm, while p-block elements like silicon or iodine have XUV penetration depths of hundreds of nm.[129] It therefore follows that the average nanoparticle diameter should be near or below the penetration depth of the material.

Sample thickness scales linearly with absorbance via Beers law, so variations in thickness alter the magnitude of the peaks. These variations cannot be subtracted out, even if the pump-on and pump-off images are measured at the same position, because the amount of photoexcited carriers will scale differently than the number of XUV transitions. The differential absorbance feature magnitude will be the mean of the magnitudes of all the thicknesses, necessitating more averages and longer data acquisition times. For thin film samples which are produced via sputtering, target evaporation, or vapor-assisted deposition methods, the uniformity is not an issue if the sample substrates are small and kept far from the source.[158]

Surface roughness affects the absorbance via scattering, which can be separated into three scattering mechanisms. In the limit of a smooth mirror surface where the wavelength is large compared to the roughness, scattering is 'specular' and will occur in a single ray with the same angle relative to the sample normal as the incoming beam (Figure 2.13a).[159] The XUV probe is close to normal to the sample surface, so specular scattering can be ignored as it will direct the beam away from the spectrometer. Any changes to the probe spectrum due to specular scattering will be subtracted out in the differential measurement. In the other limit, when the wavelength of light is much smaller than the roughness, the scattering is 'diffuse' or 'Lambert scattering' and will occur evenly at all angles radially out from the probe spot (Figure 2.13c).[160] Even mirror-smooth surfaces exhibit diffuse scattering, but the scattering centers are the nuclei in the crystal and not the surface roughness. Interference between the diffusely reflected beams from the nuclei leads to the Bragg reflections used in crystallography. Between these two limits is Mie scattering, a special case of which is the Rayleigh scattering that causes the sky to be blue. In the Mie scattering regime, the wavelength of light is comparable to the size of the scattering center (Figure 2.13b).[161] XUV light (10—125 eV) has wavelengths ranging from 10—125 nm, which is the size of nanoparticles, so Mie scattering may be the dominant scattering mechanism. Mie scattering has been observed to drastically modify the spectra and dielectric properties of dielectric nanoparticles.[162, 163] Mie scattering is directional and wavelength-dependent so it cannot be easily

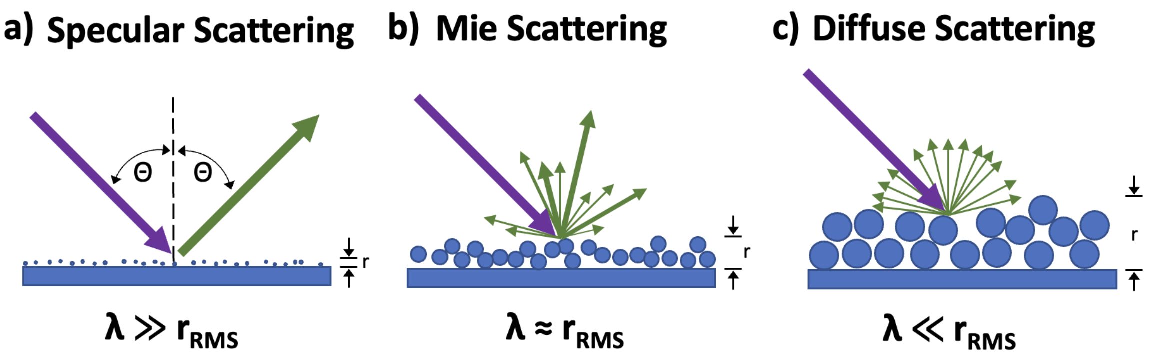

Figure 2.13: **The scattering processes that can occur on a surface coated in nanoparticles.** a) When the wavelength of the light is large compared to the average surface roughness, r_{rms}, specular scattering occurs. The incoming beam, shown in purple with an angle relative to the surface normal of θ, is scattered as a single ray (green) at angle θ. b) Mie scattering is the dominant mechanism when the wavelength of light is comparable to the surface roughness. Mie scattering is directional and wavelength dependent and is influenced by the dielectric constant of the particles and their radii. c) Diffuse scattering occurs when the wavelength is much smaller than the surface roughness and occurs evenly at all angles radially away from the surface.

subtracted from the measurement and instead must be mitigated through careful sample preparation. More details on predicting the Mie scattering spectrum can be found in Huffman and Bohren's book on scattering by small particles (reference [164]). Next, we present the technical considerations and procedures for producing a uniform film of nanoparticles to be measured with XUV transient absorption.

2.2.1 Sample Preparation

The first step in preparing an adequate nanoparticle sample for XUV study is choosing the correct substrate. The substrate must be strong enough to be handled and deposited onto, thin enough so that it does not absorb much XUV light, uniform in thickness, and without XUV resonances near those of the element of interest. It is useful for the substrate material to be insulating so as not to affect the measured dynamics. The sample substrates should also be commercially available and affordable. With all of these considerations, the most commonly used substrate in the XUV studies presented in this dissertation is silicon nitride (Si_3N_4), which is both insulating and fairly robust. Membranes can be purchased from Norcada, Inc. for approximately \$18 each that are ∼30 nm thick and 0.5 x 0.5 mm across (Figure 2.14a). When the element of interest is silicon or absorbs XUV light near the silicon $L_{2,3}$ edge at 105 eV, ∼50 nm thick 0.5 x 0.5 mm diamond membranes from Applied Diamond, Inc. are used, but these cost \$200 each and vary in thickness by ±10 nm across a single membrane. More recently, polymer films grown in the lab with a slip-coating process have shown an increased XUV transmittance over Si_3N_4 and diamond.[165] These polymer

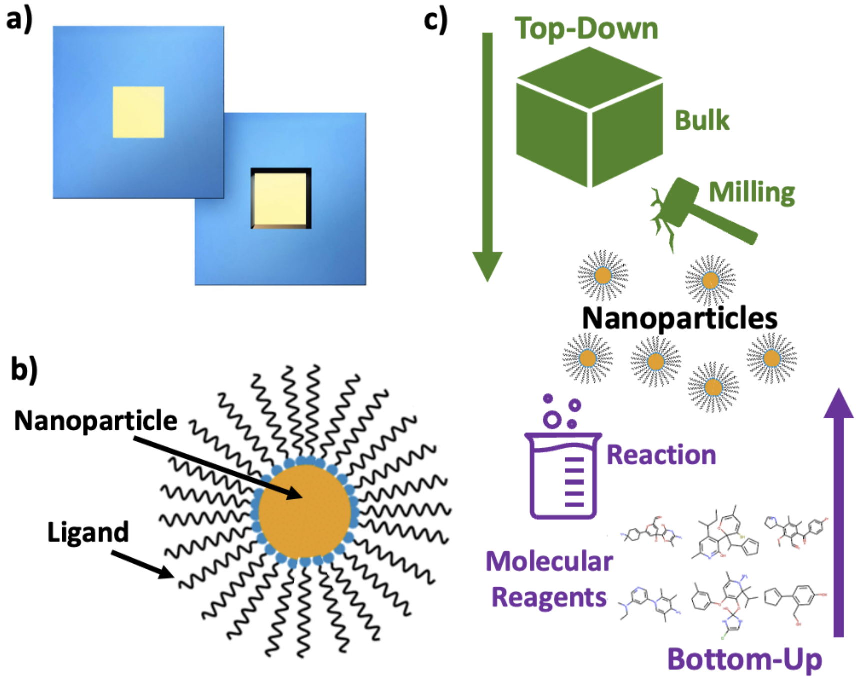

Figure 2.14: a) An image of a thin XUV membrane supported on a square window. The membrane is flush to one side of the window and the other side is beveled. b) A diagram of a nanoparticle covered in ligand molecules. c) Graphical description of the top-down and bottom-up nanoparticle synthesis methods. In the top-down approach, nanoparticles are produced from a bulk precursor, often mechanically by milling. For the bottom-up approach, the precursors are molecular reagents, which undergo some reaction to form nanoparticles.

films are either polystyrene (PS) or polyvinyl chloride (PVC), and made of hydrogen and carbon (and PVC has chlorine), which do not have edges that overlap with silicon. So far, only molecular adsorbates have been deposited on these films, and they suffer from similar variations in thickness as the diamond membranes, so further study is needed before applying them to support nanoparticles.

Nanoparticles are commonly produced either with a top-down approach (starting with a macroscopic solid) or a bottom-up approach (from molecular reagents), as shown in Figure 2.14c.[166] Top-down nanoparticle synthesis can utilize mechanical milling techniques, lithography, sputtering, or laser ablation, and the resulting nanoparticles are purified and dried into a powder. Due to the highly carcinogenic nature of inhaled nanoparticles, it is safest to store dry nanoparticle powders in the fume hood or to suspend them in liquid. Bottom-up methods include chemical vapor deposition, solvothermal or hydrothermal synthesis, sol-gel, or reverse micelle synthesis. The solvent-based solvothermal and hydrothermal methods are most commonly used to produce oxide and semiconductor quantum dots and use metal salts, such as nitrides or chlorides, as starting reagents.[167] The nanoparticles synthesized in solution are covered in long chain surface molecules called ligands, and the properties of the ligands affect many aspects of the nanoparticle binding and solvation (Figure 2.14b). The resulting colloidal nanoparticle solutions contain precursor ions and excess ligands and surfactants, which must be washed away before deposition as a film.

Once the substrate and synthesis process are chosen, the deposition method must be refined. For nanoparticles suspended in solution, the simplest way to deposit a thin film of particles is by placing a drop onto the substrate and allowing the solution to dry off, also called ‘drop-casting’. There are a variety of factors that need to be just right for this to produce an even film instead of clumps or rings.[168] Firstly, the solution must completely ‘wet’ the surface as opposed to beading up on the surface. For wetting to occur, both the solution and surface must have similar polarity. Secondly, the solution must suspend the particles well without clumping, as a clumpy surface will be too thick for the XUV probe to penetrate (Figure 2.15b). The concentration of nanoparticles must be low to deposit a thin enough film for XUV absorption, and the volume of the drop must be tuned to match the substrate size.[169] Additionally, the nanoparticles must attach reasonably well to the surface, and their rate of surface adsorption must be faster than the rate of solution drying to produce fairly uniform films. If the nanoparticles don’t stick well to the surface or if the solution dries faster than the nanoparticles can stick, then the nanoparticles are swept up in the solution bead as it dries and shrinks (Figure 2.15a).[170] This leads to barely any coverage near the edge of the substrate and a thick series of rings near the middle (see Figure 2.15b). Qualities such as low solution volatility and high surface tension and capillary forces, like water possesses, are generally bad qualities in a solvent. Methods for altering the polarity of the substrate surface or solution, removing clumps, and altering the nanoparticle binding can be found in section 2.2.2.

Although drop-casting is simple and highly tunable, the evaporation rate cannot be perfectly controlled, leading to differences in film thickness across the surface.[171] Flowing dry

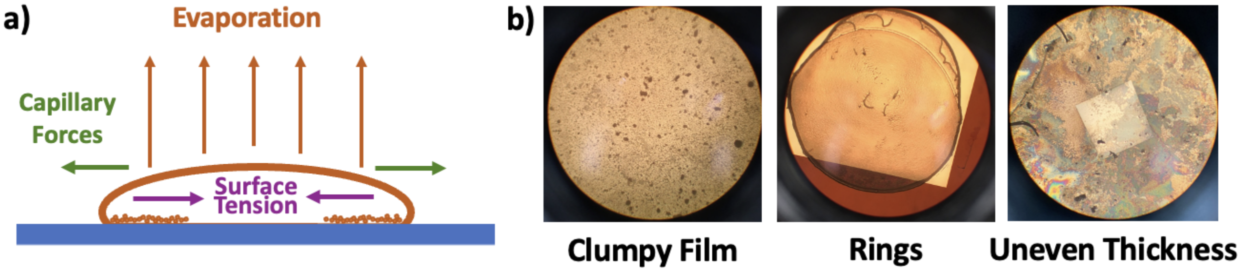

Figure 2.15: **Drop-casting a nanoparticle film and possible issues.** a) The forces occurring simultaneously inside the nanoparticle solution bead (orange) as it dries on the substrate (blue). The bead experiences capillary forces pulling it to expand laterally and surface tension and viscous forces pulling it inward while it evaporates. b) Microscope images of nanoparticle drop-cast solutions on Si_3N_4 membranes. On the left is a clumpy film, in the middle are a pair of overlapping rings, and on the right is an uneven thickness film.

air over the solution drop or changing the temperature or pressure of the drying environment can improve uniformity, but sometimes this is not enough to obtain a film suitable for XUV absorption. Next we discuss the method of spin-coating, which provides more uniform thickness films.[172] Other techniques, such as dip-coating, spray-coating and Langmuir-Blodgett are possible, but will not be covered in this dissertation.

Spin-Coating

Spin-coating is a similar technique to drop-casting, except the sample substrate and solution drop are spun at a high speed while the drop evaporates to ensure an even coating.[173] The drop is usually applied while the substrate is stationary, followed by a few seconds of rapid acceleration, a brief period (30 seconds to 1 minute) of fast spinning on the order of a few thousand rotations per minute (RPM), and then a rapid deceleration (Figure 2.16a). Alternatively, the drop can be applied while the substrate is already spinning at a low speed (around 500 RPM), which is called a ‘dynamic dispense’.[174] Once deposited, the effect of high speed rotation on the nanoparticle solution is to push the bead toward the edges of the substrate via centrifugal force.[175] The radially outward-directed centrifugal force is balanced against the inward-directed viscous forces of the solution. If we assume that the solution behaves as a Newtonian fluid, and that the substrate is rotating at an angular velocity ω, the balance of forces can be written as

$$-\eta\left(\frac{d^2\nu}{dz^2}\right)=\rho\omega^2 r \tag{2.5}$$

in polar coordinates (r,θ,z) where the coordinates are aligned with the center of the spinning substrate.[176] The solution viscosity is η, the droplet’s velocity in the r direction is ν, and the solution density is ρ. Applying boundary conditions and integrating with respect to z and r, we obtain the solution for the height of the top of the bead, h, as follows

$$\frac{dh}{dt}=\frac{-2\rho\omega^3h^3}{3\eta} \tag{2.6}$$

which can be further solved to obtain the bead height as a function of time

$$h(t)=\frac{h_0}{\sqrt{1+\frac{4\rho\omega^3h_0^3t}{3\eta}}} \tag{2.7}$$

for initial bead height h_0 and time t. Thus, the height of the bead is dependent on the viscosity and concentration of the solution, the angular velocity, and the spinning time.[177]

These equations do not include the effect of solution evaporation on the bead height, which can be included as an additional term in eq. 2.6 as

$$\frac{dh}{dt}=\frac{-2\rho\omega^3h^3}{3\eta}-e \tag{2.8}$$

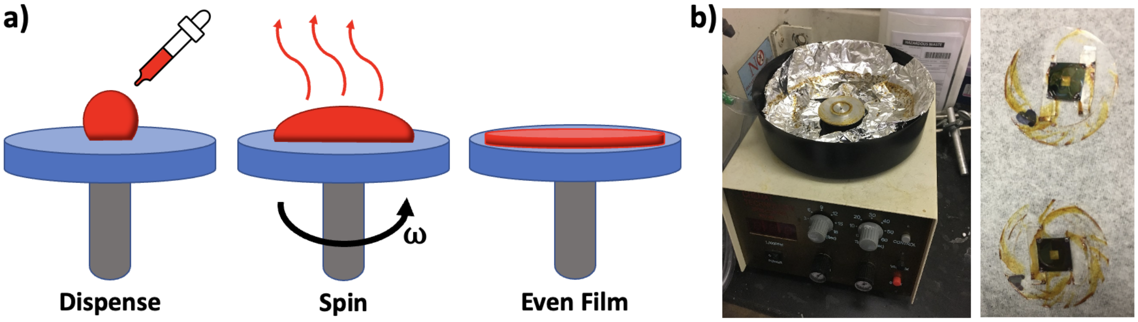

Figure 2.16: **Spin-coating the nanoparticle solution onto the XUV membrane.** a) The three steps in a spin-coating procedure. On the left, a carefully measured drop of solution is deposited on the substrate. In the middle, the substrate is spun at angular velocity ω while the solution evaporates. On the right, the fully dried solution produces an even film. b) On the left is a picture of the spin coater, covered in foil to protect the inside of the coater from getting dirty. On the right are two XUV membranes spin-coated with metal oxide nanoparticle solution. The membranes are attached with double-sided tape to glass coverslips.

where e is the evaporation rate. This equation is less simple to solve than eq. 2.6, but the final film thickness goes as $h \propto \omega^{-2/3}$.[175] Spin-coating is highly tunable to the nanoparticle system of interest via altering the solution concentration, drop volume, rotational velocity, and spin duration.[172] Another advantage that spin-coating has over drop-casting is faster processing due to less time waiting for solvents to dry.[178] Spin-coating can also be applied to sol-gel nanoparticle solutions, which are significantly thicker than a colloid and are a common precursor solution for metal oxide nanoparticles.[179] The spin coater holds the substrate in place by pulling a light vacuum on the substrate. To use it with the ultra-thin Si_3N_4 membranes, the membranes are first attached to a glass coverslip with double-sided tape, and the vacuum is pulled on the coverslip (Figure 2.16b). In the next section, we outline procedures for improving the thickness and uniformity of nanoparticle drop-cast and spin-coated films.

2.2.2 Troubleshooting

Solvent

The solution environment that the nanoparticle colloid is suspended in plays a major role in the quality of the thin film produced. The solvent must at once have the correct polarity to suspend the nanoparticles, with or without ligands, and to wet the membrane surface. Considering the silicon nitride membranes used most often here, the bare surface has a mix of hydroxide, silicon hydride, and dangling bonds and is slightly hydrophobic.[180] Water droplets readily bead up, and organic solvents like ethanol and isopropanol wet the surface completely. While an organic solvent seems like the perfect choice to drop-cast on the Si_3N_4 membrane, many types of nanoparticles cannot be suspended in organic solvents. Ligand-covered nanoparticles, like goethite nanorods covered in oleylamine (17 carbons) or silicon nanoparticles with hexadecylamine ligands (16 carbons), suspend very well in organic solvents like ethanol. Oxides produced dry via mechanical fragmentation such as IrO_2 and RuO_2, or by solid state synthesis and drying in a furnace such as $NiCo_2O_4$, do not have ligands and are more easily suspended in a polar solvent like water. Sometimes it makes sense to suspend the nanoparticle in water, or in a mixture of water and an organic solvent, and change the polarity of the Si_3N_4 surface, as will be discussed below.

Other times, it is more useful to add ligands (called functionalization) or change the ligands bound to the nanoparticle. For example, polymer coated silicon nanoparticles have been shown to aggregate less than uncoated particles and produce a more homogeneous spin-cast film.[181] Exchanging ligands is simple and usually involves heating the solution while adding an excess of the desired ligand. Most ligands are mainly carbon, which absorbs broadly across the XUV region, so too much excess ligand on the film will obscure the measured signal. Ligands play many roles in keeping the nanoparticle suspended, are sensitive to the temperature of the solution,[182] and can become destabilized at the wrong concentration.[183] Fortunately, many studies have been performed to optimize the ligands for stability of a given nanoparticle and solvent system,[184, 185] so XUV researchers have many resources to turn to.

The solution environment also contains molecules called surfactants, which possess a hydrophilic head and a hydrophobic tail similar to soap.[186] Surfactants play a major role in the stability of nanoparticles in solution and the packing and uniformity of films drop-cast from solution.[187] Unfortunately, many surfactant molecules contain elements like bromine or sodium, which absorb strongly in the XUV region.

Ultrasonication

Frequently, the nanoparticles suspended in solution prefer to bind to other nanoparticles and form clumps, or do not have a strong affinity for either nanoparticles or solvent and settle out of solution. Ultrasonication, or the application of sound waves into the liquid, can break up clumps or encourage nanoparticles to disperse in the solution.[188, 189] For the nanoparticle solutions drop-cast and spin-coated in this dissertation, 15 minutes of sonication was performed before each drop. Sonication is also necessary to create solution dispersions of dry nanoparticle powder.[190] Typically, ultrasonication is performed with a sonicator device that is a small bench-top bath of water (Figure 2.17a). Vials of nanoparticle solution are placed in the bath, and motors in the sonicator apply sound waves to the bath water, agitating the nanoparticle solution and suspending the particles.[191, 192] Significant energy is added to the bath water, causing it to heat up and in turn heat the nanoparticle solution. Too much sonication or heat can cause ligands to fall off the nanoparticles or cause the nanoparticles to precipitate out of solution faster.[193] In the experiments presented here, the bath water is replaced with room temperature water approximately every half hour.

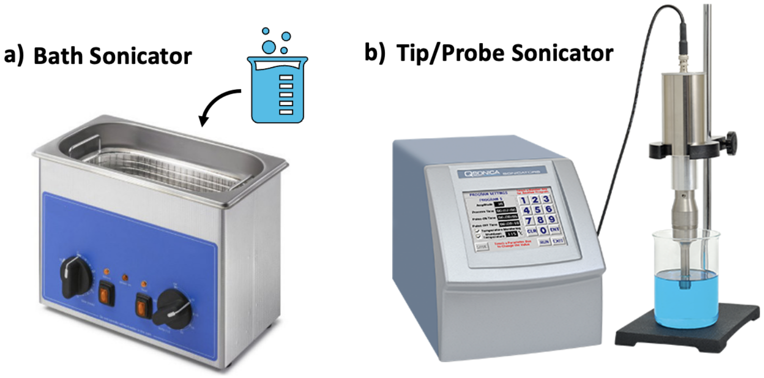

Figure 2.17: **Comparing bath sonicators and tip sonicators.** a) The bath sonicator contains a reservoir of water, which is agitated by intense sound waves. Vials of solution are placed in the reservoir. Adapted from reference [194]. b) The tip sonicator agitator is pen-shaped, and is inserted directly into the solution. Adapted from reference [195].

Sometimes, the frequency and intensity provided by the sonicator bath is not sufficient to break up clumps. Other methods can be used to break up agglomerated particles in solution, such as agitators, ball mills, roller mills, and other mechanical processes.[178] There are also commercially available ‘tip’ or ‘probe’ sonicators, which are small pen-shaped devices that are inserted directly into the nanoparticle solution (Figure 2.17b).[196] The vibration intensity applied by the tip sonicator can be much higher than a bath sonicator, but tip sonication is more likely to cause contamination, cannot be performed on multiple samples at once, and requires a large enough solution to fit the probe. Further, the increased energy applied by the tip sonicator heats the solution much more rapidly, so tip sonication is generally performed on solution vials in an ice bath. A comparison of the bath and tip sonicators is included in Figure 2.17.

Substrate Surface Treatment

As mentioned above, the silicon nitride membranes used as nanoparticle film substrates have a fairly hydrophobic surface. When it is not possible to disperse the nanoparticles in a hydrophobic solvent, the Si_3N_4 surface can be modified to be more polar and interact more favorably with polar solvents like water. One method is ozone treatment, which uses UV light (185 nm) to decompose oxygen molecules into highly reactive ozone molecules.[197] The ozone cleans the surface and reacts with any dangling bonds or hydride bonds, replacing them with a hydroxide capping layer (Figure 2.18). Ozone treatment has been shown to increase the polarity of the Si_3N_4 surface and improve its ability to attach to molecules, nanoparticles and films through van der Waals interactions.[198, 199] When a UV/Ozone furnace was applied to the $\sim$30 nm Si_3N_4 membranes used here, their water affinity was increased enough for a 20 μL drop to fully wet the entire 5.0 x 5.0 mm window surface. The

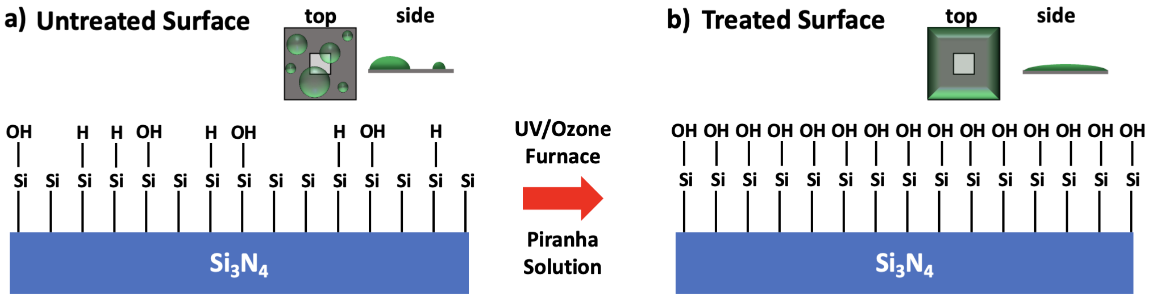

Figure 2.18: **Surface modification to create hydrophilic silicon nitride membranes.** a) The untreated Si_3N_4 surface has hydroxide bonds, hydride bonds and dangling bonds. The inset shows a top and side view of how water and other polar solvents bead up on the membrane surface. b) The surface of the Si_3N_4 membrane after treatment with the UV/Ozone furnace or piranha solution. All the surface bonds are terminated in a hydroxide. The inset shows the side and top view of the solution completely wetting the treated membrane.

ozone treatment is slightly damaging to the membranes and causes them to warp, and about half of them break during treatment.

A different approach to creating highly reactive oxygen species to functionalize the Si_3N_4 surface is through a solution called piranha. Piranha solution is 3 parts concentrated sulfuric acid (H_2SO_4) and 1 part hydrogen peroxide (H_2O_2, 30%).[200] The peroxide is added dropwise to the sulfuric acid, which reacts so exothermically that the solution boils violently. Piranha is a very powerful oxidizer, and produces a similar hydroxide capping layer on silicon nitride as the ozone treatment.[201] Piranha solution does not warp the ~30 nm membranes like the ozone does, but about half of them break when being dipped in the piranha or dried. Since the results are similar and the piranha is more dangerous to handle, the choice between using piranha or ozone depends on the availability of the UV/Ozone furnace.

Heat Treatment

Temperature has a major impact on reaction kinetics, and therefore changing the temperature of the solution or substrate can alter the deposition of nanoparticles. Heating the solution can increase its surface reaction rate and improve wetting.[202, 203] Increasing the temperature of the sample substrate can affect how well the nanoparticles stick to the surface and aggregate, and how quickly the solvent evaporates.[204] Both of these approaches have been applied when depositing nanoparticle films for this dissertation with little or no impact on film quality. The Si_3N_4 membranes were heated on a hot plate and were robust up to ~300 °C.

Thermal treatment of already drop-cast nanoparticle films has been shown to rearrange the packing of the particles. For example gold nanoparticles rearrange from a quasi-hexagonal geometry to a quasi-cubic geometry.[205] Thermal annealing of nanoparticle films on Si_3N_4

membranes has been attempted with a tube furnace under a dry nitrogen flow up to 300 °C and up to 12 hours with a 3 °C/minute heating and cooling rate. The membranes survived the furnace, but little or no change was observed in the film quality.

This chapter introduced the ultrafast laser and high vacuum experimental setup used to perform extreme ultraviolet transient absorption spectroscopy in this dissertation. The requirements and preparation methods for the nanoparticle films studied here have been described. In the next chapter, an XUV transient absorption spectroscopy study comparing small polaron formation in nanorods of goethite (α-FeO(OH)) and in a thin film of hematite (α-Fe_2O_3) is presented. The effect of the differences in sample morphology and the microscopic bonding environment experienced by the iron atoms is explored.

Chapter 3

Photoexcited Small Polaron Formation in Goethite (α-FeOOH) Nanorods Probed by Transient Extreme Ultraviolet Spectroscopy

The content and figures in this chapter are reprinted or adapted with permission from I.J. Porter, S.K. Cushing, L.M. Carneiro, A. Lee, J.C. Ondry, J.C. Dahl, H.-T. Chang, A.P. Alivisatos, S.R. Leone, "Photoexcited small polaron formation in goethite (α-FeOOH) nanorods probed by transient extreme ultraviolet spectroscopy." The Journal of Physical Chemistry Letters, 2018, 9, 4120-4124. Copyright 2018 American Chemical Society.

Small polaron formation limits the mobility and lifetimes of photoexcited carriers in metal oxides. As the ligand field strength increases, the carrier mobility decreases, but the effect on the photoexcited small polaron formation is still unknown. Extreme ultraviolet transient absorption spectroscopy is employed to measure small polaron formation rates and probabilities in goethite (α-FeOOH) crystalline nanorods at pump photon energies from 2.2 to 3.1 eV. The measured polaron formation time increases with excitation photon energy from 70 ± 10 fs at 2.2 eV to 350 ± 30 fs at 2.6 eV, whereas the polaron formation probability (85 ± 10%) remains nearly constant. By comparison to hematite (α-Fe_2O_3), an oxide analogue, the role of ligand composition and metal center density in small polaron formation time is discussed. The results presented in this chapter suggest that incorporating small changes in ligands and crystal structure could enable the control of photoexcited small polaron formation in metal oxides.

3.1 Introduction

The formation of small polarons in transition metal oxides limits carrier diffusion.[11, 37, 206–209] A small polaron is formed when the electric field of an excess carrier interacts with an optical phonon in a polar lattice, distorting the lattice and trapping the carrier in a local potential well.[36, 210, 211] For example, in the iron oxides and oxide hydroxides, small polarons form when electrons self-trap onto an iron center, forcing conduction to occur via phonon-mediated hops between centers.[207–209] In the photoexcited state, it has recently been shown that small polarons form on a sub-100 fs time scale in hematite

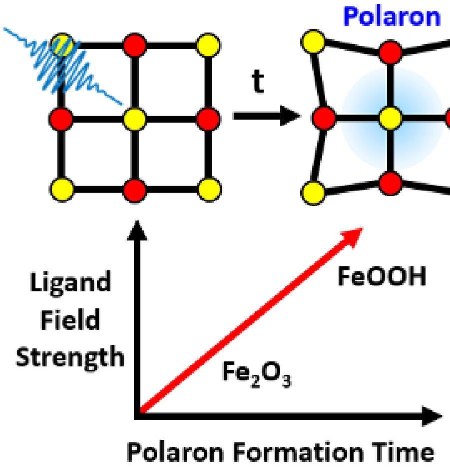

Figure 3.1: A cartoon of the process of photoexcited small polaron formation in a 2D lattice, and a visualization of the relationship between ligand field strength and small polaron formation time in iron oxides.

(α-Fe_2O_3).[81] Additionally, small polarons are found to form at the hematite surface in approximately 660 fs.[83] Small polaron formation therefore may control the trapping and lifetime of photoexcited carriers as well as the mobility.

The existence of small polarons is intrinsic to a material since it is governed by the polarity of the lattice.[210] The small polaron formation energy and hopping activation energy, however, are sensitive to the ligand field strength and hopping center density. For example, a linear relationship has been found between the polaron hopping activation barrier and the ionic polarizability at interfaces.[212] In other words, even if small polarons cannot be eliminated in a material, the small-polaron-limited mobility may be controlled through the electronic and structural properties of the material. For example, while goethite (α-FeOOH) and hematite both have an octahedral coordination geometry of oxygen ligands about an Fe^{3+} center, the replacement of some O^{2-} ligands with OH^- ligands in goethite increases the electron density about the Fe—O bonds, creating stiffer, less distortable bonds with higher vibrational frequencies.[213–218] In goethite, the iron atoms fill 1/2 of the interstitial spaces in the hexagonal close-packed array of oxygens, while in hematite the irons fill 2/3 of the interstitial spaces.[219–222] This change in iron center density corresponds to an increase in the Fe—Fe distance by greater than 5% in goethite with respect to hematite.[209, 218] These changes in structure and bonding have been shown to increase the polaron hopping activation energies in goethite, decreasing the ground-state carrier mobility compared to hematite.[207–209, 223] It has yet to be experimentally confirmed whether the same changes to structure and bonding also modulate the excited state small polaron localization and thus the lifetime of photoexcited carriers.

In the study presented in this chapter, we measure the polaron formation kinetics of goethite (α-FeOOH) crystalline nanorods using extreme ultraviolet (XUV) transient absorption spectroscopy at the Fe $M_{2,3}$ edge. This pump-probe technique is sensitive to changes in the Fe oxidation state, allowing for the observation of small polaron formation via a signature spectral shift. The small polaron formation time increases with excitation energy from 70 ± 10 fs at 2.2 eV to 350 ± 30 fs at 2.6 eV. Excited electrons are measured to have an 85 ± 10% probability of forming small polarons, and the signal associated with the polaron persists for over 300 ps. Comparison of these trends with hematite, in particular the polaron formation time (180 ± 30 fs average time in goethite nanorods and 90 ± 5 fs in hematite thin films), suggests that polaron formation may be tuned by altering the ligand composition and density of the iron centers, although the role of sample morphology still needs to be investigated.

3.2 Experimental Results

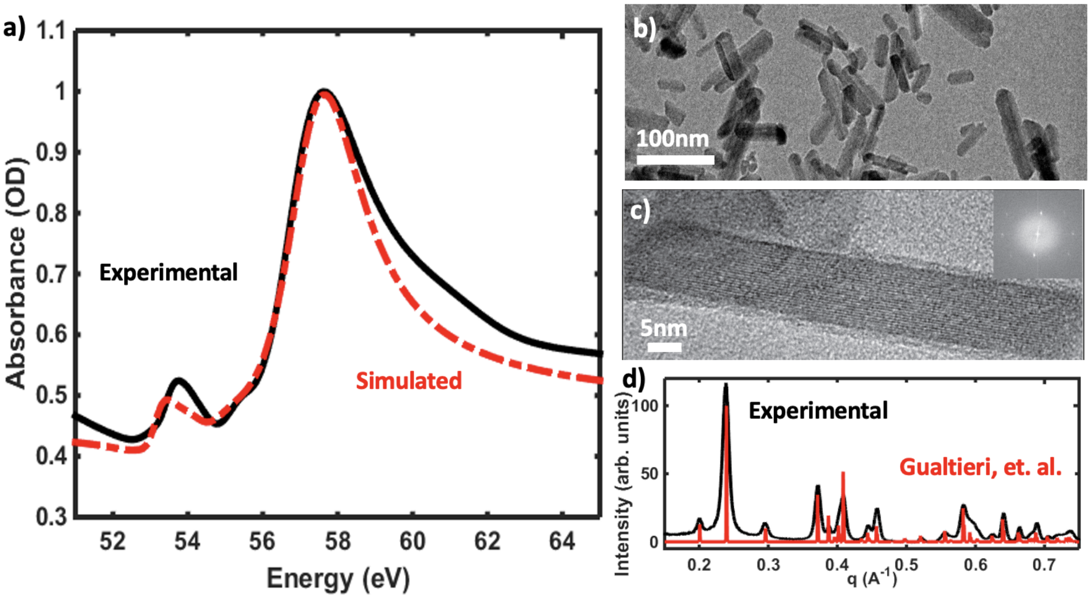

Figure 3.2: a) The ground-state XUV absorption spectrum of goethite nanorods (black) and the spectrum simulated using the CTM4XAS software (red). Input parameters for the charge transfer multiplet calculation are summarized in the text. b) A TEM image of the goethite nanorod distribution, confirming the size and the rod-like shape of the particles. c) An HRTEM image of a single nanorod reveals that the entire rod is a single crystal. d) Powder XRD of the sample (black) compared to the stick spectrum of goethite from Gualtieri et al.[219] (red), which confirms that the sample is in the goethite phase.

XUV transient absorption spectroscopy utilizes a visible or near-IR pump and a broadband XUV probe to measure semicore-to-valence transitions, which are sensitive to the oxidation state and bonding environment of first row transition metals. The apparatus, described previously,[72] utilizes the process of high harmonic generation to produce the XUV probe pulses, and it can measure thin solid state samples, such as thin films and nanoparticles, which are suspended on silicon nitride windows.

The ground-state XUV absorption spectrum of the Fe $M_{2,3}$ edge for the goethite nanorods is shown in Figure 3.2a. The observed spectral features, shown in black, are caused by the multiplet splitting between the ground-state ($3p^6 3d^5$) and the core hole excited state ($3p^5 3d^6$) and by the ligand field. The simulated spectrum, shown in dotted red, is predicted using a charge transfer multiplet calculation with a value for the crystal field splitting 10Dq of 1.55 eV.[57, 72, 81] Details of this calculation, including all other parameters, are given in the Appendix. The 1.55 eV value is obtained by performing a global fit on the experimental data with the 10Dq value as the fit parameter, resulting in a fit error of 0.01 eV. This crystal field splitting value differs from the visible light fitted value of 1.95 eV,[213, 224] with the discrepancy attributed to the core hole altered crystal field strength of the final state in the X-ray transition.[214, 225] Transmission electron microscopy (Figure 3.2b,c) confirms the size distribution and single-crystalline nature of the rods. Powder X-ray diffraction (Figure 3.2d) is compared to the stick spectra of several common polymorphs of iron oxide and iron oxide hydroxide (goethite in red, hematite and magnetite not shown) to verify the sample identity.

The differential absorption after photoexcitation of the goethite nanorods with 3.1 eV light is shown in Figure 3.3a. The change in the valence charge density upon photoexcitation alters the multiplet splitting between the 3p core levels and valence levels, modifying the X-ray absorption compared to the ground-state. First, when an interband transition is photoexcited in an iron oxide, an electron is transferred from majority O 2p hybridized orbitals to majority Fe 3d hybridized orbitals within 30 fs.[72, 81] This charge-transfer hybridized state appears in the differential absorption spectrum as an increase in absorption (blue) between 53 and 56 eV and a decrease in absorption (red) between 56 and 59 eV, crossing the zero at 56 eV as shown in Figure 3.3b as a solid blue line. The charge-transfer hybridized state is modeled by setting the final state of the absorption to be Fe^{2+} in the charge transfer multiplet simulation (dotted blue line Figure 3.3b).

Next, the photoexcited carriers thermalize via optical phonon emission. During the electron-phonon scattering process, the optical phonon and electron can couple to form a small polaron. The small polaron can cause an anisotropic lattice expansion, resulting in a splitting of the Fe 3p level.[211] This appears in the differential absorption as a broad increase in absorption between 54 and 58 eV, shown in Figure 3.3b as a solid red line. The polaron differential absorption is modeled as a splitting of the ground-state absorption following Carneiro et al.,[81] which is shown as a dotted red line. Briefly, this is accomplished by convolving the ground-state spectrum with three delta functions, and further details can be found in the Appendix. The evolution from the charge-transfer hybridized state to the polaron state is noticeable by the zero-crossing shift from 56 eV to 57.5—59 eV illustrated with the arrow in Figure 3.3b.

To further understand the small polaron formation dynamics in goethite, transient dif-

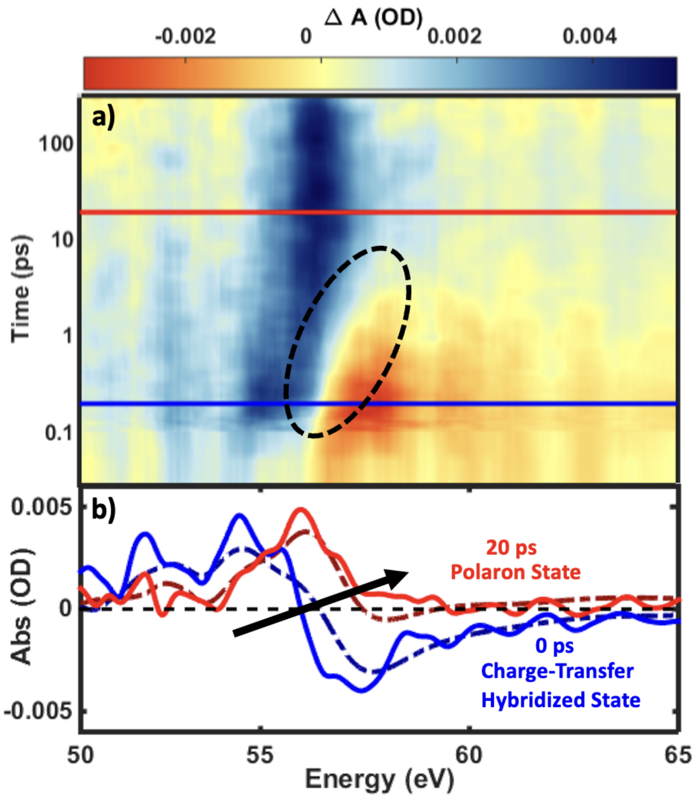

Figure 3.3: a) The transient differential absorption of goethite for the first 300 ps after optical excitation, with a logarithmic time axis. The time axis is offset by 100 fs to improve the clarity of the plot. The solid lines (red and blue) indicate the times for the lineouts shown in panel b. (b) The differential absorption at the times indicated in panel a (solid lines) are plotted with the predicted differential absorption spectra for those states (dotted lines). The differential absorption immediately following optical excitation (delay of 0 ps, shown at 0.1 ps in panel a due to the 100 fs offset) matches the prediction for a charge-transfer hybridized state (blue), and the differential absorption at 20 ps matches the prediction for a polaron (red). Solid lines are obtained by averaging the nearest 6 time delays. Details of how the predicted (dotted) spectra are generated is included in the Appendix. The arrow indicates the shift of the zero-crossing from approximately 56 eV to 57.5—59 eV, which is the most noticeable spectral feature of the polaron formation.

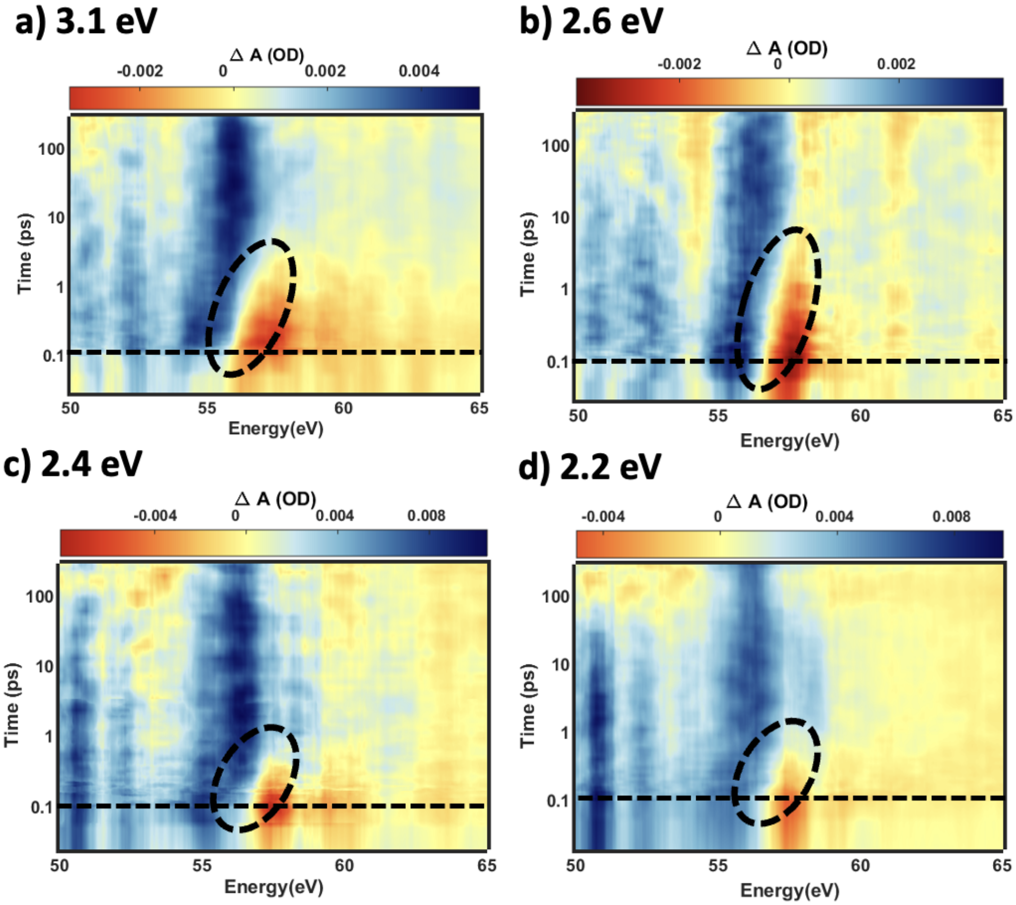

Figure 3.4: Transient absorption spectra of the nanorods pumped at different photon energies. All four spectra show the zero-crossing shift from approximately 56 eV to 57—59 eV within the first 2 ps, indicated by the thick dotted black oval. The thin horizontal dotted black line indicates time zero, which is offset my 100 fs to improve the clarity of the plot.

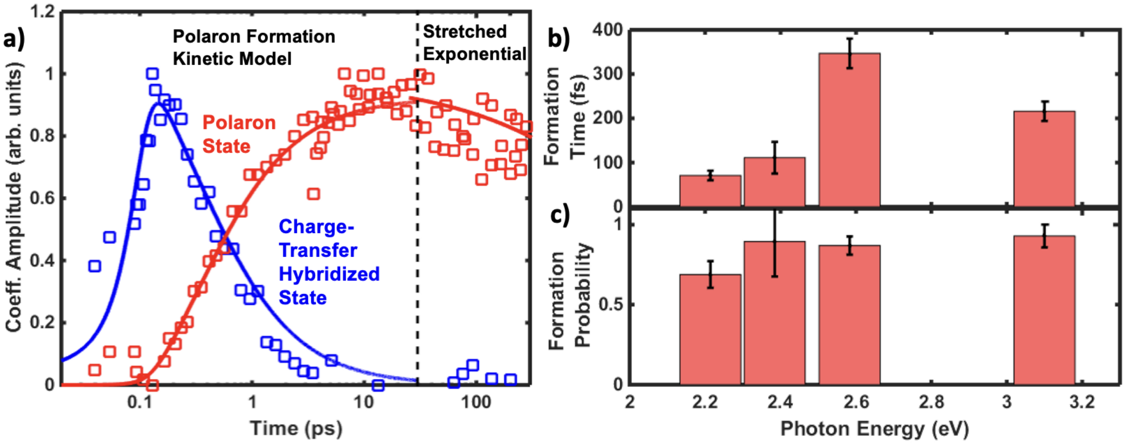

Figure 3.5: a) The result of multivariate regression on the transient absorption spectra of Figure 3.3a, with amplitudes of the charge-transfer hybridized state and polaron state shown as squares, and model fits shown as solid lines. The dotted black line indicates the split between data that are fit using the polaron formation kinetic model and the stretched exponential polaron decay model. Results here are shown with a logarithmic time axis. The results of the polaron formation kinetic model fits at various pump wavelengths are shown in panel b for polaron formation time and in panel c for polaron formation probability. Error bars shown indicate the standard error.

ferential absorption spectra were measured at four visible pump wavelengths spanning 2.2 to 3.1 eV. All four spectra are included in Figure 3.4. A multivariate regression was performed to decompose the differential absorption spectra into the charge-transfer hybridized state (blue), taken at t = 0 ps, and the polaron state (red), taken at t = 20 ps. The polaron state was chosen to be 20 ps in order to minimize the error of the regression, even though the polaron population does not increase after approximately 5 ps. The results of the multivariate regression are shown in Figure 3.5a for an excitation energy of 3.1 eV, and in Figures 3.6 and 3.7 for the other excitation wavelengths.

The resulting amplitudes are then fit with a kinetic model representing polaron formation[81] before 20 ps and a stretched exponential representing polaron hopping[226] after 20 ps, as indicated in Figure 3.5a. The kinetic model for polaron formation is based on a two-temperature rate equation for the hot electron and hot phonon populations, in which an electron and phonon can combine via bimolecular kinetics to create a small polaron. Briefly, the model fits two rate constants, the electron-phonon scattering and the small polaron formation, and two amplitudes, the average hot electron population and average polaron population. The polaron formation probability shown is the ratio of these population amplitudes. Further details of this model can be found in the Appendix.

The polaron formation time and probability resulting from this fit are shown in Figure 3.5b and c, respectively. The polaron formation time has an average value of 180 ± 30 fs across an energy range of 2.2 to 2.6 eV and shows a significant increasing trend with pump

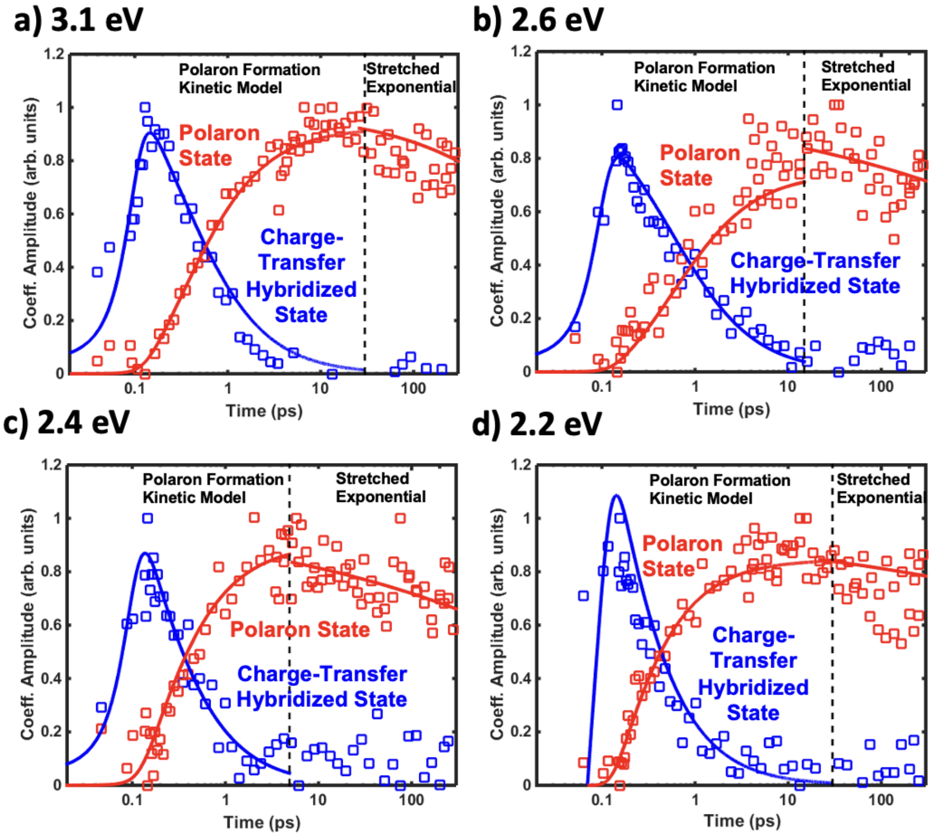

Figure 3.6: Amplitudes of the multivariate regression are shown at different pump wavelengths for the charge-transfer hybridized state (blue squares) and polaron state (red squares) with time on a logarithmic scale. For short times before the black dotted line, the fit using the polaron kinetic model is shown as solid lines. At long times, the fit using the stretched exponential decay model is shown. This long-time fit is inaccurate and does not match up with the short-time fit, as can be seen clearly in the 2.6 eV plot. The fitted polaron formation times are 215 ± 20 fs for 3.1 eV excitation, 350 ± 30 fs for 2.6 eV excitation, 110 ± 35 fs for 2.4 eV excitation, and 70 ± 10 fs for 2.2 eV excitation.

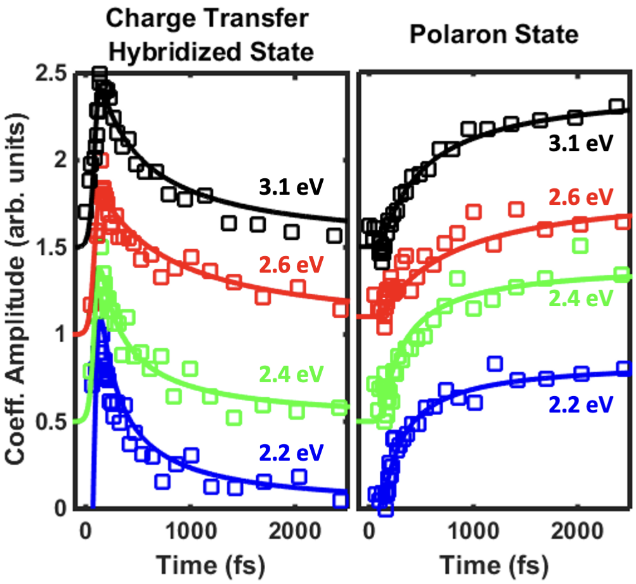

Figure 3.7: Amplitudes of the multivariate regression (squares) with the fit using the polaron kinetic model (solid lines) compared between the different pump photon energies. The amplitudes of the charge-transfer hybridized state are on the left, and the amplitudes of the polaron state are on the right. Results are shown with a linear time axis. A constant vertical offset is applied to the different pump wavelengths for clarity.

photon energy up to 2.6 eV, then decreases at 3.1 eV. The polaron formation probability is 85 ± 10% on average across all pump photon energies. Within the experimental variance the probability exhibits a slightly increasing trend with increasing excitation energy. For all excitation wavelengths, the polaron state lives longer than the 300 ps time delay of the measurement, with an unphysical average fitted lifetime of 800 ns ± 5 μs (Figure 3.8). This value is unrealistic for the time scale of the measurement and the standard error of the fit is nonphysical, indicating that the stretched exponential fit cannot be trusted to analyze the polaron decay lifetime beyond the condition that the polaron lives longer than 300 ps.

3.3 Discussion: Comparison to Hematite

The small polaron kinetics measured here can be compared to previous measurements of nanocrystalline hematite thin films and to surface-sensitive measurements of polycrystalline and crystalline hematite. While the goethite nanorods exhibit a measured average polaron formation time of 180 ± 30 fs across an energy range of 2.2 to 2.6 eV, Carneiro et al.[81] report an average polaron formation time of 90 ± 5 fs for the hematite thin films, which is calculated for the same energy range and using the same kinetic model. This difference in polaron formation time can be first considered in terms of the chemical structure of the

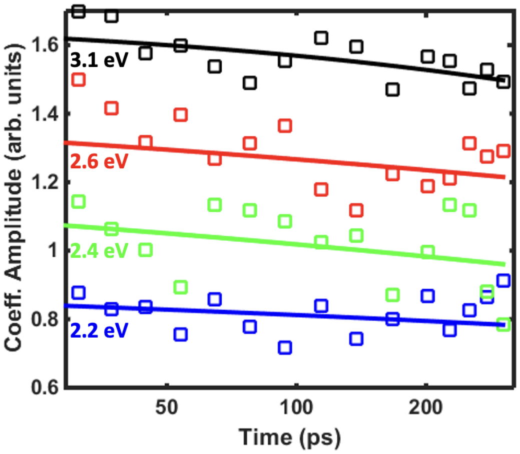

Figure 3.8: The decay of the polaron state, fit using the stretched exponential model. The multivariate regression amplitudes of the polaron state are shown as squares. The best fit using a stretched exponential is shown as solid lines. Results are shown with a logarithmic time axis. A constant vertical offset is applied to the different pump wavelengths for clarity.

two materials. According to a basic kinetic theory for polaron formation, the formation rate should depend on both the attempt frequency and the energy barrier to formation,[36] $\Gamma = \omega e^{-E_{act}/RT}$. Here, Γ is the polaron formation rate, ω is the attempt frequency, E_{act} is the activation barrier, T is the lattice temperature, and R is the Boltzmann factor. For polaron formation, since an electron and an optical phonon must interact, the attempt frequency can be estimated by the LO phonon frequency ω_{LO}. The LO phonon mode with the highest energy will have the fastest scattering rate, so the highest energy E_u mode is chosen for hematite and the highest energy Fe—O B_{3u} mode is chosen for goethite, which have periods of 50 and 53 fs, respectively.[215–217] The energy barrier for excited state polaron formation can be estimated from the activation energy for electron hopping between the Fe centers ΔE_{hop}, which is 190 meV for hematite and 235 meV for goethite.[207–209] The excited state formation kinetics can be approximated at a lattice temperature of 600 K as previously done for hematite at a similar excitation power density as used here.[36, 81]

The ratio of formation times can be estimated by

$$\frac{\Gamma_g}{\Gamma_h} = \frac{\omega_{LO}^g}{\omega_{LO}^h} e^{-(\Delta E_{hop}^g - \Delta E_{hop}^h)/RT} \tag{3.1}$$

yielding a value of 42%± 9%. This predicted ratio matches the average experimental ratio of 50%± 9% for the polaron formation time measured here for goethite versus that from Carneiro et al.[81] for hematite. Although a simplified estimate, eq 3.1 suggests that the change in polaron formation time between hematite and goethite can be accounted for by the difference in electron hopping activation energy between the Fe centers. Since the hopping activation energy is related to the ground-state mobility via Marcus Theory,[36] this means that the trends in ground-state mobility and polaron formation time may be influenced by similar changes to the ligand field and metal center density.

The above comparison of average formation times neglects the excitation energy dependence of the activation barrier.[36] The average formation time ratio of approximately 50% differs significantly from the ratio of approximately 140% observed at 2.2 eV excitation, of approximately 80% observed at 2.4 eV excitation, of approximately 25% observed at 2.6 eV excitation, and of approximately 45% observed at 3.1 eV excitation. However, the fit amplitudes that relate the initial electron population to the final polaron formation (Figure 3.5c) are relatively constant over the same excitation energy range. This indicates that multiphonon effects, which would change the ratio between photoexcited electrons and formed polarons, are not prevalent.

Additionally, Husek et al.[83] report a much longer polaron formation time in hematite surfaces (640 ± 20 fs for polycrystalline, 680 ± 30 fs for single crystal) obtained for bulk samples with an XUV probe at near grazing angle. Although the fitting routine and kinetic model differs from the model described above and used by Carneiro et al., a fit of the goethite nanorod data at the same excitation energy and with the model from Husek et al. reveals a similar polaron formation time as described above (160 ± 25 fs at 3.1 eV excitation). This indicates that the much longer polaron formation times measured at the surface could be due to the differences between localization to a 2D surface and localization to a 3D bulk site, precluding a direct comparison of the results.

The trend in polaron formation times with increasing excitation energy is measured to be reversed between hematite (decreasing) and goethite (increasing). This difference could result from the changes in the ligands and the distances between the iron centers, or it may result from the sample morphology. Specifically, the hematite transient spectra from Carneiro et al.[81] were measured for nanocrystalline films, whereas the goethite samples measured here are monocrystalline nanorods. As the excitation energy is increased, the phonon bath must dissipate more heat. For the thin film, excess heat can be dissipated throughout the film and away from the localized excitation spot. This is not the case for the nanorods, as the excess heat cannot be dissipated spatially. The localized nonthermal phonon bath in the nanorods can lead to an increase in polaron hopping and polaron detrapping, similar to an increase in the sample temperature, possibly explaining the increased formation times at higher excitation energies. However, increased crystallinity could also explain the increased polaron lifetime in the goethite nanorods, as fewer trap-states may be present at which excited carriers can become localized.[83, 227, 228] A comparison of hematite nanorods to the goethite nanorods is therefore necessary before the change in polaron formation kinetics can be completely attributed to coordination or morphology effects.

The photoexcited polaron formation kinetics of goethite nanorods has been explored with XUV transient absorption spectroscopy. By applying a simple kinetic model, the small polaron formation time is found to increase from 70 ± 10 fs at 2.2 eV to 350 ± 30 fs at 2.6 eV. In comparison to a hematite thin film, the increased formation time can be explained by considering the differences in ligand field strength and Fe hopping center density that lead to altered electron hopping activation energies. Excitation energy-dependent analysis reveals a trend in polaron formation times that differs from that of hematite, but this trend may be due to a variety of differences between the samples. Further investigations, in particular a study of hematite nanoparticles, are required to separate the effects of crystallinity and morphology from the bonding and structural changes.

3.4 Appendix

3.4.1 Experimental Methods

Extreme Ultra-Violet (XUV) Transient Absorption Spectra

Pulses that are 40 fs, 3.5 mJ centered at 800 nm are produced by a 1 kHz Ti:sapphire chirped pulse amplifier (Spitfire Pro, Spectra Physics). The XUV probe pulse is generated via high harmonic generation in a semi-infinite gas cell (40 cm) filled with 110 Torr (approximately 1.4×10^4 Pascal) neon gas. Before the gas cell, a portion of the 800 nm light is converted to 400 nm using in-line second harmonic generation, allowing for the production of both odd- and even-order harmonics.[229] A 0.5 mm thick glass capillary array (pore size 5 μm) blocks the 800 nm and 400 nm fundamental before the sample while transmitting the XUV.[144] The XUV spot size is 200 μm at the sample. After the sample, the XUV pulses are spectrally dispersed using a variable line spacing grating, which has an energy range of 35 eV—110 eV. The dispersed spectrum at each time delay is captured by a charge-coupled device (CCD) camera (PIXIS-400, Princeton Instruments).

The pump pulses are generated by passing a portion of the 800 nm beam through an optical parametric amplifier (TOPAS-Prime, Light Conversion) to create visible pulses with tunable wavelength (2.2—3.1 eV, 560—400 nm). The pump spot size is approximately 400 μm at the sample with a power density of approximately 2 mJ. Each transient spectrum consists of 200 scans that are averaged together, each consisting of 61 time delays spaced logarithmically after time zero (-2500 fs to +300 ps about time zero, delay steps ranging from 14 fs to 25 ps). Each time delay comprises a pump-on and a pump-off camera image of XUV light versus photon energy produced from the coaddition of approximately 800 pulses. To avoid thermal damage and ablation, the samples are raster scanned in 100 μm steps between each pump-probe time delay. Additionally, a stream of dry nitrogen is flowed over the sample to dissipate heat.

Sample Fabrication

Goethite, or iron (III) oxide hydroxide (FeOOH), nanorods of dimensions ranging from 5 nm x 20 nm to 30 nm x 150 nm were purchased from U.S. Research Nanomaterials, Inc. and spun-cast onto 30 nm thick 3 mm x 3 mm Si_3N_4 substrates (3 mg of FeOOH in 30

μL Millipore water, spun for 60 s, 2000 rpm). This affords an uneven-density film, and measurements are taken on a portion exhibiting the same XUV absorbance as a 35 nm thin film (from comparison to CXRO transmission).[129]

Sample Characterization

a) TEM Imaging TEM and HRTEM imaging is performed with a FEI Tecnai T20 S-TWIN TEM operating at 200 kV with a LaB_6 filament, which affords a resolving power of 2.4 Å. TEM images are collected with a Gatan Orius SC200 TEM camera with a 1 second exposure time to capture the rod-like shapes (Figure 3.2b). High resolution images are taken near the Scherzer focus without the use of an objective aperture in order to resolve the lattice fringes (Figure 3.2c).

b) Powder X-ray Diffraction Powder diffraction patterns of nanocrystalline samples (Figure 3.2d, main text) are obtained using a Bruker D-8 GADDS diffractometer equipped with a Co Kα source. XRD was collected in reflection geometry with an incident X-ray angle (ω) of 15°. Samples were prepared by drop casting a concentrated solution of nanocrystals in ethanol on an amorphous plastic low background substrate. 2D patterns were merged and integrated in the DIFFRAC.EVA software from Bruker.

3.4.2 Theory and Computation

Charge Transfer Multiplet Modeling of the Ground-State

The ground-state absorption spectrum is predicted using a charge transfer multiplet calculation performed with the CTM4XAS software.[57] The ground-state calculation was conducted for the Fe^{3+} oxidation state of iron. To include the effect of shorter Auger lifetimes at higher energies, the predicted spectra are broadened by a Lorentzian with a nominal width of 0.1 eV at 52 eV that linearly increases by 1 eV for every 1.5 eV and with a Fano asymmetry parameter of 3.5. Additionally, a Gaussian of width 0.5 eV is applied to account for the instrument response. An energetic shift of +1.7 eV to the absolute energy of the transitions is required.[72] A nonlinear fit was performed on the ground-state absorption spectrum to determine the value of 10Dq, using the simulated spectra discussed above as model data. The value of 10Dq was found to be 1.55 eV ± 0.01 eV. The simulated ground-state spectrum shown in Figure 3.2a uses a 10Dq value of 1.55 eV, with broadenings discussed above.

Charge Transfer Multiplet Modeling of the Excited State Differential Absorption

a) Charge-Transfer Hydridized State The XUV differential absorption for the optically excited state was predicted by subtracting the ground-state absorption spectrum from the excited state spectrum predicted by a charge transfer multiplet calculation. The optically induced charge transfer from the oxygen site to the iron center is accounted for by setting the final oxidation state to be Fe^{2+} and considering only the lowest energy $^5T_1$ transition.[72, 81] The calculation is otherwise performed as outlined above for the ground-state.

b) Polaron State The XUV differential absorption of the polaron state, which remains 20 ps after optical excitation, was predicted by subtracting the ground-state absorption spectrum from the modeled polaron state spectrum. The polaron state is modeled as a splitting of the 3p core level into three states, using the splitting values and weightings for the Fe^{3+} center theoretically predicted for $FePO_4$[211] and experimentally found accurate for hematite.[81] Specifically, the measured ground-state absorption spectrum is convolved with three delta functions spaced at 0 eV, 1 eV, and 2.5 eV and with weightings of 1/3, 1/2, and 1/6, respectively. No additional shifting or broadening was applied.

Polaron Formation Kinetic Model

The kinetic model for the polaron formation includes a two-temperature model for the electron-phonon equilibrium and a bimolecular kinetic term for the recombination of the electron and phonon to form the polaron. In a standard two-temperature model, first a nonthermal electron population is created by optical excitation. Subsequently, electron-phonon scattering thermalizes the hot electrons while creating a nonthermal phonon population. The energy transfer rate between these two populations depends on their relative temperature and the electron-phonon scattering time, τ_{e-ph}. Thus, the predicted excited state temperature gives a measure of the average state occupations.

Since there is no clear relationship between temperature of the hot electrons and the measured amplitude of the charge-transfer hybridized state, average population is used in this model in place of temperature. An amplitude accounting for the unknown ratio of population transfer between hot electrons and phonons is then left as an additional fit parameter. In equations 3.2 and 3.3 below, the average hot electron population is denoted as η_e and the average hot phonon population is η_{ph}. The fit amplitude is denoted as A_e.

$$\dot{\eta}_e = -\frac{A_e \cdot \eta_e - \eta_{ph}}{\tau_{e-ph}} \tag{3.2}$$

$$\dot{\eta}_{ph} = \frac{A_e \cdot \eta_e - \eta_{ph}}{\tau_{e-ph}} \tag{3.3}$$

The second part of the polaron formation kinetic model is the bimolecular recombination of an electron and optical phonon, which also uses average population. This bimolecular term involves both the electron and phonon populations and the polaron formation time, τ_{pol}. This creates a population of polarons, denoted as η_{pol} in equations 3.4, 3.5, and 3.6.

Table 3.1: Parameters of the polaron kinetic model fit at the four pump photon energies.

Excitation Photon Energy (eV)	Polaron Formation Time (fs)	Charge-Transfer Hybridized State Amplitude	Polaron State Amplitude
3.1	215 ± 20	2.0 ± 0.2	1.85 ± 0.01
2.6	350 ± 30	1.7 ± 0.1	1.49 ± 0.02
2.4	110 ± 35	2.0 ± 0.5	1.81 ± 0.09
2.2	70 ± 10	3.6 ± 0.4	2.45 ± 0.02

An additional polaron population transfer amplitude, A_{pol}, is included to account for the unknown number of phonon scattering processes that occur during polaron formation.

$$\dot{\eta}_e = -\frac{A_e \cdot \eta_e - \eta_{ph}}{\tau_{e-ph}} - \frac{A_{pol} \cdot \eta_e \cdot \eta_{ph}}{\tau_{pol}} \tag{3.4}$$

$$\dot{\eta}_{ph} = \frac{A_e \cdot \eta_e - \eta_{ph}}{\tau_{e-ph}} - \frac{A_{pol} \cdot \eta_e \cdot \eta_{ph}}{\tau_{pol}} \tag{3.5}$$

$$\dot{\eta}_{pol} = \frac{A_{pol} \cdot \eta_e \cdot \eta_{ph}}{\tau_{pol}} \tag{3.6}$$

Fitting the multivariate regression of the experimental data with this model yields the electron-phonon scattering time, the polaron formation time, and two amplitude coefficients. These amplitudes not only account for the unknown ratios between populations, they also link the predicted hot electron and polaron populations from this model to the experimental differential absorption intensities of the charge-transfer hybridized state and the polaron state, respectively. The polaron formation probability is taken as the ratio of these fit amplitudes. It is important to note that this model is only valid when the polaron formation is complete by the end of electron thermalization, as the electron population in the model is depleted after thermalization. This approximation is justified here because the measured polaron feature reaches a maximum in a few picoseconds, the same time scale as thermalization.

The electron-phonon scattering time is found to be less than 30 fs at all four excitation energies studied. Since this is within the instrument response, this variable was held constant at 30 fs for all four fits. Fixing this variable in the fit did not change the results of the other three variables within error. Results are shown in Table 3.1.

Chapter 4

Layer-Resolved Ultrafast Extreme Ultraviolet Measurement of Hole Transport in a Ni-TiO_2-Si Photoanode

The content and figures in this chapter are reprinted or adapted with permission from S.K. Cushing, I.J.Porter, B.R. de Roulet, A. Lee, B.M. Marsh, S. Szoke, M.E. Vaida, S.R. Leone, "Layer-resolved ultrafast extreme ultraviolet measurement of hole transport in a Ni-TiO_2-Si photoanode." Science Advances, 2020, 6, eaay6650. Copyright 2020 The Authors, some rights reserved; exclusive licensee American Association for the Advancement of Science. American Chemical Society.

Metal oxide semiconductor junctions are central to most electronic and optoelectronic devices, but ultrafast measurements of carrier transport have been limited to device-average measurements. Here, charge transport and recombination kinetics in each layer of a Ni-TiO_2-Si junction is measured using the element specificity of broadband extreme ultraviolet (XUV) ultrafast pulses. After silicon photoexcitation, holes are inferred to transport from Si to Ni ballistically in $\sim$100 fs, resulting in characteristic spectral shifts in the XUV edges. Meanwhile, the electrons remain on Si. After picoseconds, the transient hole population on Ni is observed to back-diffuse through the TiO_2, shifting the Ti spectrum to a higher oxidation state, followed by electron-hole recombination at the Si-TiO_2 interface and in the Si bulk. Electrical properties, such as the hole diffusion constant in TiO_2 and the initial hole mobility in Si, are fit from these transient spectra and match well with values reported previously.

4.1 Introduction

Metal oxide semiconductor (MOS) junctions are foundational to electronic devices. In solar energy research, oxide-passivated junctions have led to record photoconversion efficiencies for semiconductor solar cells and photoelectrodes.[230–232] In a solar cell, one role of the metal oxide–passivated junction is to control surface recombination velocities, slowing the recombination at the metal-semiconductor contacts.[233] In photoelectrochemical cells, the metal oxide layer also acts as a corrosion barrier.[16, 234–237] Even in solar photocatalytic reduction of CO_2, the MOS junction has proven critical by acting as a proton transport layer.[238, 239] Despite the critical applications of MOS junctions, the femtosecond-to-picosecond charge transfer processes that occur within a photoinitiated MOS junction are still debated. It is established that field-induced tunneling dominates thin <5 nm junctions. However, in photoelectrochemical junctions, thicker barriers often lead to better performance.[234] In addition, an amorphous or defect-rich oxide will often outperform a crystalline material. It has therefore been proposed that in p-type MOS junctions with TiO_2, the Ti^{3+} defect states support efficient hole or proton conduction.[16, 240, 241]

Ultrafast X-ray studies have recently brought element specificity to time-resolved dynamics.[242, 243] One approach to producing ultrafast X-ray probes is using high harmonic generation. In high harmonic generation, extreme ultraviolet (XUV) or soft X-ray pulses are produced by a noble gas using a tabletop laser.[244] The broadband X-ray pulses can have a bandwidth of 10 to 100 eV, allowing for multiple elements to be temporally correlated. However, interpreting the measured X-ray dynamics in terms of ground-state electronic properties is made difficult by the positive core hole that is produced by the core-level probe transition. Advances in theory have led to accurate interpretation of atomic and molecular dynamics, but the many-body state created by the core hole in a solid makes the theoretical interpretation of the spectral features challenging.[245, 246] Nevertheless, recent progress in approximate methods has led to extraction of the electron and hole dynamics in semiconductors. The fit dynamics accurately correspond to scattering pathways within the material's band structure.[20, 53, 75, 247]

Here, we use the element specificity of transient XUV spectroscopy to measure the charge transfer kinetics of a Ni-TiO_2-Si junction with band alignment as shown in Figure 4.1a. First, a near-infrared pump photoexcites the 200 nm-thick Si in the MOS junction. Then, a broadband XUV pulse created by high harmonic generation in Ar (30 to 60 eV) or He (60 to 110 eV) probes the photoexcited changes in the Ti $M_{2,3}$ edge at 33 eV, the Ni $M_{2,3}$ edge at 66 and 68 eV, and the Si $L_{2,3}$ edge at 100 eV from femtoseconds to 200 ps. The increased absorption feature normally ascribed to photoexcited holes in pure Si is not measured immediately in the junction. The electron spectral feature of Si is consistent with photoexcited Si alone. A subsequent negative shift in the Ni edge energy is measured within 100 fs, which is attributed to excess holes opening up transitions to states below the Fermi energy. No change is measured for the Ti edge on this short time scale. On a picosecond time scale, the Ni edge energy returns to its equilibrium value while a positive energy shift of the Ti edge is measured, attributed to an increase in the Ti oxidation state from back diffusion of excess holes. On a time scale of tens to hundreds of picoseconds, the Ti peak shift reaches its maximum, and then it begins to decay in sync with the decay of the electron signature in Si.

The initial hole transport from Si to Ni in the junction is fit and compared with the fitted hole transport time in a Ni-Si sample. The average hole transit time is delayed in the junction by 33 ± 8 fs, and the hole quantum yield is measured to be 42 ± 6%. Accounting for the TiO_2 thickness, the hole tunneling velocity in the TiO_2 is $5.8 \pm 1.4 \times 10^7$ cm/s. For the built-in electric field (1.5×10^5 V/cm) of the MOS junction, this implies a hole mobility of 390 ± 100 $cm^2/V{\cdot}s$ in Si, which matches measured Si hole mobilities. The value suggests

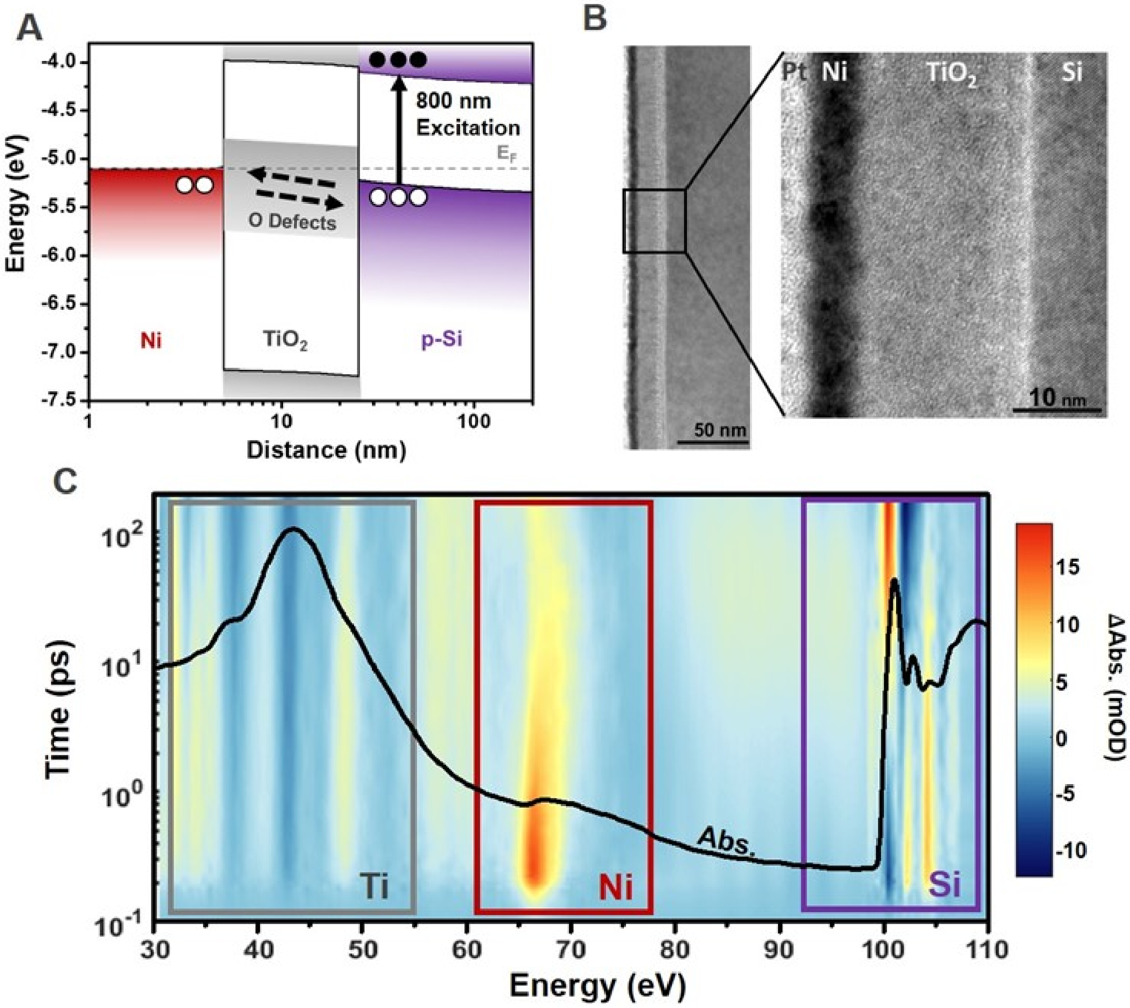

Figure 4.1: **Characterization and measurement of the Ni-TiO$_2$-Si junction.** a) The energy level alignment for the metal, oxide, and semiconductor is shown, along with the expected photoexcited hole transfer in the p-type MOS junction. The Si is p-type–doped by boron at 10^{15} per cm^3. The presence of oxygen defect levels (n-type) in the TiO$_2$ layer was previously confirmed by photoemission spectroscopy of a Si-TiO$_2$ junction.[248] The band bending is calculated using the drift-diffusion equation.[249] b) A TEM measurement of the thickness of the TiO$_2$ and Ni, which are 19 ± 0.6 nm and 5.6 ± 0.6 nm, respectively. The TiO$_2$ is amorphous, and an ∼1 nm SiO$_2$ interface is measured where the TiO$_2$ and Si contact. c) The black line overlay is the ground-state XUV absorption. The regions that correspond to the Ti $M_{2,3}$ edge, the Ni $M_{2,3}$ edge, and the Si $L_{2,3}$ edge are indicated by the colored boxes. The differential XUV absorption that results from photoexcitation is shown as the background color map, with the scale on the right of the graph. Each peak is observed to have a unique response to the photoinitiated charge transfer, which is discussed in the text.

ballistic transfer because it is unchanged by scattering in the TiO_2. After the tunneling process, the holes back-transfer through the TiO_2 with a fit diffusion constant of 1.2 ± 0.1 cm^2/s. The recombination of holes in the TiO_2 with nontransferred electrons in the Si, or injection of holes from TiO_2 to Si, is fit to a surface recombination/injection velocity of >200 cm/s.

4.2 Materials and Methods

Experimental Design

The objectives of this research were twofold. One goal was to simultaneously observe charge carrier dynamics separately in each layer of a layered thin-film junction. Second, the aim was to understand the ultrafast dynamics of charge carriers in a MOS junction following photoexcitation and to determine the time scales of charge transport. We hypothesized an initial fast tunneling of holes from the Si to Ni from simple drift-diffusion calculations. To test this hypothesis, a Si-TiO_2-Ni junction sample is studied with XUV spectroscopy. This sample is compared with control samples of pure Si, TiO_2 film supported on diamond, and Ni film supported on diamond. In addition, a Ni-Si junction is used as a control on the effects of the TiO_2 layer.

Each measurement consists of a pump-on and pump-off trace of 61 logarithmically spaced time points, and each time point is the Weiner-filtered average of thousands of laser pulses. The number of pulses used was chosen to maximize the signal-to-noise ratio of the experiment, as the stability of the high harmonic generation process decreases over the course of the measurement. An acquisition time of approximately 6 hours, or 125,000 pulses, is optimal. Measurements that resulted in obvious damage to the samples and measurements that were cut short by equipment malfunctions were excluded.

Thin-Film Growth and Characterization

The physical vapor deposition method was used to grow TiO_2 and Ni films onto a 200 nm-thick ⟨100⟩ silicon membrane (Norcada), using home-built evaporators containing Ti (99.98% pure, from Kurt J. Lesker Company) and Ni (99.98% pure, from Kurt J. Lesker Company) filaments. To make the layered sample studied here, first Ti was evaporated on the silicon membrane under an oxygen (99.998% pure) atmosphere of 7.4×10^{-9} to 8.0×10^{-9} Torr with the Ti filament at ∼1157°C. After 7.5 hours of Ti deposition, the oxygen was pumped off, and Ni was evaporated at a temperature of ∼1000°C for 3.5 hours. A cross-sectional TEM of the sample can be seen in Figure 4.1b. The samples with the TiO_2 and Ni alone were deposited on 50 nm-thick diamond membranes (Applied Diamond, Inc.).

High Harmonic Generation

The near-infrared pump pulses used in the experiment presented in this chapter are a portion of the 3.5 mJ, 40 fs pulses centered at 800 nm produced by a 1 kHz Ti:sapphire chirped pulse amplifier (Spitfire Pro, Spectra-Physics). The 266 nm pump pulses used to photoexcite the TiO_2 are produced via third harmonic generation of the 800 nm pulses. XUV probe pulses are produced by high harmonic generation of 2.5 mJ of the 800 nm pulses, a portion of which is converted to 400 nm using an in-line second harmonic generation scheme.[229] This allows for the production of both even and odd harmonics. High harmonic generation occurs in a semi-infinite gas cell (40 cm) filled with either 250 Torr (approximately 3.3×10^4 Pa) helium gas for the Ni $M_{2,3}$ and Si $L_{2,3}$ edges or 40 Torr (approximately 5.3×10^3 Pa) argon for the Ti $M_{2,3}$ edge. The residual near-infrared and visible light is blocked by a 0.5 mm-thick 5 μm pore size glass capillary array (or microchannel plate), which transmits the XUV onto the sample.[144] The XUV pulses transmitted through the sample are spectrally dispersed by a variable line spacing grating (35 to 110 eV) and captured using a charge-coupled device camera (PIXIS-400, Princeton Instruments).

The XUV probe spot size is approximately 200 μm at the sample; the samples are raster-scanned in 100 μm steps between each time delay, and a stream of dry nitrogen is flowed over the sample to dissipate heat to avoid thermal damage. Approximately 500 pulses are coadded together to produce a camera image of XUV light versus photon energy. Pump-on and pump-off camera images comprise a single time delay, with the delays spaced logarithmically after time zero (61 delay times, -2.50 to +200 ps about time zero). Approximately 250 such scans are averaged together to produce each transient absorption measurement. Static absorbances are reported as the logarithm of the ratio of XUV photon flux between no sample and the sample. Differential absorbance is reported as the difference between the absorbance measured with the pump on versus the pump off, with outlier measurements removed with Weiner filtering. The pump spot size is approximately 250 μm at the sample, which encompasses the entire probe spot. Pump power densities are approximately 2 mJ cm^{-2} for all excitations of the Si edge (junction sample, Si-Ni sample, and Si alone sample), approximately 1 mJ cm^{-2} for the TiO_2 alone sample, and approximately 0.3 mJ cm^{-2} for the Ni edge excitations (Ni alone sample and thin sample in Figure 4.4b).

Statistical Analysis

The fitting routines reported in the Discussion section and shown in Figure 4.9 all use a robust, nonlinear fit procedure. Error bars reported represent the sum of the experimental variance, including uncertainty in the pulse width, and the standard error of the fit, which includes cross terms between all fit parameters. In addition, a multistart fit procedure was performed on all fitted parameters within a range of 500% of the final value, and the resulting parameter variances were within bounds of the standard error, as expected. The multistart fit was performed using the MATLAB MultiStart algorithm. For the rise time fit, an error function is used, fitting the amplitude and time constant to the experimental data, as shown in Figure 4.9a. For the diffusion equation fit, $\frac{\partial n_h}{\partial t} = \frac{\partial}{\partial z}\left(D_h \frac{\partial n_h}{\partial z}\right) + S(t, z)$, the one-dimensional diffusion equation is solved with the diffusion constant (D_h) and surface recombination/injection velocity at the Si-TiO_2 interface held as fit parameters, as shown in Figure 4.9b. The hole population is represented by n_h. The source of holes $S(t, z)$ is the error function fit to the Ni rise time and is taken as one boundary condition. The other boundary condition includes the surface recombination/injection velocity to replicate the interface with Si. Since the hole diffusion and injection/recombination occur on such differing time scales, these parameters have very little cross-talk.

4.3 Results

The Ni-TiO_2-Si thin films (Figure 4.1a) were prepared via physical vapor deposition under ultrahigh vacuum conditions using home-built evaporators. Filaments of the Ti and Ni metals were evaporated with and without oxygen, respectively, onto a purchased silicon membrane. The 19 ± 0.6 nm of TiO_2 and 5.6 ± 0.6 nm of Ni were grown on a 200 nm-thick p-doped (B at 10^{15} per cm^3) Si membrane. The surface oxide of the Si could not be etched because of the fragility of the membrane, as attempts to perform Ar sputtering destroyed them. The $\sim$1 nm SiO_2 layer can be seen in the transmission electron microscope (TEM) image of Figure 4.1b and may act as a thin tunneling barrier; its presence is consistent with previous Ni-TiO_2-Si photoanode studies.[234, 248] The topmost Pt layer was used for TEM imaging purposes. The TEM cross section confirms the amorphous nature of the TiO_2. For this sample, the presence of the oxygen defect levels in the TiO_2 was previously quantified during growth of the Si-TiO_2 junction to have a density of states of approximately 6% of the O 2p density of states via photoemission spectroscopy.[250] The resulting Ti^{3+} defect states in the amorphous TiO_2 are generally accepted to be >1 eV below the conduction band of TiO_2 and span a range of 1 to 2 eV.[241, 251, 252]

The band bending in Figure 4.1a is calculated on the basis of a drift-diffusion model using the experimentally measured thicknesses.[249] Calculations were performed with the AFORS-HET (automat for the simulation of heterostructures) program, setting the electron affinity of the p-Si to 4.05 eV and the n-TiO_2 to 4.0 eV. More details of this calculation can be found in the Appendix. Note that in a Si-TiO_2 junction alone, the band energetics promote photoexcited electron transport from the Si to TiO_2.[253] This is because the approximately 0.1 eV difference in Fermi level between the n-TiO_2 and p-Si creates an electron accumulation layer in Si and, in turn, a negative field that transports the photoexcited electrons. The Ni layer has an electron affinity nearly 1 eV below that of both TiO_2 and Si, which creates the opposite direction field in the total device junction. Holes accumulate in the TiO_2 at the TiO_2/Ni interface, but this layer is so thin that additional holes accumulate in the Si. The Si and TiO_2 bands both bend upward, producing a positive 1.5×10^5 V/cm field across the TiO_2 layer promoting hole transport, as shown in Figure 4.1a.

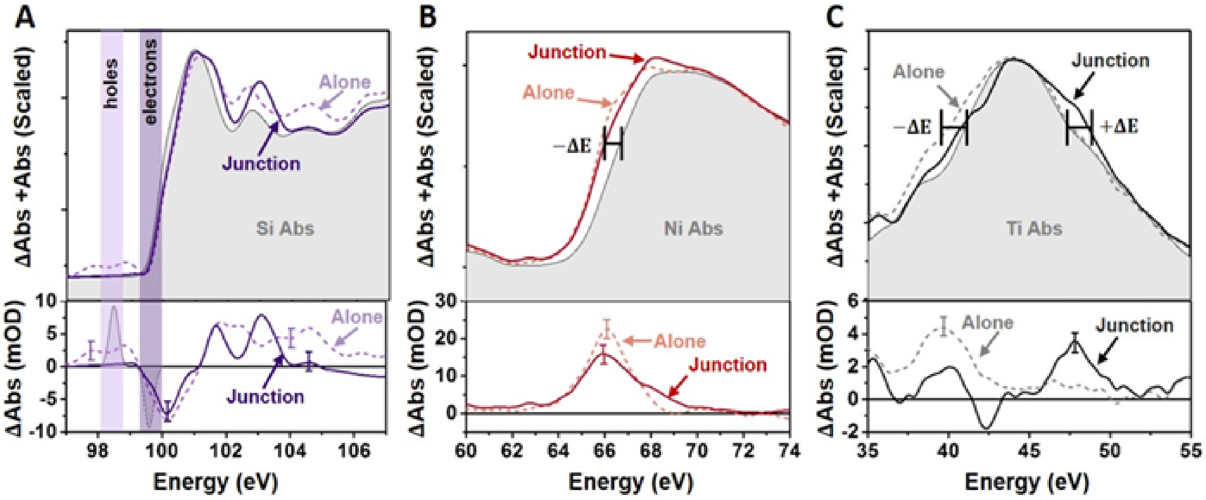

Figure 4.2: **Photoexcited changes in the Si, TiO_2, and Ni separately and in a junction.** The differential absorption versus photon energy from Figure 4.1c is plotted in the bottom row, while the top row shows the differential absorption scaled and added to the ground-state absorption. The solid lines represent the excited-state change for the elements in the junction for a) Si 100 fs after photoexcitation, b) Ni 100 fs after photoexcitation of the Si, and c) TiO_2 1 ps after the photoexcitation of Si. The same time differential absorption versus photon energy is shown for photoexcitation of each element alone as a dashed line. As discussed in the text, different excitation wavelengths and thicknesses were required to photoexcite the elements alone as compared to the junction. A representative error bar of the experimental few mOD noise is shown at key comparison energies.

The ground-state XUV absorption (black line overlay in Figure 4.1c) contains the Ti $M_{2,3}$ edge at 32.6 eV, the Ni $M_{2,3}$ edges at 66.2 and 68 eV, and the Si $L_{2,3}$ edges at 99.2 and 99.8 eV. The XUV range of 30 to 150 eV is created by high harmonic generation in Ar or He. An Al or Zr metal filter prevents second-order diffraction modes from being observed at the XUV camera. The residual 800 nm driving laser for the high harmonic generation process is removed using a microchannel plate filter before the camera.[144] The full details of the technique are found in the Materials and Methods section. The ground-state absorption amplitude for each elemental edge is determined by the film thickness (Figure 4.1b) and the absorption transition probability of the element. This is why the absorption magnitude of the ∼20 nm TiO_2 film, which has 10 empty 3d levels, is larger than the 200 nm-thick Si, which has partially occupied and sp–hybridized valence bands. Similarly, the Ni $M_{2,3}$ edge has the smallest amplitude in the static spectra because only two unoccupied 3d orbitals can absorb the XUV radiation in the relatively thin ∼5 nm film.

Charge transfer in the MOS junction is photoinitiated by a 50 fs, 800 nm laser pulse from a Ti:sapphire regenerative amplifier. The Si thin film primarily absorbs the 800 nm radiation, photoexciting electrons and holes by an indirect transition to the Δ valley. The photoexcitation density is restricted to 1×10^{20} carriers/cm^3 to minimize multiphoton absorption by

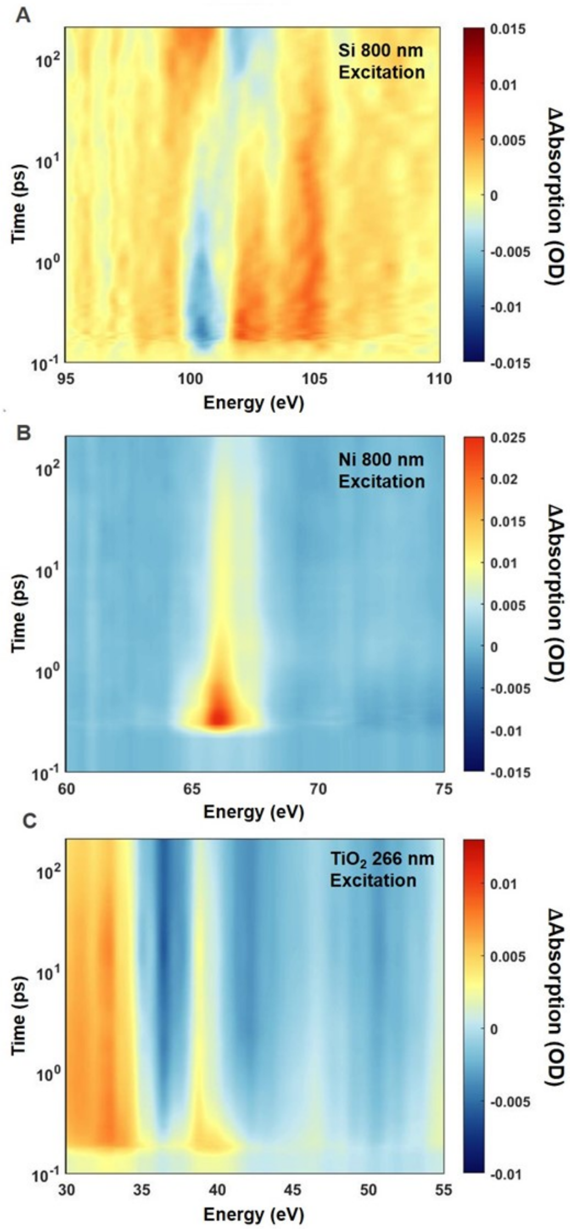

Figure 4.3: **Transient differential data for reference samples.** The differential XUV absorption is shown on a negative (blue) to positive (red) colormap. The timescale is logarithmic and offset by 100 fs for visualization. a) Differential absorption for Si alone with 800 nm light. b) Differential absorption for photoexcitation of Ni alone with 800 nm light. c) Differential absorption for 266 nm photoexcitation of TiO_2 alone.

using 800 nm pulse energy densities of approximately 2 mJ cm^{-2}.[56] The resulting changes to the XUV absorption spectrum are shown as the background color map of Figure 4.1c. The blue color represents a decrease in absorption after photoexcitation, while the red color indicates an increase in absorption. The change in absorption is displayed from tens of femtoseconds to 200 ps on a logarithmic time scale. The time scale is offset for visualization, with zero delay between pump and probe occurring at 100 fs. The absorption features in Figure 4.1c and their evolution in time represent the underlying photoexcitation, charge transfer, and heat transfer processes in the junction.

The differential absorption versus photon energy of Si and Ni at 100 fs and Ti at 1 ps is shown in the bottom row of Figure 4.2. The top row of Figure 4.2 shows the ground-state absorption plus the differential absorption, scaled for visualization. This information is plotted for each element in the junction (solid lines) as well as for Si, Ni, and TiO_2 photoexcited on their own (dashed lines). The full differential absorption plots for the elements alone are shown in Figure 4.3. For the alone samples, conditions are arranged to obtain a similar transient absorbance as for the junction. In Si, this is simply measuring a blank membrane at the same 800 nm photoexcitation density as the junction. To measure TiO_2 alone, a TiO_2 layer on a diamond substrate is measured and the pump wavelength is changed to 266 nm (approximately 1 mJ cm^{-2}) to excite above the ~3.2 eV band gap.[56] The 266 nm single-photon absorption probability of TiO_2 is 10^5 times larger than the three photon absorption at 800 nm needed to excite above the band gap, so any excitation of TiO_2 by 800 nm light can be neglected in the junction. To measure Ni alone, a diamond substrate supporting a Ni layer of the same thickness as the junction is not a good comparison. When this sample is excited by 800 nm light to the same carrier density as Si (approximately 0.3

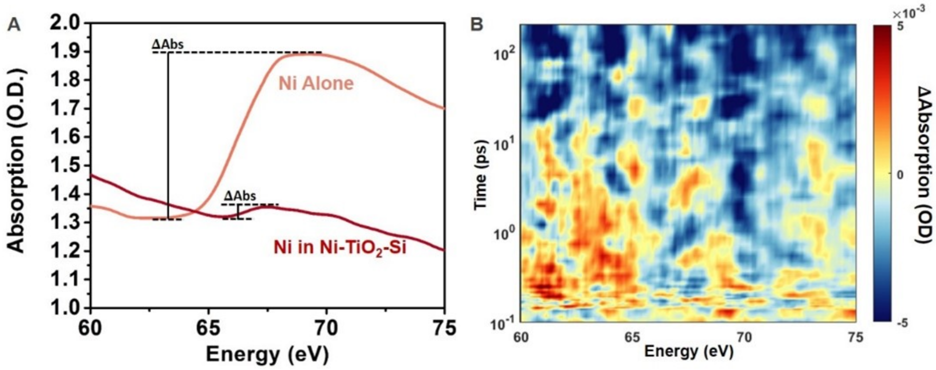

Figure 4.4: **Comparing Ni in Ni-TiO_2-Si versus Ni alone.** a) The absorption of the Ni in the junction is over ten times less than the Ni alone film when measured from pre-edge dip to peak (ΔAbs). The lines have been vertically offset for comparison. b) The differential absorption following 800 nm excitation of a thin Ni sample with similar thickness to the Ni in the junction. This thin Ni film has no signal within a few mOD noise level. The thicker Ni alone sample has an ~25 mOD signal as seen in Figure 4.3b.

mJ cm^{-2}), no signal from Ni is observed within the experimental noise (see Figure 4.4). The Ni in the junction has a 0.03 optical density (OD) absorption magnitude from the pre-edge to the peak. Instead, a thicker layer of Ni with an absorption of 0.6 OD from the pre-edge to peak is used (Figure 4.4). When the thicker Ni is photoexcited with the same density of 800 nm light, a change in absorption of ~25 milli-OD or milli-optical density (mOD) is measured. This change would be obscured in the thinner sample, as the 20× decrease in absorbed 800 nm light would be below the few mOD noise. In addition, an immediate rise time is not measured for the Ni in the junction, as it is for Ni alone, as discussed in the following section 'Comparing Ultrafast Dynamics Between the Junction and Alone Layers'.

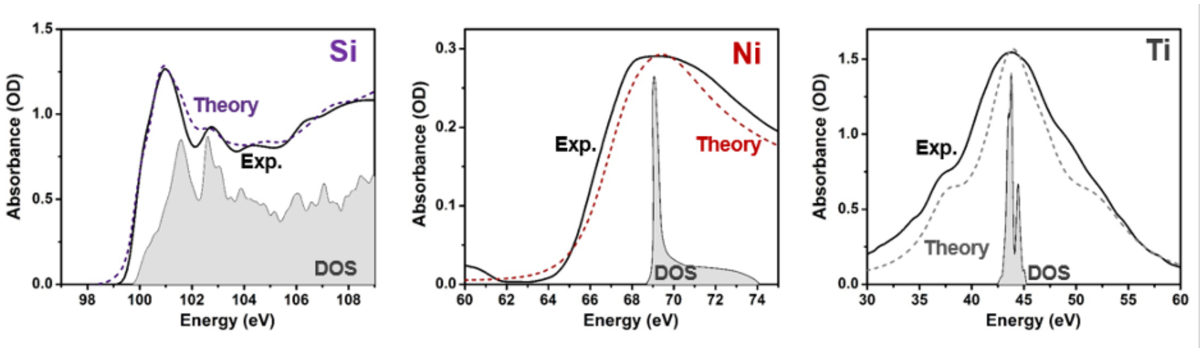

Figure 4.5: **Modeling the XUV ground and excited state absorption.** The experimental XUV absorption of each element (solid lines) is compared to the BSE-DFT calculation (dashed lines) and the approximate valence density of states (DOS) from DFT for each material. How well the valence charge density screens the core hole perturbation from the XUV excitation determines to what degree the XUV spectrum reflects the valence density of states.

4.3.1 Interpreting the Differential XUV Spectra at the Si, Ni, and Ti Edges

The core hole excited by the XUV transition perturbs the final state in the core-level transition, masking the ground-state density of states. The strength of the core hole interaction depends on the element's orbital occupation and bonding. The stronger the core hole interaction, the more the ground-state density of states is masked, and thus the information that can be obtained from the measured photoexcited state is altered. For example, the core hole in Si is well screened, and the critical points are only slightly shifted from the ground-state band structure (Figure 4.5 left panel). Changes in the Si $L_{2,3}$ edge are therefore representative of the underlying carrier and lattice dynamics, as shown by the $L_{2,3}$ edge absorption of different Si oxidation states in Figure 4.6a. After photoexcitation, the differential absorption features above 101 eV are known to correspond to structural changes.[56] Below 101 eV, a signature of the photoexcited electron and hole populations is present at approximately 100 and 99 eV, respectively, as shown in the bottom panel of Figure 4.2a. When the Si alone is photoexcited (dashed line in Figure 4.2a), an increased absorption is measured below 99 eV (holes) and above 101 eV (structural). A decreased absorption is measured around 100 eV (electrons). Following photoexcitation of the Si in the junction, an increased absorption is not measured below 99 eV, while a decreased absorption is still measured at 100 eV. In other words, the spectral signature of photoexcited holes is not observed within the signal-to-noise ratio of the experiment in the junction, but the electron signature is present. Above 101 eV, a slightly different structural change is also measured, as would be expected when comparing the strain dynamics of the free-standing 200 nm Si film versus the more rigid junction. Together, the Si edge measurement suggests that holes have left the Si but the electrons remain, as expected for the operation of this MOS junction (Figure 4.1a).

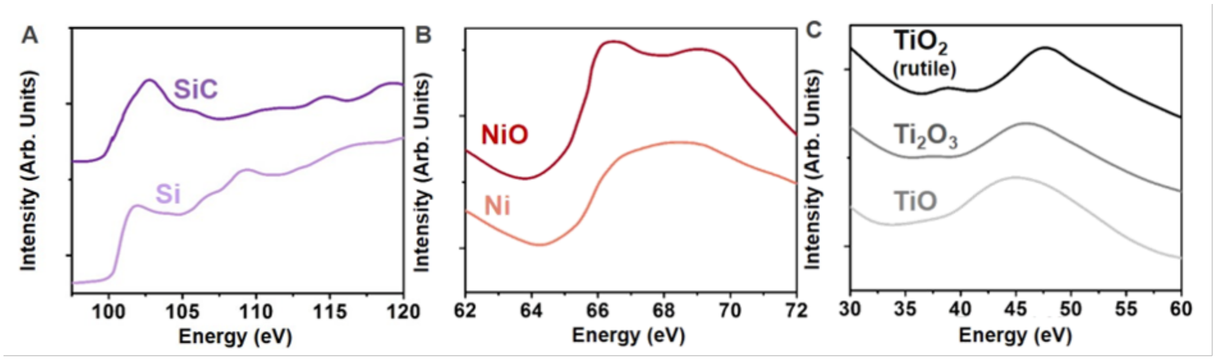

Figure 4.6: **Comparison of EELS absorption in the XUV range for different compounds.** XUV absorption data from synchrotron sources is not readily available, so the electron energy loss (EELS) absorption is shown for each element.[254] The EELS absorption process involves a one-electron excitation instead of a one-photon excitation. a) For Si, the core hole is well screened, and the peak structure and energy are more representative of the underlying band structure than the oxidation state (compare Si and SiC). b) For Ni, the edge rise is sensitive to the number of holes or oxidation state. When electrons are removed in the metal, the Fermi level changes, and the edge shifts to lower energy while increasing in absorption. c) For Ti, the broad absorption and appearance of multiplet split peaks is sensitive to the oxidation state.

Unlike the Si edge, the metallic Ni $M_{2,3}$ edge does not closely correspond to the underlying density of states (Figure 4.5 middle panel). The core hole perturbs the final-state wave function, and the resultant many-body interaction exponentially increases the number of states at energies near the Fermi level. This leads to the sharp absorption feature around 66 eV in the ground-state XUV spectrum. Any photoexcited changes in the edge therefore mostly relate to changes in occupation near the Fermi level. Following photoexcitation of the Ni alone with 800 nm light, the $M_{2,3}$ edge shifts to lower absolute energies and increases in absorption (dashed line Figure 4.2b). A similar, but slightly broader, change occurs when the Ni is photoexcited in the junction. Photoexcitation of Ni alone promotes electrons from the Fermi level to a higher lying conduction band, shifting the quasi-Fermi level to lower energy. The presence of more holes near the Fermi level also allows for more XUV transitions to be possible near the Fermi level. Correspondingly, a negative energy shift and gain in absorption is measured in Figure 4.2b. The photoexcited electrons are too high in energy to affect the many-body state near the Fermi level. In the junction, the same negative shift is measured when 800 nm light excites the Si, indicating that holes have been added to the Ni near the Fermi level. Thus, while holes are not directly observed in the Si, their rapid movement into the Ni is observed. The appearance of holes on the Ni corresponds to the absence of holes measured on Si. For reference, the hole spectral signature is also observed when comparing the static ground-state absorption of Ni^0 to Ni^{2+} in NiO (Figure 4.6b).

The measurements in Figure 4.2a,b indicate that holes are transferred from the Si to the Ni within the first 100 fs of optical excitation. No transient signal is measured for TiO_2 in this same time period, as can be seen in the color map in Figure 4.1c. Instead, the dynamics in TiO_2 start only after 1 ps and represent a shift and broadening (Figure 4.2c). The Ti $M_{2,3}$ core hole has a strong interaction with the localized Ti 3d orbitals in TiO_2. Little screening of the core hole occurs, and as a result, the measured spectrum is distorted from the ground-state density of states by atomic multiplet splitting (Figure 4.5 right panel). When the TiO_2 is photoexcited alone at 266 nm, a small negative shift in the edge energy is observed. The negative energy shift occurs immediately after photoexcitation because an electron is promoted from the O 2p orbital to the Ti 3d orbital, lowering the Ti oxidation state. The added electron helps screen the strong core hole interactions on the Ti such that the overall edge shift is negative. When the junction is photoexcited, a small positive shift to larger absolute energy is observed after 1 ps. This opposite shift when the Si is photoexcited is interpreted to mean that the Ti oxidation state has increased or that holes have been added instead of electrons. The positive and negative shifts can again be confirmed by comparing the ground-state absorption of different Ti charge states (Figure 4.6c). The spectral shifts assigned to holes have opposite signs in the Ni and TiO_2 because the predominant core-hole effects are different. The excess holes increase the Ti oxidation state, decreasing the core-hole screening and shifting the peak positively. The excess holes on the Ni perturb the many-body state at the transition edge, shifting the quasi-Fermi level and opening up new transitions.

4.3.2 Comparing Ultrafast Dynamics Between the Junction and Alone Layers

The fit kinetics for the electrons and holes on Si, as well as the Ti and Ni edge shifts, are shown in Figure 4.7. The fit procedure qualitatively mirrors the discussion of Figure 4.2 and is described in more depth in the Appendix. Briefly, the ground-state absorption is modeled (Figure 4.5) using the Bethe-Salpeter equation with density functional theory for the Si and TiO_2 while using an analytic many-body theory expression for the Ni. The photoexcited data are then fit at each time point as equilibrium changes to the ground-state. For the

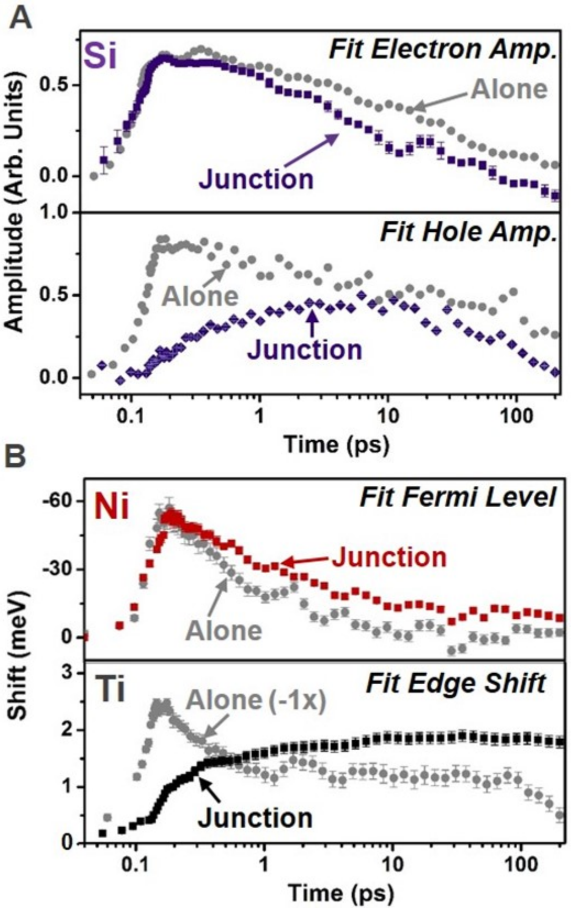

Figure 4.7: **Comparing the fit kinetics separately and in a junction.** The spectral signatures described by Figure 4.2 are fit to extract the excited-state kinetics, shown here. In each case, the error bars correspond to the nonlinear fit standard error from a robust fit weighted by the experimental uncertainty. For each plot, the junction fit parameters are shown as the colored symbols, while the gray symbols are for the isolated material. The time scale is logarithmic with a 100 fs offset for visualization. a) The amplitude of electron spectral signature in the junction (purple symbols) has a similar rise time compared to the isolated material but has an increased decay rate. In the isolated Si, the amplitude of the hole spectral feature (gray symbols in bottom panel) follows the same kinetics as the electrons. In the junction, the hole signature slowly grows until 10 ps, suggesting that the initial photoexcited hole population was transferred out from the Si. a) Top: The fit Fermi level of Ni decreases when the Si in the junction is excited with 800 nm light or when a 20× thicker Ni film alone is excited with 800 nm light. The fit Fermi level then decays on a longer time scale in the junction. The amplitudes are scaled for comparison of the rise times. Bottom: When TiO_2 alone is excited with 266 nm light, a decrease in the fitted edge energy is observed because of the ligand-to-metal charge transfer. In the junction, the Ti edge fit energy increases on a time scale that matches the decay of the Fermi level in Ni.

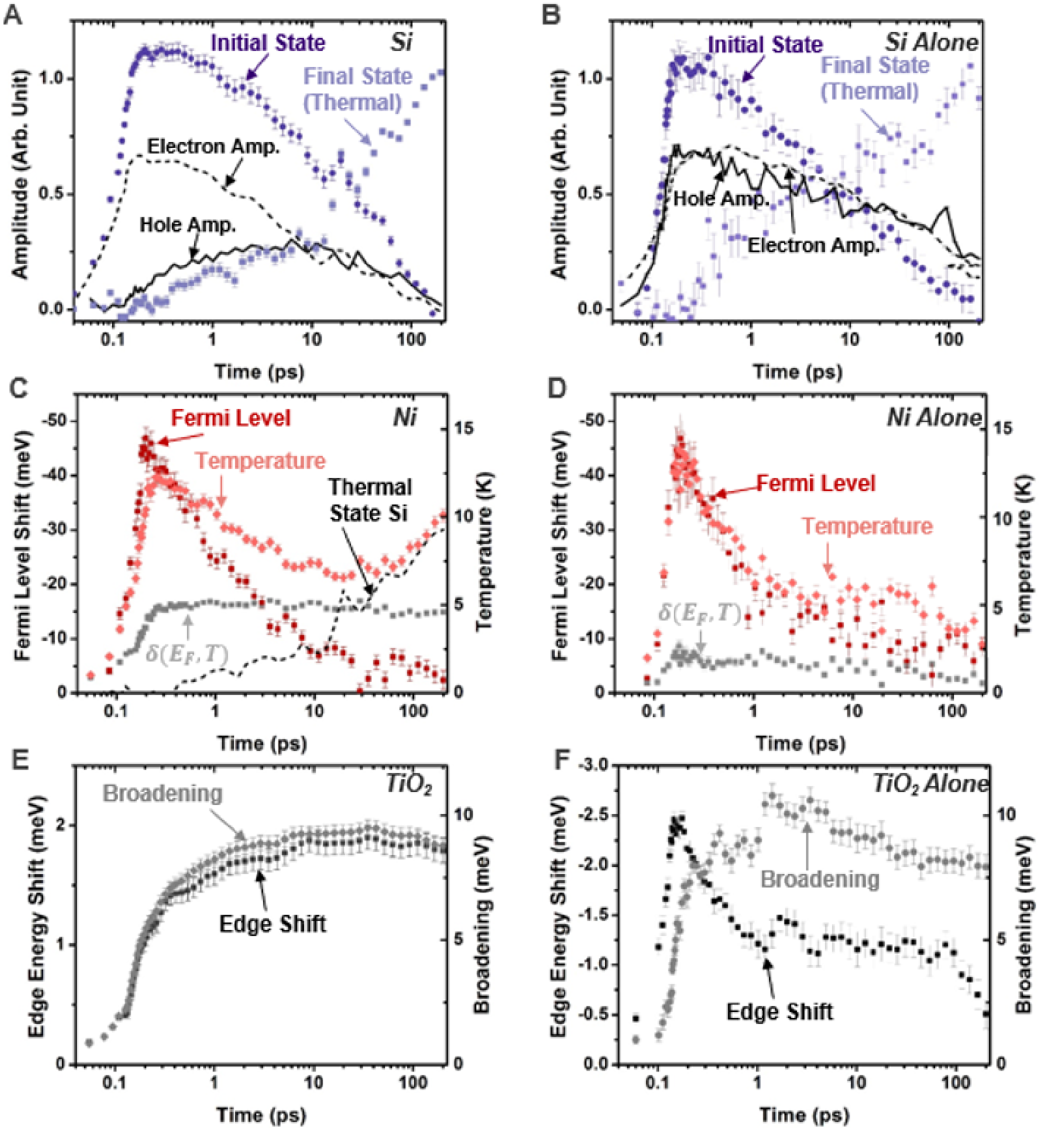

Figure 4.8: **All fit parameters for each XUV edge as a function of time.** a) For Si in the junction, the amplitude of the initial and final states used in the multivariate regression are shown as the dark purple circles and light purple squares, respectively. The final state represents a heated lattice. The electron and hole features' spectral amplitudes after removal of the final thermal state are shown as the dashed and solid black lines, respectively. b) The same as in panel a, but for Si alone. c) For Ni in the junction, the fit Fermi level (red circles), temperature in the Fermi-Dirac distribution (light red diamonds), and the phase factor (gray squares) which is co-dependent on the Fermi level and temperature are shown. The final thermal state from the Si fit is shown as a dashed black line. d) The same as in panel c but for Ni alone. e) For TiO_2, the fit broadening (grey diamonds) and edge shift (black squares) of the Ti edge. The error bars correspond to the non-linear-fit standard error from a robust-fit weighted by the experimental uncertainty. f) The same as in panel e but for TiO_2 alone.

Si, the electron and hole signatures are fit based on previous analysis (Figure 4.7a).[53, 56] For the Ni and Ti, the edge shifts are fit since no distinct spectral signature exists for the photoexcited electrons and holes (Figure 4.7b). For reference, all fit quantities are shown in Figure 4.8. In Figure 4.7, the error bars of the fit process are shown on the symbols in the graphs, and the data for the material alone are shown as the gray symbols.

The fit kinetics confirm and quantify the qualitative observations of Figure 4.2. Specifically, following photoexcitation, holes are absent on the Si in the junction, while the photoexcited electrons exist in the same magnitude as Si alone. An initial change is not measured in the Ti edge. However, an edge shift that correlates with increased holes in the Ni is measured on a sub–100 fs time scale, in agreement with the expected photoexcited tunneling of holes for the p-type MOS junction. For the first approximately 100 fs, while holes are still being transferred from the Si to the Ni, a small hole population is still present in Si. No signature of these holes is reported because of the extremely low signal-to-noise ratio of the Si (<3 mOD signal) hole population at this excitation density, while holes are more readily observed in Ni (>20 mOD signal), as can be seen in the error bars in the bottom panels of Figure 4.2a,b.

After a few hundred femtoseconds, the fit edge shift of the Ni decreases in magnitude, while the positive edge shift of the Ti begins to rise on a similar time scale. This observation correlates with the transferred holes leaving the Ni by back-diffusing through the TiO_2. The fit kinetics at >100 ps are further consistent with the arrival of holes at the Si/TiO_2 interface and the following injection into the Si bulk or surface recombination with the excited electrons left on the Si. This is evidenced by the similar time scales of the decay of the fit Si hole and electron amplitudes as the decay of the Ti fit edge shift.

4.4 Discussion

The hole transfer, diffusion, and surface recombination can be quantified using the fit kinetics of Figure 4.7 by taking advantage of the fact that the relative timing between the Ti and Ni or Si peaks is maintained in the spectra and fit kinetics. This is possible because at least two different elemental edges are measured simultaneously for each transient experiment. The Ti and Ni edges are measured simultaneously using Ar high harmonics, and the Si and Ni edges are measured simultaneously using He high harmonics. For all fitted values, the error bars are in terms of the standard error of the mean as calculated through the Jacobian and covariance of a multistart fit (MATLAB 2018b, MultiStart) of the experimental data within a 500% range of the final value. The few mOD experimental error is reflected by the scatter of the points on each plot.

The calculation of the charge carrier dynamics is developed as follows. First, the transit time for holes through the TiO_2 layer is quantified by fitting the magnitude of the Ni edge rise time to an error function that is convoluted with the 50 ± 5 fs pump pulse width (Figure 4.9a). Convolving the fit with the pulse duration accounts for the instrument response time.

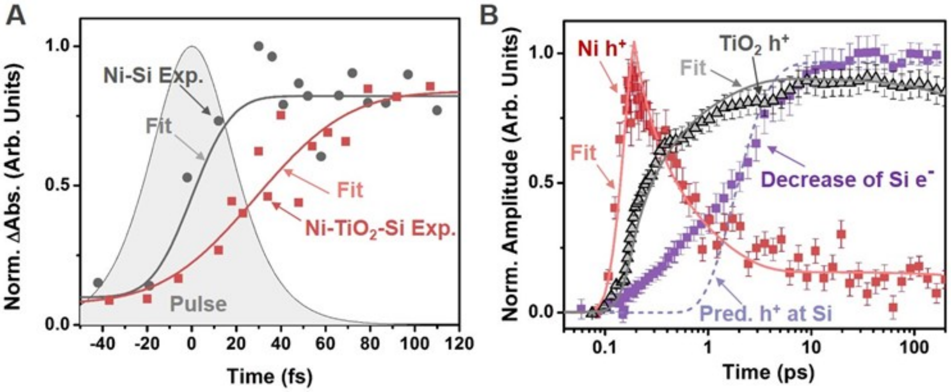

Figure 4.9: **Quantifying the photoinitiated hole tunneling and diffusion in the junction.** a) The square light red symbols represent the magnitude of the measured rise time of the Ni edge in the junction; their scatter represents the error of the experimental measurement. The gray circles represent the rise time of the Ni in a Si-Ni junction with no TiO_2 spacer. Fitting the experimental data to an error function (solid lines) convoluted with the excitation pulse gives a delayed rise of 17 ± 5 fs for the Si-Ni and 50 ± 6 fs with the TiO_2 layer. The transit time in the TiO_2 is therefore obtained as 33 ± 8 fs. b) The edge shift kinetics, which, as noted previously, indicate the hole kinetics, measured for the TiO_2 (gray triangles) and the Ni (red squares) in the junction are compared to the increase in electron recombination (or decrease in electron signature at the Si edge) in the junction (purple squares). The solid line is a fit to the diffusion equation with a diffusion constant of 1.2 ± 0.1 cm^2/s and a surface recombination velocity of 200 ± 50 cm/s. The decrease in electron density qualitatively tracks the diffusion of holes through the TiO_2. The dashed line represents the predicted (Pred.) arrival of holes at the Si-TiO_2 interface based on the fit diffusion kinetics.

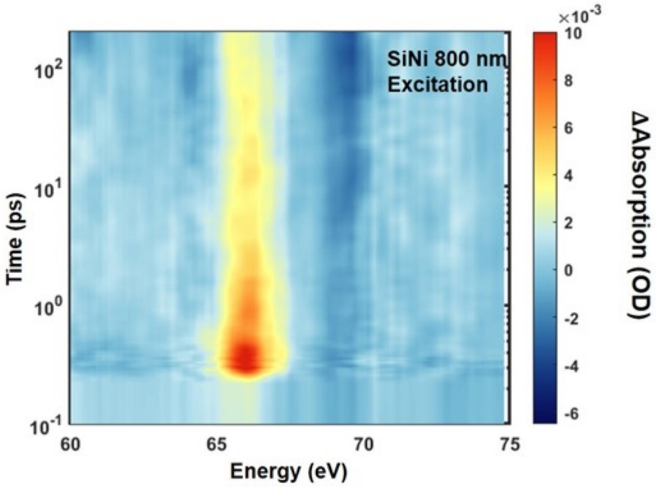

Figure 4.10: Transient differential data for 800 nm photoexcitation of Si-Ni as measured at the Ni edge.

This fit for the Ni-TiO_2-Si junction sample is compared to a separate Ni-Si sample. The Ni-Si junction is used instead of Ni alone as the reference so that any delay from carrier transport within the Si is included. The full differential absorption following photoexcitation of the Si side is shown in Figure 4.10. In the Ni-TiO_2-Si junction, the transfer time determined by convolving the 50 ± 5 fs pulse with an error function is delayed by 50 ± 6 fs relative to the excitation pulse, while in the Ni-Si junction, it is delayed by 17 ± 5 fs. These error bars are the standard error of the fit, which includes the pump pulse duration and its error. The ~20 nm TiO_2 therefore delays the arrival of holes at the Ni by 33 ± 8 fs, which, by using the measured thickness of the TiO_2, gives an average hole velocity of $5.8 \pm 1.4 \times 10^7$ cm/s for the tunneling process. The calculated built-in field of 1.5×10^5 V/cm after photoexcitation would therefore imply a hole mobility during tunneling of 390 ± 100 $cm^2/V{\cdot}s$, similar to the accepted value for 10^{15} per cm^2 p-doped Si of 450 to 500 $cm^2/V{\cdot}s$.[255]

From the unchanged hole mobility in the TiO_2 with respect to the Si at early times, which implies no scattering of the holes in the TiO_2, and the lack of a measurable hole signal in the TiO_2 during tunneling, the hole transport through the TiO_2 is therefore suggested to be ballistic. The injection efficiency of the tunnel junction is also quantifiable as 42 ± 6% from the excitation density and the fit Fermi level change in the Ni. This relationship was calibrated by the Fermi level shift of Ni alone for a given photoexcitation density and matches the expected shift calculated for a parabolic band. This injection efficiency is reasonable for the junction.[256] The approximately 60% remaining holes in Si are beneath the noise of the spectrum in that region (Figure 4.2a, bottom). Note that the peak laser field intensity is 170 GW/cm^2, which would correlate with an electric field of 5.8×10^6 V/cm. This pulse energy is one order of magnitude less than that needed for optical field–induced tunnel ionization or for optical field–induced changes in the band structure.[257–259] Although not comparable to AC modulations at the optical field frequency, the DC dielectric breakdown values for Si and TiO_2 are $>10^7$ V/cm.[260]

To test the accuracy of the element-specific kinetics, the hole back diffusion rate through the TiO_2 layer is quantified by fitting the Ni and Ti edge shifts, which represent the hole kinetics, to the diffusion equation (Figure 4.9b). The fit uses the Si-to-Ni hole transfer kinetics in Figure 4.7a as the source and is discretized over the junction. The boundary condition is fit to a constant representing the surface hole arrival velocity, which can include both surface recombination and hole injection into the Si bulk. More details can be found in the 'Statistical Analysis' section of Materials and Methods. The fit gives a diffusion constant of 1.2 ± 0.1 cm^2/s, close to the value of 0.4 cm^2/s estimated in an annealed thin film of amorphous TiO_2 nanoparticles.[260] The surface recombination or injection velocity from the fit is 200 ± 50 cm/s, which is also similar to previous measurements of >200 cm/s.[253, 261] The fit surface recombination velocity should only be taken as qualitative since the scan time range of 200 ps is too short for substantial recombination to occur. There is little dependence between the two fit parameters because they have such differing time scales. In Figure 4.9b, the measured increase in recombination for electrons on Si (purple squares) is also compared to the number of holes at the Si-TiO_2 interface as predicted by the fit diffusion equation (dashed purple line). Again, although a qualitative comparison, the arrival of holes at the interface predicted by the diffusion rate appears to correlate with the recombination of electrons on the Si. The primary source of error in these quantities is approximating the kinetics by a simple diffusion equation, rather than the experimental error or the fit standard error. This model is presented to give context to the measured dynamics in terms of the known values and is not intended to be absolute.

Conclusion

In conclusion, element-specific transient XUV spectroscopy is used to quantify the photoinitiated charge transfer in a Ni-TiO_2-Si junction. An initial ballistic hole tunneling from Si to Ni is observed on a <100 fs time scale. The injection efficiency of photoexcited carriers was measured to be 42 ± 6%. On a picosecond time scale, a back diffusion of holes from the Ni to the Si through the TiO_2 is measured. As the holes arrive at the Si-TiO_2 interface, a decrease in the electron population is measured on the Si in the junction relative to the Si alone. The drift and diffusion values quantified from the transient XUV measurement also match previously reported values, confirming transient XUV as a highly versatile analysis tool for measuring charge transfer in multiple-element materials and junctions.

4.5 Appendix: Theoretical and Computational Details

4.5.1 Silicon $L_{2,3}$ Edge

The ground-state Si XUV absorption was predicted using the OCEAN code (Obtaining Core-level Excitations using Ab initio methods and the NIST BSE solver). The energy-dependent broadening is included using a Drude-Lindhard single-plasmon pole model for the electron loss function. The ground-state electron densities and wave-functions are calculated at the density functional level (DFT) using Quantum-ESPRESSO.[262] The local density approximation (LDA) using a norm-conserving generalized gradient approximation (GGA) Perdew-Burke-Ernzerhof pseudopotential is used to calculate the density of states with a converged k-point mesh of 20x20x20 points and a plane wave cutoff of 100 Ry. The lattice constant is converged at 5.46 Angstroms. Projector augmented wave (PAW) reconstructed wave functions are used for calculating the core-level transition matrix elements. A real-space random phase approximation is used to estimate the dielectric screening inside a sphere around the atom, while the Levine-Louie dielectric function is used outside this sphere.[263, 264] The Bethe-Salpeter (BSE) equation is then used to calculate the final electron-hole states.

In the BSE-DFT calculation, the final states are converged at k-point meshes of 8x8x8 and using a total number of bands of 100. The projector augmented wave states are converged at k-point meshes of 2x2x2 and using a total number of bands of 200. The SCF mixing is taken as 0.7 with 250 iterations used. The BSE mesh is 6x6x6, with a cut-off radius of 8.0 Bohr. The projector augmented wave shell radius is taken as 8.0 Bohr with a 0.8 scaling factor of the slater G parameter. The dielectric constant of silicon is taken as 11.7. XUV dipole orientations along the [100] and [110] directions are calculated, but within the experimental broadening, little difference is found in the final predicted X-ray absorption. A comparison of this fit with the ground-state absorbance is shown in the left panel of Figure 4.5.

The excited state changes to the Si $L_{2,3}$ edge are known to originate in a variety of electronic and structural dynamics. A simplified version of the model to extract electron energies, hole energies, and the temperature of the lattice is used.[265] Specifically, the differential absorption features above 101.5 eV are mainly from structural distortions related to heating the lattice, similar to what is measured in EXAFS. A multivariate regression is used to extract the amplitude of the initial and final thermal contributions to the differential absorption. The amplitude of the structural dynamics above 101.5 eV is multiplied with the full spectrum and subtracted from each time point. The residual, filtered by the known energy ranges of the electron and hole contributions, represents the electron and hole energy as a function of time. The relative amplitudes are calculated by integrating over these ranges, giving the values shown in Figure 4.7a. All of the fitted parameters, not just the electron and hole populations shown in Figure 4.7, are included in Figure 4.8a,b for the Si in the junction and alone, respectively. Differential absorptions for these two samples can be found in Figure 4.1c for the Si in the junction and Figure 4.3a for the Si alone.

4.5.2 Nickel $M_{2,3}$ Edge

The Ni $M_{2,3}$ edge is modeled using the many-body approach of Ohtaka and Tanabe.[266] This model is derived by summing over the transition probabilities for all possible final states, assuming parabolic bands and a scattering potential caused by the core hole. The resultant ground-state absorption includes the "orthogonality catastrophe" or "white line" effect common to the X-ray absorption of metals,

$$I'(\omega^*) = \frac{1}{D}\left[\frac{D}{2\pi T}\right]^{\zeta_0} \mathrm{Re}\left[e^{i(\pi/2)(\zeta_0-1)}\frac{\Gamma\left(\frac{1-\zeta_0}{2} - \frac{i\omega^*}{2\pi T}\right)\Gamma(\zeta_0)}{\Gamma\left(\frac{1+\zeta_0}{2} - \frac{i\omega^*}{2\pi T}\right)}\right] \tag{4.1}$$

where I' is intensity, $\omega^* = (\omega - \omega_{th})$, which is the frequency with respect to the edge onset frequency ω_{th} as given by the Fermi level of the metal, D is the bandwidth or energy difference between the Fermi level and conduction band upper edge, T is temperature, and ζ_0 is the phase shift of the Fermi sea caused by scattering with the core-hole contact potential. The ground-state Ni $M_{2,3}$ edge is modeled by fitting the values of ω_{th}, T, D and ζ_0 to the ground-state absorption spectrum. To account for the spin-orbit splitting of the Ni 3p level, the total spectrum is modeled as the sum of two of such peaks, keeping all four fit variables constant, and fitting the spin-orbit splitting energy and peak ratio. A comparison of this fit with the measured spectrum is shown in Figure 4.5. Since the phase factor ζ_0 depends on the energetics of the electrons filling the Fermi sea, it contains no new information other than ω and T.

To model the differential absorption spectrum of the excited state Ni $M_{2,3}$ edge, the modeled ground-state spectrum for both spin-orbit components is subtracted from the modeled excited state fit, in which all variables are held constant from the ground-state calculation except ω_{th}, T, and ζ_0. Since Ni is not a free-electron metal, the magnitudes of D, T, and ζ_0 in the ground-state are nonphysical. The magnitude of the excited state changes, however, prove experimentally accurate. For example, the temperature shift matches the predicted value for the given carrier concentration and heat capacity. The change in Fermi level matches the number of carriers photoexcited in the Ni. The differential absorption spectrum of the photoexcited Ni in the junction can be seen in Figure 4.1c, and the differential absorption of the Ni alone is shown in Figure 4.3b. A comparison of the ground-state absorbances of these two samples is found in Figure 4.4a. All fitted parameters are shown in Figure 4.8c,d for the Ni in the junction and alone, respectively. A comparison of the fitted Fermi level for the junction and alone sample are in the top panel of Figure 4.7b.

4.5.3 Titanium $M_{2,3}$ Edge

Similar to the Si $L_{2,3}$ edge, the ground state absorption of the TiO_2 at the Ti $M_{2,3}$ edge is first modelled using the OCEAN code. The DFT k-point mesh was 6x6x4 with a lattice constant of a = 3.75 and c = 9.38 Angstroms. The local density approximation (LDA) is used with a norm-conserving Perdew-Wang pseudopotential since OCEAN cannot use LDA+U or hybrid functionals. A plane wave cut-off of 100 Ry was used for the pseudopotential. In the BSE calculation, the final states are converged at k-point meshes of 6x6x4 and using a total number of bands of 50. The projector augmented wave states are converged at k-point meshes of 2x2x2 and using a total number of bands of 100. The BSE mesh is 4x4x4, with a cut-off radius of 4.0 Bohr. The projector augmented wave shell radius is taken as 4.0 Bohr with a 0.8 scaling factor of the slater G parameter. The dielectric constant of TiO_2 is taken as 20 to approximate amorphous TiO_2. XUV dipole alignments along the [100] and [111] directions are calculated, but within the experimental broadening and amorphous TiO_2 layer, little difference is found in the final predicted X-ray absorption. An energy-dependent broadening was included by using a separate Lorentzian for each atomic multiplet split peak. The value of the broadening was 3 eV except for the central peak, which was 5 eV. This modeled spectrum is compared to the measured static absorbance in the right panel of Figure 4.5.

The atomic multiplet splitting in the metal oxide means that only charge state and a change in broadening can be extracted as a function of time. This is achieved by fitting a global Lorentzian broadening and an energetic shift to the ground state absorption, and then subtracting the unmodified ground state absorption to calculate the differential absorption. These fitted parameters are shown in Figure 4.8e for the TiO_2 in the junction and in Figure

4.8f for the TiO_2 alone. Differential absorption following photoexcitation for the TiO_2 in the junction and alone can be found in Figure 4.1c and Figure 4.3c, respectively. A comparison of the fitted edge shift for both samples is shown in the bottom panel of Figure 4.7b.

4.5.4 Drift-Diffusion Calculation

The calculation of the band bending and electric field inside the Ni-TiO_2-Si junction shown in Figure 4.1a was performed using the AFORS-HET (Automat FOR Simulation of HETerostructures) open access program.[249, 267] This simulation tool numerically solves the one-dimensional Poisson's equations for semiconductors to find the electric field, charge and current densities for a specified series of layers with given boundary conditions. Then, the resultant field and densities are applied to the semiconductor equations iteratively until a steady-state solution is reached. These so-called semiconductor equations are

$$\frac{\partial D}{\partial x} = +q(p - n + \rho + N_D - N_A) \tag{4.2}$$

$$\frac{\partial J_n}{\partial x} = -q(G - R_n) \tag{4.3}$$

$$\frac{\partial J_p}{\partial x} = +q(G - R_p) \tag{4.4}$$

where D is the field that displaces charges, p is the hole density, n is the electron density, ρ is the density of interband traps, N is the acceptor/donor concentration, J is the current density for electrons (n) or holes (p), G is the optical generation rate, and R is the recombination rate for electrons (n) or holes (p). The program models recombination using the Shockley-Read-Hall formalism, and carrier densities are calculated with Boltzmann statistics.

Many different boundary conditions can be applied to the system, including a constant voltage at one of the contacts or a constant boundary current. Additionally, interfaces between the layers can have their own specified boundary conditions. The general form is:

$$\varphi(x) = \phi_j - \phi_i - V \tag{4.5}$$

$$J_n(x) = -q \cdot S_n^i \left(n(x) - n_{eq}(x)\right) \tag{4.6}$$

$$J_p(x) = +q \cdot S_p^i \left(p(x) - p_{eq}(x)\right) \tag{4.7}$$

where φ is the potential at position x, ϕ_i and ϕ_j are the work functions of the front and back layers, V is an optional applied voltage, S is the recombination velocity of electrons (n) or holes (p) at layer i, n_{eq} is the equilibrium electron density, and p_{eq} is the equilibrium hole density. The semiconductor work functions are calculated by the AFORS-HET program from the electron affinity, band gap, and doping levels provided by the user. For the calculation of the Ni-TiO_2-Si junction band diagram in this study, the electron affinity of the p-Si is 4.05 eV, the electron affinity of the n-TiO_2 is 4.0 eV, the work function of the Ni is 5.1 eV, and the boundary voltages are set to zero.

Chapter 5

Characterization of Carrier Cooling Bottleneck in Silicon Nanoparticles by Extreme Ultraviolet (XUV) Transient Absorption Spectroscopy

The content and figures in this chapter are reprinted or adapted with permission from I.J. Porter, A. Lee, S.K. Cushing, H.-T. Chang, J.C. Ondry, A.P. Alivisatos, S.R. Leone, "Characterization of carrier cooling bottleneck in silicon nanoparticles by extreme ultraviolet transient absorption spectroscopy." The Journal of Physical Chemistry C, 2021, 125(17), 9319-9329. Copyright 2021 American Chemical Society.

Silicon nanoparticles have the promise to surpass the theoretical efficiency limit of single-junction silicon photovoltaics by the creation of a "phonon bottleneck," a theorized slowing of the cooling rate of hot optical phonons that in turn reduces the cooling rate of hot carriers in the material. Verifying the presence of a phonon bottleneck in silicon nanoparticles requires simultaneous resolution of electronic and structural changes at short timescales. In this chapter, extreme ultraviolet transient absorption spectroscopy is used to observe the excited-state electronic and lattice dynamics in polycrystalline silicon nanoparticles following 800 nm photoexcitation, which excites carriers with 0.35 ± 0.03 eV excess energy above the Δ_1 conduction band minimum. The nanoparticles have nominal 100 nm diameters with crystalline grain sizes of about $\sim$ 16 nm. The extracted carrier-phonon and phonon-phonon relaxation times of the nanoparticles are compared to those for a silicon (100) single-crystal thin film at similar carrier densities (2×10^{19} cm^{-3} for the nanoparticles and 6×10^{19} cm^{-3} for the film). The measured carrier-phonon and phonon-phonon scattering lifetimes for the polycrystalline nanoparticles are 870 ± 40 fs and 17.5 ± 0.3 ps, respectively, versus 195 ± 20 fs and 8.1 ± 0.2 ps, respectively, for the silicon thin film. The reduced scattering rates observed in the nanoparticles are consistent with the phonon bottleneck hypothesis.

5.1 Introduction

Silicon is a ubiquitous material in the solar energy industry, providing an estimated 90% of the global photovoltaic market installed base.[268, 269] Efforts to increase the efficiency of single-junction silicon solar cells are nearing the 29.43% maximum theoretical efficiency

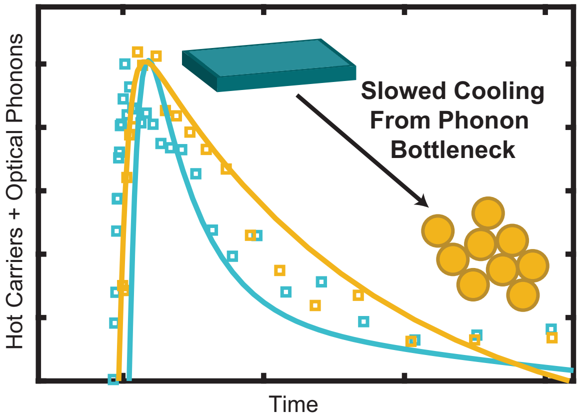

Figure 5.1: A visualization of the slowed carrier cooling time after photoexcitation in the silicon nanoparticles sample when compared to the silicon thin film sample.

limit.[270] One proposal to surpass the theoretical efficiency limit of single-junction silicon is to create stable long-lived hot carriers by altering their thermalization and decay channels so that their excess energy may be harvested in a hot carrier solar cell.[271–273] Hot carriers in semiconductors lose the majority of their heat through phonon emission,[271] and phonon density of state engineering is considered a promising route for improved efficiency. Theoretical studies show that silicon nanoparticles exhibit a reduced phonon density of states[49, 274] and lower thermal conductivity[275] than bulk silicon, in particular at the lower end of the frequency spectrum.[276] For particles less than a few hundred nanometers in any dimension, the low-frequency acoustic phonon density of states becomes altered, preventing heat dissipation and reducing the coupling with other phonon branches.[50] The loss of these low-frequency acoustic phonon modes could slow the decay of the higher-frequency optical phonons leading to a buildup of hot optical phonons after light excitation, a so-called "phonon bottleneck".[277] Fast carrier re-excitation in silicon nanoparticles by hot phonons means that long-lived optical phonons should produce longer-lived hot carriers.[278] Therefore, the phonon bottleneck is hypothesized to slow both the phonon-phonon and carrier-phonon scattering.

Measuring the relationship between the phonon decay mechanisms and hot carrier lifetime in silicon nanoparticles requires simultaneous observation of electronic and structural changes over time. Extreme ultraviolet (XUV) transient absorption spectroscopy makes this possible using a probe pulse in the XUV regime to measure core-level electronic transitions to characterize the occupancies and structural features of the valence and conduction bands. Promoting electrons from the silicon 2p orbital to unoccupied states creates localized core hole excitons that impart interpretable structural information on the XUV absorption spectra.[56, 279] The femtosecond resolution of the technique allows for the observation of short-lived excited carrier and phonon states.[280]

In the experiments presented in this chapter, XUV transient absorption spectroscopy is used to measure the electronic and structural dynamics in 200 nm thick single-crystal silicon (100) thin films, which exhibit bulklike properties, and 100 nm diameter, ∼16 nm crystalline grain size, polycrystalline silicon nanoparticles, presumed to have a confined phonon distribution. The goal is to quantify the relationship between dimensional confinement and hot carrier and phonon relaxation. Both samples are pumped with ∼35 fs pulses of 800 nm light, which excites electrons across the indirect transition into the conduction band Δ valley,[56] to create excited carrier densities of 2×10^{19} and 6×10^{19} cm^{-3} for the nanoparticle and thin film, respectively. The measurements yield values for the carrier-phonon and phonon-phonon scattering lifetimes, which are 195 ± 20 and 8.1 ± 0.2 ps, respectively, for the thin film, and 870 ± 40 and 17.5 ± 0.3 ps, respectively, for the nanoparticles. The longer phonon-phonon lifetime for the polycrystalline nanoparticles is indicative of lower heat transport and, together with the longer carrier-phonon lifetime, suggests a phonon bottleneck caused by acoustic phonon confinement.

5.2 Methods

Sample Preparation

Silicon nanoparticles of nominal 100 nm diameters (undoped) with n-hexadecylamine ligands suspended in ethanol (1 mg/mL, Meliorum Technologies) were drop cast (two drops, 0.03 mg in 0.03 mL) onto 50 nm thick (3 mm × 3 mm) diamond X-ray membranes (Applied Diamond, Inc.). The thickness of the layer is estimated to be ∼0.05 μm based on a comparison of XUV absorbance to tabulated values of silicon in literature, implying a surface coverage of approximately 50%.[206] Single-crystal silicon (100) thin-film samples (200 nm thick × 3 mm × 3 mm, B-doped, $10^{15}/\text{cm}^3$, Norcada) were used as purchased; undoped silicon films were unavailable. This doping level is 5 orders of magnitude lower than the excitation density and should therefore have little effect on the dynamics.

XUV Static Absorption

Ground-state XUV spectra were measured using an XUV supercontinuum produced by the high harmonic generation of near single-cycle laser pulses in neon high harmonic gas. In brief, 25 fs long carrier-envelope phase-stabilized pulses centered at 790 nm, produced by a 1 kHz Ti:Sapphire chirped-pulse amplifier, were focused into a 1 m long hollow-core fiber filled with 1 bar of neon to broaden the spectrum by self-phase modulation, covering 500—1000 nm, and then compressed using chirped mirrors (PC70, Ultrafast Innovations) and a 2 mm thick ammonium dihydrogen phosphate crystal to obtain <4 fs pulse duration.[281] The near single-cycle pulses were subsequently focused into a 1 mm long gas cell filled with 160 Torr of neon to generate the XUV supercontinuum ranging between 60 and 110 eV. The spectrometer is calibrated using $M_{4,5}$ edges of Kr,[282] $L_{2,3}$ edges of Al, and $L_{2,3}$ edges of single-crystalline Si. The measurement was performed on four separate nanoparticle drop-cast samples and one thin-film sample. The nanoparticle static spectrum reproduced here and analyzed below is for the sample with the highest signal-to-noise ratio in the transient measurement.

XUV Transient Absorption Spectra

Transient XUV absorption spectra were measured using a near-infrared pump and a structured XUV continuum probe produced via high harmonic generation (HHG) with 35 fs pulses centered at 800 nm with a 32 nm bandwidth from a 1 kHz Ti:Sapphire chirped-pulse amplifier.[283] The setup used for transient measurements was different than that used for the static absorption due to its narrower excitation pulse bandwidth, allowing for carriers to be excited into a particular valley in the band structure. The 3.5 mJ beam produced by the amplifier is split 30/70 into a pump and probe arm, respectively, and part of the probe arm flux is also converted into 400 nm light through in-line second harmonic generation.[229] The XUV probe spectrum is produced by focusing the 800 nm and 400 nm into a 40 cm long semi-infinite gas cell with approximately 250 Torr (3.3×10^4 Pa) helium gas, generating even and odd harmonics from 70 to 120 eV. The XUV probe is focused onto the sample with a spot size of 200 μm and then onto a variable line-space grating (35—110 eV), creating a dispersed spectrum that is measured by an XUV charge-coupled device camera (PIXIS-400, Princeton Instruments).

The 800 ± 16 nm pump arm is obtained directly from the beam splitter and routed through a retroreflector mounted on a delay stage to achieve time delays of -1 ps to 360 ps before passing through the sample with a spot size of 500 μm. The instrument response function at these wavelengths is approximately 50 fs. The fluence of the 800 nm pump beam was set to achieve a transient change in the XUV signal between 5—10 mOD. The carrier density was estimated to be 2×10^{19} carriers/cm^3 for the nanoparticle sample and 6×10^{19} carriers/cm^3 for the thin-film sample using tabulated reflectance and absorption coefficient values.[56, 284] To minimize thermal expansion, both samples were subjected to raster scanning (100 μm steps) between camera exposures, with each 0.3 s exposure capturing approximately 300 pulses (1 kHz repetition). To minimize laser ablation of the sample, the nanoparticles were further subjected to a dry nitrogen gas, room temperature cooling stream.[283] The measurement was repeated for one thin-film sample and four separate nanoparticle drop-cast samples, 2 or 3 times for each sample, and the nanoparticle measurement with the highest signal-to-noise ratio is reproduced below and used for analysis. All of the nanoparticle transient measurements captured the same qualitative signals, but differences in the local thickness of the drop-cast distributions created differences in the signal-to-noise that could not be improved by averaging scans together.

5.3 Results

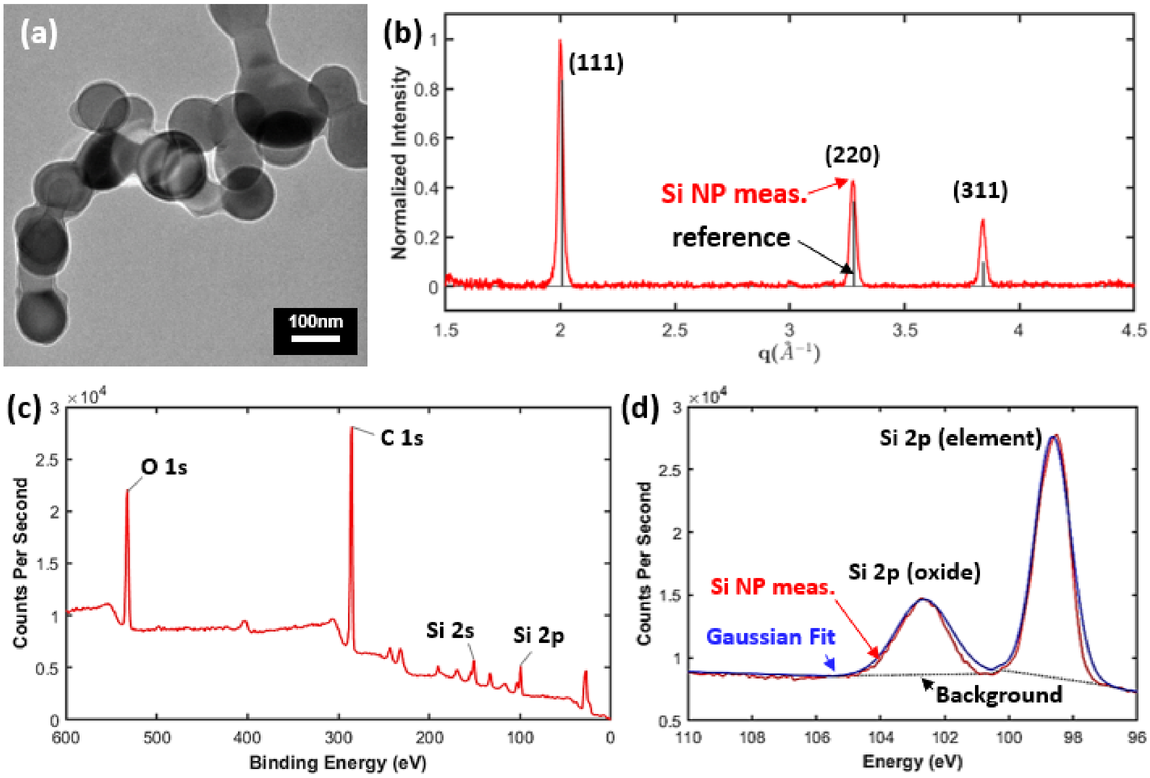

Figure 5.2: a) Transmission electron microscopy image of the silicon nanoparticle sample obtained from Meliorum Technologies, which confirms the 100 nm particle diameter and nonuniform shape. b) Powder X-ray diffraction measurement recorded here for the silicon nanoparticles (red), shown with the stick spectrum of Si taken by Downs et al. (black).[285] c) X-ray photoelectron spectrum of the silicon nanoparticle sample. The major peaks are marked based on literature values of atomic X-ray photoelectron spectra.[286] d) Expanded scale elemental silicon 2p and silicon oxide 2p peaks of the X-ray photoelectron spectra (red). The peaks are fit using a Gaussian function (blue), and the background is subtracted (dotted black).

The average diameter of the silicon nanoparticles is determined to be in the range of 100 nm from transmission electron microscopy studies (Figure 5.2a). The lack of observable lattice fringes suggests that the nanoparticles may be polycrystalline or amorphous in nature. Powder X-ray diffraction data of the nanoparticles are compared to results of previous diffraction studies performed on silicon,[285] which confirms that the particles contain crystalline Si (Figure 5.2b). The average crystallite size is estimated to be 16.3 ± 1.6 nm by fitting the Si diffraction peaks at 2.001, 3.274, and 3.84 $\AA^{-1}$ to Gaussian functions to determine the full width at half-maximum (FWHM) and then solving the Scherrer equation modified for q-space.[288] X-ray photoelectron spectroscopy was performed (Figure 5.2c), and the Si

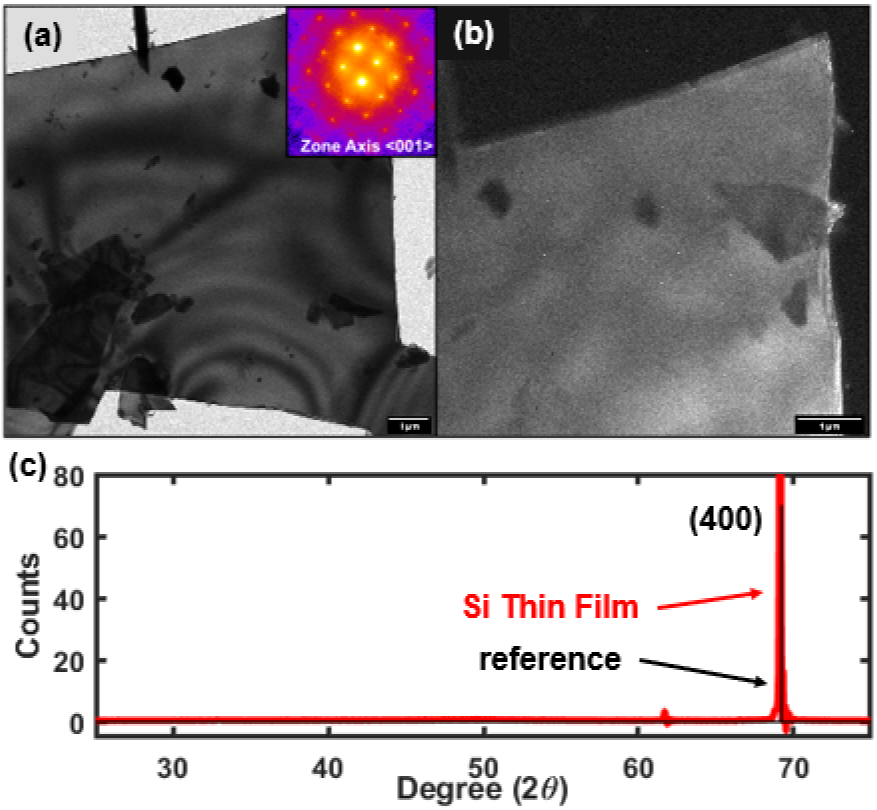

Figure 5.3: a) Bright Field TEM image of a flake of the Si thin film sample, with (inset) electron diffraction pattern indicating the ⟨001⟩ orientation of the entire thin film flake. b) Dark Field TEM image of the thin film using the (004) diffraction peak shows that the entire membrane flake is a large single crystal domain. c) X-ray diffraction of the thin film sample (red) shows only the silicon (400) peak, which is expected for a ⟨001⟩ oriented crystal. The reference XRD pattern shown is taken from Sun et al. (black).[287]

2p peak shows contributions from elemental silicon and silicon oxide (Figure 5.2d). To determine the thickness of the silicon dioxide layer, which is estimated to be sub-2 nm, the areas of the peaks were compared by fitting them to Gaussian functions and subtracting the background. The transmission electron microscopy (TEM) and X-ray photoelectron measurements were performed on four nanoparticle samples, and the X-ray diffraction measurements were repeated on two nanoparticle samples, all with identical results. Similar transmission electron microscopy and powder X-ray diffraction were each performed once on the silicon (100) thin-film samples (Figure 5.3). Electron diffraction and dark-field imaging confirm that the films are single crystals with (100) orientation. Both the particles and thin film were exposed to air, so they are likely oxidized at the surface, and the major defect at the nanoparticle grain boundaries is dangling Si bonds.[289]

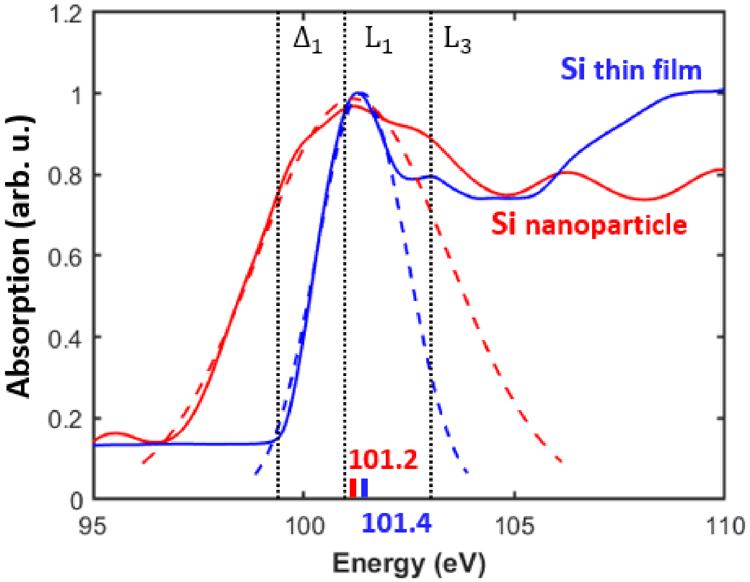

Figure 5.4: XUV ground-state absorption spectrum of silicon nanoparticles (red) and of the 200 nm silicon (100) thin film (blue). The initial rise in the silicon nanoparticle sample absorption versus XUV energy can be fitted with a Gaussian function centered at 101.2 eV (red mark), while the initial rise in the thin film is centered at 101.4 eV (blue mark). The locations of valleys in the bulk silicon band structure (Δ_1, L_1, L_3) are also included (black).[56] The absorbance intensities are normalized for visualization.

5.3.1 Static XUV Spectra

The static XUV absorption spectrum of the silicon $L_{2,3}$ edge is measured for the silicon nanoparticles deposited on diamond X-ray membranes (red) and for the freestanding 200 nm thick (3.0 mm × 3.0 mm) single-crystal silicon thin film (blue) (Figure 5.4). Here, we discuss the differences in the static spectra between the nanoparticles and single-crystalline thin film to provide the information needed to interpret the transient spectra. The edge onset can be fitted with a Gaussian to the low-energy rising edge of the lowest energy silicon feature (dashed red for the nanoparticles and dashed blue for the thin film). For the nanoparticles, the silicon edge occurs at 101.2 ± 0.1 eV (denoted by the red tick mark) and has a peak width of ~5 eV, while the silicon edge of the thin film occurs at 101.4 ± 0.1 eV (blue tick mark) and has a width of ~2.5 eV. These edge onset energies are shifted with respect to the X-ray photoelectron spectroscopy (XPS) silicon peak because the transition final state is different for an absorption vs emission process.[290] The broad line widths observed in both samples are the result of the extremely short core hole lifetime of the Si $L_{2,3}$ edge, which induces broadening on the order of several electronvolts, and by limits set by instrument resolution, on the order of tenths of an eV.[56]

Differences in properties between the two samples can explain the increased broadening and small red shift at the edge onset and the differences at higher energies observed in the XUV spectrum of the polycrystalline silicon nanoparticles. Polycrystalline Si/SiO$_x$ particles experience quantum confinement of carriers only at much smaller grain sizes (sub-5 nm), so a size-dependent blue shift in the XUV spectrum is not expected or observed from this effect.[291, 292] Instead, the small domain sizes are likely responsible for the increased broadening observed in the nanoparticles due to the increased abundance of grain boundary states. For all bonding interactions involving silicon atoms at a grain boundary, the energy of the interaction depends on the geometric and orbital configurations of the atoms, which is inhomogeneous throughout the nanoparticle.[289] These variations in bond lengths and angles lead to vacant states of various energies localized at the boundary, which has been shown to increase the broadening of the 2p core-level spectrum by nearly double the intrinsic broadening caused by state lifetime and instrument resolution.[293] Furthermore, the grain boundary states, as well as the Si/SiO$_x$ surface states that have energies in the band gap, contribute to the observed red shift.[289, 294, 295] In related optical measurements, the absorption energy can be red-shifted by tenths of an eV as the crystalline domain sizes decrease[296] and defect density increases.[297]

At higher energies above the edge onset, the silicon $L_{2,3}$ absorption spectra include contributions from the core hole modified valence and conduction bands, as well as lattice strain and increased dielectric screening at higher energies.[56] The band structure is sensitive to bonding geometry and strain, and as such silicon atoms on the grain boundaries or surfaces of the nanoparticles will exhibit altered valence and conduction band densities of states. These in turn interact differently with the Si 2p core hole, introducing features in the XUV spectrum, which may explain the appearance of the peak at $\sim$107 eV in the nanoparticle spectrum. Other explanations are surface scattering of the excited electron or certain defect and surface states, including silicon hydride bonds[293] and silicon oxide bonds in the sub-2 nm silicon oxide layer, which may open up states above the conduction band.

5.3.2 Transient XUV Spectra

The XUV transient differential absorption spectra after 800 nm optical excitation were measured for the silicon thin film (Figure 5.5a) and silicon nanoparticles (Figure 5.5b) from 0 to 200 ps. An 800 nm excitation is chosen to match the energy of the indirect transition into the Δ valley, which is the lowest energy band structure critical point because this keeps the relaxation dynamics simple by eliminating intervalley relaxation.[56] Carriers are excited at the X symmetry point with an excess energy of 0.35 ± 0.03 eV above the Δ_1 conduction band minimum. The samples are excited to similar carrier densities, approximately 2×10^{19} cm^{-3} for the nanoparticles and 6×10^{19} cm^{-3} for the film, to ensure that similar dynamics are being compared. Higher carrier densities are not used because the nanoparticles cannot dissipate the excess heat and destroy the substrate membrane at densities above 1×10^{20} cm^{-3}. The transient colormaps are plotted here with a logarithmic time axis to show more clearly the changing spectral features at early times, but the logarithmic time axis obscures timescales and makes it difficult to visually compare the decay rates. To highlight certain

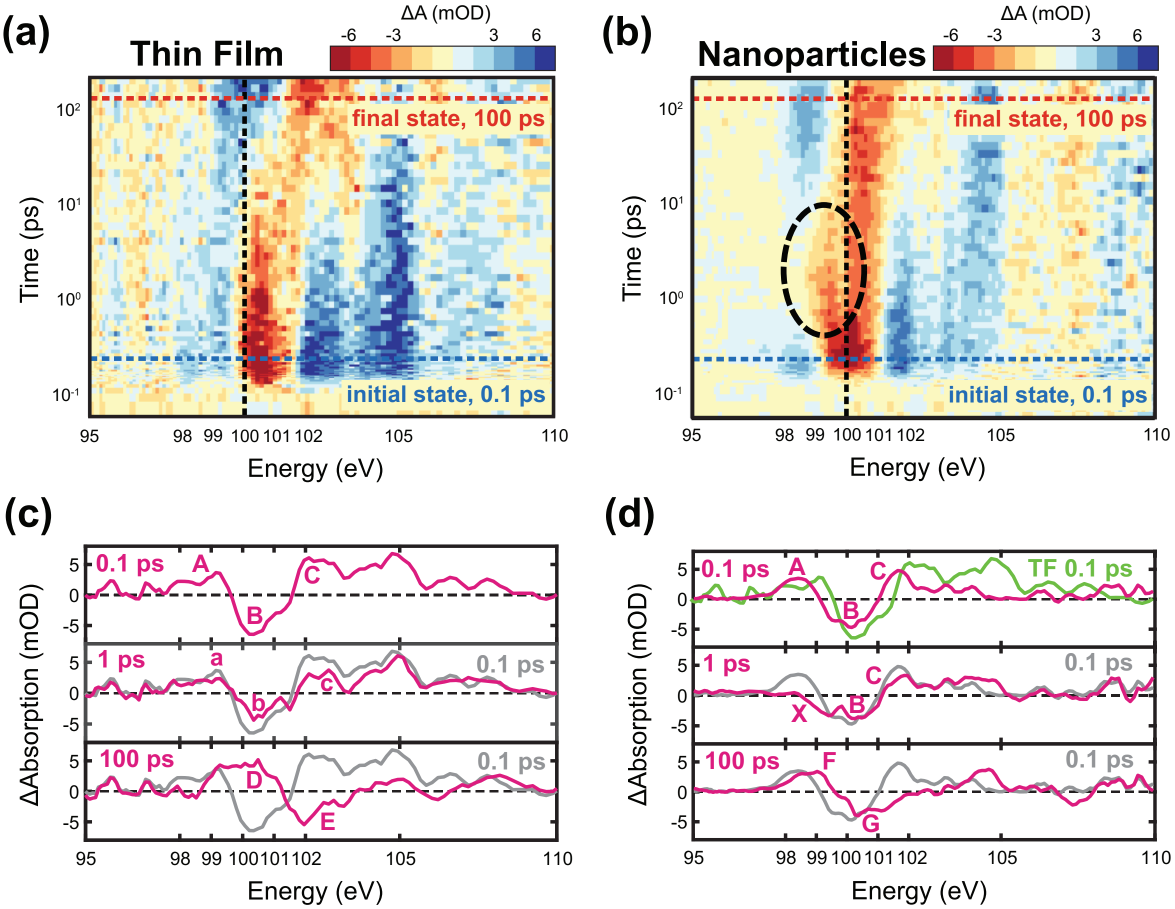

Figure 5.5: Transient XUV differential absorption spectra of the a) silicon thin film and b) silicon nanoparticles after 800 nm photoexcitation for the first 200 ps. The transient maps are shown with a logarithmic time axis, offset by +100 fs for visual clarity. The horizontal dotted lines represent the states used for multivariate regression analysis, with the dotted blue line representing the "initial state" at 0.1 ps and the dotted red representing the "final state" at 100 ps. The vertical dotted lines at 100 eV help visualize small shifts in the features. The feature in b) highlighted by the dashed black circle is explained in the text. Lineouts at three important timescales are presented below each figure to highlight the spectral features of the c) thin film and d) nanoparticles, which are labeled in magenta letters and detailed in the text. Each of the magenta lineouts, taken at approximately 0.1, 1, and 100 ps after excitation, is the average of the nearest five time slices. In the middle and bottom panels, the 0.1 ps lineout for each respective sample is displayed in gray to visualize changes to the differential spectra. In the top panel of d), the green line labeled "TF 0.1 ps" is the thin-film differential spectrum at 0.1 ps.

features, spectral lineouts are plotted (Figure 5.5c,d) of the average of the five time points surrounding 0.1, 1, and 100 ps. The most prominent effects on the transient spectra occur in the near-edge region (98—102 eV).

At 0.1 ps, immediately after photoexcitation, the thin-film differential spectrum (Figure 5.5c, top panel) has an increase in absorption centered at 99 eV labeled feature A, a decrease in absorption at ∼100.5 eV labeled feature B, and positive signals above 102 eV labeled feature C. In the nanoparticle spectrum taken at 0.1 ps after excitation (Figure 5.5d, top panel, magenta), the same three features are also observed, albeit with a slight red shift and less intensity in the >100 eV features. To compare these two spectra more easily, the thin film 0.1 ps spectrum is plotted in the top panel of Figure 5.5d in green, labeled "TF 0.1 ps". The increase in absorption labeled A that occurs at 99 eV in the thin film is closer to 98.5 eV in the nanoparticles, and the negative peak labeled B is located at 100.5 eV in the thin film and ∼100 eV in the nanoparticles. This red shift between the nanoparticle and thin-film differential spectra is expected due to the initially red-shifted and broadened onset of the absorption peak in the static ground-state spectrum of the nanoparticles (Figure 5.4). Additionally, the differences in the higher-energy features between the thin film and nanoparticles may be explained by the differences in the static spectra.

At 1 ps, an overall decrease in the magnitude of the features is observed in the thin-film transient spectrum (Figure 5.5c, middle panel, magenta) when compared to the spectrum at 0.1 ps (gray). The spectral features are therefore labeled with lowercase letters a, b, and c to denote the intensity decrease. On the other hand, the nanoparticle transient spectrum at this time (Figure 5.5d, middle panel, magenta) exhibits a broadening on the low-energy side of the negative feature centered at ∼100 eV, labeled X, when compared to the 0.1 ps spectrum (gray), and there is no decrease in the magnitude of the higher-energy B and C features. This new low-energy feature, indicated on the transient colormap (Figure 5.5b) by the black dashed circle, appears as a new decrease in absorption at ∼99 eV, and then it disappears from the spectrum within 10 ps. By 100 ps, the thin-film transient signal (Figure 5.5c, bottom panel, magenta) exhibits a positive feature at ∼100.5 eV labeled feature D, and a negative feature at ∼103 eV labeled feature E. These features appear at the same energies as the B and C features in the 0.1 ps spectrum (gray), respectively, but have opposite signs. In the nanoparticle transient signal at 100 ps (Figure 5.5d, bottom panel, magenta), large changes in the intensity and sign of the peaks are not observed when compared to the 0.1 ps spectrum (gray). The near-edge features from 98 to 102 eV, labeled F for the positive signal at 99 eV and G for the negative signal at 100.5 eV, exhibit a ∼0.5 eV blue shift from the A and B features of the 0.1 ps spectrum. These shifts are significantly smaller than the >2 eV shift of the negative peak position in the thin-film spectra from the B feature at 0.1 ps to the E feature at 100 ps (Figure 5.5c, bottom panel).

Before assigning these observed spectral changes to processes in the samples, we first present the expected dynamics for a crystalline silicon sample. After photoexcitation into the Δ valley, charge carriers in single-crystal silicon quickly form a hot thermal population within the 35 fs excitation pulse duration.[298] The new charge distribution in the conduc-

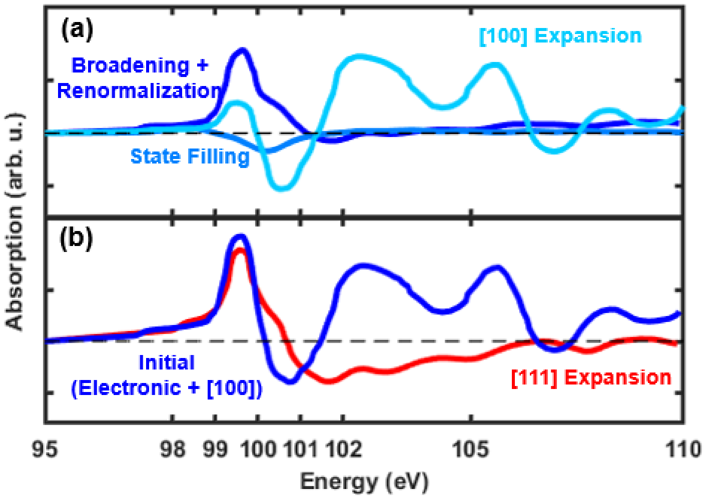

Figure 5.6: Modeled transient differential spectral signatures of the different components of the thin film Si $L_{2,3}$ edge response, taken from Cushing et al.[53] a) The electronic components of state filling (medium blue) and broadening and renormalization caused by the core hole (dark blue) are shown for a carrier density of 1 x 10^{19} cm^{-3}. The spectral signature of the optical phonons, modeled as a [100] anisotropic lattice expansion of 5%, is shown in light blue. b) The sum of the spectral signatures shown in a) for the electronic and optical phonon components are plotted in blue. The spectral signature of the acoustic phonons, modeled as a [111] isotropic lattice expansion of 5%, is shown in red.

tion and valence bands blocks certain transitions and opens others, known as state filling, and the resulting Coulombic forces between the charged bands alter their energies, causing broadening and band gap renormalization.[56] Within the first few hundred femtoseconds, hot electrons decay to the Δ valley edge via scattering with optical phonons,[299] creating a bath of hot optical phonons with a 100—250 fs scattering timescale.[32, 300] The time resolution of the experiment prevents observation of the hot carrier population before it begins to scatter with optical phonons, so the initially measured spectrum has both a hot carrier and a hot optical phonon population. After a few picoseconds, the charge carrier population is fully thermalized to the band edge, leading to diminished effects of state filling, broadening, and renormalization, while phonon-phonon scattering of energy from the optical phonon branches to the lower-frequency acoustic phonon branches has begun, with a 2—10 ps acoustic phonon scattering time.[300, 301] By 100 ps, almost all of the excess energy pumped into the system has been funneled into the hot acoustic phonon population, which corresponds to heating of the lattice, and this state persists for nanoseconds.[302] In summary, at early timescales ($\sim$0.1 ps), the primary contributions to the transient response are electronic and hot optical phonon effects, and after about 10 ps, the response is mainly caused by hot acoustic phonons and the heated lattice.

The XUV transient absorption spectrum of the silicon thin film at the $L_{2,3}$ edge can be described by three spectral components caused by the excited carriers, hot optical phonons, and hot acoustic phonons, as demonstrated in previous studies[53, 56, 303] and reproduced in Figure 5.6 for a carrier density of 1×10^{19} cm^{-3}. The hot optical phonon effects are replicated when the DFT-based model introduced in Cushing et al.[56] includes an anisotropic lattice expansion in the [100] direction, which is the expected symmetry of intravalley scattering between the degenerate Δ valleys. Similarly, the effects on the spectrum caused by the hot acoustic phonons can be modeled with a symmetric isotropic lattice expansion ([111]), which would occur due to heating. The near-edge region contributions from both the electronic and hot optical phonon effects increase the absorption (positive signal) below 100 eV and decrease the absorption (negative signal) between 100 and 102 eV (Figure 5.6a), which is the same spectral shape as is observed in the 0.1 ps spectra of both samples (Figure 5.5c,d, top panels). Therefore, both samples exhibit hot carrier and hot optical phonon populations at 0.1 ps after photoexcitation. The acoustic phonon and heated lattice contributions to the transient spectra instead increase absorption (positive signal) below about 101 eV and decrease absorption (negative signal) between 101 and 106 eV (Figure 5.6b), which is the same spectral shape as the 100 ps thin-film spectrum (Figure 5.5c, bottom panel). Thus, the thin-film sample used here exhibits a hot acoustic phonon population 100 ps after photoexcitation. Additionally, the 1 ps spectrum of the thin film has the same spectral shape as the hot carriers and hot optical phonons, but with decreased intensity. At this timescale, the photoexcited carriers are expected to have mostly decayed via phonon emission,[278, 300] so a decrease in the intensity of spectral features is expected, as the increasing contributions from acoustic phonons cancel out the decreasing contributions from electronic changes and optical phonons.[56]

The assignment is more complex for the nanoparticle sample after 1 ps. The intensities of the features associated with hot carriers and hot optical phonons do not decrease by this timescale, implying a slower transfer of energy from the hot carriers and hot optical phonons to the acoustic phonons, and a new negative feature centered at ~99 eV appears. Because this feature occurs at energies corresponding to within the band gap and is distinct from the signals caused by the core hole mediated band gap renormalization and broadening observed at 0.1 ps, it is attributed to electrons filling gap states. As mentioned above, these states are likely to be at the grain boundaries and Si/SiO$_x$ interfaces and surfaces. A more complete assessment of this feature is included in the Discussion section. By 100 ps, the nanoparticle transient spectrum does not match the modeled spectral components of hot acoustic phonons from Cushing et al. (Figure 5.6b),[56] and instead the features appear midway between the acoustic phonon features and the 0.1 ps nanoparticle spectrum containing the electronic and optical phonon features. The negative feature that blue-shifts by >2 eV between 0.1 ps (feature B at 100.5 eV) and 100 ps (feature E at 103 eV) in the thin film (Figure 5.5c, bottom panel) only blue-shifts by ~0.5 eV over the same time interval in the nanoparticle, from feature B at 100 eV to feature G at 100.5 eV (Figure 5.5d, bottom panel). This implies that the 100 ps nanoparticle spectrum is caused by a combination of the three spectral components identified previously for the excited carrier, hot optical phonons, and acoustic phonons.[56] Thus, the nanoparticle spectrum at 100 ps can be explained as the sum of the signals caused by hot acoustic phonons plus hot carriers, hot optical phonons, or both. This indicates that, for the nanoparticle sample, long-lived hot carriers or hot optical phonons may be present for up to 100 ps because their contributions to the signal are still prominent at these timescales.

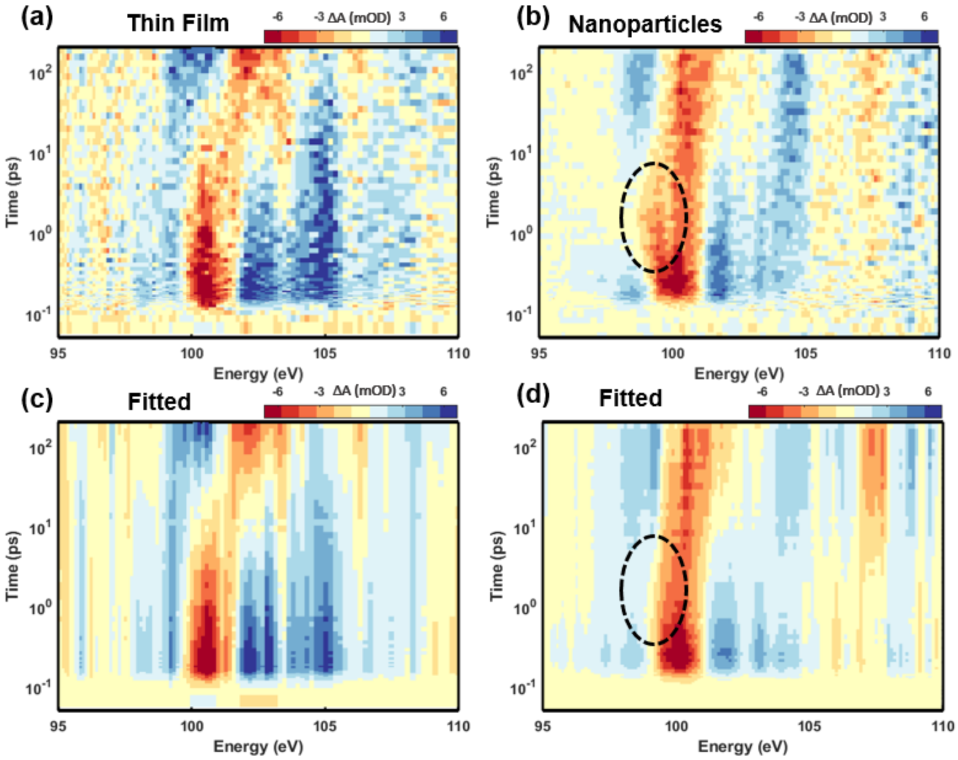

Figure 5.7: The raw transient XUV differential absorption spectra for the a) thin film and b) nanoparticle samples. These colormaps are identical to those shown in Figure 5.5a,b but without the guidelines. The results, for the c) thin film and d) nanoparticle, of the multivariate decomposition of the transient spectra into contributions from the initial and final states. Most of the features in the raw data are reproduced, except the low-energy broadening of the negative feature in the nanoparticle sample, indicated by the black dashed circles. The transient maps are shown with a logarithmic time axis out to 200 ps, offset by 100 fs for visual clarity.

5.3.3 Kinetic Modeling of the Dynamics

To quantify the timescales of the ultrafast carrier and phonon relaxation dynamics observed in the single crystal and nanoparticle samples, a multivariate regression is performed to decompose the complex transient spectra into contributions from an initial state, with hot carriers and hot optical phonons, and a final state, with a hot acoustic phonon population.

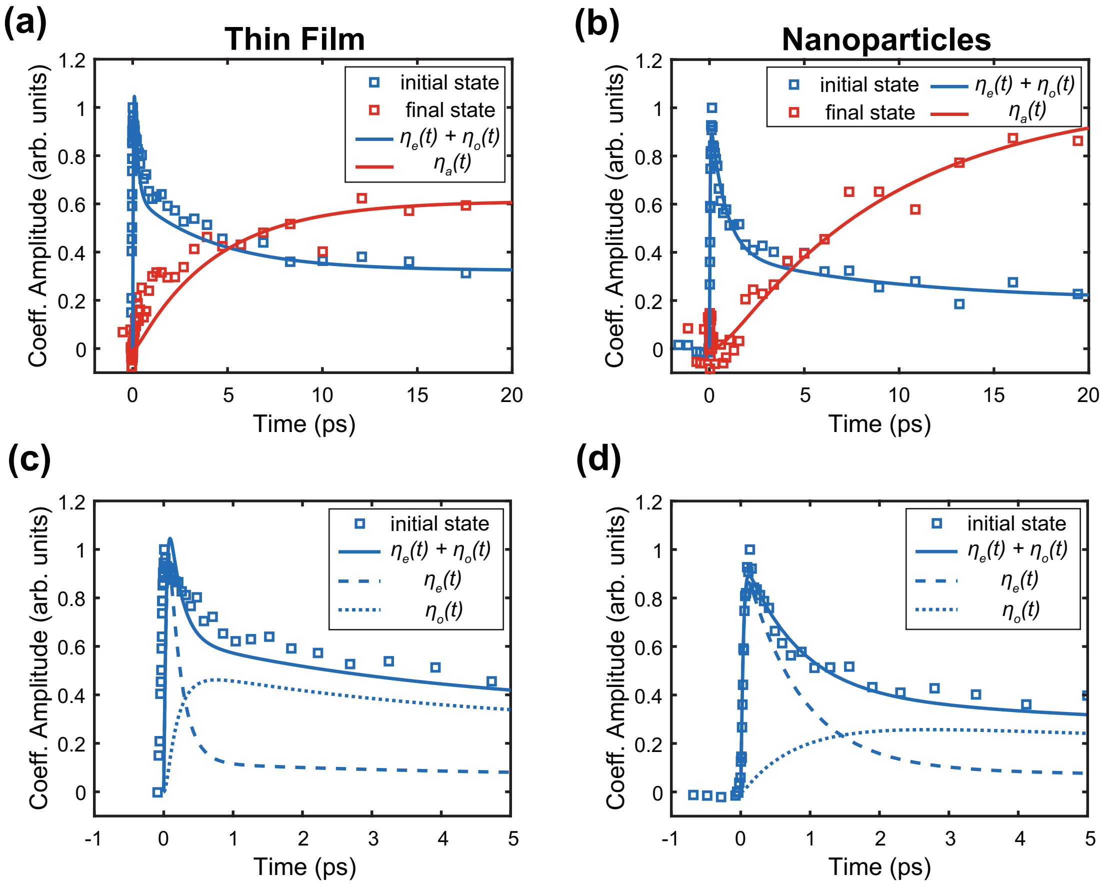

Figure 5.8: Amplitudes of the multivariate regression performed on both a) the silicon thin film and b) the nanoparticle sample for the first 20 ps are shown as the box points, blue for the initial state at 0.1 ps and red for the final state at 100 ps. The fit using the kinetic model is indicated by the solid lines. The blue lines indicate the sum of the fitted amplitudes of the hot carrier state and the hot optical phonon state, $\eta_e(t) + \eta_o(t)$, and the red lines correspond to the fitted amplitude of the acoustic phonon state, $\eta_a(t)$. Close-up early time of the initial state regression amplitudes and fits of the c) silicon thin film and d) nanoparticles are plotted for the first 5 ps to improve clarity. Boxes indicate the multivariate regression amplitude of the initial state, and the solid line is the sum $\eta_e(t) + \eta_o(t)$. The fit is decomposed into contributions from the hot carrier state fit $\eta_e(t)$ (dashed) and optical phonon state fit $\eta_o(t)$ (dotted).

These states are chosen at 0.1 and 100 ps timescales, respectively, which are indicated by the blue (initial) and red (final) dotted lines in Figure 5.5. The results of the regression fit are shown as colormaps in Figure 5.7 for the c) thin film and d) nanoparticles, plotted along with the raw data in panels a) and b), respectively. The amplitudes obtained for these states over time are denoted by the box points (blue for initial state, red for final state) in Figure 5.8a for the thin film and Figure 5.8b for the nanoparticles. This decomposition into two states, instead of three for the three hot populations (carriers, optical phonons, and acoustic phonons), is justified from the similarity between the spectra associated with hot carriers and hot optical phonons,[56] as well as the difficulty in separating the states at early times due to the limited time resolution. Although the nanoparticle state at 100 ps contains signals of all three hot populations, it persists and is unchanging for the entire 300 ps delay stage, so it is sufficient here to use this as the final state in the fit. The decrease in absorption observed near 99 eV at about 1 ps in the nanoparticle sample (black dashed circle in Figure 5.5b) is likely the result of grain boundary defect and surface carrier relaxation pathways in the polycrystalline nanoparticles. As will be discussed below, the density of these defect states is an order of magnitude below the carrier excitation density, which is too low to affect the overall carrier thermalization. Therefore, carrier decay via trap states is not included in this analysis, since neither the initial 0.1 ps spectrum nor the final 100 ps spectrum contains this negative feature, as can be seen by comparing the raw transient colormap with the multivariate regression fit (Figure 5.7).

The obtained regression amplitudes are then fit to a model to describe the carrier excitation, optical phonon scattering, and acoustic phonon scattering dynamics in both the thin film and nanoparticle samples. For laser-heated silicon, carrier and lattice decay dynamics are typically fit using a three-temperature kinetic model, in which the speed of the exchange between the three excited populations is based on the relative temperatures of the populations and the lifetime of the scattering modes.[56, 300] The heat exchange between two populations is therefore dependent on the difference in temperature between these populations, $(T_1(t) - T_2(t))$, the heat capacity, C_1, and the scattering time, τ_{12}. Thus, the three-temperature model is given by

$$C_e \frac{\partial T_e(t)}{\partial t} = N(\text{exc}) - \frac{C_e\left(T_e(t) - T_o(t)\right)}{\tau_{eo}} \tag{5.1}$$

$$C_o \frac{\partial T_o(t)}{\partial t} = \frac{C_e\left(T_e(t) - T_o(t)\right)}{\tau_{eo}} - \frac{C_o\left(T_o(t) - T_a(t)\right)}{\tau_{oa}} \tag{5.2}$$

$$C_a \frac{\partial T_a(t)}{\partial t} = \frac{C_o\left(T_o(t) - T_a(t)\right)}{\tau_{oa}} \tag{5.3}$$

where t is time, T is the population temperature, and C is the heat capacity, with the subscript e for hot carriers, o for the optical phonons, and a for the acoustic phonons. Values for the heat capacities are taken from Lee.[300] The first term in eq 5.1, $N(\text{exc})$, accounts for the initial excitation of hot carriers by the laser pulse envelope.[56] The two fitted values in this model are τ_{eo}, the lifetime of energy loss from hot carriers to optical phonons, and τ_{oa}, the lifetime of energy loss from optical phonons to acoustic phonons.[300] Direct decay of hot carriers via acoustic phonon emission is not included because the addition of this term has no effect on the fitted carrier–optical and optical–acoustic decay times. Additional processes, which are slow or have a low likelihood of occurring and are therefore below the noise floor of this measurement, have been left out of this model to allow for fewer fit parameters to be used. Auger recombination of conduction band electrons with valence holes is not included because the Auger timescale at this carrier density is very long (>100 ps).[304] Impact ionization, in which hot carrier scattering excites new hot charge carriers, is omitted because it has been shown to have an insignificant effect on the Si $L_{2,3}$ edge for similar pump fluences.[53] Thermal diffusion of carriers and lattice heat is ignored, as the addition of these terms to the model had no effect on the calculated decay times.

To apply the three-temperature model to the XUV transient spectral data, a few further modifications are included. Since there are only two states used in the multivariate regression analyses, and since the initial states at 100 fs likely comprise signals from both hot carriers and optical phonons, the amplitude of the initial state over time is treated as the linear combination of both states in the three-temperature model fit. Additionally, the average population temperatures are unknown and only the amplitudes of the regression states, η, are known. Thus, the regression amplitudes for each population, multiplied by a population weighting factor, are used instead of the temperature, as has been applied in Carneiro et al.[81] This is an acceptable simplification when solving for the average timescale of energy transfer between energy- and momentum-averaged populations, and not an energy- or momentum-specific timescale. The three-temperature model, modified to use the amplitude of the three populations instead of the temperature, is as follows

$$C_e \frac{\partial \eta_e(t)}{\partial t} = N(\mathrm{exc}) - \frac{C_e\left(\eta_e(t) - \eta_o(t)\right)}{\tau_{eo}} \tag{5.4}$$

$$C_o \frac{\partial \eta_o(t)}{\partial t} = \frac{C_e\left(\eta_e(t) - \eta_o(t)\right)}{\tau_{eo}} - \frac{C_o\left(\eta_o(t) - \eta_a(t)\right)}{\tau_{oa}} \tag{5.5}$$

$$C_a \frac{\partial \eta_a(t)}{\partial t} = \frac{C_o\left(\eta_o(t) - \eta_a(t)\right)}{\tau_{oa}} \tag{5.6}$$

where $\eta_e(t)$ is the hot carrier state amplitude, $\eta_o(t)$ is the optical phonon state amplitude, and $\eta_a(t)$ is the acoustic phonon state amplitude. The total initial state fitted amplitudes, comprising the sum of the hot carrier and optical phonon states, are given by the blue lines in Figure 5.8a,b, while the final state amplitude fits to the acoustic phonon state are the red lines. The acoustic phonon state amplitude appears to reach a plateau within 10 ps in the thin-film sample but continues to increase beyond 20 ps in the nanoparticles. As seen in Figure 5.8c for the thin film and Figure 5.8d for the silicon nanoparticle sample, the total

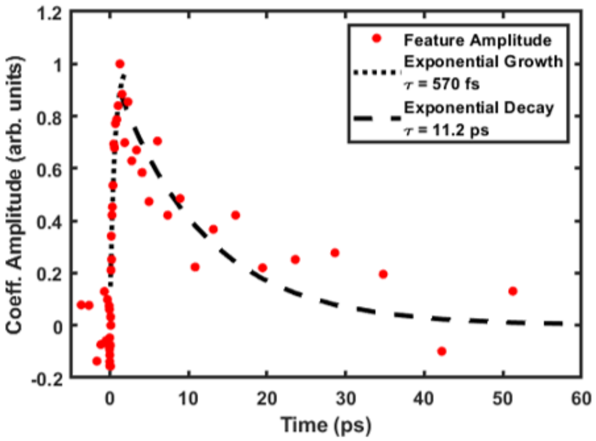

Figure 5.9: The amplitude of the 1 ps state of a 3-state multivariate regression performed on the nanoparticle sample are shown as red dots for the first 60 ps. The three states used in the regression were the 0.1 ps and 100 ps states, highlighted by dotted lines in Figure 5.5b,and the 1 ps state shown in Figure 5.5d, middle panel. The uncertainty is indicated by the scatter of the points. The fit using single exponentials of the growth and decay of this state are given by the dotted and dashed lines, respectively. The fits yield a growth time of 570 ± 60 fs and a decay time of 11.2 ± 3.4 ps.

fitted initial state (solid) is decomposed into the contributions from hot carriers (dashed) and optical phonons (dotted). The hot carrier state dominates early timescales of less than 1 ps before decaying, while the optical phonon appears and reaches a maximum within 1 ps for the thin film, but only past 2 ps for the nanoparticles, before also decaying.

Using the above model, τ_{eo} was extracted to be 195 ± 20 and 870 ± 40 fs for the thin film and nanoparticle samples, respectively, via a global fitting with multiple starting guesses (MATLAB 2018b, MultiStart). The error indicated is one standard error of the fit. τ_{oa} was calculated to be 8.1 ± 0.2 and 17.5 ± 0.3 ps for the thin film and nanoparticle samples, respectively. The values calculated for the thin-film sample agree with the previously reported values of approximately 100—250 fs for τ_{eo}[32, 300, 305] and approximately 2—10 ps for τ_{oa}.[300, 301] Even considering the range of values in various measurements, and the large uncertainty inherent in the many assumptions of this model, the lifetimes of optical phonon scattering and acoustic phonon scattering are much longer in the silicon nanoparticles. Furthermore, the slightly larger carrier excitation density used for the thin-film sample (6×10^{19} vs 2×10^{19} cm^{-3} for the nanoparticles) should have caused a longer thin-film scattering time.[305] This indicates that both hot carriers and hot optical phonons are much longer-lived in dimensionally confined polycrystalline silicon compared to single-crystalline bulk.

5.4 Discussion

Now we consider the reasons for the slowed carrier and optical phonon cooling in the nanoparticle sample. One major difference between the two samples is crystallinity, but as explained in the following calculation, the higher abundance of defects and grain boundary surface states in the nanoparticles is still much smaller than the carrier excitation density, and therefore this is not a plausible explanation for the longer-lived hot carriers and hot optical phonons in the nanoparticles. Following the model of Amit, et al.,[306] the known grain boundary surface trap state density of silicon,[307, 308] and the XRD-measured nanoparticle grain sizes of 16.3 ± 1.6 nm, the nanoparticle sample used here has a calculated grain boundary trap state density of 1—4 × 10^{18} cm^{-3}. The excited carrier density used is approximately 2 × 10^{19} carriers/cm^3, indicating that these trap states are not a majority decay channel. Instead, carrier trapping at defects and subsequent recombination occurs concurrently with phonon emission and is responsible for the distinct signal at ∼99 eV and 1 ps in the nanoparticle transient spectrum (dashed black circle in Figure 5.5b, X feature in Figure 5.5d). As discussed above, the location and sign of this feature are consistent with electrons filling vacant states right below the conduction band edge, which is the energy of the grain boundary surface states.[56] Carrier trapping into these states, which have energies in the band gap due to vacancies and the inhomogeneous bonding geometries at grain boundaries, occurs within ∼0.6—2.0 ps in nanocrystalline silicon.[309, 310] Similarly, amorphous silicon exhibits a 0.8—1 ps carrier thermalization time and a 10—30 ps recombination lifetime.[311, 312] This ∼1 ps trapping timescale and ∼10 ps recombination is similar to the timescales of the appearance and disappearance of the negative spectral feature at ∼99 eV (Figure 5.5b, black dotted circle). Exponential fitting of the growth and decay of the feature, corresponding to the amplitude of the 1 ps time delay (Figure 5.5d, middle panel), yields a growth time of 570 ± 60 fs and a decay time of 11.2 ± 3.4 ps (Figure 5.9). While the carrier trapping timescales are very similar to the 870 ± 40 fs timescale of the nanoparticles measured here, the density of midgap grain boundary surface states is too low to attribute this timescale to trapping. Furthermore, trapping in the midgap states is unlikely to alter the measured carrier–phonon scattering in the bulk. Transient reflectivity studies of polycrystalline silicon films of different nano-sized domains ranging from 9—19 nm have shown that polycrystallinity alone does not alter carrier cooling times.[313] While those films exhibited a long-lived signal from the grain boundary surface states, the carrier decay rate by phonon emission was identical to crystalline silicon.[313] Thus, while carrier trapping by grain boundary surface states occurs sufficiently to contribute to the observed transient XUV signals, it is not the majority channel for excited carrier thermalization, and thus it is not the cause of the slowed hot carrier and hot phonon decay.

It should be noted that the approximately 10^{18} cm^{-3} defect density calculated for these nanoparticles is larger than the typical photoexcited carrier densities observed in a functioning silicon photovoltaic device under standard solar illumination.[70] In order for grain boundary surface defect trapping and recombination to remain a minority carrier decay channel in these devices, silicon nanoparticle samples with larger crystalline grains, and therefore fewer defect states, must be considered in future XUV transient absorption studies.

Now we consider the explanation for the longer scattering lifetimes measured in the silicon nanoparticles in terms of the creation of a “phonon bottleneck” due to confinement of acoustic phonon modes.[276, 277] For 100 nm particles or less like the ones studied, the acoustic phonon density of states (PDOS) is altered, leading to reduced thermal transport and diminished coupling with other phonon branches.[50] When photoexcitation of these particles produces hot optical phonons, their thermalization via acoustic phonon scattering is slowed, leading to higher-energy optical phonon states being occupied for longer periods of time. This effect is not expected in the 200 nm × 3 mm × 3 mm thin film because only one dimension is small enough to have an altered PDOS, and therefore only one of the three acoustic phonon branches is reduced. In silicon, hot optical phonons can easily impart their excess energy back into carriers, a process called phonon recycling;[278] thus long-lived hot optical phonons translate to long-lived hot carriers. In this scenario, acoustic phonon confinement increases both the phonon–phonon and carrier–phonon scattering times by re-excitations, as the heat imparted by the laser cannot be efficiently removed via thermalization. This effect has been observed in 70 nm × 200 nm single-crystal silicon nanopillars, in which the electron–phonon scattering time after 800 nm excitation is increased to 400 fs.[314] The even longer 870 ± 40 fs carrier lifetime measured in this experiment is expected as the 100 nm nanoparticles and 16 nm grains are smaller. Moreover, the longer phonon–phonon scattering lifetime measured here indicates decreased heat transport, consistent with a diminished acoustic phonon bath. Thus, the phonon bottleneck hypothesis is consistent with all of the observed dynamics.

An additional effect that may be occurring in the nanoparticle sample is confinement of the optical phonons, which occurs for particles and grains of less than 25 nm.[49] Although the silicon nanoparticles studied here have nominal 100 nm diameters, the PDOS approaches zero at grain boundaries, and therefore phonons may become confined in the 16 nm grains.[315] The result of a confined optical phonon bath is slowed carrier thermalization, which is the same result observed when a hot phonon bottleneck occurs. Thus, a reduced optical phonon density of states may be present in the nanoparticles, but its effect on the carrier thermalization cannot be confirmed by these experiments.

Conclusion

The carrier dynamics of a single-crystal silicon thin film and of polycrystalline silicon nanoparticles were measured using XUV transient absorption spectroscopy. The carrier–phonon scattering and phonon–phonon scattering lifetimes for both the thin film and the nanoparticles were calculated using a three-temperature kinetic model, with coefficients obtained by a multivariate regression of the transient spectra. The carrier–phonon and phonon–phonon scattering lifetimes for the silicon nanoparticles (870 ± 40 fs and 17.5 ± 0.3

ps, respectively) were much longer than that for the silicon thin film (195 ± 20 fs and 8.1 ± 0.2 ps, respectively). In agreement with the phonon bottleneck hypothesis, carrier–phonon and phonon–phonon scattering in the nanoparticles is slowed, and this slowing is unlikely to be the result of increased surface states and defects in the polycrystalline nanoparticles. These results support the hypothesis that there is a reduction of the low-frequency and low-energy acoustic phonon mode density of states, which severely limits the optical-to-acoustic phonon scattering, and therefore the initial carrier thermalization. Further exploration into the carrier and phonon lifetimes of different sizes and shapes of nano silicon, possible simultaneously with XUV transient absorption spectroscopy, may provide further confirmation of slowed carrier cooling when the silicon phonon bath is confined.

5.5 Appendix

XPS

X-ray photoelectron spectroscopy measurements were performed at the Imaging and Manipulation of Nanostructures Facility of the Molecular Foundry at the Lawrence Berkeley Lab. Samples were produced by drop casting the nanoparticle in ethanol solution onto sonication-cleaned tantalum foil. Measurements of the silicon 2p peak were obtained using a K-Alpha Plus XPS/UPS with a spot size of 400 μm. An ion flood gun was used to minimize surface charging. Curve fitting was performed with Thermo Scientific$^{\mathrm{TM}}$ Avantage Software.

TEM

TEM imaging was performed on a FEI Tecnai T20 S-TWIN TEM operating at 200 kV with a LaB_6 filament. TEM images of the nanoparticle samples were collected with a Gatan Orius SC200 TEM camera with a 1 second exposure time. TEM images, selected area diffraction patterns, and dark field TEM images of the thin film sample were collected with a Gatan RIO16IS camera, with the dark field images collected by placing the objective aperture around the 004 diffraction peak. Nanoparticle samples were prepared by drop casting a solution of the particles onto a carbon coated copper TEM grid (CF400-CU). The density of nanoparticles on the TEM grid is lower than that used in the XUV measurements in order to resolve the individual nanoparticles. Thin film samples were prepared by breaking the thin film membrane into small pieces using a diamond scribe and gently pressing the TEM grid into the pieces.

Powder XRD

Powder diffraction patterns of the nanocrystalline samples were obtained using a Bruker D-8 GADDS diffractometer equipped with a Co Kα source. XRD was collected in reflection geometry with an incident X-ray angle (ω) of 15°. 2D patterns were merged and integrated in the DIFFRAC.EVA software from Bruker. The 1D diffraction patterns were then converted from 2Θ to q($Å^{-1}$) to remove the X-ray wavelength dependence. Nanoparticle samples were prepared by drop casting a concentrated solution of nanocrystals on a low background ⟨510⟩ oriented silicon substrate.

Diffraction patterns of the Si(100) thin film were collected using a Bruker Phaser D2 diffractometer with Cu Kα source operated at 30 kV and 10 mA with a 160 SSD detector. Low (high) resolution diffraction patterns were collected from 25° to 75° 2Θ (68° to 71° 2Θ) with a step size of 0.04° (0.01°) and an integration time of 5s (3s) per step. Contribution from the Kα_2 diffraction was removed using the DIFFRAC.EVA software. Thin film samples were prepared by placing a silicon thin film membrane face down on a ⟨510⟩ oriented low background silicon substrate and gently pressing the corners with a diamond scribe to release it from the support frame.

Chapter 6

Conclusion

The previous three chapters delved into the details of three completed experiments performed with extreme ultraviolet transient absorption spectroscopy. In Chapter 3, XUV aided in the development of a microscopic kinetic model for small polaron formation in the iron oxides. The unique capability of XUV to measure distinct ultrafast signatures of polaron formation led to the understanding that the ligand strength and density of metal hopping sites greatly affects the rate of polaron formation and that nanostructure determines how excess electron energy slows that process. In Chapter 4, the element-specificity of XUV spectroscopy allowed unambiguous tracking of the motion of holes through a three layer metal-oxide-semiconductor nanojunction. The role of the oxide layer, previously under debate, was confirmed to slow the back diffusion of holes to the semiconductor and mediate electron-hole recombination. In Chapter 5, a phonon bottleneck was observed to slow hot carrier and phonon decay in silicon nanoparticles compared to a bulk-like single-crystalline film. The ability of XUV spectroscopy to simultaneously measure carrier and lattice dynamics corroborated separate hot carrier and lattice measurements of this system.

In this chapter, recent results on a novel ferroelectric semiconducting material, $CsGeI_3$, are presented. A description of the ferroelectric properties of this material will precede discussion of these preliminary XUV results. Evidence of hot hole cooling and recombination measured at the iodine $N_{4,5}$ edge is discussed and signatures of ultrafast lattice deformation are introduced. A possible hot carrier mediated coherent phonon along the ferroelectric displacement mode is introduced. The chapter will end with outlooks for this experiment, which include XUV measurements at the germanium and cesium edges and a proposal to perform ultrafast optical pump-X-ray diffraction probe on this material at the Linac Coherent Light Source. Finally, a selection of interesting material systems for future XUV spectroscopic investigation are proposed.

6.1 $CsGeI_3$ Preliminary Results

Halide perovskites, the class of materials that contain $CsGeI_3$, have shown extremely promising single junction solar cell conversion efficiencies, reaching a record 25.6% as of 2022 for formamidinium lead iodide ($FAPbI_3$).[316] Perovskite is a cubic crystal structure of the formula unit ABX_3. For the halide perovskites, A^+ is a cation with +1 oxidation state and may be an inorganic atom like Cs or an organic small molecule like methylammonium, B^{2+} is a metal cation with +2 oxidation state such as lead or tin, and X^- is the halide ion iodide, bromide, or chloride. The crystal structure, shown in Figure 6.1, consists of the B^{2+} cation

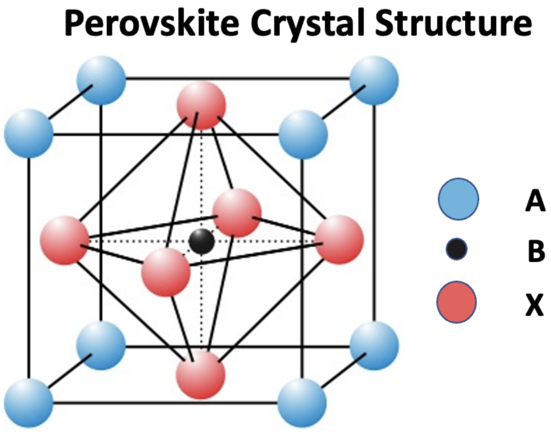

Figure 6.1: **The cubic perovskite crystal structure.** The B cation, commonly a metal with +2 oxidation state, sits in the center of the cubic unit cell surrounded by an octahedral cage of X$^-$ halide anions. The A cation, which is either an inorganic atom or small organic molecule with +1 oxidation state, sits in the interstitial spaces between the octahedra.

at the center of the cubic unit cell surrounded by an octahedral cage of X$^-$ halide anions on the faces of the cube. The A$^+$ cations sit in the interstitial spaces between the octahedral cages, which are the corners of the cube. Other formulas with this same structure, such as the oxide perovskites $A^{3+}B^{3+}O_3^{2-}$ and $A^{2+}B^{4+}O_3^{2-}$, exist and are commonly ferroelectrics used in pyroelectric, dielectric and piezoelectric application.[317]

Perovskites, especially the halide variety, are highly ionic in bonding character and may even be considered a network of ‘ionic octahedrons’.[318] Goldschmidt posited a ‘tolerance factor’ t to describe the compatibility of differently sized ions in the perovskite structure, as follows

$$t = \frac{r_A + r_X}{\sqrt{2}(r_B + r_X)} \tag{6.1}$$

where r_A, r_B and r_X are the ionic radii of the A, B and X ions, respectively.[319] When the tolerance factor equals 1, the structure is exactly cubic. A t of 0.8—1 is considered approximately cubic and is commonly called the perovskite α-phase or the black phase. A lower tolerance factor produces a nonperovskite orthorhombic structure in which the A cation is too small to stabilize the cubic structure, such as CsPbI$_3$. Higher tolerance factors produce hexagonal structures, often called the yellow phase; many of the most efficient photovoltaic perovskites, such as FAPbI$_3$ and MAPbI$_3$, exist in the black phase near or below room temperature and are easily destabilized to the yellow phase by temperature or moisture, precluding their use in commercial solar cells.[320] Alloying the perovskite with a mixture of ions, such as Cs and FA in the A site or Br and I in the X site, can produce more stable structures or more favorable band gaps.[321]

While the structural instability of halide perovskites hampers practical application, it is also the source of their exciting photovoltaic and photoluminescent properties. Lead halide perovskites exhibit properties of a ‘phonon glass electron crystal’, in which charge carriers conduct freely in the bands like a crystalline semiconductor but the phonon dispersion exhibits a high density of low frequency vibrations like those of a liquid or glass.[322] These soft phonon modes allow for large polaron formation and very effective charge screening such that carriers transport through the crystal with good mobility and high tolerance for defects.[323] The highly dynamic and disordered lattice and large polaron screening is also responsible for longer hot carrier lifetimes and reduced recombination rates.[324] Furthermore, the resilience to defects enables lead halide perovskites to be synthesized via a solution-phase drop cast method instead of the highly costly wafer synthesis of silicon cells.[325]

Protective or capping layers can overcome the long-term stability issues plaguing the lead halide perovskites,[326, 327] but they still contain lead which is toxic to humans. Efforts to identify B-site alternatives have yielded favorable solutions, such as the direct substitutes platinum and tin, or a substitution of Ag^+ and Bi^{3+} to produce a ‘double’ perovskite of the formula unit A_2AgBiX_6.[328–330] One lead replacement that has garnered recent attention is germanium Ge^{2+}, which predominantly exists in nature in the +4 oxidation state but may be stabilized as +2 in the perovskite structure.[331] The germanium halide perovskites exhibit visible light absorbing band gaps and moderate photovoltaic efficiencies,[332] but their most interesting property is their room-temperature ferroelectricity.[333] Here we present the origin and characteristics of the ferroelectricity in the germanium lead halide perovskite $CsGeI_3$ and XUV transient absorption spectroscopic results at the iodine $N_{4,5}$ edge.

6.1.1 Ferroelectric Semiconductor Properties of $CsGeI_3$

In the germanium halide perovskite crystal, the germanium ion fills the B site with an oxidation state of +2. This oxidation state is less stable than the preferred +4 that germanium usually occupies, and therefore the $CsGeX_3$ materials undergo rapid oxidation in the presence of oxygen to form CsX, GeX_4 and GeO_2.[333] Furthermore, *ab initio* calculation reveals a Born effective charge on the germanium of approximately 5—6 implying a static electronic polarization, and a lone pair localized to the germanium ion.[333] The lone pair on the germanium creates an electrostatic repulsion in the crystal, distorting away from the cubic phase into a room temperature rhombohedral structure.[334] The distortion is a germanium displacement along the <111> crystal direction by 0.318Å (Figure 6.2a). At higher temperatures above ∼290 °C, the crystal adopts the cubic phase with a Goldschmidt tolerance factor of 0.81.[335]

The static distortion produces a spontaneous electric polarization of 20 $\mu C/cm^2$, called a ferroelectric domain, in the crystal confirmed by piezo-response force microscopy (PFM) and SHG spectroscopy, as shown in Figure 6.2c taken by Zhang *et al.*, in the Peidong Yang group. The ferroelectric domains have a macroscopic polarization that is switchable via an applied electric field (Figure 6.2b). These characteristics are all hallmarks of ferroelectricity, except all other room temperature ferroelectric perovskite materials are oxides with rigid crystal

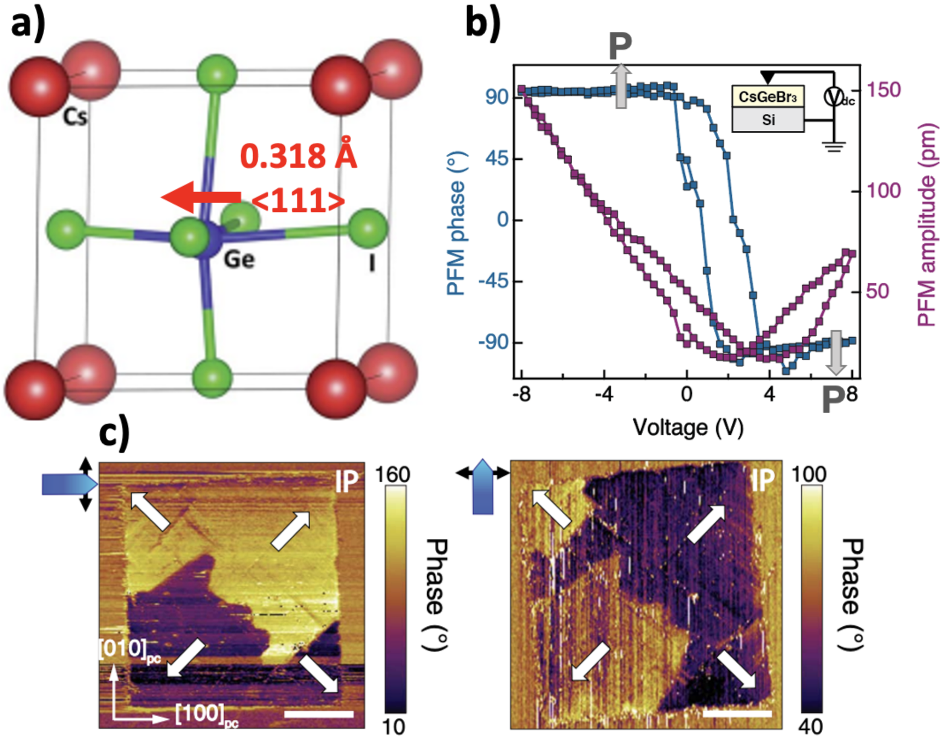

Figure 6.2: **Structure and ferroelectric properties of CsGeI$_3$.** a) A cartoon of the crystal structure of CsGeI$_3$, with the <111> distortion away from a cubic structure highlighted by the red arrow. b) Piezo-force response microscopy of a single-crystal CsGeBr$_3$ nanoplate under an applied electric field (single-crystal nanoplates of CsGeI$_3$ cannot be grown). The PFM phase and amplitude switch polarization (indicated by the light gray arrows) as the applied voltage changes. c) In-plane PFM phase images of the single-crystal CsGeBr$_3$ nanoplate show distinct ferroelectric domains. Both images shown are for the same plate but rotated 90°. The scale bar is 5 μm. Adapted from reference [333].

structures and wide insulator band gaps (except the visible light absorbing BiFeO$_3$). On the other hand, CsGeI$_3$ is a soft halide with an optical band gap of 1.6 eV.[333] The unique combination of semiconducting and ferroelectric properties in CsGeI$_3$ promise light-induced switching, which is useful for application in memory and sensing devices.[336] The built-in electric field of this semiconducting ferroelectric is an order-of-magnitude greater than in a p-n junction, allowing for a bulk photovoltaic effect (BPVE) in these materials that exceeds the Shockley-Queisser limit.[337] Aside from a classical 'ballistic'-type mechanism in which the electric field causes separation of the electrons and holes, the BPVE also separates the carriers via a quantum mechanical 'shift current' that creates a coherent electron-hole wavepacket. Coherent evolution of this wavepacket is lossless and may generate photovoltages above the band gap.[338]

Since CsGeI$_3$ has such strong coupling between its electronic and lattice degrees of freedom, we have chosen to apply the technique of XUV transient absorption spectroscopy to this system. By simultaneously probing the photoexcited carrier and lattice dynamics at each element in the crystal, a better understanding of the light-induced changes may reveal the sought after optical ferroelectric switching.

6.1.2 XUV Transient Absorption of CsGeI$_3$

The Few-Femtosecond Transient XUV Spectrometer

For this experiment, the XUV spectroscopy setup described in Chapter 2, which is located in UC Berkeley's Hildebrand Hall room D42, was not used. Instead, a setup in room D60S that produces few-femtosecond carrier-envelope phase stabilized broadband pulses to

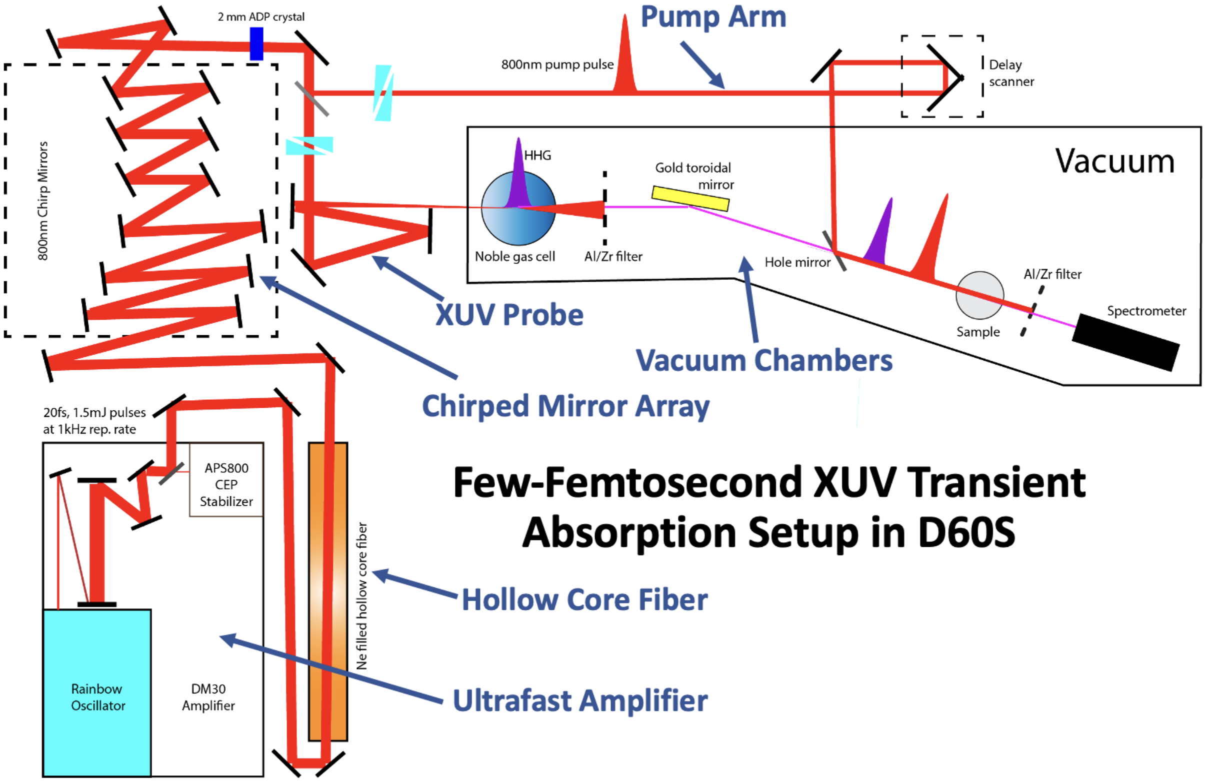

Figure 6.3: **The few-femtosecond XUV transient absorption laser system.** Major components are labeled in dark blue. The 30 fs, 1 kHz, 790 nm pulsed laser beam is produced by the Femtopower Compact Pro on the bottom left. The beam is directed through the hollow core fiber, chirped mirror assembly and ADP crystal on the top left to broaden and compress the pulses to sub-4 fs and 600—1000 nm. The beam is then split, with one portion acting as the pump and the other larger portion used to generate the continuous high-order harmonics. Both pulses are focused onto the sample inside the high vacuum system on the right, and the HHG probe is measured by the CCD spectrometer. Adapted from reference [122].

generate single-cycle continuous high harmonics is employed. This setup, which has been described previously[39, 75, 76, 78] and in great detail in the dissertation of Hung-Tzu Chang[122] utilizes a ∼30 fs pulse centered at 790 nm from a Femtopower Compact Pro Ti:sapphire multipass chirped pulse amplifier (seeded by a Femtopower Rainbow 3 oscillator). This pulse is propagated through a 250 μm hollow core fiber filled with ∼1 atm neon gas for broadening and then compressed with a chirped mirror array (PC70, Ultrafast Innovations) and ADP crystal to produce a sub-4 fs broadband 600—1000 nm pulse.

The few-femtosecond pulse is split in two, with one portion acting as the pump and the other portion sent into the high vacuum chambers to be used to generate high-order harmonics in a gas cell filled with ∼50 Torr Argon gas. The harmonics, which span 25—72 eV with an Al filter (200 μm thick, Lebow) or 70—105 eV with a Zr filter (200 μm thick, Lebow), are focused onto the sample with a toroidal mirror and then measured with a spectrometer consisting of a grating and a CCD camera (Princeton Instruments PIXIS 400B). A schematic of the experiment is shown in Figure 6.3. The continuous harmonics produced by this setup are shown in Chapter 1 in Figure 1.23.

The continuity and stability of the harmonics produced in the D60S lab allow for a higher signal-to-noise ratio in the experiment, which is evident when comparing the transient spectra in Chapters 3, 4 and 5, which were measured in D42, with the spectra presented here in Chapter 6. The D60S setup was used to measure all static (ground state) spectra shown in this dissertation. Moreover, the few-femtosecond pump duration enables the resolution of hot carrier thermalization, which is too fast to measure with the room D42 setup described in Chapter 2. But, due to the broadband nature of the D60S pump pulse, band-specific and state-specific excitation, like those described in the iron oxide experiments in Chapter 3, are not possible.

Static Absorbance at the Iodine $N_{4,5}$ Edge

The CsGeI$_3$ sample measured in the XUV transient absorption spectrometer was grown by a two-step thermal evaporation procedure.[333] First, approximately 150 nm of CsI is deposited on the Si$_3$N$_4$ substrate, followed by about 150 nm of GeI$_2$. Then, the film is annealed on a hotplate at 130 °C under Argon for 15 minutes (Figure 6.4a). An ∼350 nm film of CsGeI$_3$ is produced, confirmed by X-ray powder diffraction and profilometry (see Figure 6.4). This thickness was chosen to obtain an absorbance of approximately 0.5 OD at the iodine N$_{4,5}$ edge. SEM images show a polycrystalline film with domains of approximately 300-500 nm laterally.[339]

All three elements in CsGeI$_3$ have favorable semi-core level transition energies within the range of the XUV spectrum produced by the laser system. The Ge M$_{4,5}$ edge, which is the 3d→valence transition, is at approximately 35 eV.[129] Germanium has been studied previously with XUV transient absorption spectroscopy using this same laser system.[75, 76] The Cs N$_{4,5}$ edge, which is the 4d→valence transition, occurs near 80 eV, and the Cs O$_1$ edge, which is the 5s→valence transition, is around 20 eV. The I N$_{4,5}$ edge occurs around 45—55 eV

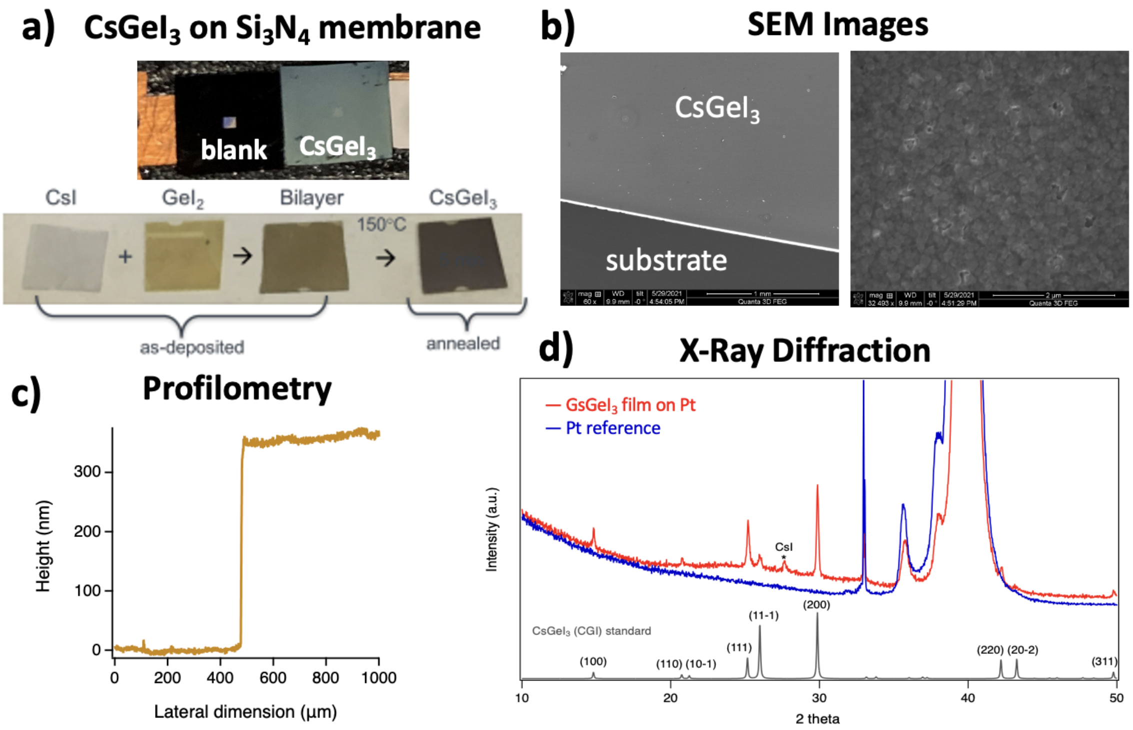

Figure 6.4: **Sample characterization of the CsGeI$_3$ thin film.** The data shown here were taken by Zhang *et al.*, in the Peidong Yang group. a) A photo of the CsGeI$_3$ thin film deposited on the Si$_3$N$_4$ membrane compared to a blank membrane on top. Below is a schematic of the two step thermal evaporation procedure. b) SEM images of the CsGeI$_3$ film deposited on silicon. The left panel has a scale bar of 1 mm and the right panel has a scale bar of 2 μm. c) Profilometry of the CsGeI$_3$ film on silicon, showing a film thickness of approximately 350 nm. d) X-ray powder diffraction of the CsGeI$_3$ film deposited on Pt in red, taken with a Cu Kα source. A Pt reference is shown in blue, and the theoretically calculated peaks for a pure CsGeI$_3$ film are shown in gray. Adapted from reference [333].

and was the elemental edge measured in previous XUV transient absorption studies of lead halide perovskites and perovskite precursors.[20, 21] It is because of these previous studies, and because the iodine $N_{4,5}$ core hole is highly screened and therefore the edge is sensitive to valence band dynamics, that we chose to measure the iodine XUV absorbance first. The Cs and Ge edges will be studied next, and expected results are described in section 6.2.1.

Before introducing the static (ground state) XUV spectrum, a brief description of the electronic band structure is presented. The band structure and electronic density of states of CsGeI$_3$ is difficult to calculate due to the large atomic number of iodine, which requires significant computer processing time and the inclusion of relativistic effects (spin-orbit coupling) to achieve the correct solution. Additionally, the reduced symmetry of the rhombohedral structure of CsGeI$_3$ causes the three iodines in each formula unit to experience three different electronic environments. Consequently, the published theoretically calculated band

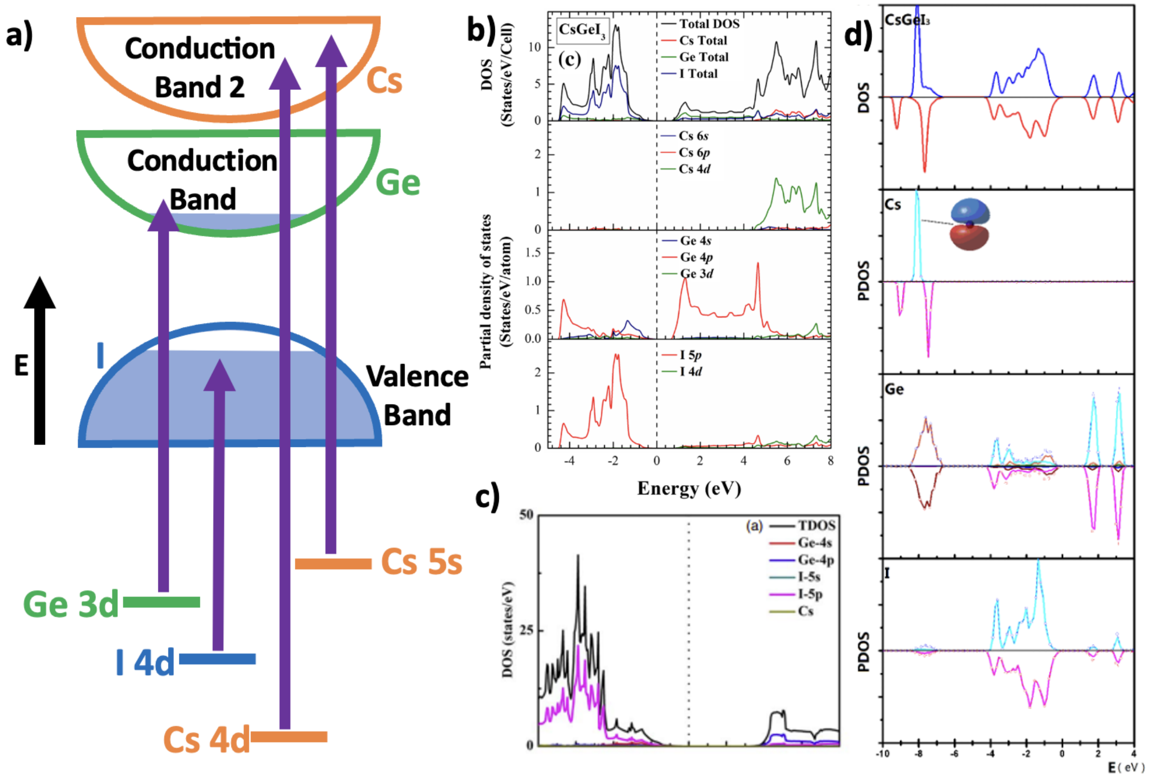

Figure 6.5: **The band structure and partial density of states of CsGeI$_3$.** a) A diagram of the semi-core levels and valence structure of CsGeI$_3$, not to scale. The predominant element character of the valence and conduction bands are indicated. b) The calculated partial density of states adapted from reference [340]. This band structure shows a Cs-dominant conduction band 4 eV above the Fermi level. c) The calculated partial density of states adapted from reference [341]. d) The calculated partial density of states adapted from reference [342]. The top panel for each element shows the calculation without spin-orbit coupling and the bottom panels include the spin-orbit coupling in the calculation. The iodine-containing conduction bands are split by ~2 eV.

structures for this material do not perfectly agree, but many of the major features are reproduced.[340–342] A few examples of the calculated element-specific partial density of states and a cartoon of the band structure of CsGeI$_3$ is shown in Figure 6.5.

Firstly, all calculated band structures severly underestimate the band gap, which is a common result for periodic semiconductor structures, but this can be overcome with hybrid functionals[343] or with a scissors correction set to the experimentally measured direct band gap of 1.6 eV.[344] Similar to the lead-based and other halide perovskites, the A site Cs$^+$ ion is not involved in the density of states near the band gap. There is moderate Cs character in higher-lying conduction bands, but calculations disagree on whether these states are 4 eV above the Fermi level[340] or more than 8 eV above the Fermi level.[341, 342] Another major similarity between CsGeI$_3$ and the other halide perovskites is the predominantly halide character of the valence band states and the predominantly B site cation (germanium) character of the conduction band states. This ligand-dominant valence band and metal-dominant conduction band fits well with the intuitive picture of polar semiconductors.[7] The calculated band structures all show small densities of iodine states in the conduction band and of germanium states in the valence band, at varying energies from the Fermi level, but these sparse states can be ignored for the rest of the analysis.

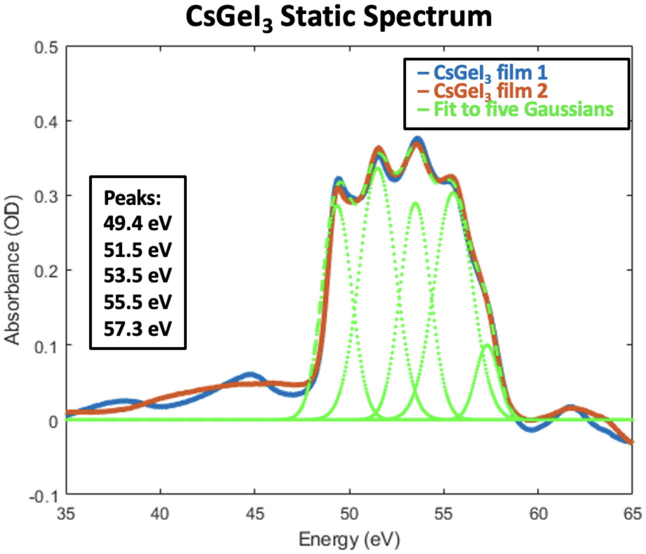

Figure 6.6: **The ground state CsGeI$_3$ XUV spectrum at the iodine edge.** The background-subtracted spectra of two identical samples are shown in red and blue. Gaussians are fitted to each of the five peaks, shown in dotted green for the individual peaks and dashed green for the sum over all peaks. The peak energies are included on the left, and are spaced roughly 2 eV apart.

The static (ground state) absorbance of the ∼350 nm CsGeI$_3$ film at the I N$_{4,5}$ edge is shown in Figure 6.6. The sharp increase in absorbance near 48 eV is the edge onset and roughly corresponds to the difference in energy between the empty valence states and the core level. The features at higher energies are caused by the local electronic environment around the atom, including higher-lying empty electronic states and the local bonding geometry. These appear as five peaks spaced approximately 2 eV apart. For the lead halide perovskites, the XUV ground state absorbance line shapes can be explained by a combination of 1) the number and energy of conduction bands with iodine character, 2) the spin-orbit coupling, which splits the I4d$_{5/2}$ and I4d$_{3/2}$ core states by ∼1.6 eV, and 3) core hole broadening.[20, 21] By this logic, the CsGeI$_3$ ground state absorbance at the iodine edge should have a total of 12 peaks caused by a combination of the two iodine-containing conduction bands spaced 2 eV apart (Figure 6.5d), the two spin-orbit split iodine 4d core levels, and the three distinct iodines in each formula unit. Therefore, we can assume that the CsGeI$_3$ ground state spectrum contains more than five peaks, but many of them are either overlapping or obscured by the core hole broadening. DFT modeling of the ground state XUV spectrum, currently in progress using the augmented plane wave DFT program The Elk Code,[345] will assist in this assignment.

Iodine Transient Absorption

The transient XUV absorbance of the CsGeI$_3$ film is measured following above-gap photoexcitation with the sub-4 fs broadband (600—1000 nm) pump. The pump photoexcites a charge transfer from the mainly iodine valence band to the mainly germanium conduction band, leaving hot holes behind on the iodine character valence band. The pump energy density is set to 10 mJ/cm^2 via attenuation with an iris. This power density was chosen because it yields a good signal-to-noise ratio without damaging the sample. The laser pulse repetition rate is reduced to 100 Hz with a chopper wheel to prevent sample heating. The differential absorbance is calculated at each time delay by taking the difference between a 'pump on' and a 'pump off' CCD camera image. Each camera image is taken with an integration time of ~1 second, and is the result of the coaddition of ~100 pulses. Following each pair of pump on-pump off measurements, the sample is translated to avoid sample damage. Correlated spectral noise caused by instability in the HHG process was removed with an edge-referencing algorithm.[346]

Four transient absorption measurements were obtained, each consisting of nearly 100 time delays and requiring 8 hours of measurement time to achieve a good signal-to-noise ratio. In

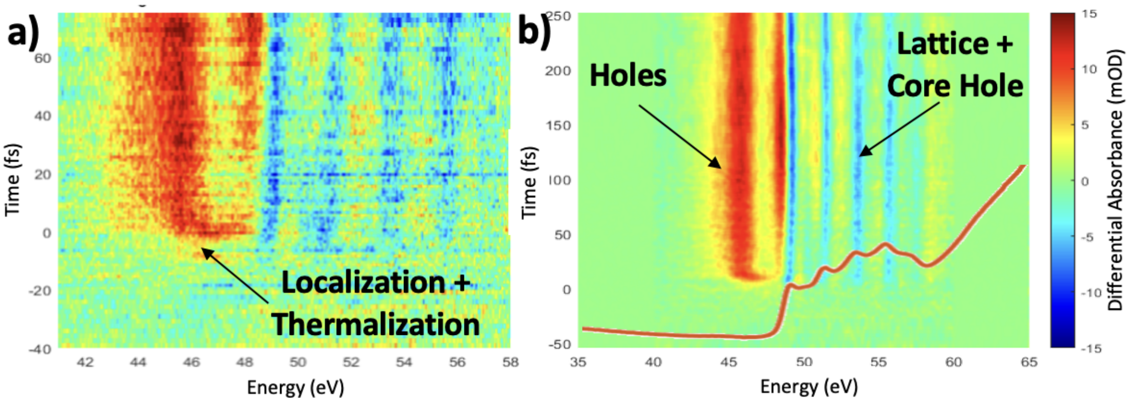

Figure 6.7: **XUV transient absorption of the CsGeI$_3$ film for the first few-hundred fs.** a) The gas-referenced (for time zero assignment) scan from -40 fs to +70 fs following photoexcitation with the sub-4 fs 600—1000 nm broadband pump. Positive differential absorbance (increase in absorbance) is red, and negative differential absorbance is blue. The below-edge positive feature and above-edge negative features all shift within 10 fs, which may be caused by hot hole localization and thermalization. b) The transient absorption color map of the scan from -50 to +250 fs. This scan shows the initial rise of the below-edge feature attributed to hot holes and of the above-edge features attributed to a combination of core hole effects and lattice distortions. The ground state absorbance is the red line.

all four measurements, distinct features appear to overlap in energy with the ground state features and a new positive feature (increase in absorbance) appears at energies below the edge onset. The below-edge feature can be assigned to new states (holes) opening up in the valence band. First, we discuss the measurement taken with the smallest time delay steps ranging from -40 to +70 fs (Figure 6.7a). In order to accurately determine the time overlap between the pump and probe, which may drift slightly over the course of this measurement, a gas cell filled with neon is measured between each scan of the full set of time delays. The doubly ionized neon states are extremely short-lived and can be used to reference the time overlap between scans. In this gas-referenced measurement, the features at and below the static iodine edge appear nearly instantaneously. A red positive feature (increase in absorbance) spanning 45—48 eV shifts within 10 fs to a narrower positive feature between 43—46 eV. Blue negative features (decrease in absorbance) above the edge onset at 48 eV shift to slightly higher energies on the same timescale. Since all of these dynamics occur within 10 fs, these features are likely caused by hot hole thermalization and localization onto the iodine.

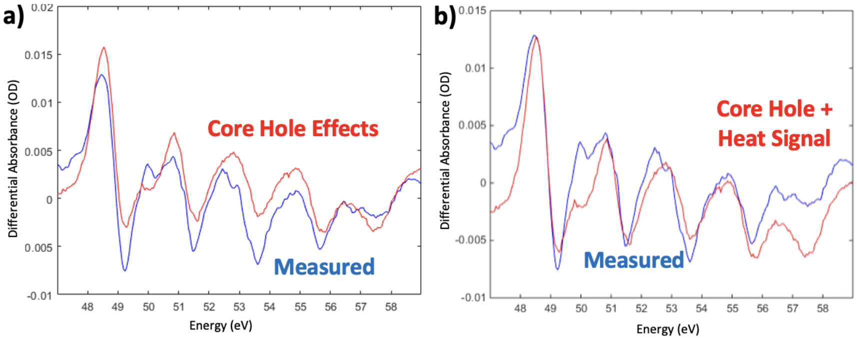

Figure 6.8: **Assignment of the above-edge features.** a) An example lineout of the above-edge features taken at approximately 200 fs delay is shown in blue. In red is the difference between the shifted, broadened and scaled static absorbance and the unmodified static absorbance from Figure 6.6 (the differential core hole effects). The feature energies line up, but the relative intensities do not match. b) The same differential absorbance lineout is shown in blue, but this time the red spectrum is the sum of the differential core hole effects and the scaled heat background (10 ms spectrum). Some relative intensities match, but the transient spectrum is still not perfectly explained.

In the next measurement, which spans -50 to +250 fs time delay (Figure 6.7b) the initial growth and decay of the below-edge positive feature and the above-edge features are more clear. The below-edge feature (45 eV) has been assigned to hot holes in the valence band. Around 48 eV there is a sharp positive-negative differential lineshape, and there are alternating positive and negative features at higher energies roughly lining up with the peaks in the static spectrum. These features appear to be the result of broadening and renormalization (red-shifting) of the band structure caused by the core hole interaction with the hot holes, but applying a shift and Gaussian broadening to the static spectrum does not accurately capture the relative peak magnitudes (see Figure 6.8a). Alternatively, these above-edge features have a similar but not identical lineshape as the differential spectrum of a heated sample (10 ms after optical pump). The hot sample spectrum is expected to be caused by lattice distortions (acoustic phonons), while the few-hundred fs spectrum shown in Figure 6.7b is expected to show features of optical phonons, which may explain why these spectra do not perfectly match (Figure 6.8b). Thus, the above-edge features may be caused by a combination of optical phonon distortions and core hole effects. Additional modeling of the optical phonon effects on the spectrum is needed to confirm this assignment.

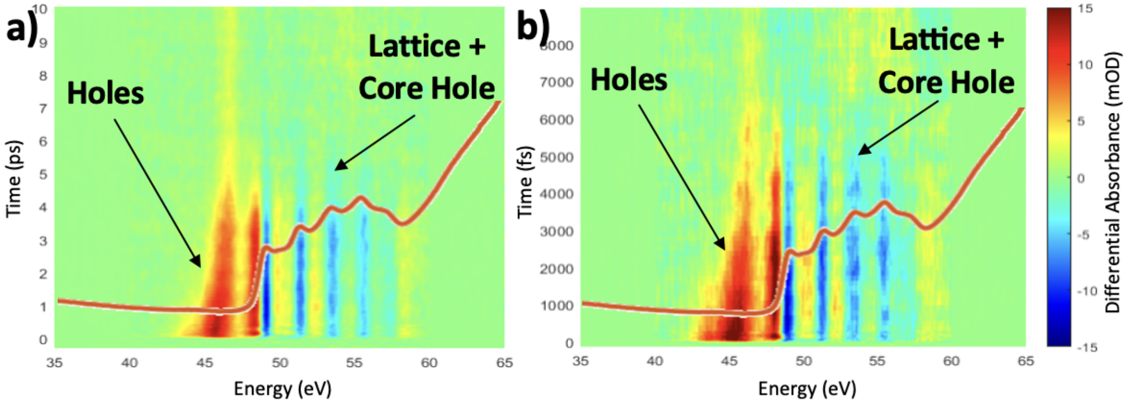

Figure 6.9: **XUV transient absorption of the CsGeI$_3$ film for the first few-ps.** a) The transient absorption color map for the scan from -300 fs to +10 ps on the sample used in the measurements shown in Figure 6.7. b) The transient absorption color map for the scan from -300 fs to +8 ps on a new sample. Positive differential absorbance is red and negative differential absorbance is blue. These scans show the decay of the below-edge hot hole feature and of the above-edge core hole and lattice distortion features. The ground state absorbance is included as the red lines.

The final two scans (Figure 6.9) were measured from -300 fs to 10 ps and from -300 fs to 8 ps, respectively. The 10 ps scan was measured using the same sample as in the previous two measurements, and the 8 ps scan was performed on a different sample of similar thickness. The decay of both the hot hole feature and the core+lattice features occur on this timescale. The hole feature is fit to a function that describes the quasi-Fermi temperature of the hot holes, similar to the fitting performed in the MAPbI$_3$ study of Vura-Weis.[21] The fit function is a convolution of the parabolic valence band density of states and the Fermi-Dirac distribution of hot holes as follows

$$f_h(E) = k \cdot \sqrt{E - E_v} \cdot \frac{1}{1 + e^{\frac{E_F - E}{k_B T}}} \tag{6.2}$$

where E is the energy variable, E_v is the valence band maximum energy, E_F is the quasi-Fermi level, k_B is the Boltzmann constant, and T is the temperature in Kelvin. k is a normalization factor to account for the intensity of the differential absorption and is set to a constant of 0.015. E_v was fixed at 46.5 eV, and E_F and T are fit at each time delay. The resulting fit at a few choice time delays is shown in Figure 6.10a, and the decay in hot hole temperature is fit with an exponential decay in Figure 6.10b to obtain a decay timescale of approximately 2.5 ps. The fitted temperatures of a few thousand Kelvin found here match the hot hole temperatures extracted for the MAPbI$_3$ sample at similar excited carrier densities, but the decay time is approximately twice as long.[21] The CsGeI$_3$ temperature decay is also slower than the similar lead-free perovskite CsSnI$_3$ at similar carrier densities.[347] CsGeI$_3$ has a larger dielectric constant, and therefore greater screening of charge carriers, which may explain the slowed hot carrier cooling.[323].

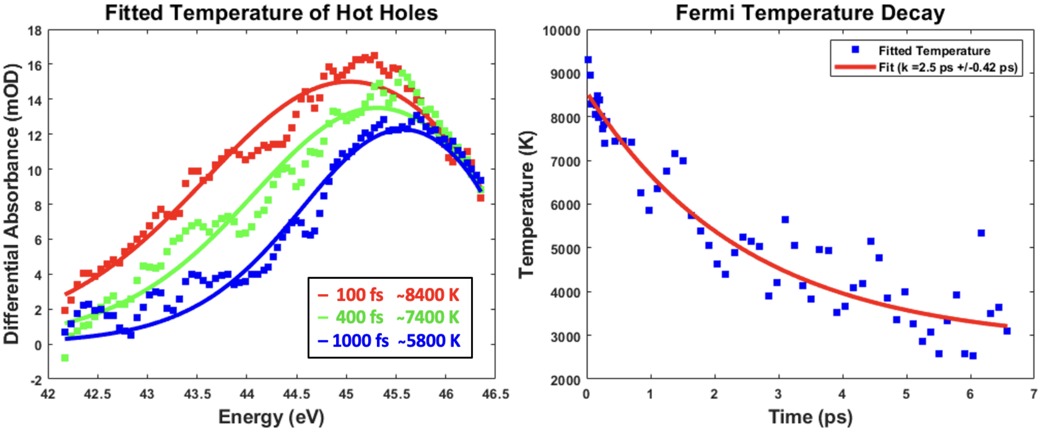

Figure 6.10: **Fitting the hot hole signal to a Fermi-Dirac distribution.** a) The fit to the quasi-Fermi temperature is shown for a few key timescales. The time and approximate temperature are indicated on the graph. b) The decay in fitted hot hole temperature (blue squares) follows an exponential (red line) with decay time of approximately 2.5 ps.

The above-edge features from 48—57 eV appear to grow and decay all together. Therefore, a simultaneous fit of these features was performed using a multivariate regression of an 'initial' state. The initial state was chosen to be the time delay with the highest intensity signals, which occurs near approximately 100 fs. The fit was performed on the raw data with the fitted core hole signal subtracted (Figure 6.11). The resulting amplitude of the initial state was fit to obtain the growth and decay timescales of these features. All the fitted time constants for both the hot hole quasi-Fermi temperature fits and the multivariate regression fits are included in Table 6.1. The rise time of the hot hole temperature is related to the thermalization time, and the initial state rise time is a convolution of the optical phonon formation time and the rise of the valence-core hole interaction.

Looking closely at the first 500 fs of the measurements shown in Figure 6.9, the above-edge features appear to shift to lower energies and then return. The amplitude of the initial state in the multivariate regression analysis also displays this signal, shown in Figure 6.12,

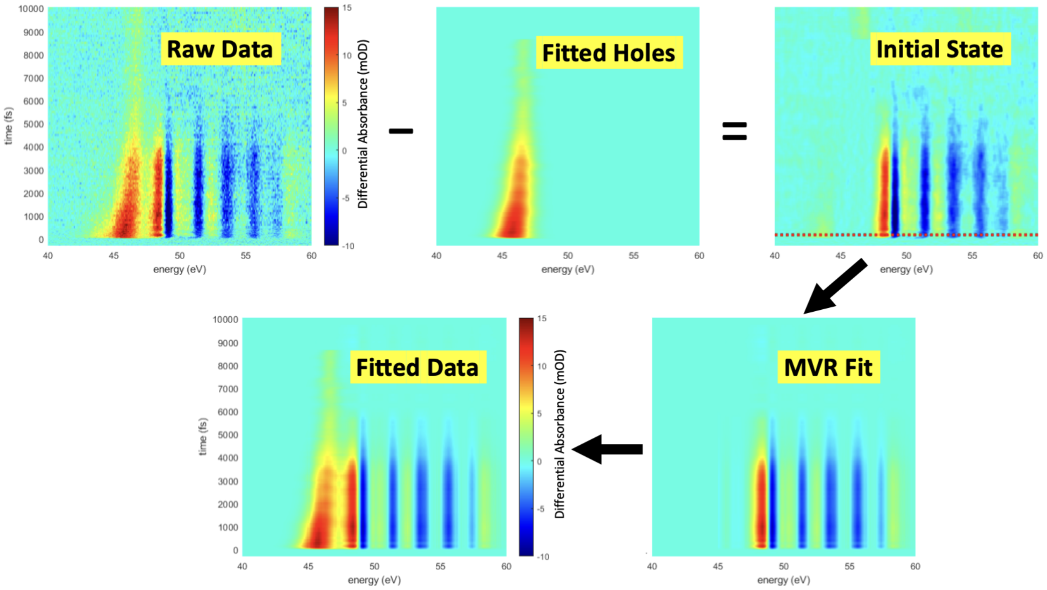

Figure 6.11: **A visualization of the multivariate regression (MVR) analysis fitting procedure.** The raw data is shown on the top left. First, the data at each time delay are fit with the quasi-Fermi temperature model from eq. 6.2, shown on the top middle. The difference, shown on the top right, is the above-edge features caused by the core hole effects and lattice distortions. These features are fit to a multivariate regression of the initial state (dotted red line). The fit result is shown on the bottom right. The sum of both the hot hole fit and the multivariate regression fit is shown on the bottom left and captures all of the features of the raw data.

which looks like a single cycle of a damped oscillation with period ~250 fs. This period matches that of the theoretically predicted a$_1$ phonon motion of the germanium ion along the <111> direction, which is the motion responsible for the ferroelectric distortion.[348] Further investigation of this possible optically-induced coherent phonon motion is discussed in section 6.2.1 as part of a proposal to use the Linac Coherent Light Source (LCLS) for femtosecond optical pump-X-ray diffraction probe measurements.

Table 6.1: The fitted time constants for the CsGeI$_3$ film at the I N$_{4,5}$ edge.

Measurement	Hole Temp. Rise Time (fs)	Hole Cooling Time (ps)	Initial State Rise (fs)	Initial State Decay (ps)
Figure 6.7b	55 ± 5	-	80 ± 10	-
Figure 6.9a	40 ± 10	2.5 ± 0.4	80 ± 10	1.5 ± 0.1[1]
Figure 6.9b	50 ± 10	3.0 ± 0.4	50 ± 10	2.7 ± 0.2[1]

[1] Fit to an error function with an offset of 4 ps.

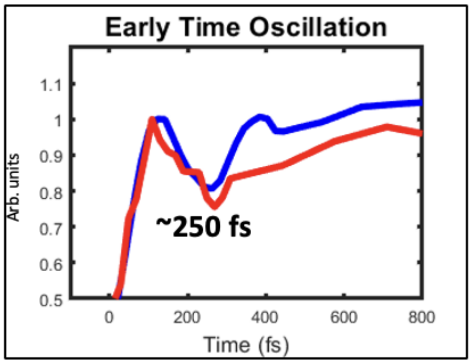

Figure 6.12: **Close up of the few hundred-fs oscillation in the above-edge features.** The blue and red curves are the amplitudes of the initial state from the multivariate regression analysis for the measurement shown in Figure 6.9a and in Figure 6.9b, respectively. Both state amplitudes show a ∼250 fs damped oscillation that begins nearly immediately after photoexcitation.

6.2 Future Directions and Outlook

Here we briefly discuss the planned XUV transient absorption experiments and proposed beamline experiments for the $CsGeI_3$ system. Then, a selection of other materials to study with extreme ultraviolet transient absorption are presented.

6.2.1 Future Experiments on $CsGeI_3$

Cs and Ge XUV Edges

As mentioned previously, the band structure of $CsGeI_3$ reveals no density of Cs states in the valence band nor in the low-lying conduction bands. The lack of Cs involvement in the states surrounding the band gap means that the transient XUV signals will not be sensitive to charge carrier fluctuations, which are also called state-filling effects. Instead, the Cs atoms will experience photoinduced lattice distortions, and the Cs $N_{4,5}$ and O_1 edges will report on these structural changes. If the rise time of the transient Cs features matches the rise of the multivariate regression from the iodine measurements, it will confirm the assignment of these features to lattice changes. Further, the presence of the ∼250 fs oscillation in the Cs edge transient will support the coherent phonon hypothesis. A simulation of the transient signal at the Cs edge, assuming both of these are true, is included in Figure 6.13. On the other hand, if neither of these signals are observed with Cs, then we can conclude that the iodine signals are artifacts of the core hole interaction with the hot holes on the iodine. Therefore, measurement of the Cs edge will be useful for the interpretation of the dynamics.

In order to measure the Cs edge, a few minor changes will need to be made to the XUV transient absorption setup. Firstly, the Cs $N_{4,5}$ edge is located around 80 eV, which is above

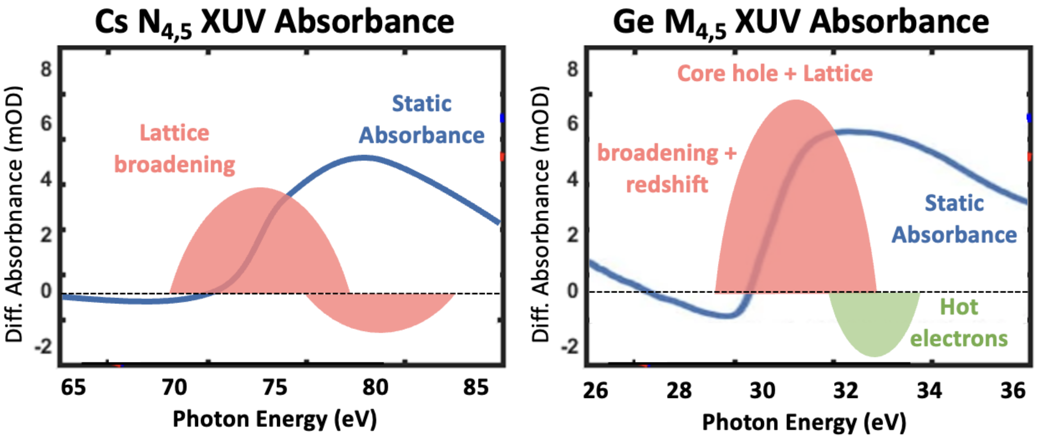

Figure 6.13: **Simulated XUV transient absorbance of the Cs $N_{4,5}$ and Ge $M_{4,5}$ edges.** On the left are the predicted transient absorption features at the Cs $N_{4,5}$ edge following above gap photoexcitation. The static absorbance shown in blue is taken from reference [129] for atomic Cs and is not to scale. The Cs will exhibit features of lattice distortions from heating, simulated as a broadening of the static spectrum. Broadening of the peak causes an increase in absorbance below the edge onset and a decrease in absorbance at the absorption maximum, shown in pink. On the right are the predicted transient absorption features at the Ge $M_{4,5}$ edge following the photoexcited hot electron transfer from iodine. The static absorbance shown in blue is taken from reference [20] for pure Ge and is not to scale. The Ge will exhibit features of lattice distortions from heating, which will broaden the spectrum. The spectrum will be further broadened due to the core hole interaction with the hot electrons, which will also cause a red-shift. The combination of these core hole and lattice features will appear as an increase in absorbance below the edge onset, shown here in pink.[20, 76] The hot electrons will appear in the transient XUV spectrum as a decrease in absorbance above the edge onset, shown in green, because they block possible transitions into the conduction band.

the energy window of the 200 μm thick Al filters used in the iodine edge measurement. These filters will need to be changed to 200 μm Zr filters, which allow the XUV spectrum above ~70 eV to pass through. Additionally, the spectrometer consisting of the grating and CCD camera will need to be angularly adjusted in order to measure the spectrum in this energy region. Finally, the high harmonic gas used in the iodine measurement was argon, which may be able to produce intense enough harmonics near the Cs edge. If not, then the gas can be changed to neon, which has a larger ionization potential and therefore a higher cutoff energy. Changing the HHG gas may require adjustment of the driving field focusing optics.

Measuring the Ge edge will require its own changes to the XUV transient absorption setup. The germanium $M_{4,5}$ edge is near 35 eV and the Al filters used for the iodine measurement will allow these wavelengths to pass through. Unfortunately the Al filters will not block the second order diffraction of the high energy harmonics near 70 eV, which will overlap with the first order diffraction of the 35 eV harmonics and confuse the measurement. Therefore, they must be replaced with Ti filters. The argon HHG gas will not produce sufficient XUV flux in this energy region, so a gas with a smaller ionization potential such as xenon will be used. Additionally, the XUV grating that was used in the iodine measurement is not designed to diffract efficiently below ∼25 eV, so a different grating may be required.

The germanium edge experiences less core hole screening than iodine, has a smaller 3d spin-orbit splitting of 0.58 eV, and only has one atom per formula unit. Therefore, the static spectrum is expected to have a less detailed fine structure. Since the germanium has significant density of states in the conduction band, the dynamics at this edge will provide information on the hot electron and lattice dynamics. The above-gap photoexcitation will initiate a transfer of hot electrons to the germanium cation. We expect a signal similar to the below-edge hot hole feature on the iodine, except the hot electron signal will occur above the edge onset energy and will be negative (decrease in absorbance) due to electrons blocking transitions into the conduction band, as has been observed previously in photoexcited germanium.[75] The hot electrons are expected to localize and thermalize on a comparable sub-100 fs timescale to the hot holes, but the total temperature that they gain and their decay timescale may be very different from the holes. If $CsGeI_3$ behaves similarly to PbI_2 and $MAPbI_3$, the electrons will have a lower initial temperature than the holes but a similar decay time constant.[21, 75]

Aside from purely electronic changes, the germanium $M_{4,5}$ edge will be sensitive to the lattice dynamics and will exhibit effects caused by the core hole interaction with the hot electrons. Lattice features are likely to appear above the edge onset and evolve on similar timescales to the iodine and cesium edges. Since the germanium ion moves in the a_1 phonon oscillation, the magnitude of features caused by this phenomenon may be larger at the Ge edge. The core hole effects will appear as the broadened and shifted static germanium XUV spectrum.[20] The simulated transient absorption for these dynamics is shown in Figure 6.13.

Once the element-specific transient XUV absorbance data from all three of the atoms in $CsGeI_3$ are obtained, a complete picture of the ultrafast processes occurring in this system and their timescales will be known. These three edges in combination afford a sensitivity and selectivity to the hot electron, hot hole, and lattice dynamics that occur after a photon is absorbed. What is missing is a direct assignment of the structural changes and modes involved. To complement the XUV transient absorption spectra, we have proposed a transient X-ray diffraction measurement of $CsGeI_3$ following above gap photoexcitation at the Linac Coherent Light Source. Details of this proposal and the expected results are discussed next.

LCLS Proposal: Optically Excited Coherent Phonons in a Visible-Light-Absorbing Ferroelectric

We have recently submitted a proposal to use the Linac Coherent Light Source (LCLS) to measure $CsGeI_3$ during run 21, which will occur between October 2022 and May 2023. In this proposal, we will photoexcite the 1.6 eV charge transfer to Ge and probe the lattice with hard X-ray powder diffraction at the LCLS XPP instrument. We aim to determine the origin of the oscillation with a period of ∼250 fs which damps within 400 fs observed in the few-femtosecond time-resolved XUV measurement (Figure 6.12). From theoretical calculation, Ge motion with a_1 symmetry along the <111> ferroelectric polarization displacement direction is predicted to occur at this frequency.[348] Thus, the goal is to observe the a_1 phonon oscillation of the Ge ion following photoexcited charge transfer from a mainly iodine valence band to a mainly Ge conduction band. We expect that, as has been proposed for the ferroelectrics $BaTiO_3$, $PbTiO_3$ and GeTe, delocalized conduction band electrons will destabilize the ferroelectricity via screening of the polarization,[349, 350] driving coherent phonon motion of the Ge toward a symmetric cubic phase, as is observed above 290°C.[333] The screening of the ferroelectric polarization by conduction band electrons is also predicted to be responsible for the observed rapid damping of the a_1 mode. Thus, optical pump-X-ray diffraction probe of this material will establish a link between optical excitation and the ferroelectric polarization. The origin of this optically excited phonon motion and its impact on the switchability and BPVE efficiency is of significant scientific and commercial interest.

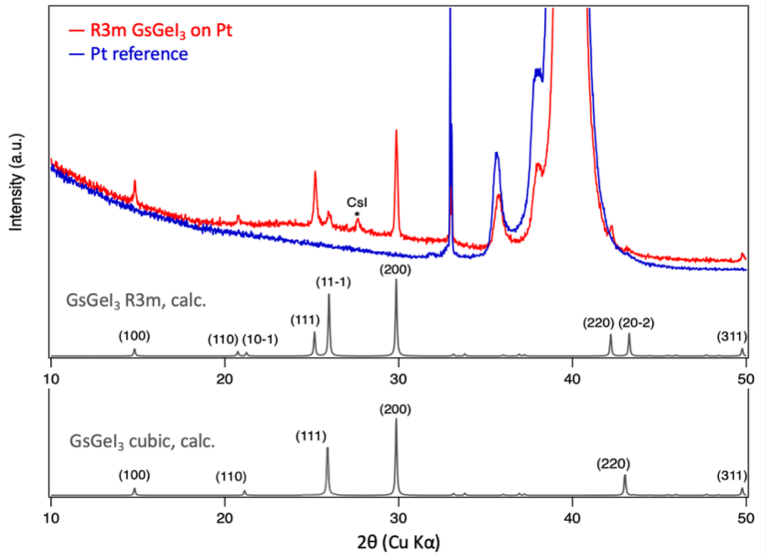

Figure 6.14: **The predicted changes to the $CsGeI_3$ X-ray powder diffraction.** Measured (red) and predicted (gray) powder XRD of the $CsGeI_3$ polycrystalline film, deposited on Pt (blue). The major difference between the R3m and cubic phases is the coalescence of three pairs of peaks into three single peaks, with the most intense pair the (111) and (11-1) at ~26 degrees. Taken with Cu Kα source.

The measurements proposed here aim to observe the coherent phonon motion of the Ge^{2+} ion along the a_1 mode, which is predicted to be the mode responsible for the distortion from a cubic lattice to the room temperature rhombohedral (distorted-cubic) lattice with space group R3m.[348] We hypothesize that the powder diffraction pattern will oscillate between the room temperature R3m pattern and a cubic pattern (Figure 6.14) via a coalescence of the observed rhombohedral (111) and (11-1) rings at approximately 26 degrees 2Θ (Cu Kα) into a single cubic (111) ring, which are the most intense peaks that display this behavior.[334, 351] Similarly, this occurs for the (110) and (10-1) rings at ~21 degrees into a single (110) ring, and for the (220) and (20-2) rings at ∼42 degrees into a single (220) ring. Furthermore, transient broadening of the (111) peak will be monitored as an indicator of incoherent motion of the Ge^{2+} ion along the axis of polarization. In order to accurately interpret these phenomena, DFT simulations of the X-ray diffraction pattern, with relativistic corrections to accurately capture the iodine, will be performed for a variety of Ge^{2+} displacements along the <111> direction. The effect of delocalized conduction band electrons on the lattice stability will be modeled utilizing the Elk Code DFT package for a range of carrier densities to simulate the effect of photoexcited screening.[345]

The XPP instrument at the LCLS is uniquely capable of measuring the dynamics of interest in $CsGeI_3$. Due to the approximately 250 fs period and single-cycle damping of the observed oscillation in the transient XUV signal, an ultrafast X-ray scattering technique is necessary to resolve the expected coherent phonon motion. While other XFEL facilities such as EuXFEL, SwissFEL and SACLA also possess the sub-100 fs hard X-ray pulses necessary,[352] these facilities lack the experience and expertise at LCLS in measuring both ferroelectric phase transitions[353–355] and the ultrafast lattice response of halide perovskites.[356] Moreover, one of the scientific programs of interest currently being pursued at the XPP instrument is the 'Dynamics of Photoinduced Phase Transitions', including those of ferroelectric solids. Thus, this beamtime proposal is well aligned with the technical capabilities, expert knowledge, and current scientific directions at the LCLS.

The proposed experiment is a series of time resolved optical pump–X-ray scattering probe measurements on $CsGeI_3$ polycrystalline thin films. The experiments will be performed in vacuum because the sample is sensitive to oxygen. The sample will be produced using the facilities at the University of California Berkeley and the Lawrence Berkeley National Laboratory as a thin film of approximately 350 nm (crystalline domains of 300-500 nm) deposited on an amorphous SiO_2 substrate The sample will be kept at room temperature as the transition to cubic phase occurs at 290 °C. The hard X-ray beam (9-13 keV) with 10^{10} photons/pulse and linear polarization will be used to measure the optically induced changes to the powder diffraction, and therefore lattice dynamics, of the sample. Potential laser induced sample damage will be mitigated by using a large optical pump spot. The X-ray focusing spot size will be smaller than the spot size of the optical pump. The optical penetration depth at 1.6 eV is approximately 2000 nm,[335] which is larger than the sample thickness of 350 nm and will ensure that the hard X-ray probe only samples the photoexcited region.

The sample will be excited by an ultrafast laser pulse of approximately 1.6 eV (775 nm) and 50 fs pulse duration from a synchronized optical laser system collinearly with the X-rays to achieve the best time resolution. The arrival time monitor (ATM) will be used to counteract timing jitter and drifts to achieve the required time resolution. The optical energy density will be 10 mJ/cm^2, which is same density used in the XUV transient absorption measurements but may be optimized to successfully trigger the coherent phonon. The repetition rate of both pulses will be the LCLS standard 120 Hz to prevent sample heating, which is similar to the 100 Hz used in the XUV measurement. The pump probe delay will be adjusted continuously to cover -200 fs to +1000 fs to resolve the first oscillations of period ~250 fs and the damping process. Additional measurements at increased photoexcitation densities will be performed to further characterize the coherent phonon oscillation and its rapid damping.

This experiment has a high likelihood of success due to the nature of the phenomenon being measured, the technical capabilities of the LCLS, and the success of similar works. Primarily, as described above, the observable phenomenon will be the coalescence of two X-ray powder rings into one ring as the crystal symmetry changes following photoexcitation. The disappearance of a ring is a significant change to the diffraction pattern and will be readily observed. A similar study performed in near-grazing incidence on a 400 nm film of 100 nm Ti_3O_5 nanocrystals at the SwissFEL revealed ultrafast laser-induced peak coalescence.[357] Additionally, the predicted phenomenon has been observed via transient XUV absorption, which has poor signal-to-noise ratios of approximately 3:1 after 8 hours of averaging and the application of noise-suppression programs.[346] Much of the noise is a consequence of the instability of the highly nonlinear XUV high harmonic generation mechanism and low photon counts of approximately 10^7/pulse. The 10^{10} photons/pulse available at the LCLS and the increased shot-to-shot stability of the XFEL will allow for shorter acquisition times and a greater signal-to-noise ratio of the proposed experiment. While the improved signal-to-noise ratio is essential, an X-ray diffraction probe is also necessary to provide detailed information about the lattice modes involved in the observed transient changes as the XUV absorption spectrum is not sensitive to these details. Furthermore, an optical pump-XRD lattice probe has been applied to $BiFeO_3$ to observe coherent shear phonon motion[358] and to the lead halide perovskites to observe lattice phase transitions[356, 359] with great success.

The primary goal of the proposed experiment is to unambiguously identify photoinduced coherent polarization switching suggested by the ~250 fs oscillation observed in transient XUV absorption measurements. We hypothesize that the charge transfer will trigger lattice motion of the Ge^{2+} ion along the <111> direction a_1 phonon mode toward the cubic phase. We expect a coalescence of the rhombohedral (111) and (11-1) powder rings into a single cubic (111) ring, the signature of ferroelectric switching in this material. To investigate optical ferroelectric switching, the unique capabilities of the XPP instrument at LCLS are essential. A greater understanding of the coupled electron and lattice dynamics in ferroelectrics will inform the design and control of ferroelectricity in future materials.

6.2.2 Proposed Experiments

Extreme ultraviolet transient absorption spectroscopy is an excellent technique to unravel the ultrafast dynamics that occur in nanoparticles and thin films. The experiments presented in this dissertation only begin to cover the possible phenomena that can be understood with this femtosecond resolution probe of charge carrier and lattice dynamics. Here we present future material systems that possess unanswered questions about their ultrafast dynamics of interest to the XUV transient absorption community.

Zero-D Tellurium Halide Perovskite: Cs_2TeX_6

XUV transient absorption studies of the lead halide perovskite $MAPbI_3$ and the perovskite precursor PbI_2 have yielded interesting results regarding the differing temperatures between the hot electron and hot hole distributions and evidence of a hole-only cooling bottleneck due to the high carrier screening in these materials by low frequency phonon modes.[20, 21] These studies have centered on the role of the iodine ligands, as lead and carbon do not yield good XUV signals. Questions still remain about the impacts of the ligand octahedral cage vibrations and the A site cation rotations on the hot carrier relaxation process. It therefore follows that XUV should be applied to more halide perovskite structures to unravel these competing processes. A very helpful halide perovskite derivative for such studies is the double perovskite Cs_2TeX_6 (X is the halide Cl, Br or I), which exhibits a 'zero dimensional' (0D) perovskite-like structure of corner-sharing octahedral cages.

This material, which exhibits an optical band gap of $\sim$1.5 eV and is stable at room temperature up to 250 °C, behaves like a series of isolated octahedral units.[360] It can be thought of as a perovskite crystal missing every other B site cation. The extent of the isolation has been probed by photoluminescence and Raman measurements, which show that chlorine and bromine heavy octahedra are more molecule-like and iodine rich octahedra behave more like a dispersive band structure.[361] Intra-octahedral harmonic vibrations are observed in all crystals, and inter-octahedral anharmonic vibrations caused by exciton-phonon coupling are observed to be present in the iodide crystals (Figure 6.15). The strong degree of carrier-lattice coupling in this system indicates that polaron formation is likely.

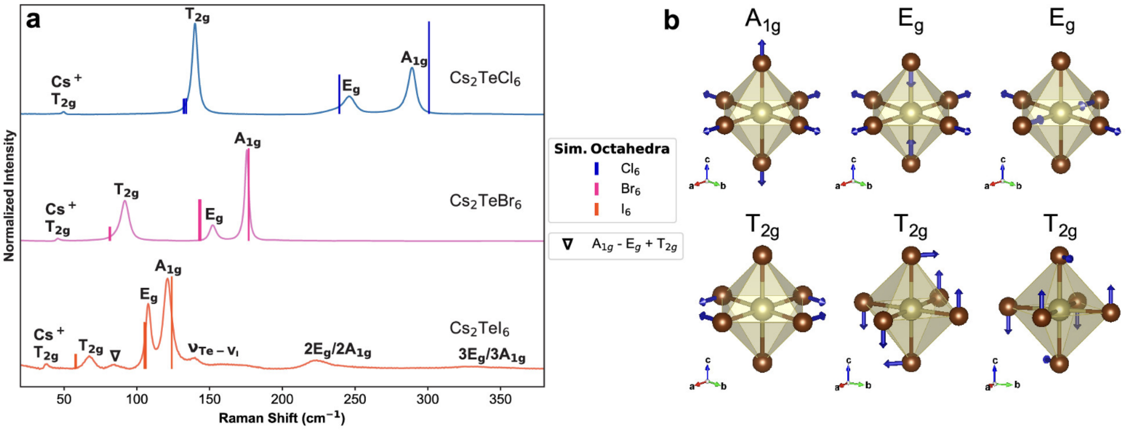

Figure 6.15: **Raman spectra of the Cs_2TeX_6 compounds.** a) The Raman spectra of Cs_2TeCl_6, Cs_2TeBr_6 and Cs_2TeI_6. The chloride and bromide compounds display the three intra-octahedral modes and can be treated like isolated molecules. The iodide compound displays additional inter-octahedral modes, implying that the octahedral building blocks of this compound interact to form a dispersive band structure.
b) Cartoons of the Raman active modes observed in panel a. Adapted from reference [361].

Thin films[360] and single-crystals[361] of Cs_2TeI_6 are possible to synthesize. The films are produced very similarly to the $CsGeI_3$ in a two layer process (CsI and TeI_4 layers) followed by annealing. Br and Cl do not yield good XUV edges, but the iodine and cesium edges described above and the tellurium $N_{4,5}$ edge are all accessible with the XUV spectrometer. The Te $N_{4,5}$ edge is very narrow and intense and occurs around 40 eV, which should not overlap too badly with the I $N_{4,5}$ edge centered around 50 eV. Therefore, all three pure halide crystals Cs_2TeCl_6, Cs_2TeBr_6 and Cs_2TeI_6 can be probed with XUV transient absorption spectroscopy. By studying the charge carrier, phonon and possible polaron dynamics of the Cs_2TeX_6 isolated octahedral building blocks of the perovskite structure, we will gain insight into the ultrafast phonon mediated processes that occur in halide perovskite materials.

IrO_2 and RuO_2 Nanoparticle Catalysts

A persisting impediment to commercial photoelectrochemical water splitting is the slow kinetics of the oxygen evolution half reaction (OER), which significantly lags behind the rate of the hydrogen evolution reaction and limits electrochemical water splitting and electrolysis.[362] The highest activity and most stable oxygen evolution catalysts, IrO_2 and RuO_2, have recently displayed improved photocatalytic activity when synthesized as rutile nanoparticles.[363, 364] These nanoparticle catalysts exhibit higher stability and improved activity in both acidic and alkaline environments. DFT calculation has predicted that hole polarons will form on rutile surfaces (see Figure 6.16) and reduce the overpotential of the first step of the water splitting reaction, the water molecule adsorption, which is the reaction-limiting step.[365] XUV transient absorption spectroscopy is uniquely able to resolve the signatures of ultrafast polaron formation to determine the impact on water splitting.

For this experiment, drop cast films of RuO_2 and IrO_2 nanoparticles will be photoexcited by above-gap 400 nm photons to initiate the ultrafast charge transfer from oxygen to the Ru/Ir metal. An extreme ultraviolet probe of the Ir $O_{2,3}$ edge near 50—60 eV and Ru $N_{2,3}$ edge near 45 eV will allow tracking of charge carrier and lattice dynamics in these photocat-

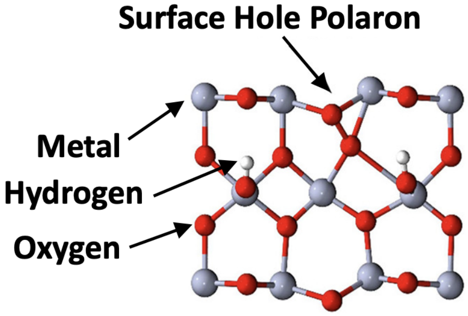

Figure 6.16: **Polaron formation at the rutile surface.** Metal atoms (Ru or Ir) are shown in gray, H atoms in white, and O atoms in red. Adapted from reference [365].

alyst materials.[129] The core holes of these heavy elements experience more shielding and therefore longer core hole lifetimes and narrower XUV edges. Light-induced modifications to the band structures, state filling and lattice distortions will therefore be more easily resolved as sharp changes to the absorbance. Further, the simple structure of the IrO_2 and RuO_2 materials will provide a useful inroads for studying more complex iridate and ruthenate structures with XUV, such as the superconductor Sr_2RuO_4.[366]

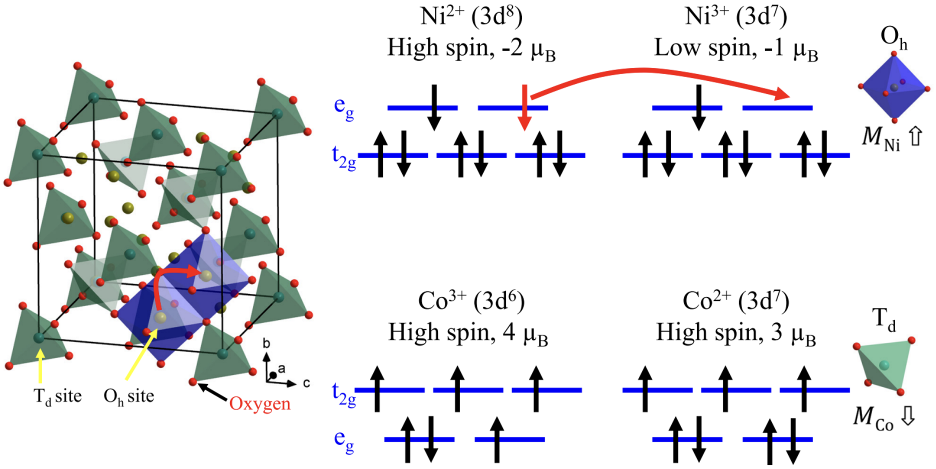

Figure 6.17: **A diagram of the spin states and structure of $NiCo_2O_4$.** On the left is the inverse spinel crystal structure, which is a cubic array of O^{2-} ligands with all of the octahedral (O_h) sites and half the tetrahedral (T_d) sites filled with metal cations. The Ni and Co ions adopt both the +2 and +3 oxidation state and both fill the T_d and O_h sites. All Co ions and the Ni^{2+} ions are in the high spin state, and the Ni^{3+} ions are in the low spin state. In this diagram, double exchange between neighboring O_h Ni^{2+} and Ni^{3+} cations is responsible for the polaronic hopping, but other studies suggest Jahn-Teller type distortions of the T_d site Ni are responsible. Adapted from reference [367].

Supercapacitor: $NiCo_2O_4$ Nanoporous Film

Another highly effective catalyst material for the oxygen evolution reaction that may exhibit polarons is $NiCo_2O_4$.[368] This highly conductive nanoporous material also has a high surface area for application as a supercapacitor[369] and as a catalyst for the oxidation of toxic industrial byproducts.[370] $NiCo_2O_4$ has a mixed-valent inverse spinel structure, in which both the Ni and Co ions occupy the tetrahedral T_d sites and the octahedral O_h sites in the cubic O^{2-} lattice.[367] The Co and Ni ions both inhabit +2 and +3 oxidation states, with the Ni^{2+} $3d^8$ ions in a high spin configuration, the Ni^{3+} $3d^7$ ions in a low spin configuration, and the Co^{2+} $3d^7$ and Co^{3+} $3d^6$ ions both in a high spin configuration (Figure 6.17). The mixed-valent O_h Ni sites are predicted to allow for polaronic hopping due to the double exchange interaction between their anti-aligned magnetic moments.[371]. The ferrimagnetic ordering of the Ni^{3+}—O^{2-}—Ni^{2+} and the resulting double exchange interaction may also be responsible for the metallic-like conduction observed in this material, even though it has a semiconductor-like optical band gap of ∼2 eV. Alternatively, first principles calculations reveal a structural Jahn-Teller disorder in $NiCo_2O_4$ via elongation of the NiO_4 tetrahedron and improved electronic conduction due to Jahn-Teller type polarons.[372] XUV transient absorption spectroscopy, which is sensitive to the spin state, oxidation state, crystal structure and small polarons is required to understand the origin of the increased photoconductivity of this material.

In the proposed XUV transient absorption measurement, an optical pump will excite the electron transfer from Ni to Co, altering their oxidation states and spin states, and possibly causing the formation of polarons.[373] XUV transient absorption is sensitive to both the oxidation state and spin state of Ni and Co containing materials, and this selectivity has been used to track the optically induced spin state crossover in $NiFe_2O_4$ and $CoFe_2O_4$.[90, 91] In the case of $NiCo_2O_4$, both the Ni $M_{2,3}$ edge at 68 eV and Co $M_{2,3}$ edge at 62 eV will be measured simultaneously to report on the spin and oxidation state changes at each edge following above-gap photoexcitation. XUV transient absorption spectroscopy can reveal whether the origin of the improved polaronic conduction in this material is Jahn-Teller type polarons on the Ni T_d sites or the double exchange interaction polarons on the Ni O_h sites, and further the understanding of supercapacitance in nanoscale materials.

Bibliography

(1) Heiligtag, F. J.; Niederberger, M. The Fascinating World of Nanoparticle Research. *Materials Today* **2013**, *16*, 262–271.

(2) Jeevanandam, J.; Barhoum, A.; Chan, Y. S.; Dufresne, A.; Danquah, M. K. Review on Nanoparticles and Nanostructured Materials: History, Sources, Toxicity and Regulations. *Beilstein Journal of Nanotechnology* **2018**, *9*, 1050–1074.

(3) Becquerel, E. On Electric Effects Under the Influence of Solar Radiation. *Comptes Rendus de l'Académie des Sciences, Paris* **1839**, *9*, 561.

(4) Fujishima, A.; Honda, K. Electrochemical Photolysis of Water at a Semiconductor Electrode. *Nature* **1972**, *238*, 37–38.

(5) Goetzberger, A.; Hebling, C.; Schock, H.-W. Photovoltaic Materials, History, Status and Outlook. *Materials Science and Engineering R: Reports* **2003**, *40*, 1–46.

(6) Joy, J.; Mathew, J.; George, S. C. Nanomaterials for Photoelectrochemical Water Splitting - Review. *International Journal of Hydrogen Energy* **2018**, *43*, 4804–4817.

(7) Simon, S. H., *The Oxford Solid State Basics*; Oxford University Press: United Kingdom, 2013.

(8) Grätzel, M. Photoelectrochemical Cells. *Nature* **2001**, *414*, 338–344.

(9) Shockley, W.; Queisser, H. J. Detailed Balance Limit of Efficiency of *p-n* Junction Solar Cells. *Journal of Applied Physics* **1961**, *32*, 510.

(10) Van de Krol, R.; Grätzel, M., *Photoelectrochemical Hydrogen Production*; Springer Science+Business Media: New York, 2012.

(11) Sivula, K.; van de Krol, R. Semiconducting Materials for Photoelectrochemical Energy Conversion. *Nature Review Materials* **2016**, *1*, 15010.

(12) Drude, P. Zur Elektronentheorie der Metalle (On the Electron Theory of Metals). *Annalen der Physik* **1900**, *306*, 566–613.

(13) Hubbard, J. Electron Correlations in Narrow Energy Bands. *Proceedings of the Royal Society A* **1963**, *276*, 238–257.

(14) Altland, A.; Simons, B., *Condensed Matter Field Theory*; Cambridge University Press: Cambridge, UK, 2010.

(15) Carneiro, L. M. Electron-Lattice Dynamics in Solid-State Materials Relevant for Solar Energy Conversion Studied by Femtosecond Extreme Ultraviolet Absorption Spectroscopy, Ph.D. Thesis, University of California, Berkeley, 2018.

(16) Scheuermann, A. G.; Lawrence, J. P.; Kemp, K. W.; Ito, T.; Walsh, A.; Chidsey, C. E. D.; Hurley, P. K.; McIntyre, P. C. Design Principles for Maximizing Photovoltage in Metal-Oxide-Protected Water-Splitting Photoanodes. *Nature Materials* **2016**, *15*, 99–105.

(17) Huda, M. N.; Walsh, A.; Yan, Y.; Wei, S.-H.; Al-Jassim, M. M. Electronic, Structural, and Magnetic Effects of 3d Transition Metals in Hematite. *Journal of Applied Physics* **2010**, *107*, 123712.

(18) Lin, J.-F.; Tse, J. S.; Alp, E. E.; Zhao, J.; Lerche, M.; Sturhahn, W.; Xiao, Y.; Chow, P. Phonon Density of States of Fe_2O_3 Across High-Pressure Structural and Electronic Transitions. *Physical Review B* **2011**, *84*, 064424.

(19) Pankove, J. I., *Optical Processes in Semiconductors*; Dover Publications: New York, 1971.

(20) Lin, M.-F.; Verkamp, M. A.; Leveillee, J.; Ryland, E. S.; Benke, K.; Zhang, K.; Weninger, C.; Shen, X.; Li, R.; Fritz, D.; Bergmann, U.; Wang, X.; Schleife, A.; Vura-Weis, J. Carrier-Specific Femtosecond XUV Transient Absorption of PbI_2 Reveals Ultrafast Nonradiative Recombination. *The Journal of Physical Chemistry C* **2017**, *121*, 27886–27893.

(21) Verkamp, M.; Leveillee, J.; Sharma, A.; Lin, M.-F.; Schleife, A.; Vura-Weis, J. Carrier-Specific Hot Phonon Bottleneck in $CH_3NH_3PbI_3$ Revealed by Femtosecond XUV Absorption. *Journal of the American Chemical Society* **2021**, *143*, 20176–20182.

(22) Brudevoll, T.; Fjeldly, T. A.; Baek, J.; Shur, M. S. Scattering Rates for Holes Near the Valence-Band Edge in Semiconductors. *Journal of Applied Physics* **1990**, *67*, 7373.

(23) Kane, D. E.; Swanson, R. M. Effect of Electron-Hole Scattering on the Current Flow in Semiconductors. *Journal of Applied Physics* **1992**, *72*, 5294–5304.

(24) Mnatsakanov, T. T.; Levinshtein, M. E.; Ivanov, P. A.; Palmour, J. W.; Tandoev, A. G.; Yurkov, S. N. Parameters of Electron-Hole Scattering in Silicon Carbide. *Journal of Applied Physics* **2003**, *93*, 1095–1098.

(25) Kosina, H.; Kampl, M. Effect of Electron-Electron Scattering on the Carrier Distribution in Semiconductor Devices. *International Conference on Simulation of Semiconductor Processes and Devices* **2018**, 18–21.

(26) Chen, C. et al. Distinguishing Attosecond Electron-Electron Scattering and Screening in Transition Metals. *PNAS* **2017**, *114*, E5300–E5307.

(27) Trimpl, M. J.; Wright, A. D.; Schutt, K.; Buizza, L. R. V.; Wang, Z.; Johnston, M. B.; Snaith, H. J.; Müller-Buschbaum, P.; Herz, L. M. Charge-Carrier Trapping and Radiative Recombination in Metal Halide Perovskite Semiconductors. *Advanced Functional Materials* **2020**, *30*, 2004312.

(28) Qian, R.; Zong, H.; Schneider, J.; Zhou, G.; Zhao, T.; Li, Y.; Yang, J.; Bahnemann, D. W.; Panl, J. H. Charge Carrier Trapping, Recombination and Transfer During TiO_2 Photocatalysis: An Overview. *Catalysis Today* **2019**, *335*, 78–90.

(29) Cordones, A. A.; Leone, S. R. Mechanism for Charge Trapping in Single Semiconductor Nanocrystals Probed by Fluorescence Blinking. *Chemical Society Reviews* **2012**, *42*, 3209–3221.

(30) Devreese, J. T.; Alexandrov, A. S. Fröhlich Polaron and Bipolaron: Recent Developments. *Reports on Progress in Physics* **2009**, *72*, 066501.

(31) Fröhlich, H. Theory of Electrical Breakdown in Ionic Crystal. *Proceedings of the Royal Society* **1937**, *A160*, 230.

(32) Letcher, J. J.; Kang, K.; Cahill, D. G.; Dlott, D. D. Effects of High Carrier Densities on Phonon and Carrier Lifetimes in Si by Time-Resolved Anti-Stokes Raman Scattering. *Applied Physics Letters* **2007**, *90*, 252104.

(33) Hartig, M.; Haacke, S.; Deveaud, B. Femtosecond Luminescence Measurements of the Intersubband Scattering Rate in AlGaAs/GaAs Quantum Wells Under Selective Excitation. *Physical Review B* **1996**, *54*, R14269.

(34) Shah, J., *Ultrafast Spectroscopy of Semiconductors and Semiconductor Nanostructures*; Springer: Berlin, Heidelberg, 1999.

(35) Landau, L. D. About the Movement of Electrons in Crystal Lattices. *Physikalische Zeitschrift* **1933**, *3*, 644–645.

(36) Ge, N.-H.; Wong, C. M.; Harris, C. B. Femtosecond Studies of Electron Dynamics at Interfaces. *Accounts of Chemical Research* **2000**, *33*, 111–118.

(37) Rettie, A. J. E.; Chemelewski, W. D.; Emin, D.; Mullins, C. B. Unravelling Small-Polaron Transport in Metal Oxide Photoelectrodes. *The Journal of Physical Chemistry Letters* **2016**, *7*, 471–479.

(38) Ferry, D. K.; Osman, M. A.; Joshi, R.; Kann, M.-J. Ultrafast Relaxation of Hot Photoexcited Carriers in GaAs. *Solid-State Electronics* **1998**, *31*, 401–406.

(39) Chang, H.-T.; Guggenmos, A.; Cushing, S. K.; Cui, Y.; Din, N. U.; Acharya, S. R.; Porter, I. J.; Kleineberg, U.; Turkowski, V.; Rahman, T. S.; Neumark, D. M.; Leone, S. R. Electron Thermalization and Relaxation in Laser-Heated Nickel by Few- Femtosecond Core-Level Transient Absorption Spectroscopy. *Physical Review B* **2021**, *103*, 064305.

(40) Ramalingam, G.; Kathirgamanathan, P.; Ravi, G.; Elangovan, T.; Kumar, B. A.; Manivannan, N.; Kaviyarasu, K., Quantum Confinement Effect of 2D Nanomaterials In *Quantum Dots - Fundamental and Applications*; Intech Open: 2020.

(41) Bigot, J.-Y.; Portella, M. T.; Schoenlein, R. W.; Cunningham, J. E.; Shank, C. V. Two-Dimensional Carrier-Carrier Screening in a Quantum Well. *Physical Review Letters* **1991**, *67*, 636–639.

(42) Voisin, C.; Christofilos, D.; Loukakos, P. A.; del Fatti, N.; Vallée, F.; Lermé, J.; Gaudry, M.; Cottancin, E.; Pellarin, M.; Broyer, M. Ultrafast Electron-Electron Scattering and Energy Exchanges in Noble-Metal Nanoparticles. *Physical Review B* **2004**, *69*, 195416.

(43) Wang, H.; Zhang, C.; Rana, F. Surface Recombination Limited Lifetimes of Photoexcited Carriers in Few-Layer Transition Metal Dichalcogenide MoS_2. *Nano Letters* **2015**, *15*, 8204–8210.

(44) Richter, H.; Wang, Z. P.; Ley, L. The One Phonon Raman Spectrum in Microcrystalline Silicon. *Solid State Communications* **1981**, *39*, 625–629.

(45) Nemanich, R. J.; Solin, S. A.; Martin, R. M. Light Scattering Study of Boron Nitride Microcrystals. *Physical Review B* **1981**, *23*, 6348–6356.

(46) Osswald, S.; Mochalin, V. N.; Havel, M.; Yushin, G.; Gogotsi, Y. Phonon Confinement Effects in the Raman Spectrum of Nanodiamond. *Physical Review B* **2009**, *80*, 075419.

(47) Bersani, D.; Lottici, P. P.; Ding, X.-Z. Phonon Confinement Effects in the Raman Scattering by TiO_2 Nanocrystals. *Applied Physics Letters* **1997**, *72*, 73–75.

(48) Kim, J.; Kim, H.; Kilic, M. E.; Gayner, C.; Koltun, R.; Park, H.; Soon, A.; Bowers, J.; Palmstrøm, C.; Kim, W. Effect of Phonon Confinement on the Thermal COnductivity of $In_{0.53}Ga_{0.47}As$ Nanofilms. *Journal of Applied Physics* **2018**, *123*, 245103.

(49) Meier, C.; Lüttjohann, S.; Kravets, V. G.; Neinhaus, H.; Lorke, A.; Wiggers, H. Raman Properties of Silicon Nanoparticles. *Physical Review E* **2006**, *32*, 155–158.

(50) Ju, Y. S.; Goodson, K. E. Phonon Scattering in Silicon Films with Thickness of Order 100 nm. *Applied Physics Letters* **1999**, *74*, 3005–3007.

(51) Zewail, A. H. Laser Femtochemistry. *Science* **1988**, *242*, 1645–1653.

(52) Nilsson, A. Applications of Core Level Spectroscopy to Adsorbates. *Journal of Electron Spectroscopy and Related Phenomena* **2002**, *126*, 3–42.

(53) Cushing, S. K.; Lee, A.; Porter, I. J.; Carneiro, L. M.; Chang, H.-T.; Zürch, M.; Leone, S. R. Differentiating Photoexcited Carrier and Phonon Dynamics in the Δ, L, and Γ Valleys of Si(100) with Transient Extreme Ultraviolet Spectroscopy. *The Journal of Physical Chemistry C* **2019**, *123*, 3343–3352.

(54) Fermi, E., *Nuclear Physics*; The University of Chicago Press: University of Chicago, 1949.

(55) De Groot, F.; Kotani, A., *Core Level Spectroscopy of Solids*; CRC Press, Taylor & Francis Group: Boca Raton, FL, 2008.

(56) Cushing, S. K.; Zürch, M.; Kraus, P. M.; Carneiro, L. M.; Lee, A.; Chang, H.-T.; Kaplan, C. J.; Leone, S. R. Hot Phonon and Carrier Relaxation in Si(100) Determined by Transient Extreme Ultraviolet Spectroscopy. *Structural Dynamics* **2018**, *5*, 054302.

(57) Stavitski, E.; de Groot, F. M. F. The CTM4XAS Program for EELS and XAS Spectral Shape Analysis of Transition Metal L Edges. *Micron* **2010**, *41*, 687–694.

(58) Andrews, D. L., Transition Rates and Selection Rules In *Molecular Photophysics and Spectroscopy*; 2053-2571; Morgan & Claypool Publishers: 2014, 9-1 to 9–4.

(59) De Groot, F. Multiplet Effects in X-ray Spectroscopy. *Coordination Chemistry Reviews* **2005**, *249*, 31–63.

(60) De Groot, F. M. F.; Fuggle, J. C.; Thole, B. T.; Sawatzky, G. A. $L_{2,3}$ X-ray-Absorption Edges of d^0 compounds: K^+, Ca^{2+}, Sc^{3+}, and Ti^{4+} in O_h (Octahedral) Symmetry. *Physical Review B* **1990**, *41*, 928.

(61) Tanabe, Y.; Sugano, S. On the Absorption Spectra of Complex Ions. I. *Journal of the Physical Society of Japan* **1954**, *9*, 753–766.

(62) Zhang, K.; Girolami, G. S.; Vura-Weis, J. Improved Charge Transfer Multiplet Method to Simulate M- and L-Edge X-ray Absorption Spectra of Metal-Centered Excited States. *Journal of Synchrotron Radiation* **2018**, *25*, 1600–1608.

(63) Vinson, J.; Rehr, J. J.; Kas, J. J.; Shirley, E. L. Bethe-Salpeter Equation Calculations of Core Excitation Spectra. *Physical Review B* **2011**, *83*, 115106.

(64) Gilmore, K.; Vinson, J.; Shirley, E. L.; Prendergast, D.; Pemmaraju, C. D.; Kas, J. J.; Vila, F. D.; Rehr, J. J. Efficient Implementation of Core-Excitation Bethe–Salpeter Equation Calculations. *Computational Physics Communications* **2015**, *197*, 109.

(65) Shank, C. V.; Auston, D. H.; Ippen, E. P.; Teschke, O. Picoseond Time Resolved Reflectivity of Direct Gap Semiconductors. *Solid State Communications* **1978**, *26*, 567–570.

(66) Auston, D. H.; McAfee, S.; Shank, C. V.; Ippen, E. P.; Teschke, O. Picoseond Spectroscopy of Semiconductors. *Solid-State Electronics* **1978**, *21*, 147–150.

(67) Chang, W. S. C., *Principles of Lasers and Optics*; Cambridge University Press: United Kingdom, 2005.

(68) Beer Bestimmung der Absorption des Rother Lichts in Fabigen Flüssigkeiten (Determination of the Absorption of Red Light in Colored Liquids). *Annalen der Physik und Chemie* **1852**, *162*, 78–88.

(69) Berera, R.; van Grondelle, R.; Kennis, J. T. M. Ultrafast Transient Absorption Spectroscopy: Principles and Application to Photosynthetic Systems. *Photosynthesis Research* **2009**, *101*, 105–118.

(70) Uprety, P.; Subedi, I.; Junda, M. M.; Collins, R. W.; Podraza, N. J. Photogenerated Carrier Transport Properties in Silicon Photovoltaics. *Scientific Reports* **2019**, *9*, 19015.

(71) Cuevas, A.; Macdonald, D. Measuring and Interpreting and Lifetime of Silicon Wafers. *Solar Energy* **2004**, *76*, 255–262.

(72) Vura-Weis, J.; Jiang, C.-M.; Liu, C.; Gao, H.; Lucas, J. M.; de Groot, F. M. F.; Yang, P.; Alivisatos, A. P.; Leone, S. R. Femtosecond $M_{2,3}$-Edge Spectroscopy of Transition-Metal Oxides: Photoinduced Oxidation State Change in α-Fe_2O_3. *The Journal of Physical Chemistry Letters* **2013**, *4*, 3667–3671.

(73) Geneaux, R.; Marroux, H. J. B.; Guggenmos, A.; Neumark, D. M.; Leone, S. R. Transient Absorption Spectroscopy Using High Harmonic Generation: A Review of Ultrafast X-ray Dynamics in Molecules and Solids. *Philosophical Transactions of the Royal Society A* **2018**, *377*, 20170463.

(74) Zhang, K.; Lin, M.-F.; Ryland, E. S.; Verkamp, M. A.; Benke, K.; de Groot, F. M. F.; Girolami, G. S.; Vura-Weis, J. Shrinking the Synchrotron: Tabletop Extreme Ultraviolet Absorption of Transition-Metal Complexes. *The Journal of Physical Chemistry Letters* **2016**, *7*, 3383–3387.

(75) Zürch, M.; Chang, H.-T.; Borja, L. J.; Kraus, P. M.; Cushing, S. K.; Gandman, A.; Kaplan, C. J.; Oh, M. H.; Prell, J. S.; Prendergast, D.; Pemmaraju, C. D.; Neumark, D. M.; Leone, S. R. Direct and Simultaneous Observation of Ultrafast Electron and Hole Dynamics in Germanium. *Nature Communications* **2017**, *8*, 15734.

(76) Zürch, M.; Chang, H.-T.; Kraus, P. M.; Cushing, S. K.; Borja, L. J.; Gandman, A.; Kaplan, C. J.; Oh, M. H.; Prell, J. S.; Prendergast, D.; Pemmaraju, C. D.; Neumark, D. M.; Leone, S. R. Ultrafast Carrier Thermalization and Trapping in Silicon-Germanium Alloy Probed by Extreme Ultraviolet Transient Absorption Spectroscopy. *Structural Dynamics* **2017**, *4*, 044029.

(77) Géneaux, R.; Kaplan, C. J.; Yue, L.; Ross, A. D.; Bækhøj, J. E.; Kraus, P. M.; Chang, H.-T.; Guggenmos, A.; Huang, M.-Y.; Zürch, M.; Schafer, K. J.; Neumark, D. M.; Gaarde, M. B.; Leone, S. R. Attosecond Time-Domain Measurement of Core-Level-Exciton Decay in Magnesium Oxide. *Physical Review Letters* **2020**, *124*, 207401.

(78) Chang, H.-T.; Guggenmos, A.; Chen, C. T.; Oh, J.; Géneaux, R.; Chuang, Y.-D.; Schwartzberg, A. M.; Aloni, S.; Neumark, D. M.; Leone, S. R. Coupled Valence Carrier and Core-Exciton Dynamics in WS_2 Probed by Few-Femtosecond Extreme Ultraviolet Transient Absorption Spectroscopy. *Physical Review B* **2021**, *104*, 064309.

(79) Gaynor, J. D.; Fidler, A. P.; Lin, Y.-C.; Chang, H.-T.; Zuerch, M.; Neumark, D. M.; Leone, S. R. Solid State Core-Exciton Dynamics in NaCl Observed by Tabletop Attosecond Four-Wave Mixing Spectroscopy. *Physical Review B* **2021**, *103*, 245140.

(80) Biswas, S.; Husek, J.; Londo, S.; Baker, L. R. Ultrafast Electron Trapping and Defect-Mediated Recombination in NiO Probed by Femtosecond Extreme Ultraviolet Reflection-Absorption Spectroscopy. *Proceedings of the National Academy of Science* **2017**, *114*, 9558–9563.

(81) Carneiro, L. M.; Cushing, S. K.; Liu, C.; Su, Y.; Yang, P.; Alivisatos, A. P.; Leone, S. R. Excitation-Wavelength-Dependent Small Polaron Trapping of Photoexcited Carriers in α-Fe_2O_3. *Nature Materials* **2017**, *16*, 819–825.

(82) Chen, W.; Xiong, W. Polaron-Formation Revealed by Transient XUV Imaginary Refractive Index Changes in Different Iron Compounds. *Physical Chemistry Chemical Physics* **2021**, *23*, 4486–4490.

(83) Husek, J.; Cirri, A.; Biswas, S.; Baker, L. R. Surface Electron Dynamics in Hematite (α-Fe_2O_3): Correlation Between Ultrafast Surface Electron Trapping and Small Polaron Formation. *Chemical Science* **2017**, *8*, 8170–8178.

(84) Biswas, S.; Husek, J.; Londo, S.; Baker, L. R. Ultrafast Electron Trapping and Defect-Mediated Recombination in NiO Probed by Femtosecond Extreme Ultraviolet Reflection-Absorption Spectroscopy. *The Journal of Physical Chemistry Letters* **2018**, *9*, 5047–5054.

(85) Attar, A. R.; Chang, H.-T.; Britz, A.; Zhang, X.; Lin, M.-F.; Krishnamoorthy, A.; Linker, T.; Fritz, D.; Neumark, D. M.; Kalia, R. K.; Nakano, A.; Ajayan, P.; Vashishta, P.; Bergmann, U.; Leone, S. R. Simultaneous Observation of Carrier-Specific Redistribution and Coherent Lattice Dynamics in 2H-$MoTe_2$ with Femtosecond Core-Level Spectroscopy. *ACS Nano* **2020**, *14*, 15829–15840.

(86) Weisshaupt, J.; Rouzée, A.; Woerner, M.; Vrakking, M. J. J.; Elsaesser, T.; Shirley, E. L.; Borgschulte, A. Ultrafast Modulation of Electronic Structure by Coherent Phonon Excitations. *Physical Reviews B* **2017**, *95*, 081101.

(87) Papalazarou, E.; Boschetto, D.; Gautier, J.; Valentin, C.; Rey, G.; Zeitoun, P.; Rousse, A.; Balcou, P.; Marsi, M. Probing Coherently Excited Optical Phonons by Extreme Ultraviolet Radiation with Femtosecond Time Resolution. *Applied Physics Letters* **2008**, *93*, 041114.

(88) Géneauz, R.; Timrov, I.; Kaplan, C. J.; Ross, A. D.; Kraus, P. M.; Leone, S. R. Coherent Exchange Between Carriers and Phonons in Peierls-Distorted Bismuth Unveiled by Broadband XUV Pulses. *Physical Reviews Research* **2021**, *3*, 033210.

(89) Jager, M. F.; Ott, C.; Kraus, P. M.; Kaplan, C. J.; Pouse, W.; Marvel, R. E.; Haglund, R. F.; Neumark, D. M.; Leone, S. R. Tracking the Insulator-to-Metal Phase Transition in VO_2 with Few-Femtosecond Extreme UV Transient Absorption Spectroscopy. *Proceedings of the National Academy of Science* **2017**, *114*, 9558–9563.

(90) Londo, S.; Biswas, S.; Pinchuk, I. V.; Boyadzhiev, A.; Kawakami, R.; Baker, L. R. Ultrafast Optical Spin Switching in Ferrimagnetic Nickel Ferrite ($NiFe_2O_4$) Studied by XUV Reflection-Absorption Spectroscopy. *The Journal of Physical Chemistry C* **2022**, *126*, 2669–2678.

(91) Londo, S.; Biswas, S.; Husek, J.; Pinchuk, I. V.; Newburger, M. J.; Boyadzhiev, A.; Trout, A. H.; McComb, D. W.; Kawakami, R.; Baker, L. R. Ultrafast Spin Crossover in a Room-Temperature Ferrimagnet: Element-Specific Spin Dynamics in Photoexcited Cobalt Ferrite. *The Journal of Physical Chemistry C* **2020**, *124*, 11368–11375.

(92) Attwood, D.; Sakdinawat, A., *X-rays and Extreme Ultraviolet Radiation: Principles and Applications*; Cambridge University Press: University of California, Berkeley, 2017.

(93) Pfeifer, T.; Spielmann, C.; Gerber, G. Femtosecond x-ray science. *Reports on Progress in Physics* **2006**, *69*, 443–505.

(94) Liu, B. et al. The SXFEL Upgrade: From Test Facility to User Facility. *Applied Sciences* **2022**, *12*, 176.

(95) Paul, A.; Bartels, R. A.; Tobey, R.; Green, H.; Weiman, S.; Christov, I. P.; Murnane, M. M.; Kapteyn, H. C.; Backus, S. Quasi-Phase-Matched Generation of Coherent Extreme-Ultraviolet Light. *Nature* **2003**, *421*, 51–54.

(96) Li, J.; Lu, J.; Chew, A.; Han, S.; Li, J.; Wu, Y.; H, W.; Ghimire, S.; Chang, Z. Attosecond Science Based on High Harmonic Generation From Gases and Solids. *Nature Communications* **2020**, *11*, 2748.

(97) Popmintchev, T. Tunable Ultrafast Coherent Light in the Soft and Hard X-ray Region of the Spectrum: Phase Matching of Extreme High-Order Harmonic Generation, Ph.D. Thesis, University of Colorado, 2009.

(98) Ishikawa, K. L., High-Harmonic Generation In *Advances in Solid State Lasers Development and Applications*, Grishin, M., Ed.; Intech Open: Croatia, 2010.

(99) Corkum, P. B. Plasma Perspective on Strong-Field Multiphoton Ionization. *Physical Review Letters* **1993**, *71*, 1994–1997.

(100) Becker, W.; Lohr, A.; Kleber, M. Light at the End of the Tunnel: Two- and Three-Step Models in Intense-Field Laser-Atom Physics. *Quantum and Semiclassical Optics* **1995**, *7*, 423.

(101) Krause, J. L.; Schafer, K. J.; Kulander, K. C. High-Order Harmonic Generation from Atoms and Ions in the High Intensity Regime. *Physical Review Letters* **1992**, *68*, 3535.

(102) Uphues, T., High Harmonic Generation In Ultrafast Optics and X-rays Group at CFEL: 2013.

(103) Keldysh, L. V. Ionization in the Field of a Strong Electromagnetic Wave. *Soviet Physics JETP* **1965**, *20*, 1307.

(104) Ammosov, M. V.; Delone, N. B.; Kraĭnov, V. P. Tunnel Ionization of Complex Atoms and of Atomic Ions in an Alternating Electromagnetic Field. *Soviet Physics JETP* **1986**, *64*, 1191.

(105) Winterfeldt, C.; Spielmann, C.; Gerber, G. Colloquium: Optimal Control of High-Harmonic Generation. *Reviews of Modern Physics* **2008**, *80*, 117–140.

(106) Gallmann, L.; Cirelli, C.; Keller, U. Attosecond Science: Recent Highlights and Future Trends. *Annual Review of Physical Chemistry* **2012**, *63*, 447–469.

(107) Popmintchev, T. et al. Bright Coherent Ultrahigh Harmonics in the keV X-ray Regime from Mid-Infrared Femtosecond Lasers. *Science* **2012**, *336*, 1287–1291.

(108) Loh, Z.-H.; Khalil, M.; Correa, R. E.; Leone, S. R. A Tabletop Femtosecond Time-Resolved Soft X-ray Transient Absorption Spectrometer. *Review of Scientific Instruments* **2008**, *79*, 073101.

(109) Lewenstein, M.; Balcou, P.; Ivanov, M. Y.; L'Huillier, A.; Corkum, P. B. Theory of High-Harmonic Generation by Low-Frequency Laser Fields. *Physical Review A* **1994**, *49*, 2117–2132.

(110) Levesque, J.; Zeidler, D.; Marangos, J. P.; Corkum, P. B.; Villeneuve, D. M. High Harmonic Generation and the Role of Atomic Orbital Wave Functions. *Physical Review Letters* **2007**, *98*, 183903.

(111) Li, J.; Chew, A.; Hu, S.; White, J.; Ren, X.; Han, S.; Yin, Y.; Wang, Y.; Wu, Y.; Chang, Z. Double Optical Gating for Generating High Flux Isolated Attosecond Pulses in the Soft X-ray Regime. *Optics Express* **2019**, *27*, 30280–30287.

(112) Jiang, C.-M. Charge Carrier Dynamics in Transition Metal Oxides Studied by Femtosecond Transient Extreme Ultraviolet Absorption Spectroscopy, Ph.D. Thesis, University of California, Berkeley, 2015.

(113) Gerardo, J. B.; Verdeyen, J. T. Plasma Refractive Index by a Laser Phase Measurement. *Applied Physics Letters* **1963**, *3*, 121.

(114) Popmintchev, T.; Chen, M.-C.; Bahabad, A.; Gerrity, M.; Sidorenko, P.; Cohen, O.; Christov, I. P.; Murnane, M. M.; Kapteyn, H. C. Phase Matching of High Harmonic Generation in the Soft and Hard X-ray Regions of the Spectrum. *PNAS* **2009**, *106*, 10516–10521.

(115) Rothhardt, J.; Krebs, M.; Hädrich, S.; Demmler, S.; Limpert, J.; Tünnermann, A. Absorption-Limited and Phase-Matched High Harmonic Generation in the Tight Focusing Regime. *New Journal of Physics* **2014**, *16*, 033022.

(116) Balcou, P.; L'Huillier, A. Phase-Matching Effects in Strong-Field Harmonic Generation. *Physical Review A* **1993**, *47*, 1447–1459.

(117) Kroh, T.; Jin, C.; Krogen, P.; Keathley, P. D.; Calendron, A.-L.; Siqueira, J. P.; Liang, H.; Falcão-Filho, E. L.; Lin, C. D.; Kärtner, F. X.; Hong, K.-H. Enhanced High-Harmonic Generation up to the Soft X-ray Region Driven by Mid-Infrared Pulses Mixed with their Third Harmonic. *Optics Express* **2018**, *26*, 16955–16969.

(118) Samson, J. A. R.; Stolte, W. C. Precision Measurements of the Total Photoionization Cross-Sections of He, Ne, Ar, Kr, and Xe. *Journal of Electron Spectroscopy and Related Phenomena* **2002**, *123*, 265–276.

(119) Wahlström, C.-G.; Larsson, J.; Persson, A.; Starczewski, T.; Svanberg, S.; Salières, P.; Balcou, P.; L'Huillier, A. High-Order Harmonic Generation in Rare Gases with an Intense Short-Pulse Laser. *Physical Review A* **1993**, *48*, 4709–4720.

(120) Christov, I. P.; Bartels, R.; Kapteyn, H. C.; Murnane, M. M. Attosecond Time-Scale Intra-Atomic Phase Matching of High Harmonic Generation. *Physical Review Letters* **2000**, *86*, 5458–5461.

(121) Loriot, V.; Marciniak, A.; Quintard, L.; Despré, V.; Schindler, B.; Compagnon, I.; Concina, B.; Celep, G.; Bordas, C.; Catoire, F.; Constant, E.; Lépine, F. Resolving XUV Induced Femtosecond and Attosecond Dynamics in Polyatomic Molecules with a Compact Attosecond Beamline. *Journal of Physics: Conference Series* **2015**, *635*, 012006.

(122) Chang, H.-T. Electronic and Structural Dynamics in Solids with Attosecond Transient Absorption Spectroscopy, Ph.D. Thesis, University of California, Berkeley, 2021.

(123) Shafir, D.; Y, M.; Villeneuve, D. M.; Corkum, P. B.; Dudovich, N. Atomic Wavefunctions Probed Through Strong-Field Light-Matter Interaction. *Nature Physics* **2009**, *5*, 412–416.

(124) Timmers, H.; Sabbar, M.; Hellwagner, J.; Kobayashi, Y.; Neumark, D. M.; Leone, S. R. Polarization-Assisted Amplitude Gating and a Route to Tunable, High-Contrast Attosecond Pulses. *Optica* **2016**, *3*, 707–710.

(125) Porter, I. J.; Lee, A.; Cushing, S. K.; Chang, H.-T.; Ondry, J. C.; Alivisatos, A. P.; Leone, S. R. Characterization of Carrier Cooling Bottleneck in Silicon Nanoparticles by Extreme Ultraviolet (XUV) Transient Absorption Spectroscopy. *The Journal of Physical Chemistry C* **2021**, *125*, 9319–9329.

(126) Misoguti, L.; Christov, I. P.; Backus, S.; Murnane, M. M.; Kapteyn, H. C. Nonlinear Wave-Mixing Processes in the Extreme Ultraviolet. *Physical Review A* **2005**, *72*, 063803.

(127) He, X.; Dahlström, J. M.; Rakowski, R.; Heyl, C. M.; Persson, A.; Mauritsson, J.; L'Huillier, A. Interference Effects in Two-Color High-Order Harmonic Generation. *Physical Review A* **2010**, *82*, 033410.

(128) Kfir, O.; Bordo, E.; Haham, G. I.; Lahav, O.; Fleischer, A.; Cohen, O. In-Line Production of a Bi-Circular Field for Generation of Helically Polarized High-Order Harmonics. *Applied Physics Letters* **2016**, *108*, 211106.

(129) Henke, B. L.; Gullikson, E. M.; Davis, J. C. X-ray Interactions: Photoabsorption, Scattering, Transmission, and Reflection at E=50-30000 eV, Z=1-92. *Atomic Data and Nuclear Data Tables* **1993**, *54*, 181–342.

(130) *The Fundamentals of High, Ultra-High & Extreme High Vacuum*; Vacuum Science World: 2022.

(131) Hablanian, M. H., 11. Design of High Vacuum Systems In *Methods in Experimental Physics*, Weissler, G. L., Carlson, R. W., Eds.; Academic Press: 1980; Vol. 14.

(132) Danielson, P. Understanding Virtual Leaks. *The Vacuum Lab* **2009**, *20*.

(133) Song, X.-G.; Park, Y.-C.; Park, J.-H. Blowdown Prediction of a Conventional Pressure Relief Valve with a Simplified Dynamic Model. *Mathematical and Computer Modelling* **2013**, *57*, 279–288.

(134) Masharipovich, Q. U. Laboratory Equipment of Overpressure Determination on Standard. *International Journal of Development and Public Policy* **2021**, *1*, 138–143.

(135) Takahasi, E.; Tosa, V.; Nabekawa, Y.; Midorikama, K. Experimental and Theoretical Analyses of a Correlation Between Pump-Pulse Propagation and Harmonic Yield in a Long-Interaction Medium. *Physical Review A* **2003**, *68*, 023808.

(136) Barreau, L.; Ross, A. D.; Garg, S.; Kraus, P. M.; Neumark, D. M.; Leone, S. R. Efficient Table-Top Dual-Wavelength Beamline for Ultrafast Transient Absorption Spectroscopy in the Soft X-Ray Region. *Scientific Reports* **2020**, *10*, 5773.

(137) Steingrube, D. S.; Schulz, E.; Binhammer, T.; Vockerodt, T.; Morgner, U.; Kovačev, M. Generation of High-Order Harmonics with Ultra-Short Pulses from Filamentation. *Optics Express* **2009**, *17*, 16177–16182.

(138) Sayrac, M.; Kolomenskii, A. A.; Strohaber, J.; Schuessler, H. A. High Harmonic Generation in Ne and H_2 Gas Mixtures. *Journal of the Optical Society of America B* **2015**, *32*, 2400–2405.

(139) Kanai, T.; Takahashi, E. J.; Nabekawa, Y.; Midorikawa, K. Destructive Interference During High Harmonic Generation in Mixed Gases. *Physical Review Letters* **2007**, *98*, 153904.

(140) Feng, L.; Li, W.; Liu, H. Intensity Enhancement of Attosecond XUV Pulse by Using Asymmetric Inhomogeneous Mid-Infrared Down-Chirped Field. *International Journal of Modern Physics B* **2017**, *31*, 1750185.

(141) Petrakis, S.; Bakarezos, M.; Tatarakis, M.; Benis, E. P.; Papadogiannis, N. A. Electron Quantum Path Control in High Harmonic Generation Via Chirp Variation of Strong Laser Pulses. *Scientific Reports* **2021**, *11*, 23882.

(142) Krüger, M.; Azoury, D.; Bruner, B. D.; Dudovich, N. The Role of Electron Trajectories in XUV-Initiated High-Harmonic Generation. *Applied Science* **2019**, *9*, 378.

(143) Sutherland, J. R. M. Phase-Matching Optimization of Laser High-Order Harmonics Generated in a Gas Cell, Ph.D. Thesis, Brigham Young University, 2005.

(144) Zhang, Q.; Zhao, K.; Li, J.; Chini, M.; Cheng, Y.; Wu, Y.; Cunningham, E.; Chang, Z. Suppresion of Driving Laser in High Harmonic Generation with a Microchannel Plate. *Optics Letters* **2014**, *39*, 3670–3673.

(145) Hagelstein, P. Design Studies of a Nearly Stigmatic EUV Toroidal Grating Spectrometer. *Proceedings of SPIE, Ultrashort Wavelength Lasers* **1992**, *1551*, 138–142.

(146) Huber, M. C. E.; Tondello, G. Stigmatic Performance of an EUV Spectrograph with a Single Toroidal Grating. *Applied Optics* **1979**, *18*, 3948–3953.

(147) Shin, H.-J.; Kim, D.-E.; Lee, T.-N. Space-Resolved Extreme Ultraviolet (XUV) Spectroscopy Using a Toroidal Mirror. *Reviews of Scientific Instruments* **1995**, *66*, 4222–4226.

(148) Poletto, L.; Frassetto, F.; Calegari, F.; Anumula, S.; Trabattoni, A.; Nisoli, M. Micro-Focusing of Attosecond Pulses by Grazing-Incidence Toroidal Mirrors. *Optics Express* **2013**, *21*, 13040–13051.

(149) Takahashi, E. J.; Hasegawa, H.; Nabekawa, Y.; Midorikawa, K. High-Throughput, High-Damage-Threshold Broadband Beam Splitter for High-Order Harmonics in the Extreme-Ultraviolet Region. *Optics Letters* **2004**, *29*, 507–509.

(150) Lin, M.-F.; Verkamp, M. A.; Ryland, E. S.; Zhang, K.; Vura-Weis, J. Impact of Spatial Chirp on High-Harmonic Extreme Ultraviolet Absorption Spectroscopy of Thin Films. *Journal of the Optical Society of America B* **2016**, *33*, 1986–1992.

(151) Boyle, W. S.; Smith, G. E. Charge Coupled Semiconductor Devices. *Bell Systems Technology Journal* **1970**, *49*, 587–593.

(152) Fossum, E. R.; Hondongwa, D. B. A Review of the Pinned Photodiode for CCD and CMOS Image Sensors. *IEEE Journal of the Electron Devices Society* **2014**, *2*, 33–43.

(153) Tompsett, M. F.; Amelio, G. F.; W. J. Bertram, J.; Buckley, R. R.; McNamara, W. J.; J. C. Mikkelsen, J.; Sealer, D. A. Charge-Coupled Imaging Devices: Experimental Results. *IEEE Transactions on Electron Devices* **1971**, *18*, 992–996.

(154) Jansen, R. A. Astronomy with Charge Coupled Devices, 2013.

(155) PIXIS-XO: 400B, 400B, Rev. P1; Teledyne Princeton Instruments, 2022.

(156) Van Nieuwenhove, V.; de Beenhouwer, J.; de Carlo, F.; Mancini, L.; Marone, F.; Sijbers, J. Dynamic Intensity Normalization Using Eigen Flat Fields in X-ray Imaging. *Optics Express* **2015**, *23*, 27975–27989.

(157) Künzel, S.; Williams, G. O.; Boutu, W.; Galtier, E.; Barbrel, B.; Lee, H. J.; Nagler, B.; Zastrau, U.; Dovilaire, G.; Lee, R. W.; Merdji, H.; Zeitoun, P.; Fajardo, M. Shot-to-Shot Intensity and Wavefront Stability of High-Harmonic Generation. *Applied Optics* **2015**, *54*, 4745–4749.

(158) Abegunde, O. O.; Akinlabi, E. T.; Oladijo, O. P.; Akinlabi, S.; Ude, A. U. Review: Overview of Thin Film Deposition Techniques. *AIMS Materials Science* **2019**, *6*, 174–199.

(159) Tan, R. T., Specularity, Specular Reflectance In *Computer Vision*, Ikeuchi, K., Ed.; Springer: Boston, MA, 2013.

(160) Fuller, M. P.; Griffiths, P. R. Diffuse Reflectance Measurements by Infrared Fourier Transform Spectrometry. *Analytical Chemistry* **1978**, *50*, 1906–1910.

(161) Stratton, J. A., *Electromagnetic Theory*; McGraw-Hill: New York, 1941.

(162) Zhu, G.; Kitur, J. K.; Gu, L.; Vella, J.; ad E. E. Narimanov, A. U.; Noginov, M. A. Gigantic Optical Nonlinearity: Laser-Induced Change of Dielectric Permittivity of the Order of Unity. *ACS Photonics* **2015**, *2*, 622–627.

(163) Tserkezis, C.; Gonçalves, P. A. D.; Wolff, C.; Todisco, F.; Busch, K.; Mortensen, N. A. Mie Excitons: Understanding Strong Coupling in Dielectric Nanoparticles. *Physical Review B* **2018**, *98*, 155439.

(164) Huffman, D. R.; Bohren, C. F., *Absorption and Scattering of Light by Small Particles*; Wiley and Songs, Incorporated: 1998.

(165) Shari'ati, Y.; Vura-Weis, J. Polymer Thin Films as Universal Substrates for Extreme Ultraviolet Absorption Spectroscopy of Molecular Transition Metal Complexes. *Journal of Synchrotron Radiation* **2021**, *28*, 1850–1857.

(166) Baig, N.; Kammakakam, I.; Falath, W. Nanomaterials: A Review of Synthesis Methods, Properties, Recent Progress, and Challenges. *Materials Advances* **2021**, *2*, 1821–1871.

(167) Wang, N.; Fuh, J. Y. H.; Dheen, S. T.; Kumar, A. S. Synthesis Methods of Functionalized Nanoparticles: A Review. *Bio-Design and Manufacturing* **2021**, *4*, 379–404.

(168) Chávez, F.; Pérez-Sánchez, G. F.; Goiz, O.; Zaca-Morán, P.; Peña-Sierra, R.; Morales-Acevedo, A.; Felipe, C.; Soledad-Priego, M. Sensing Performance of Palladium-Functionalized WO_3 Nanowires by a Drop-Casting Method. *Applied Surface Science* **2013**, *275*, 28–35.

(169) Qdemat, A.; Kentzinger, E.; Buitenhuis, J.; Rücker, U.; Ganeva, M.; Brückel, T. Self Assemlbed Monolayer of Silica Nanoparticles with Improved Order by Drop Casting. *RSC Advances* **2020**, *10*, 18339–18347.

(170) Zhang, Y.; Kumar, A. K. S.; Li, D.; Yang, M.; Compton, R. G. Nanoparticle- and Nanotube-Modified Electrodes: Response of Drop-Cast Surfaces. *ChemElectroChem* **2020**, *7*, 4614–4624.

(171) Kumar, A. K. S.; Zhang, Y.; Li, D.; Compton, R. G. A Mini-Review: How Reliable is the Drop Casting Technique? *Electrochemistry Communications* **2020**, *121*, 106867.

(172) Nayfeh, O. M.; Antoniadis, D. A.; Mantey, K.; Nayfeh, M. H. Uniform Delivery of Silicon Nanoparticles on Device Quality Substrates Using Spin Coating from Isopropyl Alcohol Colloids. *Applied Physics Letters* **2009**, *94*, 043112.

(173) Pi, X.; Li, Q.; Li, D.; Yang, D. Spin-Coating Silicon-Quantum-Dot Ink to Improve Solar Cell Efficiency. *Solar Energy Materials and Solar Cells* **2011**, *95*, 2941–2945.

(174) Tyona, M. D. A Theoretical Study on Spin Coating Technique. *Advances in Materials Research* **2013**, *2*, 195–208.

(175) Sahu, N.; Parija, B.; Panigrahi, S. Fundamental Understanding and Modeling of Spin Coating Process: A Review. *Indian Journal of Physics* **2009**, *83*, 493–502.

(176) Lee, U. G.; Kim, W.-B.; Han, D. H.; Chung, H. S. A Modified Equation for Thickness of the Film Fabricated by Spin Coating. *Symmetry* **2019**, *11*, 1183.

(177) Bornside, D. E.; Macosko, C. W.; Scriven, L. E. Spin Coating: One-Dimensional Model. *Journal of Applied Physics* **1989**, *66*, 5185–5193.

(178) Iskandar, F. Nanoparticle Processing for Optical Applications - A Review. *Advanced Powder Technology* **2009**, *20*, 283–292.

(179) Norouzi, M.; Garekani, A. A. Corrosion Protection by Zirconia-Based Thin Films Deposited by a Sol-Gel Spin Coating Method. *Ceramics International* **2013**, *40*, 2857–2861.

(180) Diao, J.; Ren, D.; Engstrom, J. R.; Lee, K. H. A Surface Modification Strategy on Silicon Nitride for Developing Biosensors. *Analytical Biochemistry* **2005**, *343*, 322–328.

(181) Ribiero, T.; Baleizão, C.; Farinha, J. P. S. Functional Films from Silica/Polymer Nanoparticles. *Materials* **2014**, *7*, 3881–3900.

(182) Born, P.; Kraus, T. Ligand-Dominated Temperature Dependence of Agglomeration Kinetics and Morphology in Alkyl-Thiol-Coated Gold Nanoparticles. *Physical Review E* **2013**, *87*, 062313.

(183) Wan, J.; Kim, Y.; Mulvihill, M. J.; Tokunaga, T. K. Dilution Destabilizes Engineered Ligand-Coated Nanoparticles in Aqueous Suspensions. *Environmental Toxicology and Chemistry* **2018**, *37*, 1301–1308.

(184) Garbin, V.; Crocker, J. C.; Stebe, K. J. Nanoparticles at Fluid Interfaces: Exploiting Capping Ligands to Control Adsorption, Stability and Dynamics. *Journal of Colloid and Interface Science* **2012**, *387*, 1–11.

(185) Wawrzynczyk, D.; Bednarkiewicz, A.; Nyk, M.; Cichos, J.; Karbowiak, M.; Hreniak, D.; Strek, W.; Samoc, M. Optimisation of Ligand Exchange Towards Stable Water Suspension of Crystalline $NaYF_4$:Er^{3+}, Yb^{3+} Nanoluminophors. *Journal of Nanoscience and Nanotechnology* **2012**, *12*, 1886–1891.

(186) Morsy, S. M. I. Role of Surfactants in Nanotechnology and Their Applications. *International Journal of Current Microbiology and Applied Sciences* **2014**, *3*, 237–260.

(187) Kida, T.; Oka, T.; Nagano, M. Synthesis and Application of Stable Copper Oxide Nanoparticle Suspensions for Nanoparticulate Film Fabrication. *Journal of the American Ceramic Society* **2007**, *90*, 107–110.

(188) Traina, C. A.; Schwartz, J. Surface Modification of Y_2O_3 Nanoparticles. *Langmuir* **2007**, *23*, 9158–9161.

(189) Pradhan, S.; hedberg, J.; Blomberg, E.; Wold, S.; Wallinder, I. O. Effect of Sonication on Particle Dispersion, Administered Dose and Metal Release of Non-Functionalized, Non-Inert Metal Nanoparticles. *Journal of Nanoparticle Research* **2016**, *18*, 285.

(190) Zhang, Y.; Chen, Y.; Westerhoff, P.; Hristovski, K.; Crittenden, J. C. Stability of Commercial Metal Oxide Nanoparticles in Water. *Water Research* **2008**, *42*, 2204–2212.

(191) Cohen, J. M.; Beltran-Huarac, J.; Pyrgiotakis, G.; Demokritou, P. Effective Delivery of Sonication Energy to Fasr Settling and Agglomerating Nanomaterial Suspensions for Cellular Studies: Implications for Stability, Particle Kinetics, Dosimetry and Toxicity. *NanoImpact* **2018**, *10*, 81–86.

(192) Kawashima, S.; Seo, J.-W. T.; Corr, D.; Hersam, M. C.; Shah, S. P. Dispersion of $CaCO_3$ Nanoparticles by Sonication and Surfactant Treatment for Application in Fly Ash-Cement Systems. *Materials and Structures* **2013**, *47*, 1011–1023.

(193) Kamalgharibi, M.; Hormozi, F.; Zamzamian, S. A. H.; Sarafraz, M. M. Experimental Studies on the Stability of CuO Nanoparticles Dispersed in Different Base Fluids: Influence of Stirring, Sonication and Surface Active Agents. *Heat and Mass Transfer* **2015**, *52*, 55–62.

(194) Grant Product Portfolio; Grant Instruments, 2022.

(195) Ultrasonic Liquid Processors; QSonica Sonicators, 2018.

(196) Baig, Z.; Mamat, O.; Mustapha, M.; Mumtaz, A.; Munir, K. S.; Sarfraz, M. Investigation of Tip Sonication Effects on Structural Quality of Graphene Nanoplatelets (GNPs) for Superior Solvent Dispersion. *Ultrasonics Sonochemistry* **2018**, *45*, 133–149.

(197) Sham, M. L.; Li, J.; Ma, P.; Kim, J.-K. Cleaning and Functionalization of Polymer Surfaces and Nanoscale Carbon Fillers by UV/Ozone Treatment: A Review. *Journal of Composite Materials* **2009**, *43*, 1537–1564.

(198) Diéguez, L.; Caballero, D.; Calderer, J.; Moreno, M.; Martínez, E.; Samitier, J. Optical Gratings Coated with Thin Si_3N_4 Layer for Efficient Immunosensing by Optical Waveguide Lightmode Spectroscopy. *Biosensors* **2012**, *2*, 114–126.

(199) Fan, F. R.; Luo, J.; Tang, W.; Li, C.; Zhang, C.; Tian, Z.; Wang, Z. L. Highly Transparent and Flexible Triboelectric Nanogenerators: Performance Improvements and Fundamental Mechanisms. *Journal of Materials Chemistry A* **2014**, *2*, 13219–13225.

(200) Crick, C. R.; Bachu, D. S.; Parkin, I. P. Superhydrophobic Silica Wool - A Facile Route to Separating Oil and Hydrophobic Solvents from Water. *Science and Technology of Advances Materials* **2014**, *15*, 065003.

(201) Sarkar, A.; Daniels-Race, T. Electrophoretic Deposition of Carbon Nanotubes on 3-Amino-Propyl-Triethoxysilane (APTES) Surface Functionalized Silicon Substrates. *Nanomaterials* **2013**, *3*, 272–288.

(202) Wagner, J.; Peng, W.; Vana, P. Polyethylene-Grafted Gold and Silver Nanoparticles Using Catalyzed Chain Growth (CCG). *Polymers* **2018**, *10*, 407.

(203) Bag, M.; Gehan, T. S.; Algaier, D. D.; Liu, F.; Nagarjuna, G.; Lahti, P. M.; Russel, T. P.; Venkataraman, D. Efficient Change Transport in Assemblies of Surfactant-Stabilized Semiconducting Nanoparticles. *Advanced Materials* **2013**, *25*, 6411–6415.

(204) Zhang, S.; Shen, L.; Deng, H.; Liu, Q.; You, X.; Yuan, J.; Jiang, Z.; Zhang, S. Ultrathin Membranes for Separations: A New Era Driven by Advanced Nanotechnology. *Advanced Materials* **2022**, 2108457.

(205) Fontana, L.; Fratoddi, I.; Venditti, I.; Ksenzov, D.; Russo, M. V.; Grigorian, S. Structural Studies on Drop-Cast Film Based on Functionalized Gold Nanoparticles Network: The Effect of Thermal Treatment. *Applied Surface Science* **2016**, *369*, 115–119.

(206) Alexandrov, V.; Rosso, K. M. Ab Initio Modeling of Fe(II) Adsorption and Interfacial Electron Transfer at Goethite (α-FeOOH) Surfaces. *Physical Chemistry Chemical Physics* **2015**, *17*, 14518.

(207) Rosso, K. M.; Smith, D. M. A.; Dupuis, M. An Ab Initio Model of Electron Transport in Hematite (α-Fe_2O_3) Basal Planes. *The Journal of Chemical Physics* **2003**, *118*, 6455.

(208) Iordanova, N.; Dupuis, M.; Rosso, K. M. Charge Transport in Metal Oxides: A Theoretical Study of Hematite α-Fe_2O_3. *The Journal of Chemical Physics* **2005**, *122*, 144305.

(209) Alexandrov, V.; Rosso, K. M. Electron Transport in Pure and Substituted Iron Oxyhydroxides by Small-Polaron Migration. *The Journal of Chemical Physics* **2014**, *140*, 234701.

(210) Devreese, J. T., Polarons In *Encyclopedia of Applied Physics*, Trigg, G. L., Ed.; Wiley-VCH: Hoboken, NJ, 1996; Vol. 14, pp 383–409.

(211) Wang, Z.; Bevan, K. H. Exploring the Impact of Semicore Level Electronic Relaxation on Polaron Dynamics: An Adiabatic Ab Initio Study of $FePO_4$. *Physical Review B: Condensed Matter and Marerials Physics* **2016**, *93*, 024303.

(212) Hulea, I. N.; Fratini, S.; Xie, H.; Mulder, C. L.; Iossad, N. N.; Rastelli, G.; Ciuchi, S.; Morpurgo, A. F. Tunable Frölich Polarons in Organic Single-Crystal Transistors. *Nature Materials* **2006**, *5*, 982–986.

(213) Sherman, D. M.; Waite, T. D. Electronic Spectra of Fe^{3+} Oxides and Oxide Hydroxides in the Near IR to Near UV. *American Mineralogist* **1985**, *70*, 1262–1269.

(214) Von der Heyden, B. P.; Roychoudhury, A. N.; Tyliszczak, T.; Myneni, S. C. B. Investigating Nanoscale Mineral Compositions: Iron L_3-Edge Spectroscopic Evaluation of Iron Oxide and Oxy-hydroxide Coordination. *American Mineralogist* **2017**, *102*, 674–685.

(215) Shim, S.-H.; Duffy, T. S. Raman Spectroscopy of Fe_2O_3 to 62 GPa. *American Mineralogist* **2002**, *87*, 318–326.

(216) Jubb, A. M.; Allen, H. C. Vibrational Spectroscopic Characterization of Hematite, Maghemite, and Magnetite Thin Films Produced by Vapor Deposition. *ACS Applied Materials and Interfaces* **2010**, *2*, 2804–2812.

(217) Blanchard, M.; Balan, E.; Giura, P.; Béneut, K.; Yi, H.; Morin, G.; Pinilla, C.; Lazzeri, M.; Floris, A. Infrared Spectroscopic Properties of Goethite: Anharmonic Broadening, Long-Range Electrostatic Effects and Al Substitution. *Physics and Chemistry of Minerals* **2014**, *41*, 289–302.

(218) Catti, M.; Valerio, G.; Dovesi, R. Theoretical Study of Electronic, Magnetic, and Structural Properties of α-Fe_2O_3, (Hematite). *Physical Review B: Condensed Matter and Marerials Physics* **1995**, *51*, 7441–7450.

(219) Gualtieri, A. F.; Venturelli, P. In Situ Study of the Goethite-Hematite Phase Transformation by Real Time Synchrotron Powder Diffraction. *American Mineralogist* **1999**, *84*, 895–904.

(220) Nagai, T.; Kagi, H.; Yamanaka, T. Variation of Hydrogen Bonded O—O Distances in Goethite at High Pressure. *American Mineralogist* **2003**, *88*, 1423–1427.

(221) Yang, H.; Lu, R.; Downs, R. T.; Costin, G. Goethite, α-FeO(OH), From Single-Crystal Data. *Acta Crystallographica Section E: Structure Reports Online* **2006**, *62*, i250–i252.

(222) Sivula, K.; le Formal, F.; Grätzel, M. Solar Water Splitting: Progress Using Hematite (α-Fe_2O_3) Photoelectrodes. *ChemSusChem* **2011**, *4*, 432–449.

(223) Zhou, X.; Yang, H.; Wang, C.; Mao, X.; Wang, Y.; Yang, Y.; Liu, G. Visible Light Induced Photocatalytic Degradation of Rhodamine B on One-Dimensional Iron Oxide Particles. *The Journal of Physical Chemistry C* **2010**, *114*, 17051–17061.

(224) Scheinost, A. C.; Schulze, D. G.; Schwertmann, U. Diffuse Reflectance Spectra of Al Substituted Goethite: A Ligand Field Approach. *Clays and Clay Minerals* **1999**, *47*, 156–164.

(225) Miedema, P. S.; de Groot, F. M. F. The Iron *L* Edges: Fe 2p X-ray Absorption and Electron Energy Loss Spectroscopy. *Journal of Electron Spectroscopy and Related Phenomena* **2013**, *187*, 32–48.

(226) Sturman, B.; Podivlov, E.; Gorkunov, M. Origin of Stretched Exponential Relaxation for Hopping-Transport Models. *Physical Review Letters* **2003**, *91*, 176602.

(227) Kerisit, S.; Rosso, K. M. Kinetic Monte Carlo Model of Charge Transport in Hematite. *The Journal of Chemical Physics* **2007**, *127*, 124706.

(228) Smart, T. J.; Ping, Y. Effect of Defects on the Small Polaron Formation and Transport Properties of Hematite from First Principles Calculations. *Journal of Physics: Condensed Matter* **2017**, *29*, 394006.

(229) Kfir, O.; Bordo, E.; Haham, G. I.; Lahav, O.; Fleischer, A.; Cohen, O. In-line Production of a Bi-circular Field for Generation of Helically Polarized High-Order Harmonics. *Applied Physics Letters* **2016**, *108*, 211106.

(230) Green, M. A.; Hishikawa, Y.; Dunlop, E. D.; Levi, D. H.; Hohl-Ebinger, J.; Ho-Baillie, A. W. Y. Solar Cell Efficiency Tables (version 52). *Progress in Photovoltaics* **2018**, *26*, 427–436.

(231) Ager, J. W.; Shaner, M. R.; Walczak, K. A.; Sharp, I. D.; Ardo, S. Experimental Demonstrations of Spontaneous, Solar-Driven Photoelectrochemical Water Splitting. *Energy and Environmental Science* **2015**, *8*, 2811–2824.

(232) Cheng, W.-H.; Richter, M. H.; May, M. M.; Ohlmann, J.; Lackner, D.; Dimroth, F.; Hannappel, T.; Atwater, H. A.; Lewerenz, H.-J. Monolithic Photoelectrochemical Device for Direct Water SPlitting with 19% Efficiency. *ACS Energy Letters* **2018**, *3*, 1795–1800.

(233) Aberle, A. G. Surface Passivation of Crystalline Silicon Solar Cells: A Review. *Progress in Photovoltaics* **2000**, *8*, 473–487.

(234) Hu, S.; Shaner, M. R.; Beardslee, J. A.; Lichterman, M.; Brunschwig, B. S.; Lewis, N. S. Amorphous TiO_2 Coatings Stabilize Si, GaAs, and GaP Photoanodes for Efficient Water Oxidation. *Science* **2014**, *344*, 1005–1009.

(235) Pan, L.; Kim, J. H.; Mayer, M. T.; Son, M.-K.; Ummadisingu, A.; Lee, J. S.; Hagfeldt, A.; Luo, J.; Grätzel, M. Boosting the Performance of Cu_2O Photocathodes for Unassisted Solar Water Splitting Devices. *Nature Catalysis* **2018**, *1*, 412–420.

(236) Bae, D.; Seger, B.; Vesborg, P. C. K.; Hansen, O.; Chorkendorff, I. Strategies for Stable Water Splitting via Protected Photoelectrodes. *Chemical Society Reviews* **2017**, *46*, 1933–1954.

(237) Gu, J.; Yan, Y.; Young, J. L.; Steirer, K. X.; Neale, N. R.; Turner, J. A. Water Reduction by a p-$GaInP_2$ Photoelectrode Stabilized by an Amorphous TiO_2 Coating and a Molecular Cobalt Catalyst. *Nature Materials* **2016**, *15*, 456–460.

(238) Zeng, G.; Qiu, J.; Li, Z.; Pavaskar, P.; Cronin, S. B. CO_2 Reduction to Methanol on TiO_2-Passivated GaP Photocatalysts. *ACS Catalysis* **2014**, *4*, 3512–3516.

(239) Kalamaras, E.; Maroto-Valer, M. M.; Shao, M.; Xuan, J.; Wang, H. Solar Carbon Fuel via Photoelectrochemistry. *Catalysis Today* **2018**, *317*, 56–75.

(240) Pham, H. H.; Wang, L.-W. Oxygen Vacancy and Hole Conduction in Amorphous TiO_2. *Physical Chemistry Chemical Physics* **2015**, *17*, 541–550.

(241) Hu, S.; Richter, M. H.; Lichterman, M. F.; Beardslee, J.; Mayer, T.; Brunschwig, B. S.; Lewis, N. S. Electrical, Photoelectrochemical, and Photoelectron Spectroscopic Investigation of the Interfacial Transport and Energetics of Amorphous TiO_2/Si Heterojunctions. *The Journal of Physical Chemistry C* **2016**, *120*, 3117–3129.

(242) Young, L. et al. Roadmap of Ultrafast X-ray Atomic and Molecular Physics. *Journal of Physics B: Atomic, Molecular and Optical Physics* **2018**, *51*, 032003.

(243) Kraus, P. M.; Zürch, M.; Cushing, S. K.; Neumark, D. M.; Leone, S. R. The Ultrafast X-ray Spectroscopic Revolution in Chemical Dynamics. *Nature Reviews Chemistry* **2018**, *2*, 82–94.

(244) Brabec, T.; Krausz, F. Intense Few-Cycle Laser Fields: Fronteirs of Nonlinear Optics. *Reviews of Modern Physics* **2000**, *72*, 545–591.

(245) Rehr, J. J. Failure of the Quasiparticle Picture of X-ray Absorption? *Foundations of Physics* **2003**, *33*, 1735–1742.

(246) Campbell, L.; Hedin, L.; Rehr, J. J.; Bardyszewski, W. Interference Between Extrinsic and Intrinsic Losses in X-ray Absorption Fine Structure. *Physical Review B* **2002**, *65*, 064107.

(247) Biswas, S.; Husek, J.; Londo, S.; Baker, L. R. Ultrafast Electron Trapping and Defect-Mediated Recombination in NiO Probed by Femtosecond Extreme Ultraviolet Reflection-Absorption Spectroscopy. *Journal of Physical Chemistry Letters* **2018**, *9*, 5047–5054.

(248) McDowell, M. T.; Lichterman, M. F.; Carim, A. I.; Liu, R.; Hu, S.; Brunschwig, B. S.; Lewis, N. S. The Influence of Structure and Processing on the Behavior of TiO_2 Protective Layers for Stabilization of n-Si/TiO_2/Ni Photoanodes for Water Oxidation. *ACS Applied Materials and Interfaces* **2015**, *7*, 15189–15199.

(249) Varache, R.; Leendertz, C.; Gueunier-Farret, M. E.; Haschke, J.; Muñoz, D.; Korte, L. Investigation of Selective Junctions Using a Newly Developed Tunnel Current Model for Solar Cell Applications. *Solar Energy Materials and Solar Cells* **2015**, *141*, 14–23.

(250) Vaida, M. E.; Leone, S. R. Femtosecond Extreme Ultraviolet Photoemission Spectroscopy: Observation of Ultrafast Charge Transfer at the n-TiO_2/p-Si(100) Interface with Controlled TiO_2 Oxygen Vacancies. *The Journal of Physical Chemistry C* **2016**, *120*, 2769–2776.

(251) Cushing, S. K.; Meng, F.; Zhang, J.; Ding, B.; Chen, C. K.; Chen, C.-J.; Liu, R.-S.; Bristow, A. D.; Bright, J.; Zheng, P.; Wu, N. Effects of Defects on Photocatalytic Activity of Hydrogen-Treated Titanium Oxide Nanobelts. *ACS Catalysis* **2017**, *7*, 1742–1748.

(252) Nowotny, J.; Alim, M. A.; Bak, T.; Idris, M. A.; Ionescu, M.; Prince, K.; Sahdan, M. Z.; Sopian, K.; Teridi, M. A. M.; Sigmund, W. Defect Chemistry and Defect Engineering of TiO_2-Based Semiconductors for Solar Energy Conversion. *Chemical Society Reviews* **2015**, *44*, 8424–8442.

(253) Nagamatsu, K. A.; Avasthi, S.; Sahasrabudhe, G.; Man, G.; Jhaveri, J.; Berg, A. H.; Schwartz, J.; Kahn, A.; Wagner, S.; Sturm, J. C. Titanium Dioxide/Silicon Hole-Blocking Selective Contact to Enable Double-Heterojunction Crystalline Silicon-Based Solar Cell. *Applied Physics Letters* **2015**, *106*, 123906.

(254) Garvie, L. A. J.; Craven, A. J.; Brydson, R. Use of Electron-Energy Loss Near-Edge Fine Structure in the Study of Minerals. *American Mineralogist* **1994**, *79*, 411–425.

(255) Dorkel, J. M.; Leturcq, P. Carrier Mobilities in Silicon Semi-Empirically Related to Temperature, Doping and Injection Level. *Solid State Electronics* **1981**, *24*, 821–825.

(256) Gao, L.; Li, Q.; Chen, H.; Hayase, S.; Ma, T. In Situ Fabrication of Nanoepitaxial TiO_2 Protection Layer on Si Substrate: Hole Chemical Conduction Instead of Tunneling Effect. *Solar RRL* **2017**, *1*, 1700064.

(257) Schultze, M.; Bothschafter, E. M.; Sommer, A.; Holzner, S.; Schweinberger, W.; Fiess, M.; Hofstetter, M.; Kienberger, R.; Apalkov, V.; Yakolev, V. S.; Stockman, M. I.; Krausz, F. Controlling Dielectrics with the Electric Field of Light. *Nature* **2012**, *493*, 75–78.

(258) Schiffrin, A. et al. Optical-Field-Induced Current in Dielectrics. *Nature* **2012**, *493*, 70–74.

(259) Lenzner, M.; Krüger, J.; Sartania, S.; Cheng, Z.; Spielmann, C.; Mourou, C.; Kautek, W.; Krausz, F. Femtosecond Optical Breakdown in Dielectrics. *Physical Review Letters* **1998**, *80*, 4076–4079.

(260) Neusel, C.; Schneider, G. A. Size-Dependence of the Dielectric Breakdown Strength from Nano- to Millimeter Scale. *Journal of the Mechanics and Physics of Solids* **2014**, *63*, 201–213.

(261) Titova, V.; Startsev, D.; Schmidt, J. Electron-Selective Atomic-Layer-Deposited TiO_X Layers: Impact of Post-Deposition Annealing and Implementation into n-Type Silicon Solar Cells. *AIP Conference Proceedings* **2018**, *1999*, 040022.

(262) Giannozzi, P. et al. Quantum ESPRESSO: A Modular and Open-Source Software Project for Quantum Simulations of Materials. *Journal of Physics: Condensed Matter* **2009**, *21*, 395502.

(263) Shirley, E. L. Local Screening of a Core Hole: A Real-Space Approach Applied to Hafnium Oxide. *Ultramicroscopy* **2006**, *106*, 986–993.

(264) Levine, Z. H.; Louie, S. G. New Model Dielectric Function and Exchange-Correlation Potential for Semiconductors and Insulators. *Physical Review B* **1982**, *25*, 6310–6316.

(265) Evans, C. C.; Bradley, J. D. B.; Martí-Panameño, E. A.; Mazur, E. Mixed Two- and Three-Photon Absorption in Bulk Rutile (TiO_2) Around 800 nm. *Optics Express* **2012**, *20*, 3118–3128.

(266) Ohtaka, K.; Tanabe, Y. Golden-Rule Approach to the Soft-X-ray-Absorption Problem. III. The Temperature Dependence. *Physical Review B* **1984**, *30*, 4235–4258.

(267) Froitzheim, A.; Stangl, R.; Elstner, L.; Kriegel, M.; Fuhs, W., AFORS-HET: A Computer-Program for the Simulation of Heterojunction Solar Cells to be Distributed for Public Use In *Proceedings of 3rd World Conference on Photovoltaic Energy Conversion*; IEEE: 2003, pp 279–282.

(268) Battaglia, C.; Cuevas, A.; de Wolf, S. High-Efficiency Crystalline Silicon Solar Cells: Status and Perspectives. *Energy and Environmental Science* **2016**, *9*, 1552–1576.

(269) Liu, J.; Yao, Y.; Xiao, S.; Gu, X. Review of Status Developments of High-Efficiency Crystalline Silicon Solar Cells. *The Journal of Physics D: Applied Physics* **2018**, *51*, 123001.

(270) Richter, A.; Hermle, M.; Glunz, S. W. Reassessment of the Limiting Efficiency for Crystalline Silicon Solar Cells. *IEEE Journal of Photovoltaics* **2013**, *3*, 1184–1191.

(271) Conibeer, G.; Elkins-Duakes, N.; Guillemoles, J. F.; König, D.; Cho, E.-C.; Jiang, C.-W.; Shrestha, S.; Green, M. Progress on Hot Carrier Cells. *Solar Energy Materials and Solar Cells* **2009**, *93*, 713–719.

(272) Esmaielpour, H.; Whiteside, V. R.; Piyathilaka, H. P.; Vijeyaragunathan, S.; Wang, B.; Adcock-Smith, E.; Roberts, K. P.; Mishima, T. D.; Santos, M. B.; Bristow, A. D.; Sellers, I. R. Enhanced Hot Electron Lifetimes in Quantum Wells with Inhibited Phonon Coupling. *Scientific Reports* **2018**, *8*, 12473.

(273) König, D.; Casalenuovo, K.; Takeda, Y.; Conibeer, G.; Guillemoles, J. F.; Patterson, R.; Huang, L. M.; Green, M. A. Hot Carrier Solar Cells: Principles, Materials and Design. *Physical Review E* **2010**, *42*, 2862–2866.

(274) Meyer, R.; Comtesse, D. Vibrational Density of States of Silicon Nanoparticles. *Physical Review B: Condensed Matter and Materials Physics* **2011**, *83*, 014301.

(275) Fang, K.-C.; Weng, C.-I.; Ju, S.-P. An Investigation into the Structural Features and Thermal Conductivity of Silicon Nanoparticles Using Molecular Dynamics Simulations. *Nanotechnology* **2006**, *17*, 3909–3914.

(276) Conibeer, G.; Patterson, R.; Huang, L.; Guillemoles, J. F.; König, D.; Shrestha, S.; Green, M. Modelling of Hot Carrier Solar Cell Absorbers. *Solar Energy Materials and Solar Cells* **2010**, *94*, 1516–1521.

(277) Conibeer, G. J.; König, D.; Green, M. A.; Guillemoles, J. F. Slowing of Carrier Cooling in Hot Carrier Solar Cells. *Thin Solid Films* **2008**, *516*, 6948–6953.

(278) Prokofiev, A. A.; Poddubny, A. N.; Yassievich, I. N. Phonon Decay in Silicon Nanocrystals: Fast Phonon Recycling. *Condensed Matter and Material Physics* **2014**, *89*, 125409.

(279) Seres, E.; Namba, J. S. C. S. S. Core-Level Attosecond Transient Absorption Spectroscopy of Laser-Dressed Solid Films of Si and Zr. *Physical Review B* **2016**, *94*, 165125.

(280) Vrakking, M., Attosecond and XUV Physics: Ultrafast Dynamics and Spectroscopy In *Attosecond and XUV Physics: Ultrafast Dynamics and Spectroscopy*, Schultz, T., Vrakking, M., Eds.; Wiley-VCH: Weinheim, Germany, 2014, pp 1–16.

(281) Timmers, H.; Kobayashi, Y.; Chang, K. F.; Reduzzi, M.; Neumark, D. M.; Leone, S. R. Generating High-Contrast, Near Single-Cycle Waveforms with Third-Order Dispersion Compensation. *Optics Letters* **2017**, *42*, 811.

(282) King, G. C.; Tronc, M.; Read, F. H.; Bradford, R. C. An Investigation of the Structure Near the $L_{2,3}$ Edges of Argon, the $M_{4,5}$ Edges of Krypton and the $N_{4,5}$ Edges of Xenon, Using Electron Impact with High Resolution. *The Journal of Physics B: Atomic and Molecular Physics* **1977**, *10*, 3357.

(283) Porter, I. J.; Cushing, S. K.; Carneiro, L. M.; Lee, A.; Ondry, J. C.; Dahl, J. C.; Chang, H.-T.; Alivisatos, A. P.; Leone, S. R. Supporting Information for: Photoexcited Small Polaron Formation in Goethite (α-FeOOH) Nanorods Probed by Transient Extreme Ultraviolet Spectroscopy. *The Journal of Physical Chemistry Letters* **2018**, *9*, 4120–4124.

(284) Green, M. A. Self-Consistent Optical Parameters of Intrinsic Silicon at 300 K Including Temperature Coefficients. *Solar Energy Materials and Solar Cells* **2008**, *92*, 1305–1310.

(285) Downs, R. T.; Bartelmehs, K. L.; Gibbs, G. V.; Boisen, M. B. Interactive Software for Calculating and Displaying X-ray or Neutron Powder Diffractometer Patterns of Crystalline Materials. *American Mineralogist* **1993**, *78*, 1104–1107.

(286) NIST X-ray Photoelectron Spectroscopy Database, NIST Standard Reference Database Number 20, National Institute of Standards and Technology: Gaithersburg, MD, 2000.

(287) Sun, Y.; Wu, D.; Liu, K.; Zheng, F. Colossal Permittivity and Low Dielectric Loss of Thermal Oxidation Single-Crystalline Si Wafers. *Materials (Basel)* **2019**, *12*, 1102.

(288) Smilgies, D. M. Scherrer Grain-Size Analysis Adapted to Grazing-Incidence Scattering with Area Detectors. *Journal of Applied Crystallography* **2009**, *42*, 1030–1034.

(289) Jackson, W. B.; Johnson, N. M.; Biegelsen, D. K. Density of Gap States of Silicon Grain Boundaries Determined by Optical Absorption. *Applied Physics Letters* **1983**, *43*, 195–197.

(290) Nilsson, A. Applications of Core Level Spectroscopy to Adsorbates. *The Journal of Electron Spectroscopy and Related Phenomena* **2002**, *126*, 3–42.

(291) Dinh, L.; Chase, L.; Balooch, M.; Siekhaus, W.; Wooten, F. Optical Properties of Passivated Si Nanocrystals and SiO_X Nanostructures. *Physical Review B: Condensed Matter and Materials Physics* **1996**, *54*, 5029–5037.

(292) Matsumoto, T.; Suzuki, J. I.; Ohnuma, M.; Kanemitsu, Y.; Matsumoto, Y. Evidence of Quantum Size Effect in Nanocrystalline Silicon by Optical Absorption. *Physical Review B: Condensed Matter and Materials Physics* **2001**, *63*, 195322.

(293) Ley, L.; Reichardt, J.; Johnson, R. L. Static Charge Fluctuations in Amorphous Silicon. *Physical Review Letters* **1982**, *49*, 1664–1667.

(294) Sakurai, T.; Sugano, T. Theory of Continuously Distributed Trap States at Si-SiO_2 Interfaces. *The Journal of Applied Physics* **1981**, *52*, 2889–2896.

(295) Kubota, T.; Asano, A.; Nishioka, Y.; Kobayashi, H. Theoretical and Spectroscopic Studies of Gap-States at Ultrathin Silicon Oxide/Silicon Interfaces. *The Journal of Chemical Physics* **1999**, *111*, 8136–8143.

(296) Janai, M.; Allred, D. D.; Booth, D. C.; Seraphin, B. O. Optical Properties and Structure of Amorphous Silicon Films Prepared by CVD. *Solar Energy Materials* **1979**, *1*, 11–27.

(297) Demichelis, F.; Minetti-Mezzetti, E.; Tagliaferro, A.; Tresso, E.; Rava, P.; Ravindra, N. M. Optical Properties of Hydrogenated Amorphous Silicon Carbide Films. *Journal of Applied Physics* **1986**, *59*, 611–618.

(298) Schultze, M.; Ramasesha, K.; Pemmaraju, C. D.; Sato, S. A.; Whitmore, D.; Gandman, A.; Prell, J. S.; Borja, L. J.; Prendergast, D.; Yabana, K.; Neumark, D. M.; Leone, S. R. Attosecond Band-Gap Dynamics in Silicon. *Science* **2014**, *346*, 1348–1352.

(299) Sabbah, A. J.; Riffe, D. M. Femtosecond Pump-Probe Reflectivity Study of Silicon Carrier Dynamics. *Physical Review B: Condensed Matter and Materials Physics* **2002**, *66*, 165217.

(300) Lee, S. H. Nonequilibrium Heat Transfer Characteristics During Ultrafast Pulse Laser Heating of a Silicon Microstructure. *Journal of Mechanical Science and Technology* **2005**, *19*, 1378–1389.

(301) Harb, M.; Ernstorfer, R.; Dartigalongue, T.; Hebeisen, C. T.; Jordan, R. E.; Miller, R. J. D. Carrier Relaxation and Lattice Heating Dynamics in Silicon Revealed by Femtosecond Electron Diffraction. *The Journal of Physical Chemistry B* **2006**, *110*, 25308–25313.

(302) Cuffe, J.; Ristow, O.; Chávez, E.; Shchepetov, A.; Chapuis, P.-O.; Alzina, F.; Hettich, M.; Prunnila, M.; Ahopelto, J.; Dekorsy, T.; Sotomayor-Torres, C. M. Lifetimes of Confined Acoustic Phonons in Ultrathin Silicon Membranes. *Physical Review Letters* **2013**, *110*, 095503.

(303) Cushing, S. K.; Porter, I. J.; de Roulet, B. R.; Lee, A.; Marsh, B. M.; Szoke, S.; Vaida, M. E.; Leone, S. R. Layer-Resolved Ultrafast XUV Measurement of Hole Transport in a Ni-TiO_2-Si Photoanode. *Science Advances* **2020**, *6*, eaay6650.

(304) Richter, A.; Glunz, S. W.; Werner, F.; Schmidt, J.; Cuevas, A. Improved Quantitative Description of Auger Recombination in Crystalline Silicon. *Physical Review B: Condensed Matter and Materials Physics* **2012**, *86*, 165202.

(305) Sjodin, T.; Petek, H.; Dai, H.-L. Ultrafast Carrier Dynamics in Silicon: A Two-Color Transient Reflection Grating Study on a (111) Surface. *Physical Review Letters* **1998**, *81*, 5664–5667.

(306) Amit, I.; Englander, D.; Horvitz, D.; Sasson, Y.; Rosenwaks, Y. Density and Energy Distribution of Interface States in the Grain Boundaries of Polysilicon Nanowire. *Nano Letters* **2014**, *14*, 6190–6194.

(307) Seto, J. Y. W. The Electrical Properties of Polycrystalline Silicon Films. *The Journal of Applied Physics* **1975**, *46*, 5247–5254.

(308) De Graaff, H. C.; Huybers, M.; de Groot, J. G. Grain Boundary States and the Characteristics of Lateral Polysilicon Diodes. *Solid-State Electronics* **1982**, *25*, 67–71.

(309) Esser, A.; Seibert, K.; Kurz, H.; Parsons, G. N.; Wang, C.; Davidson, B. N.; Lucovsky, G.; Nemanich, R. J. Ultrafast Recombination and Trapping in Amorphous Silicon. *Physical Review B* **1990**, *41*, 2879–2884.

(310) Fekete, L.; Kŭzel, P.; Němec, H.; Kadlec, F.; Dejneka, A.; Stuchlík, J.; Fejfar, A. Ultrafast Carrier Dynamics in Microcrystalline Silicon Probed by Time-Resolved Terahertz Spectroscopy. *Physical Review B: Condensed Matter and Materials Physics* **2009**, *79*, 115306.

(311) Fauchet, P. M.; Hulin, D. Ultrafast Carrier Relaxation in Amorphous Semiconductors. *Journal of the Optical Society of America B* **1989**, *6*, 1024–1029.

(312) Titova, L. V.; Cocker, T. L.; Xu, S.; Baribeau, J.-M.; Wu, X.; Lockwood, D. J.; Hegmann, F. A. Ultrafast Carrier Dynamics and the Role of Grain Boundaries in Polycrystalline Silicon Thin Films Grown by Molecular Beam Epitaxy. *Semiconductor Science and Technology* **2016**, *31*, 105017.

(313) Myers, K. E.; Wang, Q.; Dexheimer, S. L. Ultrafast Carrier Dynamics in Nanocrystalline Silicon. *Physical Review B: Condensed Matter and Materials Physics* **2001**, *64*, 1613091–1613094.

(314) Chekulaev, D.; Kaplan, A. Diffusion-Free Ultrafast Carrier Dynamics in Silicon Nano-Pillars. *arXiv* **2009**, *cond-mat.mtrl-sci*, 0902.0939.

(315) Camus, C.; Rudigier, E.; Abou-Ras, D.; Allsop, N. A.; Unold, T.; Tomm, Y.; Schorr, S.; amd T. Köhler, S. E. G.; Klaer, J.; Lux-Steiner, M. C.; Fischer, C.-H. Phonon Confinement and Strain in $CuInS_2$. *Applied Physics Letters* **2008**, *92*, 101922.

(316) Jeong, J. et al. Pseudo-Halide Anion Engineering for α-$FAPbI_3$ Perovskite Solar Cells. *Nature* **2021**, *592*, 381–385.

(317) Mao, Y.; Zhou, H.; Wong, S. S. Synthesis, Properties, and Applications of Perovskite-Phase Metal Oxide Nanostructures. *Material Matters* **2010**, *5*, 50–54.

(318) Jin, J.; Folgueras, M. C.; Gao, M.; Yu, S.; Louisia, S.; Zhang, Y.; Quan, L. N.; Chen, C.; Zhang, R.; Seeler, F.; Schierle-Arndt, K.; Yang, P. A New Perspective and Design Principle for Halide Perovskites: Ionic Octahedron Network (ION). *Nano Letters* **2021**, *21*, 5415–5421.

(319) Goldschmidt, V. M. Die Gesetze der Krystallochemie (The Laws of Crystallochemistry). *Naturwissenschaften* **1926**, *14*, 477–485.

(320) Li, Z.; Yang, M.; Park, J.-S.; Wei, S.-H.; Berry, J. J.; Zhu, K. Stabilizing Perovskite Structures by Tuning Tolerance Factor: Formation of Formamidinium and Cesium Lead Iodide Solid-State Alloy. *Chemistry of Materials* **2016**, *28*, 284–292.

(321) Zarik, H. F.; Soetan, N.; Erwin, W. R.; Bardhan, R. Mixed Halide Hybrid Perovskites: A Paradigm Shift in Photovoltaics. *Journal of Materials Chemistry A* **2018**, *6*, 5507–5537.

(322) Miyata, K.; Atallah, T. L.; Zhu, X.-Y. Lead Halide Perovskites: Crystal-Liquid Duality, Phonon Glass Electron Crystals, and Large Polaron Formation. *Science Advances* **2017**, *3*, e1701469.

(323) Zhu, H.; Miyata, K.; Fu, Y.; Wang, J.; Joshi, P. P.; Niesner, D.; Williams, K. W.; Jin, S.; Zhu, X.-Y. Screening in Crystalline Liquids Protects Energetic Carriers in Hybrid Perovskites. *Science* **2016**, *353*, 1409–1413.

(324) Miyata, K.; Meggiolaro, D.; Trinh, M. T.; Joshi, P. P.; Mosconi, E.; Jones, S. C.; de Angelis, F.; Zhu, X.-Y. Large Polarons in Lead Halide Perovskites. *Science Advances* **2017**, *3*, e1701217.

(325) Zhang, D.; Eaton, S. W.; Yu, Y.; Dou, L.; Yang, P. Solution-Phase Synthesis of Cesium Lead Halide Perovskite Nanowires. *Journal of the American Chemical Society* **2015**, *137*, 9230–9233.

(326) Poli, I.; Hintermair, U.; Regue, M.; Kumar, S.; Sackville, E. V.; Baker, J.; Watson, T. M.; Eslava, S.; Cameron, P. J. Graphite-Protected $CsPbBr_3$ Perovskite Photoanodes Functionalized with Water Oxidation Catalyst for Oxygen Evolution in Water. *Nature Communications* **2019**, *10*, 2097.

(327) Hartono, N. T. P.; Tremblay, M.-H.; Wieghold, S.; Dou, B.; Thapa, J.; Tiihonen, A.; Bulovic, V.; Nienhaus, L.; Marder, S. R.; Buonassisi, T.; Sun, S. Tailoring Capping-Layer Composition for Improved Stability of Mixed-Halide Perovskites. *Journal of Materials Chemistry A* **2022**, *10*, 2957–2965.

(328) Wang, X.; Li, T.; Xing, B.; Faizan, M.; Biswas, K.; Zhang, L. Metal Halide Semiconductors Beyond Lead-Based Perovskites for Promising Optoelectronic Applications. *The Journal of Physical Chemistry Letters* **2021**, *12*, 10532–10550.

(329) Hoefler, S. F.; Trimmel, G.; Rath, T. Progress on Lead-Free Metal Halide Perovskites for Photovoltaic Applications: A Review. *Monatshefte für Chemie* **2017**, *148*, 795–826.

(330) Yang, B.; Chen, J.; Yang, S.; Hong, F.; Sun, L.; Han, P.; Pullerits, T.; Deng, W.; Han, K. Lead-Free Silver-Bismuth Halide Double Perovskite Nanocrystals. *Angewandte Chemie* **2018**, *130*, 5457–5461.

(331) Nagane, S.; Ghosh, D.; Hoye, R. L. Z.; Zhao, B.; Ahmad, S.; Walker, A. B.; Islam, M. S.; Ogale, S.; Sadhanala, A. Lead-Free Perovskite Semiconductors Based on Germanium-Tin Solid Solutions: Structural and Optoelectronic Properties. *Journal of Physical Chemistry C* **2018**, *122*, 5940–5947.

(332) Kopacic, I.; Friesenbichler, B.; Hoefler, S. F.; Kunert, B.; Plank, H.; Rath, T.; Trimmel, G. Enhanced Performance of Germanium Halide Perovskite Solar Cells Through Compositional Engineering. *ACS Applied Energy Materials* **2018**, *1*, 343–347.

(333) Zhang, Y.; Parsonnet, E.; Fernandez, A.; Griffin, S. M.; Huyan, H.; Lin, C.-K.; Lei, T.; Jin, J.; Barnard, E. S.; Raja, A.; Behera, P.; Pan, X.; Ramesh, R.; Yang, P. Ferroelectricity in a Semiconducting All-Inorganic Halide Perovskite. *Science Advances* **2022**, *8*, eabj5881.

(334) Thiele, G.; Rotter, H. W.; Schmidt, K. D. Kristallstrukturen und Phasentransformationen von Caesiumtrihalogenogermanaten(II) $CsGeX_3$ (X = Cl, Br, I) (Crystal Structures and Phase Transformations of Cesium Trihalogermanate(II) $CsGeX_3$ (X = Cl, Br, I)). *Zeitschrift für anorganische und allgemeine Chemie* **1987**, *545*, 148–156.

(335) Gao, L.-K.; Tang, Y.-L.; Diao, X.-F. First-Principles Study on the Photoelectric Properties of $CsGeI_3$ Under Hydrostatic Pressure. *Applied Science* **2020**, *10*, 5055.

(336) Martin, L. W.; Rappe, A. M. Thin-Film Ferroelectric Materials and Their Applications. *Nature Reviews Materials* **2017**, *2*, 16087.

(337) Huang, H. Ferroelectric Photovoltaics. *Nature Photonics* **2010**, *4*, 134–135.

(338) Tan, L. Z.; Zheng, F.; Young, S. M.; Wang, F.; Liu, S.; Rappe, A. M. Shift Current Bulk Photovoltaic Effect in Polar Materials: Hybrid and Oxide Perovskites and Beyond. *npj Computational Materials* **2016**, *2*, 16026.

(339) Montiel, K. A.; Yang, C.; Andreasen, C. H.; Gottlieb, M. S.; Pfefferkorn, M. R.; Wilson, L. G.; Carter, J. L. W.; Martin, I. T. Lead-Free Perovskite Thin Film Solar Cells from Binary Sources. *IEEE 46th Photovoltaic Specialists Conference (PVSC)* **2019**, 1183–1186.

(340) Houari, M.; Bouadjemi, B.; Matougui, M.; Haid, S.; Lantri, T.; Aziz, Z.; Bentata, S.; Bouhafs, B. Optoelectronic Properties of Germanium Iodide Perovskites $AGeI_3$ (A = K, Rb and Cs): First Principles Investigations. *Optical and Quantum Electronics* **2019**, *51*, 234.

(341) Liu, D.; Li, Q.; Jing, H.; Wu, K. Pressure-Induced Effects in the Inorganic Halide Perovskite $CsGeI_3$. *RSC Advances* **2019**, *9*, 3279–3284.

(342) Qian, J.; Xu, B.; Tian, W. A Comprehensive Theoretical Study of Halide Perovskites ABX_3. *Organic Electronics* **2016**, *37*, 61–73.

(343) Mao, X.; Sun, L.; Wu, T.; Chu, T.; Deng, W.; Han, K. First-Principles Screening of All-Inorganic Lead-Free ABX_3 Perovskites. *Journal of Physical Chemistry C* **2018**, *122*, 7670–7675.

(344) Walters, G.; Sargent, E. H. Electro-Optic Response in Germanium Halide Perovskites. *The Journal of Physical Chemistry Letters* **2018**, *9*, 1018–1027.

(345) Müller, T.; Sharma, S.; Gross, E. K. U.; Dewhurst, J. K. Extending Solid-State Calculations to Ultra-Long-Range Length Scales. *Physical Review Letters* **2020**, *125*, 256402.

(346) Géneaux, R.; Chang, H.-T.; Schwartzberg, A. M.; Marroux, H. J. B. Source Noise Suppression in Attosecond Transient Absorption Spectroscopy by Edge-Pixel Referencing. *Optics Express* **2021**, *29*, 951–960.

(347) Verma, S. D.; Gu, Q.; Sadhanala, A.; Venugopalan, V.; Rao, A. Slow Carrier Cooling in Hybrid Pb-Sn Halide Perovskites. *ACS Energy Letters* **2019**, *4*, 736–740.

(348) Huang, L.-Y.; Lambrecht, W. R. L. Vibrational Spectra and Nonlinear Optical Coefficients of Rhombohedral $CsGeX_3$ Halide Compounds with X = I, Br, Cl. *Physical Review B* **2016**, *94*, 115202.

(349) Chen, N.-K.; Bang, J.; Li, X.-B.; Wang, X.-P.; Wang, D.; Chen, Q.-D.; Sun, H.-B.; Zhang, S. Optical Subpicosecond Nonvolatile Switching and Electron-Phonon Coupling in Ferroelectric Materials. *Physical Review B* **2020**, *102*, 184115.

(350) Gu, F.; Murray, É.; Tangney, P. Carrier-Mediated Control Over the Soft Mode and Ferroelectricity in $BaTiO_3$. *Physical Review Materials* **2021**, *5*, 034414.

(351) Lin, Z.-G.; Tang, L.-C.; Chou, C.-P. Characterization and Properties of Novel Infrared Nonlinear Optical Crystal $CsGe(Br_XCl_{1-X})_3$. *Inorganic Chemistry* **2008**, *47*, 2362–2367.

(352) Huang, N.; Deng, H.; Liu, B.; Wang, D.; Zhao, Z. Features and Futures of X-ray Free-Electron Lasers. *The Innovation* **2021**, *2*, 28.

(353) Chen, F. et al. Ultrafast Terahertz-Field-Driven Ionic Response in Ferroelectric $BaTiO_3$. *Physical Review B* **2016**, *94*, 180104(R).

(354) Kozina, M.; van Driel, T.; Chollet, M.; Sato, T.; Glownia, J. M.; Wandel, S.; Radovic, M.; Staub, U.; Hoffmann, M. C. Ultrafast X-ray Diffraction Probe of Terahertz Field-Driven Soft Mode Dynamics in $SrTiO_3$. *Structural Dynamics* **2017**, *4*, 054301.

(355) Kozina, M.; Fechner, M.; Marsik, P.; van Driel, T.; Glownia, J. M.; Bernhard, C.; Radovic, M.; Zhu, D.; Bonetti, S.; Staub, U.; Hoffmann, M. C. Terahertz-Driven Phonon Upconverstion in $SrTiO_3$. *Nature Physics* **2019**, *15*, 387–392.

(356) Guzelturk, B. et al. Visualization of Dynamic Polaronic Strain Fields in Hybrid Lead Halide Perovskites. *Nature Materials* **2021**, *20*, 618–623.

(357) Mariette, C. et al. Strain Wave Pathway to Semiconductor-to-Metal Transition Revealed by Time-Resolved X-ray Powder Diffraction. *Nature Communications* **2021**, *12*, 1239.

(358) Juvé, V.; Gu, R.; Gable, S.; Maroutian, T.; Vaudel, G.; Matzen, S.; Chigarev, N.; Raetz, S.; Gusev, V. E.; Viret, M.; Jarnac, A.; Laulhé, C.; Maznev, A. A.; Dkhil, B.; Ruello, P. Ultrafast Light-Induced Shear Strain Probed by Time-Resolved X-ray Diffraction: Multiferroic $BiFeO_3$ as a Case Study. *Physical Review B* **2020**, *102*, 220303(R).

(359) Kirschner, M. S.; Diroll, B. T.; Guo, P.; Harvey, S. M.; Helweh, W.; FLanders, N. C.; Brumberg, A.; Watkins, N. E.; Leonard, A. A.; Evans, A. M.; Wasielewski, M. R.; Dichtel, W. R.; Zhang, X.; abd R. D. Schaller, L. X. C. Photoinduced, Reversible Phase Transitions in All-Inorganic Perovskite Nanocrystals. *Nature Communications* **2019**, *10*, 504.

(360) Vázquez-Fernández, I.; Mariotti, S.; Hutter, O. S.; Birkett, M.; Veal, T. D.; Hobson, T. D. C.; Phillips, L. J.; Danos, L.; Nayak, P. K.; Snaith, H. J.; Xie, W.; Sherburne, M. P.; Asta, M.; Durose, K. Vacancy-Ordered Double Perovskite Cs_2TeI_6 Thin Films for Optoelectronics. *Chemistry of Materials* **2020**, *32*, 6676–6684.

(361) Folgueras, M. C.; Jin, J.; Gao, M.; Quan, L. N.; Steele, J. A.; Srivastava, S.; Ross, M. B.; Zhang, R.; Seeler, F.; Schierle-Arndt, K.; Asta, M.; Yang, P. Lattice Dynamics and Optoelectronic Properties of Vacancy-Ordered Double Perovskite Cs_2TeX_6 ($X = Cl^-$, Br^-, I^-) Single Crystals. *The Journal of Physical Chemistry C* **2021**, *125*, 25126–25139.

(362) Ping, Y.; Galli, G.; W. A. Goddard, I. Electronic Structure of IrO_2: The Role of the Metal d Orbitals. *The Journal of Physical Chemistry C* **2015**, *119*, 11570–11577.

(363) Lee, Y.; Suntivich, J.; May, K. J.; Perry, E. E.; Shao-Horn, Y. Synthesis and Activities of Rutile IrO_2 and RuO_2 Nanoparticles for Oxygen Evolution in Acid and Alkaline Solutions. *The Journal of Physical Chemistry Letters* **2012**, *3*, 399–404.

(364) Zhong, W.; Lin, Z.; Feng, S.; Wang, D.; Shen, S.; Zhang, Q.; Gu, L.; Wang, Z.; Fang, B. Improved Oxygen Evolution Activity of IrO_2 by *In Situ* Engineering of an Ultra-Small Ir Sphere Shell Utilizing a Pulsed Laser. *Nanoscale* **2019**, *11*, 4407–4413.

(365) Gono, P.; Wiktor, J.; Ambrosio, F.; Pasquarello, A. Surface Polarons Reducing Overpotentials in the Oxygen Evolution Reaction. *ACS Catalysis* **2018**, *8*, 5847–5851.

(366) Anwar, M. S.; Lee, S. R.; amd Y. Sugimoto, R. I.; Tano, Y.; Kang, S. J.; Shin, Y. J.; Yonezawa, S.; Manske, D.; Takayanagi, H.; Noh, T. W.; Maeno, Y. Direct Penetration of Spin-Triplet Superconductivity into a Ferromagnet in $Au/SrRuO_3/Sr_2RuO_4$ Junctions. *Nature Communications* **2016**, *7*, 13220.

(367) Zhen, C.; Zhang, X.-Z.; Wei, W.; Guo, W.; Pant, A.; Xu, X.; Shen, J.; Ma, L.; Hou, D. Nanostructural Origin of Semiconductivity and Large Magnetoresistance in Epitaxial $NiCo_2O_4/Al_2O_3$ Thin Films. *Journal of Physics D: Applied Physics* **2018**, *51*, 145308.

(368) Xu, H.; Shi, Z.-X.; Tong, Y.-X.; Li, G.-R. Porous Microrod Arrays Constructed by Carbon-Confined NiCo@$NiCoO_2$ Core@Shell Nanoparticles as Efficient Electrocatalysys for Oxygen Evolution. *Advanced Materials* **2018**, *30*, 1705442.

(369) Li, Y.; Peng, H.; Yang, L.; Dong, H.; Xiao, P. Investigating the Effect of Sulfur and Selenium on the Electrochemical Properties of Nickel-Cobalt Oxides: Enhanced Charge Capacity and Composition-Property Relationships. *Journal of Materials Science* **2016**, *51*, 7108–7118.

(370) Velegraki, G.; Wamvasakis, I.; Papadas, I. T.; Tsatsos, S.; Pournara, A.; Manos, M. J.; Choulis, S. A.; Kennou, S.; Kopidakis, G.; Armatas, G. S. Boosting Photochemical Acticvity by Ni Doping of Mesoporous CoO Nanoparticle Assemblies. *Inorganic Chemistry Frontiers* **2019**, *6*, 765–774.

(371) Bitla, Y.; Chin, Y.-Y.; Lin, J.-C.; Van, C. N.; Liu, R.; Zhu, Y.; Liu, H.-J.; Zhan, Q.; Lin, H.-J.; Chen, C.-T.; Chu, Y.-H.; He, Q. Origin of Metallic Behaviour in $NiCo_2O_4$ Ferrimagnet. *Scientific Reports* **2015**, *5*, 15201.

(372) Ni, D.; Liu, S.; Wu, M.; Lei, X.; Xu, B.; Jun, S.-C.; Ouyang, C. Strong Jahn-Teller Effect at NiO_4 Tetrahedron in $NiCo_2O_4$ Spinel. *Physics Letters A* **2020**, *384*, 126114.

(373) Dileep, K.; Loukya, B.; Silwal, P.; Gupta, A.; Datta, R. Probing Optical Band Gaps at Nanoscale from Tetrahedral Cation Vacancy Defects and Variation of Cation Ordering in $NiCo_2O_4$ Epitaxial Thin Films. *Journal of Physics D: Applied Physics* **2014**, *47*, 405001.